Lehrstuhl und Institut für Kraftwerkstechnik, Dampf- und Gasturbinen
IKDG
RWTH AACHEN UNIVERSITY

The present work was submitted to the Institute of Power Plant Technology, Steam and Gas Turbines

Numerical investigation of the mistuning influence on the vibration characteristics of a radial turbomachine rotor

Master Thesis

Testa Pietro
Matr. Nr. 463481:

Aachen, the December 26, 2024

Supervising Assistants: M. Sc. Marios Sasakaros
Supervising Professors: Prof. Manfred Wirsum
Prof. Alessandro Fasana

Information (1)

Im ersten Abgabeexemplar ersetzt das Original der Aufgabenstellung (vom Institutsleiter unterschrieben) diese Seite. Im zweiten Abgabe-exemplar ersetzt eine Kopie der Aufgabenstellung diese Seite)

Information (2)

Im ersten Abgabeexemplar ersetzt das Original der Vertraulichkeitserklärung (vom Studierenden und vom Institutsleiter unterschrieben) diese Seite. Im zweiten Abgabeexemplar ersetzt eine Kopie der Vertraulichkeitserklärung diese Seite)

Information (3)

In beiden Abgabeexemplaren ersetzt die vom ZPA bereitgestellte Vor-lage der Eidesstattlichen Versicherung diese Seite. Wichtig ist es hier, dass das ORIGINAL verwendet wird, das Formular vollständig ausgefüllt und unterschrieben ist (das ZPA ist hier recht unerbittlich!)!

Das Formular findet man hier...

http://www.rwth-aachen.de/cms/root/Studium/Im-Studium/Pruefungen-Abschlussarbeiten/ ccwp/

Formularschrank-mit-Suche-und-Filter/

Kurzfassung

Synchrone Schaufelschwingungen können die Lebensdauer von Rotoren stark beeinträchtigen, da ihr Auftreten zu „Limit Cycle Oscillations“ führen kann, die mit der Zeit das Risiko von Bauteilversagen aufgrund von „High Cycle Fatigue“ erhöhen. Eine Eigenschaft, die die Schwingungseigenschaften des Rotors wesentlich beeinflussen kann, ist Mistuning. Mistuning entsteht durch strukturelle Unterschiede zwischen den Schaufeln, welche die Periodizität des Laufrads verletzen. Hauptursachen hierfür sind Fertigungstoleranzen, Materialinhomogenitäten sowie ungleichmäßiger Verschleiß der Schaufeln im Betrieb. Mistuning führt zu einer Lokalisierung der Dissipation von Schwingungsenergie und erheblichen Amplitudenüberschreitungen. Dadurch können die Amplituden einzelner Schaufeln deutlich höher sein als die eines rotationssymmetrischen Systems. Zudem führt Mistuning zu einer Mischung von Schwingungsmoden, die im Frequenzbereich eng beieinander liegen, was zu „mistuned“ Modenformen führt. In diesem Zusammenhang können verstimmte Modenformen, die sich aus Verdichter- und Turbinenmoden zusammensetzen, beide Rotorseiten koppeln und somit Schwingungen über den gesamten Rotor verursachen. Diese Arbeit untersucht das Schwingungsverhalten eines verstimmten Rotors numerisch mittels eines verstimmten FEM-Modells. Ein Vergleich zwischen einem „tuned“ und einem „mistuned“ Rotor wird im Hinblick auf die Lokalisierung von Schwingungen und die Rotorkopplung durchgeführt. Zudem wird die Untersuchung der durch Mistuning auftretenden gekoppelten Moden vorgenommen, um die Mechanismen hinter der Entstehung dieser Moden zu identifizieren. Darüber hinaus werden der Einfluss der Randbedingungen sowie die Auswirkungen verschiedener Mistuning-Muster auf die gekoppelten Moden analysiert. Für die Implementierung der Mistuning-Muster werden experimentelle Daten herangezogen.

IKDG Lehrstuhl und Institut für Kraftwerkstechnik, Dampf- und Gasturbinen
RWTH AACHEN UNIVERSITY

Abstract

Synchronous blade vibrations can have a severe impact on the service life of rotors as their occurrence leads to limit cycle oscillations, which over time increase the risk of component failure due to high cycle fatigue. A property that can substantially influence the vibration characteristics of the rotor is mistuning. Mistuning appears due to structural differences between the blades, which violates the rotational periodicity of the impeller. Manufacturing tolerances, material inhomogeneities and uneven wear of the blades during operation are the main causing factors. Mistuning leads to localized dissipation of the vibration energy and significant amplitude overshoots. As a result, the amplitude of individual blades can be significantly higher than those of rotationally periodic structures. Additionally, mistuning mixes vibration modes that are closely spaced in the frequency domain, leading to mistuned mode shapes. In this context, mistuned mode shapes, which are composed of compressor- and turbine-expressed modes, can couple both rotor sides, causing vibrations across the entire rotor. This thesis investigates the vibrational behaviour of a mistuned rotor numerically using a mistuned FEM model. A comparison between a tuned and a mistuned rotor is conducted in regard to vibration localization and rotor coupling, while an examination of the coupled modes occurring due to mistuning is performed to identify the mechanism behind the appearance of these modes. Furthermore, the impact of the boundary conditions as well as the effect of different mistuning patterns on the coupled modes is investigated. For the implementation of mistuning patterns, experimental data are employed.

Contents

Nomenklatur

Latin symbols

Formelzeichen	Einheit	Beschreibung
$[A]$		Dynamic matrix, state space formulation
AR_{rot}	–	Displacement ampitude ratio for the rotational displaement components on the shaft
AR_{bend}	–	Displacement ampitude ratio for the bending displacement components on the shaft
AR_{norm}	–	Displacement ampitude ratio for the axial displacement components on the shaft
$a_{m,n}$		Best fit estimation for Young's Modulus-Frequency relation, for the mode BMm, NDn
$\mathbf{B}(x, y, z)$	–	Gradients of the shape functions
$[C]$		Generalized damping matrix
$[C_{nr}]$	–	Non-rotating damping matrix
$[C_r]$	–	Rotating damping matrix
$DFT_{ax}(NDn)$	–	Amplitude of the NDn component in the tangential nodal diameter spectrum
$DFT_{ax}(NDn)$	–	Amplitude of the NDn component in the axial nodal diameter spectrum
$DFT_{ND0\&1,eqv}$	–	Parameter quantifying the amount of ND0 and ND1 components, both axial and tangential, on a turbine mode
$f(t)$	N	Forcing function of time
$f_0(t)$	N	Amplitude of harmonic forces
$\mathbf{E}$	–	Elasticity matrix of the element
$E_c^{(test)}$	Pa	Test value of Young's modulus, input of the simulation case of index number c
$[F]$	–	Vandermonde matrix
$\{\mathfrak{F}\}$	–	Nodal diameter spectrum
$\{\mathfrak{F}_\mathfrak{t}\}$	–	Nodal diameter spectrum, considering the tangential components
$\{\mathfrak{F}_\mathfrak{a}\}$	–	Nodal diameter spectrum, considering the axial components
$[G]$	–	Gyroscopic matrix
$[H]_{A\rightarrow B}(\omega)$	m/N	Displacement transfer function matrix i.e. receptance between generic point A and B
$[H]_A(\omega)$	m/N	Displacement transfer function ,matrix i.e. receptance of the subsystem A
$[H]_B(\omega)$	m/N	Displacement transfer function ,matrix i.e. receptance of the subsystem B
j	–	Blade index
k	N/m	In 1-DOF per sector model, stiffness linking mass with frame, idealizing sector internal stiffness
k_i	N/m	In 1-DOF per sector model, stiffness linking masses, idealizing sector-to-sector coupling

Formelzeichen	Einheit	Beschreibung
k_1	N/m	In 2-DOF per sector model, stiffness linking blade to respective disk part
k_2	N/m	In 2-DOF per sector model, stiffness linking disk part to shaft
k_3	N/m	In 2-DOF per sector model, stiffness linking two neighboring blades
$[K]$	–	Stiffness matrix
$[K_\Omega]$	–	Centrifugal stiffening matrix
$[K_S]$	–	Spin softening matrix
$[K_{unsym}]$	–	Anti-symmetric contribution to the stiffness matrix
$\mathbf{K}$	–	Elemental stiffness matrix
i	–	$\sqrt{-1}$
$[I]$	–	Identity matrix
$[O]$	–	Null matrix
$\mathbf{B}(x, y, z)$	–	Mode shape functions
m	kg	Concentrated mass in ROMs
M	kg	In 2-DOF per sector model, disk sector mass
$[M]$	–	Mass matrix
ND_{max}	–	Maximum nodal diameter
ND_{dom}	–	Dominant nodal diameter
N_{nodes}	–	Number of nodes on a given shaft section
$\{q\}$	–	Vector of the degrees of freedom of the system
$q_{CS}^{(n)}$	–	Cyclic symmetry reduced vector of degrees of freedom
t	s	Time
$[T]$	none	Cyclic simmetry reduction matrix
$\mathcal{T}$	J	Kinetic energy
$\mathcal{U}$	J	Potential energy
$u_{x,q}, u_{y,q}, u_{z,q}z$	–	Mode displacement of the q-th node in x,y,z directions
U_x, U_y, U_z	–	Mode displacement sof the shaft in x,y,z directions
u	–	Mode shape nondimensional displacement
u_{turb}	–	Maximum mode shape displacement on turbine tips
u_{comp}	–	Maximum shape displacement on compressor tips
u_{shaft}	–	Maximum mode shape displacement on shaft
$x_{1,j}$	–	In 2-DOF per sector model, coordinate idealizing j-th blade motion
$x_{2,j}$	–	In 2-DOF per sector model, coordinate idealizing j-th disk part motion
$\{z\}$	–	State space vector of the DOFs of the rotor
Z	–	Number of blades/sectors on rotor
Z_{stator}	–	Number of blades/sectors on stator
$\mathfrak{Re}$		Real part
$\mathfrak{Im}$		Imaginary part

Greek symbols

Formelzeichen	Einheit	Beschreibung
symbol	unit	Description
β	s	Coefficient of proportionality of damping to stiffness matrix
γ_j	–	Nondimensional mistuning of j-th blade
δ	N/m	Variation in blade stiffness due to mistuning
Δ	Hz^2	Difference between turbine and compressor eigenvalues (absolute value)
$\phi_{j,j+1}$	–	Inter-blade phase angle
ϕ_r	–	Mode shape r of subsystem
λ	–	Eigenvalue
λ_R	–	Real part of eigenvalue
λ_I	–	Imaginary part of eigenvalue
$[\Lambda^2]$	–	Diagonalized tuned stiffness matrix
ξ	–	Ratio of the maximum blade deflection ans RMS (defined by Klauke)
$\{\eta\}$	–	Modal amplitudes
ν	–	Poisson's Ratio
π	–	3.1415...
ψ	–	Generic element of eigenvector, mode shape evaluated at a point
$[\psi_m]$	–	Mistuned modal matrix
$[\psi_t]$	–	Tuned modal matrix
$\{\psi_m\}$	–	Mistuned eigenvector
$\{\psi_t\}$	–	Tuned eigenvector
$\{\psi_t\}$	–	Tuned eigenvector
ψ_r	–	Mass normalized mode shape r of subsystem
$\psi_r^{(tips)}$	–	Mass normalized mode shape r of subsystem, evaluated on tips points
$\psi_r^{(tips)}$	–	Mass normalized mode shape r of subsystem, evaluated on interface points
$\psi_A^{(i)}$	–	Mode shape evaluated in interface degree of freedom for the subsystem A
$\psi_B^{(i)}$	–	Mode shape evaluated in interface degree of freedom for the subsystem B
$\psi_A^{(t)}$	–	Mode shape evaluated in a tips degree of freedom for the subsystem A
$\psi_B^{(t)}$	–	Mode shape evaluated in a tips degree of freedom for the subsystem B
$\{\rho\}$	kg/m^3	Material density
Θ	1/m	Rotation angle of one section of the shaft, according to mode shape
$\sigma_{\mathbf{0}}(x,y,z)$	Pa	Stress due to centrifugal forces
ω	1/s	Generic frequency coordinate
$\omega_{BMm,NDn,j}^{exp}$	1/s	Experimentally measured frequency of j-th blade, of mode BMm, NDn
ω_E	1/s	Frequency of excitation
ω_r	1/s	Real part of λ_r
$\zeta_{j,j+1}$	–	Ratio of the fourier coefficients (as defined by Klauke)

Acronyms

Abkürzung	Beschreibung
AR	Amplitude Ratio
BC	Boundary Condition
BM	Blade Mode
CFD	Computational Fluid Dynamics
DFT	Discrete Fourier Transform
EO	Engine Order
IKDG	Institut für Kraftwerkstechnik, Dampf- und Gasturbinen
IM	Intentional Mistuning
LokaGra	Degree of Localisation
ND	Nodal Diameter
NDS	Nodal Diameter Spectrum
MAC	Modal Assurance Criterion
MB	Main Blades (compressor blades)
MDOF	Multi Degree Of Freedom
MM	Mixed Mode
ROM	Reduced Order Model
SB	Splitter Blades (of the compressor)
Turb.	Turbine
Comp.	Compressor
Tun	Tuned
Mist	Mistuned

List of Figures

List of Tables

1 Introduction

1.1 Global context

In recent years, the reduction of carbon dioxide emissions has become increasingly important. In the context of turbo machinery, this translates into the need to increase the operational efficiency of the machines.
A substantial part of research and development efforts is focused on optimizing the geometry of mechanical components. In particular, reduction in blade thickness leads to the following advantages:

- Reduction of friction forces and wear between rotor and stator [10]
- Reduction of heat losses due to conduction [10]
- Reduction in dissipations at the trailing edge [11]
- At the same speed and inlet pressure, the turbine can achieve a higher mass flow rate at the outlet [2]

In summary, the optimization of the geometry of the blades would lead to an increase in thermo-mechanical efficiency. Moreover, reducing the rotor mass increases the power-to-mass ratio, which is particularly relevant for aeronautical and transport applications.

One of the main causes of failure during the operation of bladed impellers is High Cycle Fatigue, caused by dynamic stresses resulting from blade vibrations [10]. In fact, most cases of impeller blade fracture are caused by fatigue fracture, as shown in Fig. 1.1 [2]. A typical blade failure due to fatigue is illustrated in Fig. 1.1.

The thickness optimization problem requires knowledge of the exact values of the dynamic stresses and, therefore, of turbine dynamics and aerodynamic interactions. A reduction in the blade thickness would magnify dynamic stresses due to vibration. Therefore, it is important to investigate all aspects of rotor dynamic behaviour of rotors for adequate prediction of vibration-induced dynamic loads. In particular, the precise determination of the resonance operating points and the estimation of the vibration magnitudes are crucial for an accurate assessment of the service life of the impeller.
Flow dynamics aspects like the study of flow dynamics, such as aerodynamic excitation and

Figure 1.1: Example of crack fatigue overwhelmed impeller [2]

damping as well as the structural aspects of damping and mistuning are essential for enhancing understanding toward this goal this goal.

1.2 Synchronous vibration in real operation

Rotor blades travel through an uneven flow field (Fig. 1.2) , which exerts cyclic, time-varying pressure fluctuations on the blades. As a result, in radial turbines, the primary cause of excitation is the interaction between the flow field at the guide vane outlet and the impeller inlet. [10]

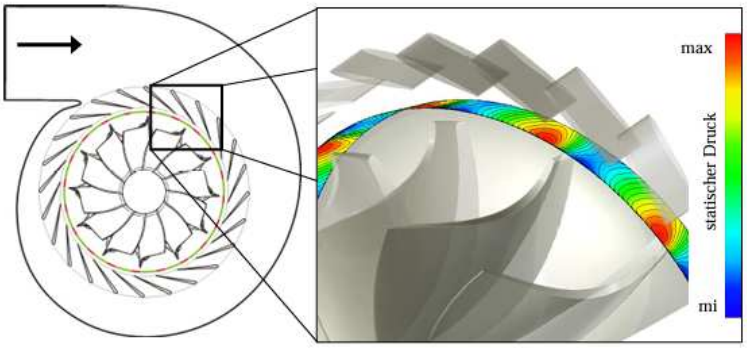

Figure 1.2: Schematic representation of the excitation in a radial turbine stage (left) and static pressure distribution in a plane between guide vanes and rotor blades of a radial turbine from a CFD simulation (right) [3]

[4] For this reason, the primary vibration component occurs at a frequency equal to the rotor speed multiplied by the number of vanes. In general, the excitation frequency ω_E equals an integer times the rotation frequency Ω. This integer multiplier, called the Engine Order (EO), represents the number of excitation periods a blade encounters during one full rotation. (1.1)

$$\omega_E = EO \cdot \Omega, \quad EO \in N^+ \tag{1.1}$$

Equation 1.1 represents the condition of synchronous vibration which discriminates the presence of a resonance point based on the excitation frequency, but this is not the only condition. For resonance to be possible, it is in fact necessary that the excitation is in phase with the vibration mode to be excited. To express this condition it is necessary to consider the modes of a bladed assembly. Consider a tuned bladed assembly composed of Z sectors. Due to cyclic symmetry (rotational periodicity) in the rotor geometry, the sectors of the bladed assembly share identical mode shapes. Each sector mode shape corresponds to Z bladed assembly modes, where the same mode shape repeats across sectors with a constant phase difference ϕ.

$$\phi_{i,j} = 2\pi\frac{ND}{Z} \ , \ ND = 0, 1, ...ND_{max} \tag{1.2}$$

ND is an integer typical of each mode, called *nodal diameter* or *harmonic index*. The ND determines the constant phase difference between two neighbouring blades. This constant phase difference produces mode shapes that follow a harmonic function (sine or cosine) along the rotor circumference.

$$\psi_t, j = \psi_0 \cdot \sin(2\pi ND\frac{j}{Z}) \tag{1.3}$$

We can now explain the meaning of the integer ND, known as the *Nodal diameter*. The Nodal diameter represents the number of periods along the circumference, according to Eq. (1.3). Thus, ND also represents the number of diameter lines where the mode shape evaluates to zero (nodes), which explains the name. From equation (1.2), we see that for ND = 0, modes have zero phase difference between sectors. The other limiting case occurs when the number of blades, Z, is even, and ND = $ND_{max} = Z/2$. In this case, the phase difference between neighboring blades (IBPA) is equal to $\phi_{i,j} = 180°$, each blade vibrates with a phase that is opposite to that of the adjacent blades.

The maximum number of nodal diameters ND_{max} depends on the number of sectors Z (1.4).

$$ND_{max} = \begin{cases} \frac{Z-1}{2}, & \text{for odd } Z \\ \frac{Z}{2}, & \text{for even } Z \end{cases} \tag{1.4}$$

If the number of sectors Z is even, the modes with ND between 1 and $\frac{Z}{2}$ have multiplicity 2 . However, if Z is odd, the modes with ND between 1 and $\frac{Z-1}{2}$ also have multiplicity 2. These are orthogonal solutions, which have the same sector mode and the same number of nodal diameters, are called *twin modes*.

The occurrence of synchronous vibration requires that the excitation frequency matches the natural frequency of the impeller and that the excitation is phase-aligned. For radial centrifugal turbines, Wilson and Utengen [12] proved the condition that links the engine order of excitation to the ND of the mode predominantly excited by that excitation.

$$EO - k \cdot Z = \pm ND, \quad k = 1, 2, 3... \tag{1.5}$$

Equation (1.5) is called *Phase correctness* condition or *internal resonance* condition and it defines the condition for the occurrence of a mode of nodal diameter ND. In a more simpified form, eq. (1.5) can be written as $2\pi\frac{EO}{Z} = \pm 2\pi\frac{ND}{Z} + 2k\pi$. This means that the phase of the excitation seen by the blades $2\pi\frac{EO}{Z}$ must match the inner blade phase angle $2\ \pi\frac{ND}{Z}$.

1.3 Mistuning, definition and effects

The modes of the impeller are obtained by solving the equation of motion for free vibration. When all mode shapes have the same dynamical properties due to symmetry, the *Inter Blade Phase Angle* (IBPA) remains constant, as shown in (1.2). This constant phase difference between neighbouring blades results in mode shapes that form a pure harmonic periodic pattern along the circumferential coordinate of the impeller. The number of periods in this pattern along the circumferential coordinate is equal to the ND of the mode.

In fact, a perfectly tuned impeller, where all the blades have identical properties, cannot be manufactured. Mistuning is the difference in the dynamical properties between turbine blades, due to material inhomogeneities, manufacturing tolerances and uneven wear. Mistuning causes localized hardening and softening on individual blades, disrupting the symmetry between blade sectors. This causes phase difference between blades to be not constant. Mistuning causes the frequencies of *twin modes* to split, whereas for a tuned rotor, these frequencies are coincident. This splitting increases the number of critical speeds.

It is possible to represent the mistuned mode shapes as a superposition of the tuned mode shapes(1.6) [13] . Tuned mode shapes form a linear basis [14], and therefore every single mistuned mode shape $\{\psi_m\}$ can be expressed as a weighted sum of tuned mode shapes $[\Psi_t]$ as shown in equation (1.6)

$$[\Psi_m] = [W][\Psi_t] \tag{1.6}$$

For this reason a mistuned mode shape can be represented as a sum of single harmonics, that correspond to the tuned modes. This leads to a nodal diameter spectrum, which is defined as the series of ND components that compose the mistuned mode. Nodal diameter spectrum is

calculated as **Discrete Fourier Transform** of the mistuned mode across the circumference of the impeller. [13] [15]

Furthermore, mistuning causes random hardening and softening on blades, leading to the concentration of high modal amplitudes on individual blades. This phenomenon is called mode localization. In [8] it is demonstrated numerically that localization in the modes shapes and mode localization increases as a function of the mistuning intensity up to a certain threshold. It is also demonstrated that there is a maximum value of mistuning intensity at which mode localization reaches its peak, beyond which localization decreases. This property is exploited by implementing *intentional mistuning*, where artificially applied high-intensity blade mistuning is used with a pattern designed to reduce modal localization. [5]

1.4 Coupled modes

Furthermore, this thesis aims to investigate the effect of mistuning on the turbine - compressor coupled vibration. The mechanisms that allow coupled vibration of the turbine and compressor are known in the literature [7] [16], and are due to torsion, 'thrust', bending and transverse translation of the shaft. The torsional coupling of the turbine and compressor is associated with nodal diameter of 0 on both the turbine and the compressor. The coupling due to normal 'thrust' forces of the turbine and compressor causes homogeneous movement of the rotors in the axial direction and is therefore associated with a nodal diameter 0.

Coupling mechanisms involving transverse translation on the shaft accompanied by shaft bending that causes 'tilting' of the turbine and compressor wheels is associated with nodal diameter 1 on both wheels. All turbine-compressor coupled modes known in the literature are associated with Nodal Diameter 0 or 1. Therefore, it is established that, in tuned rotors, only ND 0 and ND 1 vibration travels through the shaft.
In fact, for $ND > 1$ modes, resultant momentum carried by blades in rotational or translational directions is equal to 0 and therefore mode does not transmit thoriugh the shaft.

1.5 Research questions

These statements are confirmed by a numerical study of the rotor object of this thesis [17]. In this study researchers have investigated different bearing configurations and their effect on the turbine-compressor coupling. To evaluate the degree of coupling of modes they employed the *Amplitude ratio*, defined by equation (1.7) as the ratio between maximum displacement on turbine and compressor. In this thesis we repeat this study, this time considering the mistuning on the turbine.

$$AR_{\text{turb, comp}} = \frac{\max\{u_{\text{turb}}\}}{\max\{u_{\text{comp}}\}} \tag{1.7}$$

Despite the results of the study, in a previous investigation conducted at IKDG [4] it was observed that an interaction between both impellers and the shaft can exist for modes of higher ND than 0 & 1. Particularly, vibrations with an EO equal to the number of diffuser blades at the compressor were observed at the turbine. Nevertheless the EO of this vibration, according to the Wilson and Utengen phase correctness criterion, leads to a ND5 mode to the turbine impeller. Moreover, the compressor flow seems to significantly influence the vibration characteristics on the turbine side. These results seem to contradict the findings of Klaus and others [16] [7] as it is evident that vibrations with nodal diameter higher than 1 can cause interaction between both impellers. This thesis investigates the hypothesis that mistuning might be responsible for these turbine-compressor interactions with ND>1.

In synthesis, this work targets the following questions:

- ***Is it possible to encounter coupled modes with ND > 1 in mistuned impellers?***
- ***Can the measured resonances with ND¿1, like those observed on the EO17 line, be explained by introducing mistuning?***
- ***What are the physical mechanisms responsible of turbine - compressor coupling?***
- ***What is the influence of the boundary conditions on coupled modes?***

Chapter 2 is presents a resume of the knowledge on the dynamics of tuned and mistuned bladed assemblies. Chapter 3 briefly presents the techniques and the materials used in order to measure mistuning as well as the main results obtained in the experimental bench by my tutor M. Sasakaros. Chapter 4 presents the Finite element Models used to calculate the tuned and mistuned modal properties of the impeller. Chapter 5 presents the procedure used for implementing mistuning on the finite element model. Chapter 6 are presents the evaluation procedure and the results and the comparison the tuned and a mistuned systems. Chapter 7 is presents the interpretation of the coupling between turbine and compressor according to theory considerations. In Chapter 8, we observe the sensitivity of the system to different configurations. Influence of bearing and the interaction with mistuning, has been taken into account repeating the study [17]. Different mistuning patterns on the turbine are tested. Furthermore, mistuning on the compressor blades is implemented.

2 State of the art

2.1 Equations of motion

Rotor vibration can be described through the equation of motion (2.1).

$$[M]\{\ddot{q}\} + [C(\Omega)]\{\dot{q}\} + [K(\Omega)]\{q\} = \{f(t)\} \tag{2.1}$$

$\{q\}$ is a vector that contains all the degrees of freedom on the rotor. [M] is the mass matrix,$[C(\Omega)]$ is generalized damping matrix, while $[K(\Omega)]$ is the generalized stiffness matrix. These generalized stiffness and damping effects are generally dependant on the rotational speed.

f(t) is the forcing function. For a bladed rotor this term is given by the interaction forces with the fluid. Knowledge of these interactions is given by fluid-dynamics simulations. The primary contribution to the forcing function is given by the uneven pressure field in the outlet of the stator vanes [4] [10]. Therefore, the dominant forcing function is harmonic with an EO equal to the number of stator vanes.

$$\{f(t)\} \approx \{f_0(t)\}e^{i \cdot EO \cdot \Omega t},\ E0 = Z_{stator} \tag{2.2}$$

It is useful to consider the equations of motion without the forcing effect due to fluid interactions in order to better understand the properties of the rotor. The homogeneous equations of motion for a generic rotor can be written in matrix form by expanding Eq. (2.1) into the general form given in Eq. (2.3) : [18]

$$[M]\{\ddot{q}\} + ([C_r] + [C_{nr}] + \Omega[G])\{\dot{q}\} + ([K] + [K_\Omega]\Omega^2 - \Omega[C_r] - [K_S])\{q\} = 0 \tag{2.3}$$

The matrices in Eq. (2.3) represent:

$[M]$	Mass matrix
$[C_{nr}]$	Non rotating damping matrix
$[C_r]$	Rotating damping matrix
$[G]$	Gyroscopic matrix
$[K]$	Stiffness matrix
$[K_\Omega]$	Centrifugal stiffening matrix
$[K_S]$	Spin softening matrix

The **mass matrix** represents the inertia carried by the degrees of freedom of the structure.
The **non rotating damping matrix** represents the damping force exerted from outside the rotor, for example the bearings and the action of fluids. Non rotating damping always increases the margin of stability.
Rotating damping matrix, on the other hand represents the sources of damping internal to the rotor, such as the structural damping (hysteresis damping). As the speed increases, rotating damping proportionally reduces the stiffness formulation, potentially causing instability.
Stiffness matrix, (in this notation the stiffness of rotor at speed = 0) represents the link by linear elastic forces between two degrees of freedom.
Gyroscopic terms are inertial terms of a rotor whose sections can rotate and translate along axes perpendicular to the axis of rotation. Physically, it arises from the Coriolis forces. These forces arise from a cross product, coupling the two transverse axes with opposite actions; therefore, the gyroscopic matrix is anti-symmetric.
Centrifugal stiffness matrix $[K_\Omega]\Omega^2$ represents the increase in stiffness due to the state of stress induced by the centrifugal forces on the different parts of the rotor. The matrix $[K_\Omega]$ is a matrix of constant values. To compute this matrix, it is necessary to calculate the stress-strain state by performing a static analysis of the steady-state rotation.
Spin softening effect, [19] is an effect due to the rotational velocity of the structure that reduces the stiffness matrix. The vibration of a spinning body will cause relative circumferential motions, which will change the direction of the centrifugal load which, in turn, will tend to destabilize the structure. It is usually the result of centrifugal forces, causing deformations that modify the geometry of the structure resulting in a less stable configuration. The spin softening contribution is included in Ansys analysis if the model includes pre stress, Coriolis effects and large deformations.

Equation (2.3) can be represented in state space form (2.4)

$$\{\dot{z}\} = [A]\{z\} \tag{2.4}$$

$$[A] = \begin{bmatrix} -[M]^{-1}([C_{nr}] + [C_r] - \Omega[G]) & -[M]^{-1}([K] + \Omega^2[K_\Omega] - \Omega[C_r] - [K_S]) \\ [I] & [0] \end{bmatrix}$$
$$\{\mathbf{z}\} = \begin{bmatrix} \{\dot{q}\} \\ \{q\} \end{bmatrix}$$

Looking for a solution of the type $\{z_0\} \cdot e^{\lambda t}$ the state space formulation yields the eigenvalue problem:

$$([A] - [I]\lambda)\{z_0\} = 0 \tag{2.5}$$

This equation can be expanded to the 2N degree polynomial with real coefficients (N Number of degrees of freedom) whose roots are complex conjugate.

$$\lambda = \lambda_R \pm i\lambda_I \tag{2.6}$$

Where the real part of the eigenvalue in Eq. 2.6 contains information on the stability of the mode. In particular, if the real part is negative, the mode is stable, and its amplitude will decrease exponentially unless the system is externally excited.
The imaginary part of the eigenvalue represents the oscillation frequency of the free response of the rotor. The modes whose eigenvalue have positive imaginary part are called *forward* modes. The modes whose eigenvalues have negative imaginary part are called *backwards* modes. Forward modes represent vibrations that travel in the direction of rotation, while backward modes represent vibrations that travel in the opposite direction. See Fig. 2.1 for illustration.

In general, eigenvalue λ changes with the rotational speed Ω. A plot of the real part of the eigenvalue as a function of the speed is called *stability map*. A plot of the imaginary part as a function of the speed is called *Campbell diagram*.

2.2 Vibration of tuned impellers

This section provides a brief overview on the vibration properties of a single bladed disk, for example the turbine or the compressor can be considered isolated from the rest of the rotor.

Modes of a blade-disk assembly are conventionally subdivided into three families: [5]

- Disk modes, if 70% of the strain energy of the mode resides in the disk structure

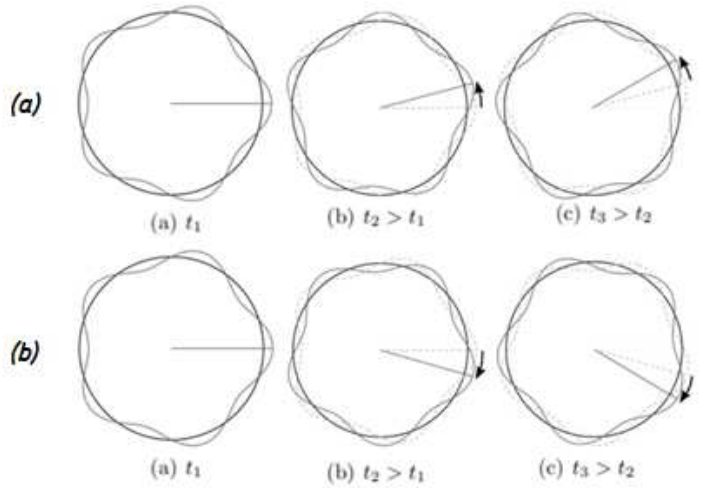

Figure 2.1: Illustration of backward mode (a), forward mode (b)

- Blades modes, if 70% of the strain energy of the mode resides in the blade
- Mixed modes, in case it cannot be clearly classified in one of the previous categories.

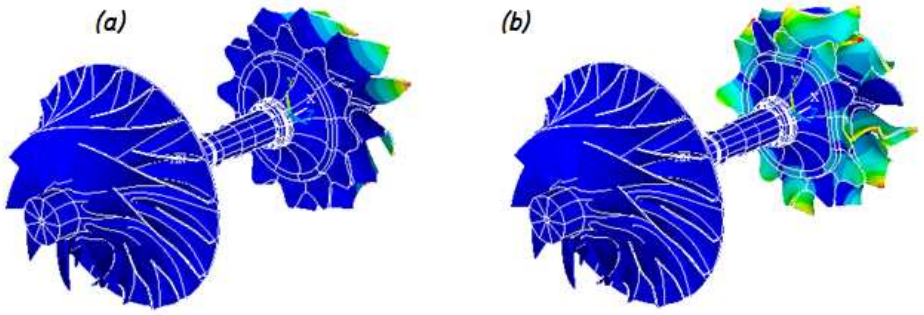

Figure 2.2: Example of a blade dominant mode (a) , and of a mixed mode with strong disk participation (b)

When vibration is concentrated in the blade, the vibration energy is primarily dissipated in a localized area—the blades and the blade root. This leads to high stress levels, which, over time, cause considerable fatigue on the impeller. For this reason, the blade modes are of particular concern.

2.2.1 Blade modes

To describe the vibration of bladed disks, it is helpful to first consider the vibration of individual blades. Using FEM analysis and experimental methods, the mode shapes and the mode frequen-

cies can be computed. Fig. 2.3 shows the FEM calculated blade mode shapes which occur in the frequency range 0 : 18000 Hz.

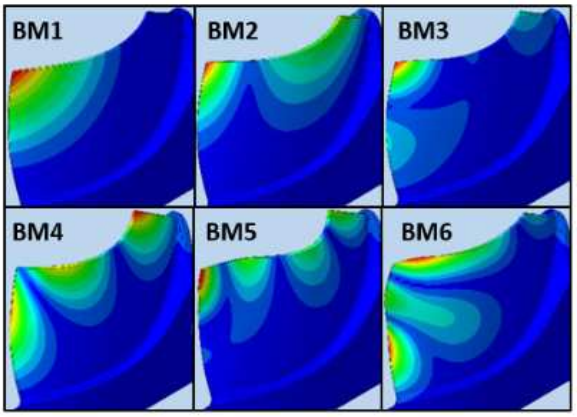

Figure 2.3: Deflection of mode shapes of the turbine blades, of the radial turbine of this thesis [4] [5]

Table 2.1: Approximate frequency ranges for the first six blade mode families

Blade mode 1	$\approx$ 3500:4000 Hz
Blade mode 2	$\approx$ 7500:8000 Hz
Blade mode 3	$\approx$ 8800:9700 Hz
Blade mode 4	$\approx$ 9000:9400 Hz
Blade mode 5	$\approx$ 13500:14000 Hz
Blade mode 6	$\approx$ 15000:17800 Hz

The resonant frequencies are given as an interval (Tab. (2.1)) because the single blades are not independent. Instead neighbouring blades interact elastically with each other, creating blade assembly modes. For each blade mode there are Z bladed assembly modes. Frequencies of modes belonging to the same blade mode family differ slightly from one another, depending on the strength of the elastic coupling between the blades. Moreover, due to centrifugal stiffening, spin softening, gyroscopic effect and rotating damping, blade mode frequency are also influenced by the speed of rotation Ω of the rotor, as shown by the Campbell diagram, presented in Sec. 2.2.3.

2.2.2 Blade interaction and Nodal diameter spectrum

Since the blades are mounted on a disk that is not infinitely rigid, they interact elastically with the neighbouring blades. Besides the disk, the aero-elastic coupling between two blades contributes to this interaction, but it is usually of a much lower order of magnitude relative to blade coupling [20]. The blade to blade interaction can be conceptualized with the use *Reduced-order models (ROM)*. The simplest and most commonly adopted ROMs are the "One Degree of Freedom per Sector" model (1-DOF), represented in Fig. 2.5 or the "Two Degree of Freedom per Sector"

2-DOF, represented in Fig. 2.4 [13] [6]. However, to ensure the accurate representation of the interaction, finite element models with thousands of degrees of freedom are required.

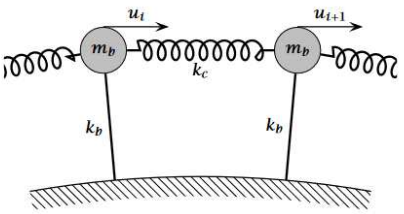

Figure 2.4: Scheme of the 1-DOF per sector model

The 1-DOF per sector model is the simplest conceptualization of a turbine rotor. It abstracts the motion of the blade mode with a mass and a stiffness attached on a rigid frame. Coupling between blades is modelled as a spring between two blades.

The equation of motion for the i-th sector is then:

$$m\ddot{u_j} + ku_j - k_i(u_{j+1} + u_{j-1}) = f \tag{2.7}$$

- j: blade index
- m : mass idealizing sector inertia
- k : stiffness linking mass with frame, idealizing sector internal stiffness
- k_i : stiffness linking masses, idealizing sector to sector coupling
- u_j: j-th sector displacement

Imposing harmonic solution as $u_j = u_{j,0} \cdot e^{i\Omega t}$ and solving for $u_{j+1,0}$ we obtain the algebraic equation which relates the amplitudes of the sectors:

$$u_{j+1,0} = \frac{1}{R}(1 - \frac{\Omega^2}{\omega_N^2})u_{j,0} - u_{j-1,0} \tag{2.8}$$

Where $R = \frac{k_i}{k}$ and $\omega_N = \sqrt{\frac{k}{m}}$

Since the assembly is circular, with Z sectors, it is evident that the periodicity constraint in Eq. 2.9 must be respected:

$$u_{j+Z,0} = u_{j,0} \tag{2.9}$$

Assuming that $u_j = u_{j,0}$ and that there is a phase difference between j-th and j+1-th blade equal to $\phi = 2\pi(h-1)/Z$, then, in complex notation, $u_{j+1} = u_{j,0} \cdot e^{i\phi}$

It can be written:

$$[1 + 2R(1 - \cos(2\pi\frac{h-1}{Z} - \frac{\Omega_r^2}{\omega_N^2})] \cdot u_{j,0} = 0 \tag{2.10}$$

looking for non null solutions of Ω_r^2:

$$\Omega_r^2 = \omega_N^2 \cdot \left[1 + 2R\left(1 - \cos\left(\frac{2\pi(h-1)}{Z}\right)\right)\right] \tag{2.11}$$

and

$$u_j = \cos(2\pi h \cdot \frac{j}{Z}) \tag{2.12}$$

Where h is a scalar harmonic index. It represents the number of periods of the mode shape along the tangential coordinate. The maximum value of h depends on the number of sectors Z,it evaluates to Z/2 if Z is even, and (Z-1)/2 if Z is odd. This index takes the name of **Nodal diameter**. For $n = 0$, all the sectors vibrate in phase and $\Omega_r = \omega_n$. In the 1-DOF per sector model the natural frequency increases monotonically with the nodal diameter.

The maximum nodal diameter, with Z even, is equal to Z/2 and represents the mode in which neighbouring sectors have a phase difference of 180°.

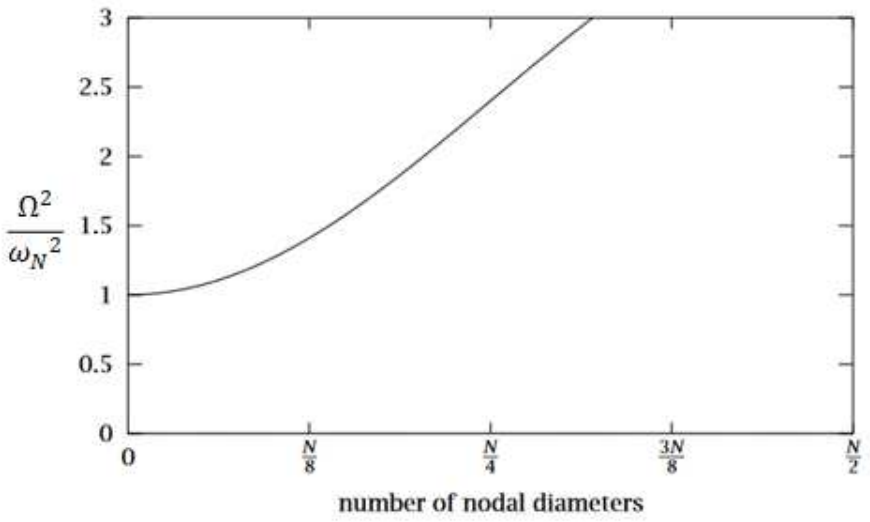

Figure 2.5: Resonance frequency dependency on Nodal diameter for 1-DOF per sector model

A slightly more complex model is the two degrees of freedom of the blade mass and the sector disk mass respectively. The blade is coupled to the disk with a spring. The sector disk masses are connected to each other by a spring, representing the inter-disk stiffness.

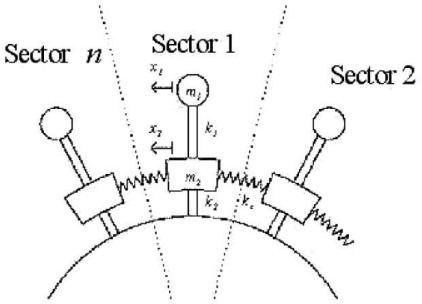

Figure 2.6: Scheme of the 2-DOF per sector model

The equations of the model are: For the disk masses:

$$M\ddot{x_{2,j}} + k_2 x_{2,j} - k_3 x_{2,j+1} - k_3 x_{2,j-1} - k_1(x_{1,j} - x_{2,j}) = 0 \tag{2.13}$$

and for the blade masses:

$$m\ddot{x_{1,i}} + k_1(x_{1,i} - x_{2,i}) = 0 \tag{2.14}$$

- $x_{1,j}$ coordinate idealizing i-th blade motion
- $x_{2,j}$ coordinate idealizing i-th disk part motion
- m blade mass
- M disk sector mass
- k_1 stiffness linking blade to respective disk part
- k_2 stiffness linking disk part to shaft
- k_3 stiffness linking two neighbouring blades

By solving the eigenvalue problem in the same way as the 1-DOF per sector model Z blade dominant modes and Z disk dominant modes are found.

An important result of this simplified model (Fig. 2.7) , which is a general property of all bladed assemblies [20], is that the disk dominant modes, compared to the blade dominated modes, have a stronger elastic inter-sector interaction, therefore show a larger frequency variation with different nodal diameter modes within the same blade mode family.

By solving the eigenproblem of a realistic bladed assembly model realized with FEM, the harmonic patterns described by Eq.(2.12) are revealed for each blade mode family, and are represented in Tab. 2.2 .

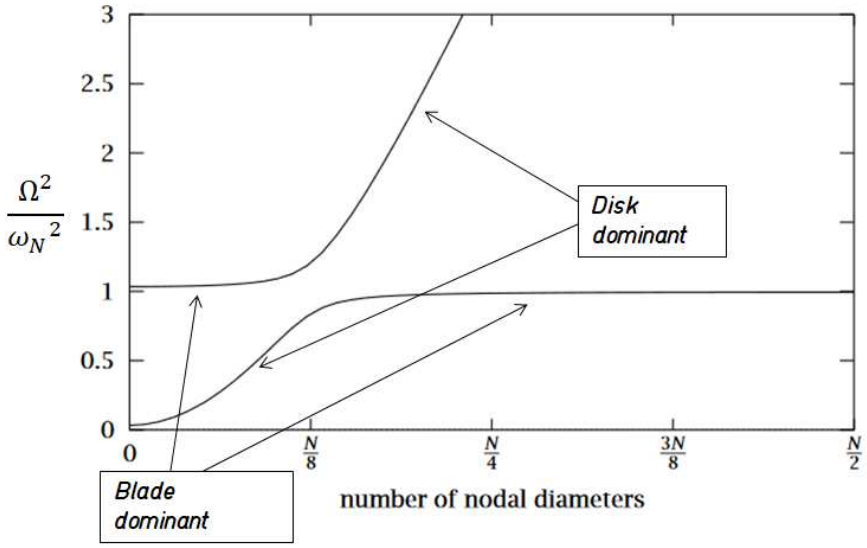

Figure 2.7: Resonance frequency dependency on Nodal diameter for the 2-DOF per sector model [6]

ND	0	1	2	...	6
BM1	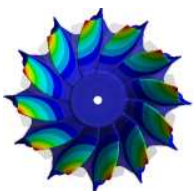	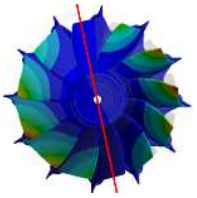	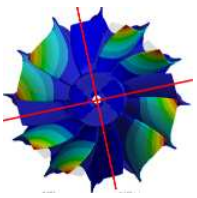	...	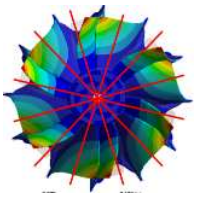
BM2	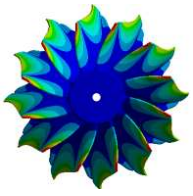	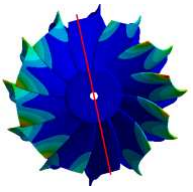	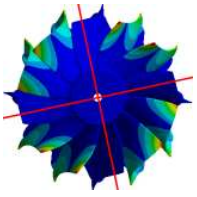	...	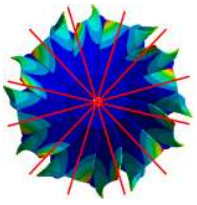
BM3	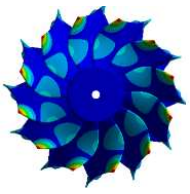	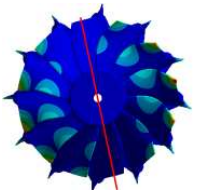	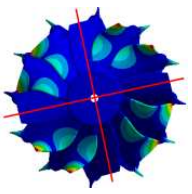	...	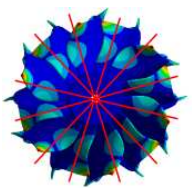
⋮	⋮	⋮	⋮	⋮	⋮

Table 2.2: Mode shapes of turbine model, showing harmonic patterns with number of nodal diameter ND = 0,1,...ND_{max}

Nodal diameter 6 is the highest possible nodal diameter observable in this assembly, as it is composed of 12 sectors. For the highest nodal diameter, each sector vibrates in opposition to the neighbouring sectors.

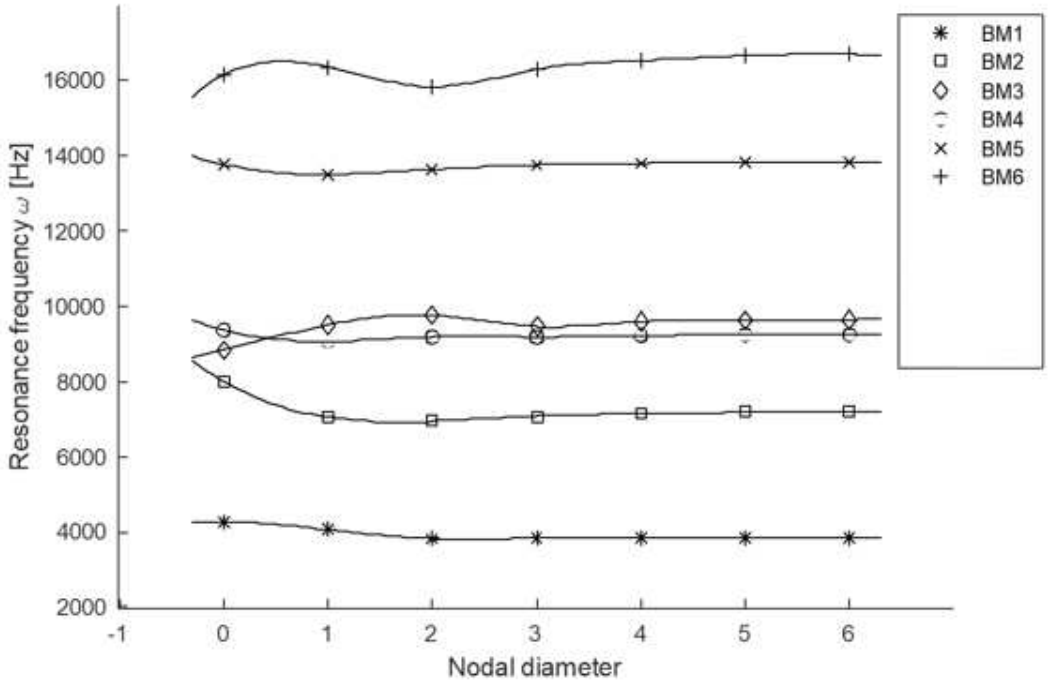

Figure 2.8: Chart of first 6 blade mode families frequency and Nodal diameter

Fig. 2.8 shows , for the turbine object of this thesis, the variation of each blade mode family's natural frequency with its nodal diameter. Unlike the 1-DOF per sector model frequency does not increase monotonically with ND.

2.2.3 Campbell diagram

The Campbell diagram offers great insights on the dynamic behaviour of the rotor. the imaginary part of a mode's eigenvalue represents the vibration frequency of the mode. Modes whose frequency curve increases with speed are modes in which hardening prevails. Figure 2.10 shows that in turbo machines, the blade dominated modes are strongly hardening as the centrifugal effects prevail. Disk dominant modes are less sensitive to speed. Coupled blade-disk modes present a veering region, as the blade part becomes more important with increasing frequency, or conversely it may transition to blade dominant to disk dominant by increasing rotating speed. [7]

Not all points on the Campbell curve represent possible resonances. In fact, in order for synchronous vibration to occur, excitation frequency must be an integer multiple of the rotational speed, satisfying the condition in Eq. (2.15).

$$\omega = \pm EO \cdot \Omega, \quad EO = 1, 2, 3, ... \tag{2.15}$$

Equation (2.15) can be represented on the Campbell diagram as a straight line passing through the origin. Intersection points between Campbell curves and Engine order lines represent the synchronous vibration resonance points. Fig.2.9 shows an exemplary Campbell diagram. Assuming an engine order of excitation EO, forward synchronous vibration resonance points are given by the intersection in the positive ω between Campbell curves and the line $\omega = EO \cdot \Omega$, and are represented in blue. Backward synchronous vibration resonance points are given by the intersection between Campbell curves and the line $\omega = -EO \cdot \Omega$, and are represented in red.

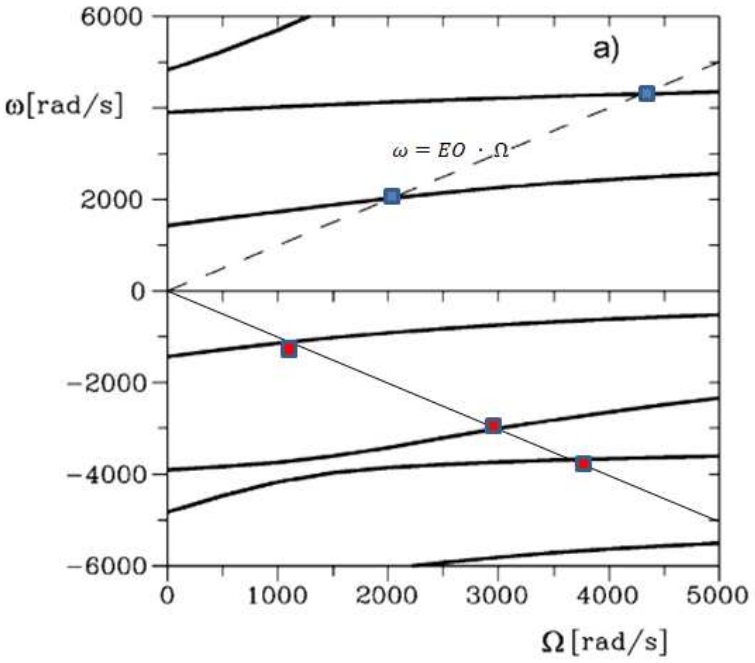

Figure 2.9: Exemplary Campbell diagram showing multiple modes and respective *forwards* and *backwards* synchronous resonance points.

Figure 2.10 shows, for a mixed blade-disc mode, the mutual interaction of the Campbell curves. Blade modes (solid black line) exhibit marked hardening behaviour due to centrifugal actions, which leads to an increase in natural frequency as speed increases. Disk modes, on the other hand, are relatively insensitive to centrifugal hardening (solid brown line). The coupling of blade and disk gives rise to two modes (dashed black lines). The lower frequency curve corresponds to the mode that represents the vibration in the blade and disk phase. The higher frequency mode represents phase-opposed vibration of disk and blade.

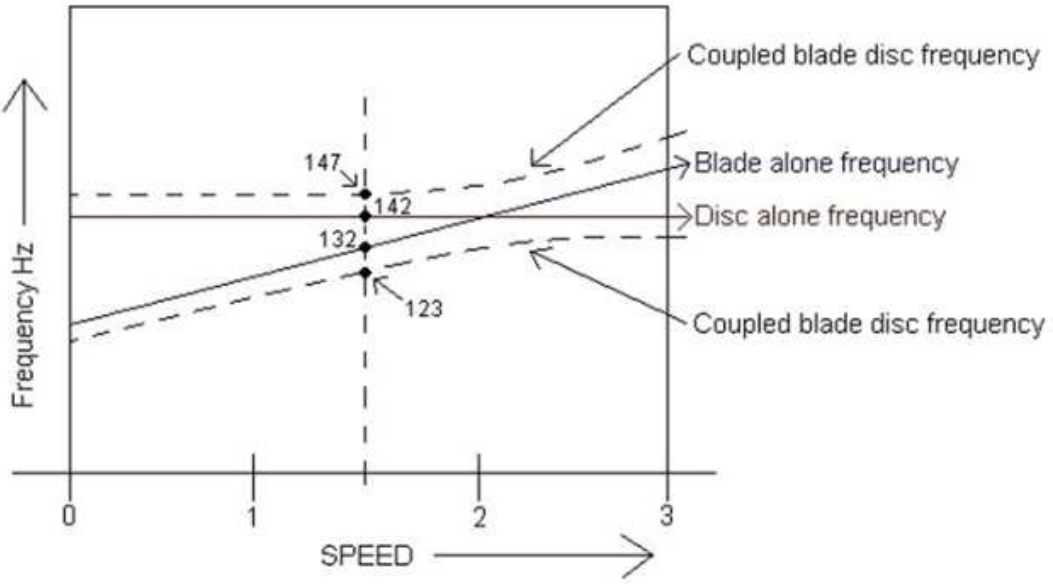

Figure 2.10: Exemplary Campbell diagram of a disk-blade coupled mode [7]

2.2.4 ZZENF diagram

A useful tool for visualising the conditions for synchronous resonances is the ZZENF diagram.In this diagram (Fig. 2.11), the nodal diameter is represented on the x-axis, while the vibration frequency is represented on the y-axis. The vibration frequency for synchronous vibrations depends on the rotational speed and the engine order EO of the excitation. The engine order and mode nodal diameter are related through the Wilson Utengen equation. The coloured zig-zag lines represent, for a given rotation speed, the locus of the synchronous vibration conditions and the phase correctness criterion. The upward part of the zig-zag line represents forward modes, while the downward part represents the backward modes. Blue dots represent the resonant frequency of blade mode families and mixed modes families with their different nodal diameter configurations. A resonance occurs when the blue dots representing a mode lies on a coloured line representing the synchronous vibration conditions.

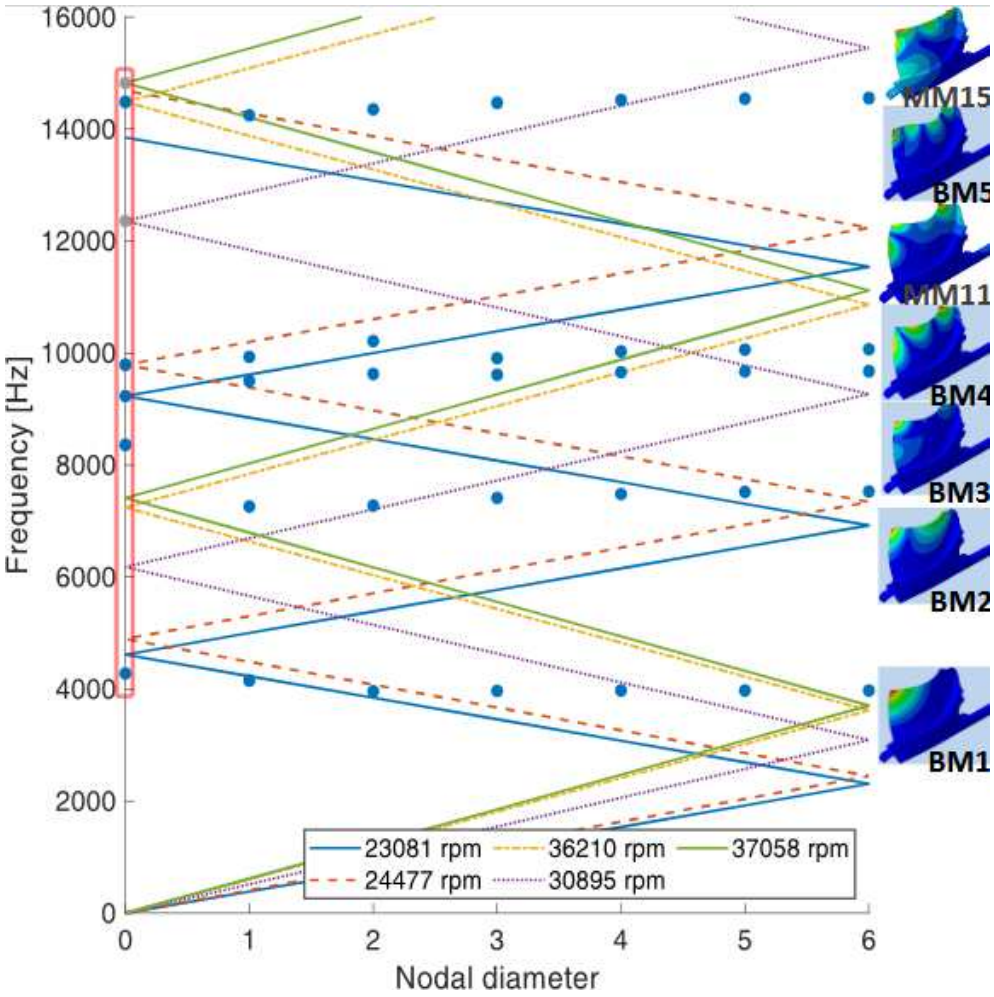

Figure 2.11: ZZENF diagram of the turbine rotor part of the impeller object of this thesis [1]

2.2.5 Impact of operating conditions

Effect of speed

The effect of rotational speed is captured in the Campbell diagram of the system. The effects that cause frequency change with speed, with reference to the equation of motion (2.3) are:

- Centrifugal stiffening or *Spin stiffening*, proportional to Ω^2
- Spin softening
- Rotating damping, softening effect proportional to Ω
- Gyroscopic effect, stiffening effect proportional to Ω

The Campbell diagram of the rotor is analysed in Section 4.7. This diagram is generated by performing a prestressed modal analysis of the system at various rotational speeds. By solving

this analysis, the relationship between the rotor's natural frequencies and its rotational speed can be effectively captured.

To understand the influence of rotational speed on the natural frequencies of the impeller, it is crucial to account for the stress distribution within the impeller at a given speed when solving the eigenvalue problem. This can be achieved numerically through a prestressed modal analysis, which incorporates the effect of centrifugal forces. The detailed procedure for performing this analysis is outlined in 2.4.2.

Centrifugal stiffening arises from the static state of stress and deformation induced by centrifugal forces during rotation. As the rotor spins, these forces cause the material of the impeller to stretch outward, which, in turn, alters the stiffness characteristics of the system. This effect must be incorporated into the analysis to ensure accurate predictions of the dynamic behaviour.

Prestressed modal analysis begins with a static solution for the stationary rotor rotating at a specific speed, Ω. The result of this static analysis includes the stress distribution (illustrated in Figure 2.12) and the associated deformations (depicted in Figure 2.13) caused by the centrifugal forces. These results form the basis for the subsequent modal analysis.

Using the stress and deformation state obtained from the static analysis, the software computes the centrifugal stiffening matrix $[K_\Omega]$. This matrix represents the changes in the system's stiffness due to the rotational speed. Incorporating $[K_\Omega]$ into the modal analysis ensures that the natural frequencies reflect the effects of centrifugal forces, providing a realistic assessment of the rotor's dynamic characteristics at various operating conditions.

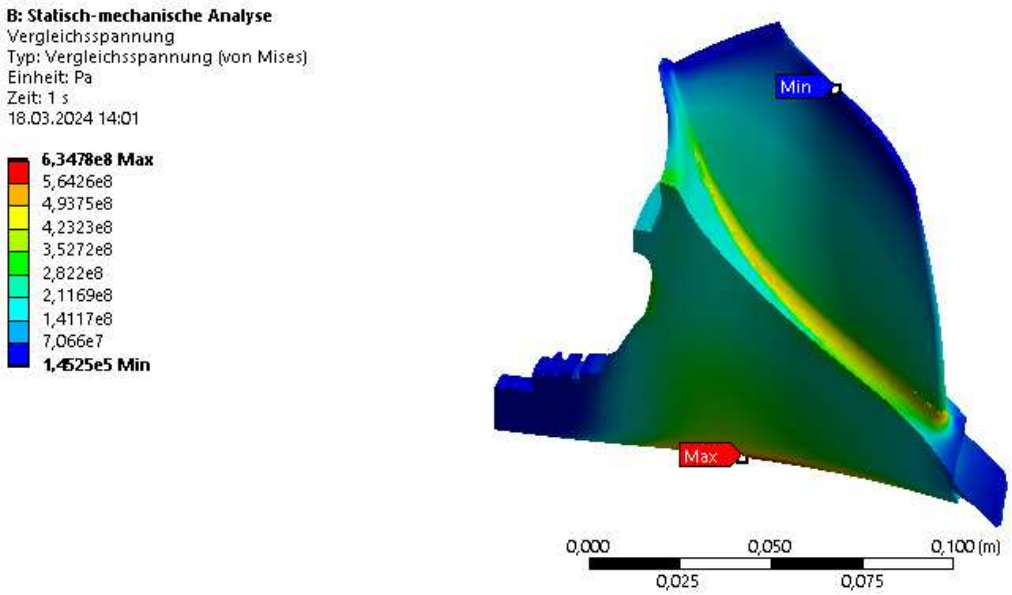

Figure 2.12: Von Mises stress on the sector due to centrifugal forces at 35000 RPM

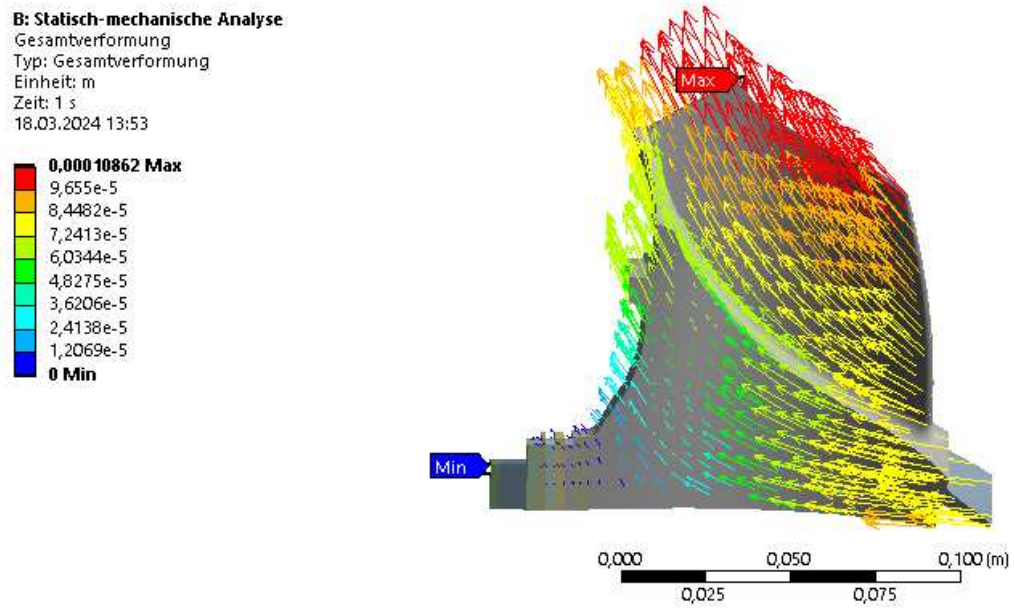

Figure 2.13: Deformation field on the sector due to centrifugal forces at 35000 RPM

Effect of gas temperature

Turbine comes into contact with exhaust gas from a heat source whose temperature changes substantially with working conditions of the machine. An increase in temperature causes a decrease in the elastic properties, causing softening in the turbine blades, according to data in table 2.3. The effect of temperature can be taken into account by downscaling the eigenvalues of the turbine proportionally as a function of the square root of the Young Modulus.

Table 2.3: Young's Modulus IN713C/LC (Pratt & Whitney)

Temp. [°F / °C]	Young's Modulus [psi / GPa]
78 / 25.6	29.94×10^6 / 206.4
200 / 93.3	29.48×10^6 / 203.3
400 / 204.4	28.72×10^6 / 198.0
600 / 315.6	27.97×10^6 / 192.8
800 / 426.7	27.17×10^6 / 187.3
1000 / 537.8	26.16×10^6 / 180.4
1200 / 648.9	25.14×10^6 / 173.3

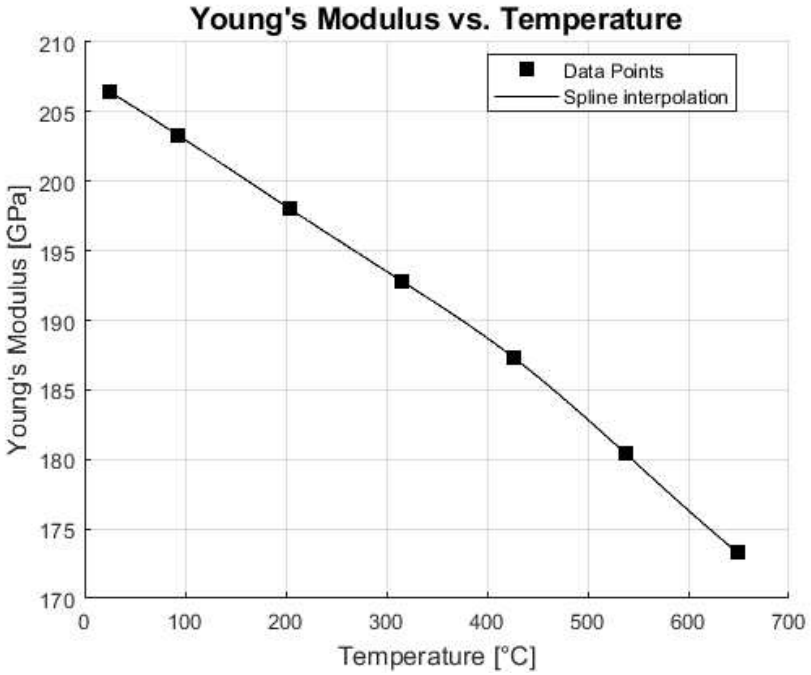

Figure 2.14: Young Modulus of the turbine material dependence on the temperature IN713C/LC (Pratt & Whitney)

2.2.6 Coupling of turbine and compressor

There are only four mechanisms known in the literature that allow coupled vibration between the turbine and compressor. [7]. These are:

- Torsional vibration of the shaft, causing in-phase vibration of the blades (with nodal diameter 0) as shown in figure 2.15
- Normal (axial) vibration of the shaft, causing umbrella-like in phase vibration of the blades (with nodal diameter 0) shown in figure. 2.16
- The rigid vibration of the shaft transversal to its axis, causing vibration of the blades with opposite phase (ND = 1) on the two sides.
- Bending vibration of the shaft, resulting in tilting of the rotor, causing the blades on opposite sides to vibrate with opposite phase (ND1). It is represented in figure 2.17

From this, it follows that coupled vibrations between turbine and shaft, and between compressor and shaft, are possible only for rotor modes with nodal diameter 0 or 1.

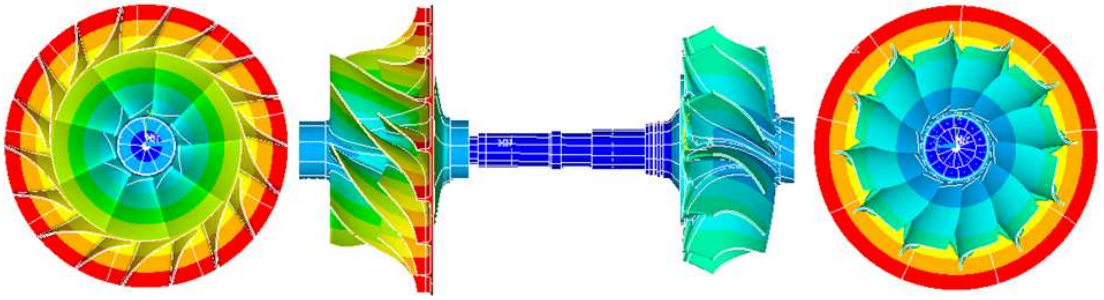

Figure 2.15: Torsion coupled mode, with ND0 vibration of the turbine and compressor

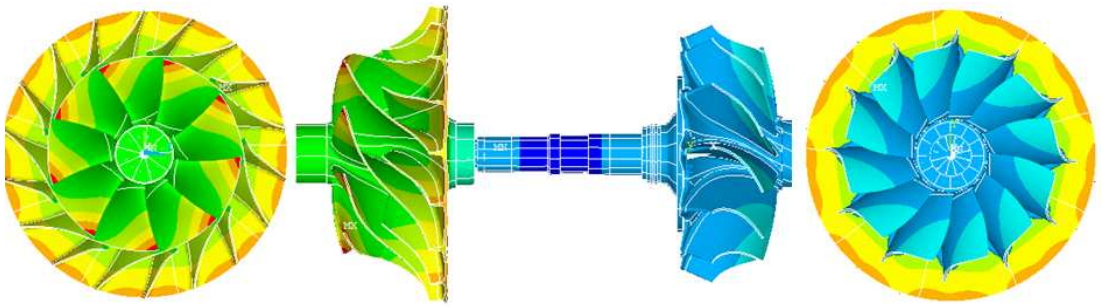

Figure 2.16: Axially coupled mode, with *umbrella* ND0 vibration of the turbine and compressor

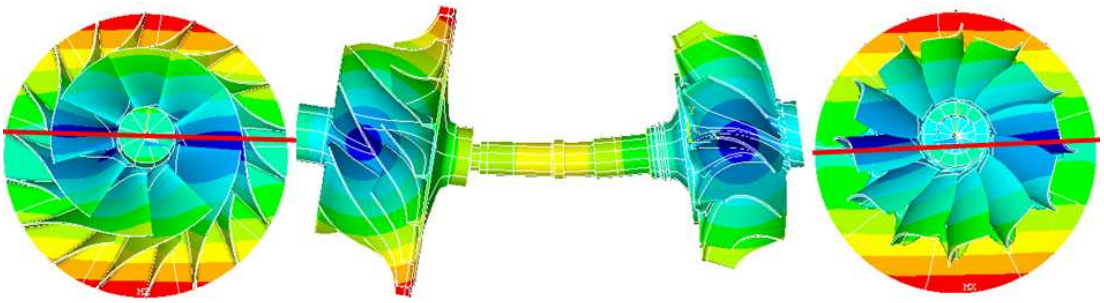

Figure 2.17: Bending coupled mode, with ND1 vibration on turbine and compressor

2.2.7 Effect of boundary conditions (bearings)

For the same turbo-compressor geometry used in this thesis, Zobel et al. [17], investigated the modes of a tuned rotor with different bearing configurations.

In their work, they analysed changes in axial and radial bearing stiffnesses, showing comparisons of the main modes' frequencies and shapes.

Higher bearing stiffnesses cause an increase in frequency of the 'rigid' mode shapes of the shaft, but also lead to changes in the higher frequency modes which is not intuitive and can be in both directions.

Name	Description	Setup of bearings
FRB	Fixed at radial bearings	radial: all DOF suppressed thrust: not modeled
FBC	Full modeled boundary condition	radial: Ref. values thrust: Ref. values
LOW	Low damped setup	radial: Ref. values thrust: 1% of Ref. values
FAD	Fixed DOF in axial direction	radial: Ref. values thrust: axial DOF suppressed

Table 2.4: Description and setup of bearings in the paper of Beirow & others

To quantify the degree of coupling of a mode, authors use the displacement **Amplitude Ratio**, defined as the ratio between maximum displacement on the two impellers:

$$AR_{turb} = \frac{u_{max,turb}}{u_{max,comp}}; AR_{comp} = AR_{turb}^{-1} \tag{2.16}$$

A mode is more coupled the closer the AR is to 1.

Authors' results can be summarised:

- In all cases authors confirm that only ND0 and ND1 can cause AR close to 1.
- For the Fixed Radial Bearings (FRB) condition, authors found there are no coupled modes, as the lowest AR is 2500
- Releasing radial degrees of freedom, from FRB to FRC, allows many coupled modes to emerge, as bending and rotation/torsion of the shaft are allowed.
- Between LOW, FBC, FAD few significant variations are observed. Particularly, a few selected modes seem to show significant variability in AR.

2.3 Vibration of mistuned impellers

2.3.1 Mistuning definition

Mistuning is defined as the difference in the dynamic properties of a bladed assembly. It is caused by various phenomena of different nature. The main causes of mistuning are:

- Blade geometric tolerances associated with manufacturing techniques: The complex geometry of a radial turbine requires tolerances to allow manufacturing. Even small variations in blade thickness and surfaces have effects on the natural frequencies of the blade.

- Material inhomogeneity leads to variations in density and Young's modulus, both between different blades and even within a single blade. In steel alloy castings, density in particular tends to be inhomogeneous due to the solidification process.

- Uneven wear, during the operational life of the turbine can develop or increase existing mistuning. Existing mistuning causing vibration intensification increases wear rate on selected blades and leads to the formation of micro-cracks on the blade root.

2.3.2 Effect of mistuning on frequencies

To understand the effect of mistuning on the natural frequencies of an impeller it is possible to refer to the simplest model: the 1-DOF per sector model. A reasonable way to represent mistuning by introducing a variation in the value of the spring k to the $k + \delta k$. Experimental evidence shows that mistuning on the disk is less significant, and since the coupling is primarily determined by the disk, the coupling stiffness can be considered tuned.

Representing the equation of the 1-DOF per sector in matrix form as:

$$m\ddot{u_j} + (k + \delta)u_j - k_i u_{j-1} - k_i u_{j+1} = 0 \tag{2.17}$$

$$\begin{pmatrix} m & 0 & \dots & 0 \\ 0 & m & \dots & 0 \\ \vdots & \vdots & \ddots & \vdots \\ 0 & 0 & \dots & m \end{pmatrix} \begin{pmatrix} \ddot{u_1} \\ \ddot{u_2} \\ \vdots \\ \ddot{u_Z} \end{pmatrix} + \begin{pmatrix} k+\delta_1 & -k_i & \dots & -k_i \\ -k_i & k+\delta_2 & \dots & 0 \\ \vdots & \vdots & \ddots & \vdots \\ -k_i & 0 & \dots & k+\delta_Z \end{pmatrix} \begin{pmatrix} u_1 \\ u_2 \\ \vdots \\ u_Z \end{pmatrix} = 0 \tag{2.18}$$

δ is the random variable representing blade stiffness mistuning. It is possible to estimate the range of the natural frequencies of the mistuned wheel using Gerschgorin's circle theorem. The eigenvalues of the system are located within the union of Z circles, where each circle corresponds to a column of the stiffness matrix. The position of the centres of the circles is equal to the value on the diagonal: $k + \delta_i$. The radius of each circle is given by the sum of all the off-diagonal elements in the corresponding row, therefore Radius $= 2k_i$. Since the interface stiffness k_i is not affected by mistuning it is constant, and the radius is the same for all circles. Due to the random parameter δ each circle centre shifts of the mistuning term δ_i of the i-th blade.

The superposition of all the circles, Fig. 2.18, gives an envelope of possible eigenvalues in the interval $[\frac{k}{m} - 2\frac{k_i}{m} - \frac{|\delta_{max}|}{m}, \frac{k}{m} + 2\frac{k_i}{m} + \frac{|\delta_{max}|}{m}]$.
A general result of this mistuning model is that random mistuning broadens the span of the eigenvalues of the bladed assembly. For a tuned system, the span between the maximum and the minimum eigenvalue of the structure is given by the *strength of the coupling* k_i. When random mistuning is considered , all eigenvalues and eigenvectors are randomly perturbed. Furthermore, the mistuning term δ_i causes the range of the impeller eigenvalues to expand. For a mistuned

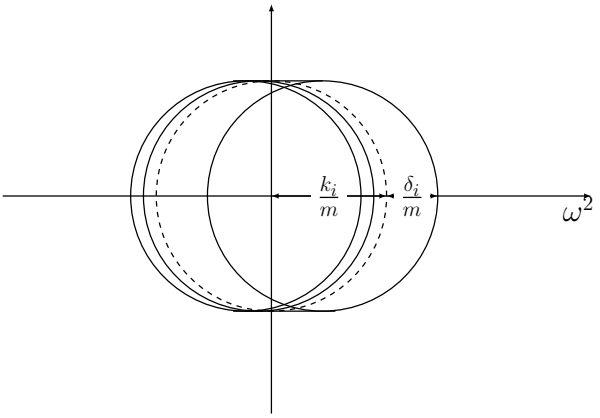

Figure 2.18: Gerschgorin circles for the 1-DOF per sector ROM, represented in the complex plane. Dotted circle represents the tuned range for eigenvalues.

impeller this implies a wider resonance area for any given blade mode family, resulting in increased fatigue issues and larger critical speed areas.

Furthermore, the frequencies of the *twin modes*, which in a tuned case are equal at pairs, in the mistuned case split into two very close natural frequencies [15]. This split has little effect for modes which in frequency domain are spaced enough from other modes. In such cases, it is possible to relate a mistuned mode to its corresponding tuned mode. In cases when modes with different ND are closely spaced in frequency domain, it is not possible to relate a mistuned mode to a single tuned mode. Figure 2.19 shows the output of a BTT measurement after applying a rotational speed sweep. The resonance peaks observed correspond to the natural frequencies of the modes. If the turbine were tuned, only one peak corresponding to ND0 in left picture, ND6 in right picture would be observed. However, mistuning causes the modes to exhibit a combination of NDs, with all modes being excited to some degree. Additionally, frequency splitting can be observed in peaks that are closely spaced in frequency.

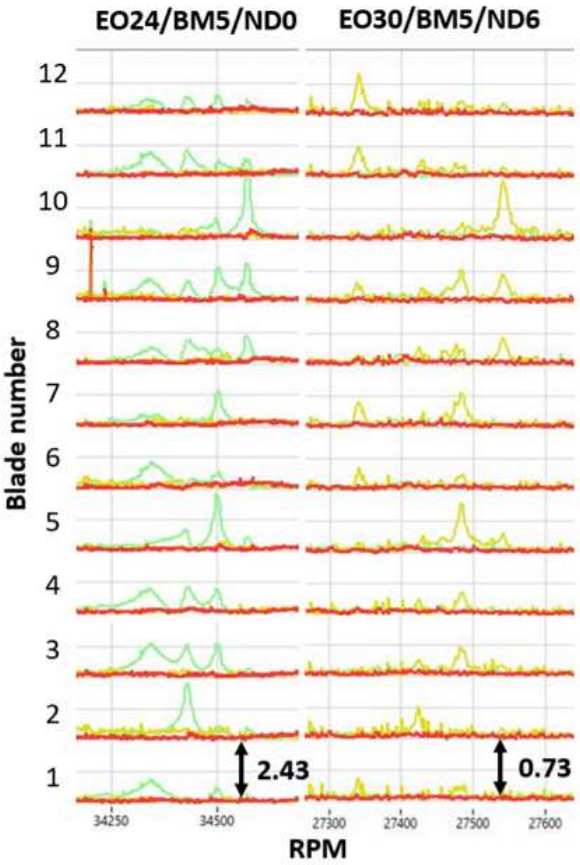

Figure 2.19: Turbine Blade tip timing output for modes BM5 ND0 and BM5 ND6

2.3.3 Mistuned mode shapes and Nodal diameter spectrum

Tuned mode shapes have the characteristic of having the same amplitude with a phase shift from sector to sector which depends on the nodal diameter, and thus build a sine wave along the tangential coordinate of the type: $\sin(\mathrm{ND} \cdot 2\pi\frac{i-1}{Z})$, where i is the sector index, Z is the number of sectors.
Mistuning effect consists in a localized softening or hardening, thus it breaks the symmetry of the harmonic mode shapes.

It is possible to employ oversimplified 1-DOF per sector model as an analogy of the vibration behavour of a turbine. Introducing non dimensionalized mistuning parameter $\gamma_j = \delta_j/k$ on equation (2.8), Eq. (2.19) relating mode shapes of two consequent blades is obtained [6]:

$$\begin{bmatrix} q_{j+1} \\ q_j \end{bmatrix} = \begin{bmatrix} (1+\gamma_j+2R-(\frac{\Omega^2}{\omega_N^2}))/R & -1 \\ 1 & 0 \end{bmatrix} \begin{bmatrix} q_j \\ q_{j-1} \end{bmatrix}, \quad j = 1, \ldots, Z \tag{2.19}$$

Due to the random mistuning contribution γ_j to the j-th blade stiffness, the phase difference between two neighbouring blades is no longer constant, thus for a mode shape sectors no longer follow a pure harmonic.

Tuned mode shapes form an orthogonal linear basis for the space of the system's degrees of freedom. This allows the mistuned mode shapes to be expressed as a superposition of tuned modes. These tuned mode shapes are represented by harmonic functions along the circumferential coordinate.

Let the tuned eigenvector matrix, containing the tuned eigenvectors as columns, be denoted by $[\Phi_t]$, and a mistuned eigenvector by $[\Phi_m]$. It is possible to express the mistuned eigenvector as a linear combination of the tuned eigenvectors, as shown in Eq. (2.20) [13].

$$\{\Phi_m\} = \sum_{i=1}^{Z} w_i \{\Phi_t\} \tag{2.20}$$

Definition of the nodal diameter spectrum

Tuned modes form an harmonic along the circumference of the shaft:

$$\{\Phi_{t,j}\} = A_m \cos(2\pi \cdot \mathrm{ND}\frac{j-1}{Z} + \phi_m) \tag{2.21}$$

The mistuned mode, which is a sum of harmonic forms, therefore no longer has a single nodal diameter component, but rather can be written as the sum of different nodal diameter components, each with varying intensities. These components form the nodal diameter spectrum.

Nodal diameter spectrum $\{\mathfrak{F}\}$ of the mistuned mode can be calculated by performing a **Discrete Fourier transform** over the sectors mode shapes, ordered along the circumferential coordinate.

$$\{\mathfrak{F}\} = \frac{1}{Z}[F]\{\Phi_m\} \tag{2.22}$$

with the matrix [F] being defined as:

$$F_{i,j} = e^{\frac{2\pi i}{F}\cdot(i-1)\cdot(j-1)} \tag{2.23}$$

Mode localization

Klauke numerically demonstrated the effect of a harmonic mistuning pattern with growing intensity on a bladed disk. [8] He implemented a sine-wave mistuning with root mean square

value $\Delta K = \sigma_{Verstimmung} \cdot K$. Fig. 2.20 shows the evolution of an ND0 turbine mode shape with the growth of the mistuning amplitude. An increase in mistuning amplitude increases the mode localization.

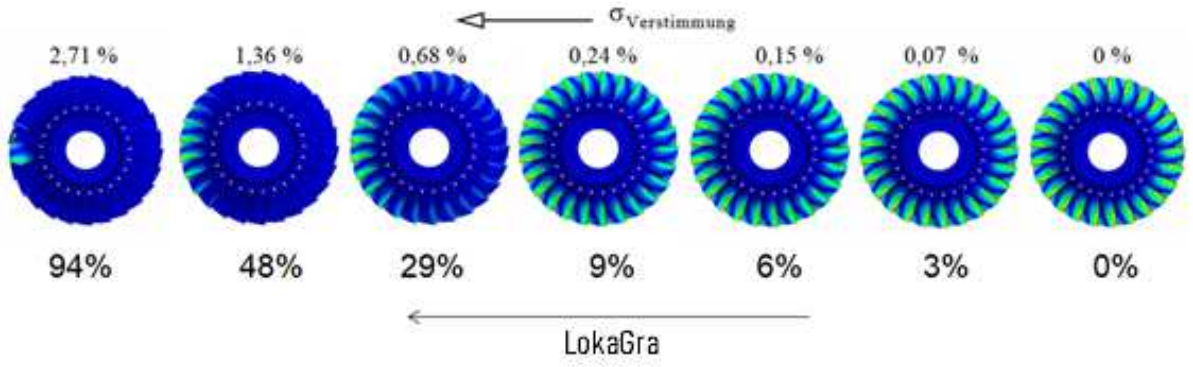

Figure 2.20: Localization effect due to the increasing level of mistuning $\sigma_{Verstimmung}$ on an ND0 mode shape of a bladed assembly and on the localization factor (def. in Eq. 2.28) (percentage below) [8]

Nevertheless, in general, it has been shown that there exists a level of mistuning at which both the localization and the amplification of modal amplitude reach a maximum. [21] [13]. Above this level, the degree of localization tends to decrease.

Klauke provided definitions for the complete set of parameters to quantify the modal localization effect [8].

First, he defines, based on the nodal diameter spectrum, the ratio of the maximal Fourier coefficient ξ as a measure of how equal are the levels of the nodal diameter components in a mistuned mode. (2.24). In a perfectly tuned mode there is only one non-zero nodal diameter component. In a worst-case mistuned mode, vibration is concentrated on one blade. In this case all components of the nodal diameter spectrum have equal amplitude.

$$\xi = \left(\frac{\sum_{\mathrm{j}=0}^{\mathrm{ND_{max}}} \mathrm{DFT_j}}{\mathrm{DFT_{max}}} \right) \tag{2.24}$$

For the tuned case , the DFT spectrum is composed by just one ND component, the sum (numerator) is also the maximum (denominator) and therefore $\xi_{unverstimmt} = 1$.

The worst-case mistuned mode occurs when only one blade participates in the vibration. In this case, all DFT_j components have equal amplitude. Thus, the maximum mistuning ratio is given by:

$$\xi_{\mathrm{verstimmt,max}} = \left(\frac{\sum_{\mathrm{j}=0}^{\mathrm{ND_{max}}} \mathrm{DFT_j}}{\mathrm{DFT_{max}}} \right)_{\mathrm{verstimmt,max}} = \mathrm{ND_{max}} + 1 \tag{2.25}$$

Klauke defined the parameter Modenfulligkeit (i.e Mode Fill Factor in English) to achieve 0% for the tuned case and 100% for the maximum mistuning case, as in Eq. (2.26).

$$\text{Modenfülligkeit} := \frac{1}{ND_{\max}}(\xi - 1) \tag{2.26}$$

Furthermore, by considering the ratio between the maximum amplitude and the mean square value (RMS) of the mode between the different blades, the ratio ζ is defined in order to evaluate the resemblance of the mistuned mode shape to a pure harmonic Eq. (2.27) . In fact for a perfect harmonic the RMS value of the blade deflections is equal to the maximum deflection divided by $\sqrt{2}$. In the worst-case mistuned scenario, the deflection is concentrated on a single blade, so the ratio between the maximum value and RMS is 1 for $0 < \text{ND} < \text{NDmax}$, and $1/\sqrt{2}$ for $\text{ND} = 0$ or $\text{ND} = \text{NDmax}$. Therefore a normalizing factor β is introduced.

$$\zeta = \frac{\max\{u\}}{\sqrt{\sum u^2}} \tag{2.27}$$

In order to compare rotors with different numbers of blades, the ratio ζ is normalized as shown in Eq. (2.28), resulting in value called localization factor (LokaGra). This factor ranges from 0 to 100 % and represents the degree of deviation from a perfect harmonic shape of the mistuned mode.

$$\text{LokaGra} := \frac{\zeta - \beta}{\sqrt{Z} - \beta}, \quad \text{where } \beta = \begin{cases} \sqrt{2}, & 0 < \text{ND}_{dom} < \text{ND}_{\max}, \\ 1, & \text{ND}_{dom} = 0 \text{ or } \text{ND}_{dom} = \text{ND}_{\max}. \end{cases} \tag{2.28}$$

2.4 Numerical analysis

2.4.1 Basics of Finite element method

Discretization

The Finite element method is a mathematical technique widely used in all fields of engineering for solving partial differential equation problems with complex domain geometry and boundary conditions.

Finite element method allows the discretization of a structure into elements with simple geometry such as tetrahedrons, hexahedrons, rectangular plates and beams which have a finite number of degrees of freedom, and can be assembled into a structure with a mathematical procedure. The degrees of freedom of the elements are typically the displacements at specific points, known as nodes. In 3D space each node has three degrees of freedom that represent displacement in x,y and

z directions. The displacement of all other points of the element is linked to the nodal degrees of freedom by means of specific interpolation functions $N(x, y, x)$, called **shape functions**.

$$\begin{Bmatrix} u_x(x,y,z,t) \\ u_y(x,y,z,t) \\ u_z(x,y,z,t) \end{Bmatrix} = \begin{bmatrix} \mathbf{N}(x,y,z) & 0 & 0 \\ 0 & \mathbf{N}(x,y,z) & 0 \\ 0 & 0 & \mathbf{N}(x,y,z) \end{bmatrix} \begin{Bmatrix} \mathbf{q}_x(t) \\ \mathbf{q}_y(t) \\ \mathbf{q}_z(t) \end{Bmatrix} \tag{2.29}$$

- $u_x(x, y, z, t)$ displacement in x direction in a generic point of the element with coordinates (x,y,z)
- $u_y(x, y, z, t)$ displacement in y direction in a generic point of the element with coordinates (x,y,z)
- $u_z(x, y, z, t)$ displacement in z direction in a generic point of the element with coordinates (x,y,z)
- $\mathbf{q}_x(t)$ matrix containing displacement of nodes in x direction
- $\mathbf{q}_x(t)$ matrix containing displacement of nodes in y direction
- $\mathbf{q}_x(t)$ matrix containing displacement of nodes in z direction
- $\mathbf{N}(x, y, z)$ matrix containing shape functions

Shape functions must satisfy several criteria to ensure the effectiveness and convergence of the FEM solution:

- **Interpolation condition:** The shape function for node i should have value 1 at that node and 0 at all other nodes.
- **Local support:** The shape function should vanish outside the element containing the node.
- **Interelement compatibility:** Shape functions must ensure at least C^0 continuity between adjacent elements .
- **Completeness:** The set of shape functions should be able to represent any linear polynomial exactly within the element .
- **Partition of unity:** The sum of all shape functions at any point within the element should equal 1.
- **Continuity:** Shape functions must be able to grant the continuity of the solution across element boundaries.

Shape functions are usually polynomial functions derived for an element type in its natural coordinates through a mathematical procedure. The degree of the polynomial is, in cases of isoparametric elements, equal to the number of degrees of freedom of the element considering one

direction only. The procedure used to determine the polynomial coefficients of the shape functions is called p-method. Shape functions determined for an element in natural coordinates (perfect cubes of perfect hexaedrons) are then generalized by means of geometric transformation to the distorted elements that form the mesh of the model. This geometric transformation involves an error in the evaluation of stiffness, called distortion error, which can be limited by limiting the element distortion.

Elemental matrices derivation

It is thus possible to calculate the strains internal to the element as:

$$\epsilon(x,y,z,t) = \mathbf{B}(x,y,z)\mathbf{q}(t), \;\; \mathbf{B}(x,y,z) = \nabla\, \mathbf{N}(x,y,z) \tag{2.30}$$

Stresses are linked to the deformations by a linear characteristic equation typical of the material, representable in matrix form as **E**.

$$\boldsymbol{\sigma}(x,y,z,t) = \mathbf{E}\boldsymbol{\epsilon} = \mathbf{E}\,\mathbf{B}(x,y,z)\mathbf{q}(t) \tag{2.31}$$

Once stresses and strains are known it is possible to calculate, with the virtual works formulation, the elastic potential energy absorbed in the element as a volume integral:

$$\mathcal{U} = \frac{1}{2}\int_V \epsilon^T \boldsymbol{\sigma} dV = \frac{1}{2}\mathbf{q}^T \left(\int_V \mathbf{B}^T\mathbf{E}\mathbf{B} dV\right)\mathbf{q} \tag{2.32}$$

Nodal degrees of freedom **q** do not depend of the position and can be written outside the volume integral. Therefore the integral assumes the typical form $\frac{1}{2}q^T K q$, highlighting the stiffness matrix K.

$$\mathbf{K} := \int_V \mathbf{B}^T\mathbf{E}\mathbf{B} dV \tag{2.33}$$

By applying time derivative to Eq. (2.29) it is possible to derive the velocity:

$$\dot{\mathbf{u}}(x,y,z,t) = \mathbf{N}(x,y,z)\dot{\mathbf{q}}(t) \tag{2.34}$$

In a manner similar to the potential energy, it is possible to express the kinetic energy and derive the mass matrix, **M**.

$$\mathcal{T} = \frac{1}{2}\int_V \rho \dot{\mathbf{u}}^T \dot{\mathbf{u}} dV = \frac{1}{2}\dot{\mathbf{q}}^T \left(\int_V \rho \mathbf{N}^T \mathbf{N} dV\right) \dot{\mathbf{q}}, \tag{2.35}$$

$$\mathbf{M} := \int_V \rho \mathbf{N}^T \mathbf{N} dV \tag{2.36}$$

In the case of the discretization of a structure which is rotating, the expression of the kinetic energy is slightly more complex. In fact the velocity can be written as:

$$\dot{\mathbf{u}}^* = \dot{\mathbf{u}} + \bar{\Omega} \times \mathbf{u} \tag{2.37}$$

Therefore the kinetic energy integral is equal to:

$$\begin{aligned} \mathcal{T} &= \frac{1}{2}\int_V \rho \dot{\mathbf{u}^*}^T \dot{\mathbf{u}^*} dV \\ &= \frac{1}{2}\int_V \rho[\dot{\mathbf{u}}^T \dot{\mathbf{u}} + 2\dot{\mathbf{u}}^T \bar{\Omega} \times \mathbf{u} + (\bar{\Omega} \times \mathbf{u})^T (\bar{\Omega} \times \mathbf{u})] dV \end{aligned} \tag{2.38}$$

The second term of this formulation represents the work of the Coriolis forces, and leads to the formulation of the Gyroscopic matrix:

$$\mathbf{G} := 2\frac{\rho}{\Omega}\int_V \mathbf{N}^T \bar{\Omega} \mathbf{N} dV \tag{2.39}$$

Assembling

The matrices (2.33), (2.36), (2.39) refer to one single element. In order to study an entire structure, composed by multiple elements it is necessary to assemble the model, satisfying balance and consistency. Assembly method is based on the *topology map* of the system, which is a simple table in which indexes of the degrees of freedom of one element are related to the indexes of the degrees of freedom of the whole assembled structure.

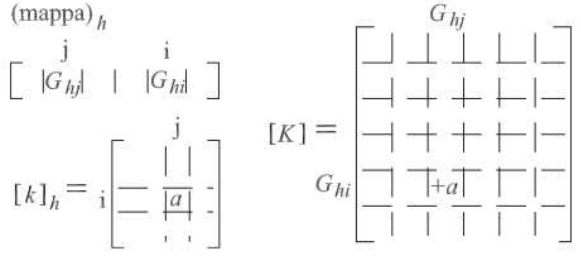

Figure 2.21: Assembling scheme of a global matrix [9]

The contributions of individual elements to the global matrix are additive. As shown in Figure 2.21, [K], the global matrix, is constructed by assembling the elemental matrices $[k]h$ of the h-th element. The entry [i, j] of the elemental matrix $[k]h$ is added to the global matrix at index position $[Ghi, Ghj]$. The relation $[i, j] \rightarrow [Ghi, G_{hj}]$ is determined by the topology map, which is automatically generated during the meshing phase in finite element software like Ansys.

2.4.2 Prestressed modal analysis

Pre-stressed modal analysis requires performing a static structural analysis first. Static structural output is used as the initial condition for the modal analysis. Static structural analysis outputs deformations ϵ_0 and stresses σ_0 on the rotor elements. In the equation of motion Eq.(2.3), pre stress is represented by a positive stiffness contribution matrix named $[K_\Omega]$. This matrix is computed for each element in a similar way as the other matrices (2.36) (2.33) and is then assembled according to the scheme in Fig. 2.21. [18].

$$[K_\Omega] := \frac{1}{2\Omega^2} \int_V (\mathbf{B}^T \sigma_\mathbf{0}(x, y, z)\mathbf{B}))dV \tag{2.40}$$

where $\sigma_\mathbf{0}(x, y, z)$ is the stress tensor created by the centrifugal forces, calculated in static analysis.

2.4.3 Eigenvalue solver

The damped eigensolver (accessed in MAPDL with MODOPT, QRDAMP) [19] is applied only when the system damping matrix needs to be included in the eigenproblem. This eigensolver allows for nonsymmetric [K] and [C] matrices. This method employs the modal orthogonal coordinate transformation of system matrices to reduce the eigenvalue problem into the modal subspace.

The method initially solves the symmetric undamped problem by dropping the matrix [C]. Thus real eigenvalues and the corresponding eigenvectors are found, and it is possible to write the modal transformation (2.41).

$$\{u\} = [\Phi]\{\eta\} \tag{2.41}$$

Then using the modal transformation Eq. (2.41) the equation of motion (2.1) is rewritten as:

$$[I]\{\ddot{\eta}\} + [\Phi]^T[C][\Phi]\{\dot{\eta}\} + \{[\Lambda^2] + [\Phi]^T[K_{unsym}][\Phi]\}\{\eta\} = \{0\} \tag{2.42}$$

The stiffness matrix is written as a sum of symmetric matrix and antisymmetric matrix which is diagonalized by the transformation Eq. (2.41), forming the eigenvalue matrix $[\Lambda^2]$. The antisymmetric matrix $[K_{unsym}]$ is diagonalized by the modal transformation Eq. (2.41).

Successively, Eq. (2.42) is written in state space formulation as:

$$[I]\{\dot{w}\} = [D]\{w\},\ \{w\} = \begin{Bmatrix}\{\eta\}\\ \{\dot{\eta}\}\end{Bmatrix},\ [D] = \begin{bmatrix}[O] & [I]\\ -[\Lambda^2] - [\Phi]^T[K_{unsym}][\Phi] & -[\Phi]^T[C][\Phi]\end{bmatrix} \tag{2.43}$$

Finally the inverse iteration method (Wilkinson and Reinsch) [19] is used to calculate the complex modal subspace eigenvectors. The full complex eigenvector of the original system is recovered using the following equation:

$$[\Psi] = [\Phi]\{\eta\} \tag{2.44}$$

2.4.4 Cyclic symmetry

Cyclic symmetry allows the reduction of the computational load for analysing one component with the finite elements method. A model can be reduced by means of cyclic symmetry if we can divide it in Z sectors around a principal axis and each sector must have:

- Same geometry
- Same distribution of material properties
- Same load distribution
- Same boundary conditions

If these characteristics are fulfilled, it is possible to reduce the number of nodes of the model and thus the computational effort by studying only one sector, called reference sector.

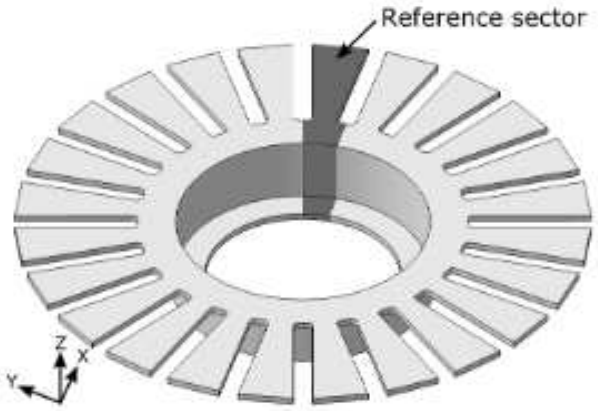

Figure 2.22: Example of a cyclic symmetric structure and its reference sector

Considering the reference sector, it is possible to divide the degrees of the freedom of the reference sector in three arrays:

- Array containing the Interface nodes degrees of freedom, which are in common with the sector on the left, with size I, we call it $q_i^{(n)}$
- Array containing Internal nodes degrees of freedom, of size R, we call it $q_r^{(n)}$
- Array containing Interface nodes degrees of freedom, which are in common with the sector on the right,with size I, we call it $q_i^{(n+1)}$ because they coincide with the left interface nodes of the sector on the right (n+i -th sector)

Thus the reference sector's degree of freedom vector can be written:

$$\mathbf{q^{(n)}} = \left\{ \begin{array}{c} q_i^{(n)} \\ q_r^{(n)} \\ q_i^{(n+1)} \end{array} \right\} \tag{2.45}$$

Note that the number of elements of the vectors $q_i^{(n)}$ and $q_i^{(n+1)}$ must be equal.

The fundamental concept used in a cyclic symmetry model is that the deflection of one sector has the same amplitude and a constant phase difference from the deflection of the previous sector. It is therefore possible to analyse the complete structure by considering only one substructure, and applying appropriate complex constraints at its boundary with the following substructure, so as to impose this phase difference.[22]

$$q_i^{(n+1)} = q_i^{(n)} e^{ih\frac{2\pi}{Z}} \tag{2.46}$$

Where h is called 'harmonic index' or 'nodal diameter'. $\frac{2\pi}{Z}$ represents the angle which each sector occupies, which is also called IBPA *Inter Blade Phase Angle*. It can be observed that the harmonic index is the number of phase rounds we allow on the circumferential coordinate *theta*. By virtue of hypothesis (2.46) we can write the equation:

$$\mathbf{q^{(n)}} = \begin{Bmatrix} q_i^{(n)} \\ q_r^{(n)} \\ q_i^{(n+1)} \end{Bmatrix} = \begin{bmatrix} I^{(L)} & 0 \\ 0 & I^{(K)} \\ I^{(L)} e^{ih\frac{2\pi}{Z}} & 0 \end{bmatrix} \begin{Bmatrix} q_i^{(n)} \\ q_r^{(n)} \end{Bmatrix} = \mathbf{T}\, \mathbf{q_{CS}^{(n)}} \tag{2.47}$$

$\mathbf{T}$ is the transformation matrix and $q_{CS}^{(n)}$ is the vector of the degrees of freedom under the hypothesis of cyclic symmetry.

On the equation of motion (2.3), if we only consider the $R+2I$ degrees of freedom of the reference sector, we will have the equation:

$$[M]^{(n)}\ddot{q}^{(n)} + ([C_r]^{(n)} + [C_{nr}]^{(n)} + \Omega[G]^{(n)})\dot{q}^{(n)} + ([K]^{(n)} + [K_\Omega]^{(n)}\Omega^2 - \Omega[C_r]^{(n)} - [K_S]^{(n)})q^{(n)} = 0 \tag{2.48}$$

It is possible to premultiply the equation by the transpose of T and substitute the expression (2.47), so all the matrices will written in the form:

$$M_{CS}^{(n)} = T^T M^{(n)} T \tag{2.49}$$

$$G_{CS}^{(n)} = T^T G^{(n)} T \tag{2.50}$$

$$K_{\Omega CS}^{(n)} = T^T K_\Omega^{(n)} T \tag{2.51}$$

$$K_{CS}^{(n)} = T^T K^{(n)} T \tag{2.52}$$

Similarly,for all the matrices that appear in the complete equation of motion (2.3), it is possible to apply the linear transformation. This way the eigenvalue problem is reduced in size to roughly 1/Z of its original size.

3 Experimental measurements

3.1 Experimental setup

An experimental test bench for testing the behaviour of a radial impeller of a turbocharger turbine in real operation has been built in *Instutut für Kraftswerktechnik Dampf und Gasturbinen* in Aachen.
The bench is open loop, which means the flow of the turbine and the flow of the compressor are uncoupled. The inlet flow of the turbine is not the output flow of the turbocharger compressor, but is instead the output of a separate supply compressor. The supply compressor can output 12 kg/s @ 30 bar. Different lamination valves are placed on the circuit for flow control and ensure a controllability on mass flow rate both for the turbine and the compressor. [1]

The radial turbine has 12 blades. The compressor has 9 main blades and 9 splitter blades.

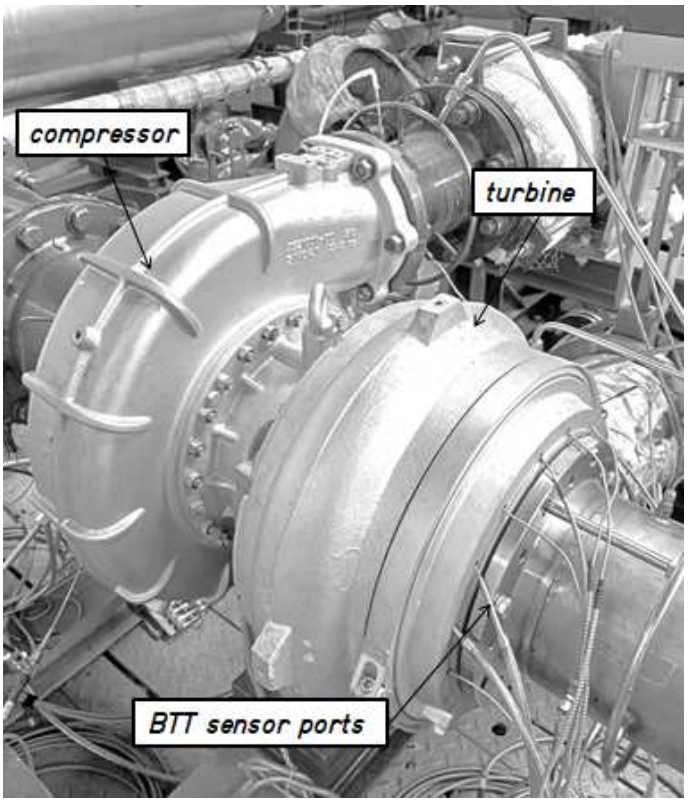

Figure 3.1: View of the turbo-charger unit in the experimental setup

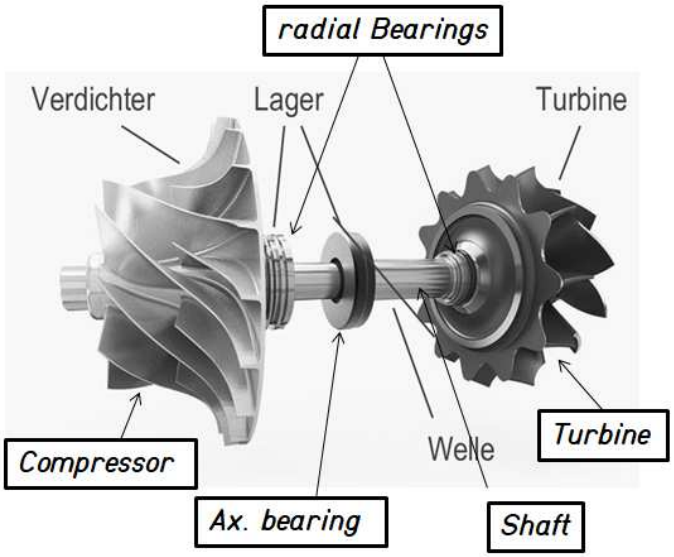

Figure 3.2: View of the turbo-charger impeller in the experimental setup

Figure 3.3: Axial view of the turbine impeller, dismounted

3.2 Blade tip timing [1]

The technique is based on the measurement of the 'time of arrival', i.e. the time that passes between the passage of one blade edge and the next. It is conventionally measured using optical sensors that are distributed along the circumference. This sensor detects the passage of the blades, and it is possible through a mathematical procedure to calculate the deflection of the blade based on the 'time of arrival' of the different blades. Conventionally, a sensor mounted on the shaft, called 'once per revolution', detects the number of revolutions, and by measuring the

relative position of the various blades, allows the identification of the blades.

Advantages of BTT: contactless, therefore the sensor does not influence the dynamics of the turbine, unlike Strain Gauge techniques which alter the mass of the blade, and therefore require taking into account. It also allows all blades to be measured simultaneously, which makes this technique particularly suitable for identifying localizations of vibration amplitudes due to mistuning.

Limits of BTT: Due to space constraints, the number of sensors is limited, so the measurement of the vibrations of a blade is not continuous but necessarily discrete, with few readings per revolution. The signal will therefore be under-sampled and will not meet the minimum Nyquist-Shannon requirement of at least two samples per period. The signal cannot therefore be perfectly reconstructed. This is a problem that mainly affects high EOs, and can be contained but not eliminated by adopting mathematical noise reduction techniques such as the Savitzky Golay filter.

To allow the sensors to recognize the different blades as they pass, 'blade fingerprint' identifiers can be adopted. Conveniently, a reliable identifier can be the angle between two pairs of blades, which due to manufacturing process defects is not uniform but rather variable, and therefore allows the sensor to recognize the blade.

Time of arrival (TOA) is the chronometer time registered at the passage of a blade in front of a sensor. It is possible to calculate the time elapsed between two blades as the time difference between two consequtive TOAs mesaured at the same sensor.

With a series of mathematical passages it is possible to calculate the exact speeds of each blade, and then, by filtering out the rotational speed, the relative positions of the blades can be calculated as they pass in front of the sensors. Furthermore, by carrying out the test at different speeds, it is possible to filter the static component of the deformation. This results in a series of frames of each blade at different times. These frames represent a subsampled signal of the blade vibration. For this reason it is not immediate to calculate the vibration frequencies, as the Fourier transform of the subsampled signal would give rise to aliasing phenomena. In fact, a more advanced technique is used, known as the 'multi sampling method'. This technique consists in carrying out several Fourier fits considering at each repetition only the data coming from a subset of the sensors. The intersection of the different subsamples gives rise to a series of frequencies, some of which correspond to the true critical frequencies.

To estimate the characteristics of the vibrations at these critical speeds, the 'conventional Fourier fit' is used, i.e. a least squares fit to decompose the deflection signal over time into harmonic functions. Maintaining a particular constant rotation speed Ω results in a deflection of the type:

$$d(t) = A_1 sin(\omega t + \phi) + B_1 cos(\omega t + \phi) + D \tag{3.1}$$

where

$$\omega t = 2\pi f_R t = EO \cdot \theta \tag{3.2}$$

thus

$$d(\theta) = A_1 sin(EO \cdot \theta) + B_1 cos(EO \cdot \theta) \tag{3.3}$$

This equation for each blade i. Subtracting the deflections of two consecutive blades gives:

$$d_1 - d_2 = A_1(\sin(EO \cdot \theta_1) - \sin(EO \cdot \theta_2)) + B_1(\cos(EO \cdot \theta_1) - \cos(EO \cdot \theta_2)) \tag{3.4}$$

This equation can be written for any pair of samples, and thus leads to the overdetermined linear system:

$$\begin{pmatrix} d_1 - d_2 \\ d_1 - d_3 \\ \vdots \\ d_{S-1} - d_S \end{pmatrix} = \begin{pmatrix} \sin(EO\theta_1) - \sin(EO\theta_2) & \cos(EO\theta_1) - \cos(EO\theta_2) \\ \sin(EO\theta_1) - \sin(EO\theta_3) & \cos(EO\theta_1) - \cos(EO\theta_3) \\ \vdots & \vdots \\ \sin(EO\theta_{S-1}) - \sin(EO\theta_S) & \cos(EO\theta_{S-1}) - \cos(EO\theta_S) \end{pmatrix} \begin{pmatrix} A_1 \\ B_1 \end{pmatrix} \tag{3.5}$$

It is then possible to solve for the amplitudes A and B with a linear best fit. It is not granted that the fitting error is small. In fact the error is a good criterion for testing if the critical speeds resulting from the *Multi sampling method* are real resonant points or numerical aliasing points.

$$A = \sqrt{A_1^2 + B_1^2} \quad , \quad \varphi = \tan^{-1}(\frac{A_1}{B_1}) \tag{3.6}$$

3.3 Strain gauge

Strain gauge is an invasive measurement technique which allows to measure vibration in operation. It consists of the application of strain gauges oriented radially on the surfaces of the blades (Fig. 3.4). The strain gauges affect the measurement of a few Hz as they increase the mass and stiffness of the blades.

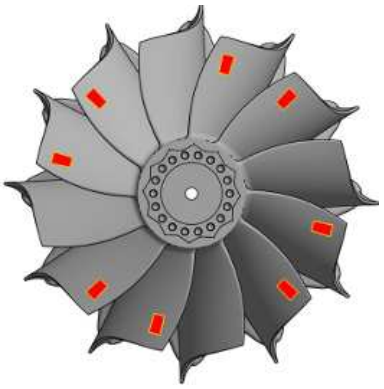

Figure 3.4: Arrangement of strain gauge sensors on the blade [1]

3.4 Experimental results

On the experimental bench located at IKDG, M. Sasakaros & M. Shafferus measured the frequency and amplitudes of the vibration modes of the turbine impeller with the Blade Tip Timing technique and strain gauges in a real operation scenario.[4]

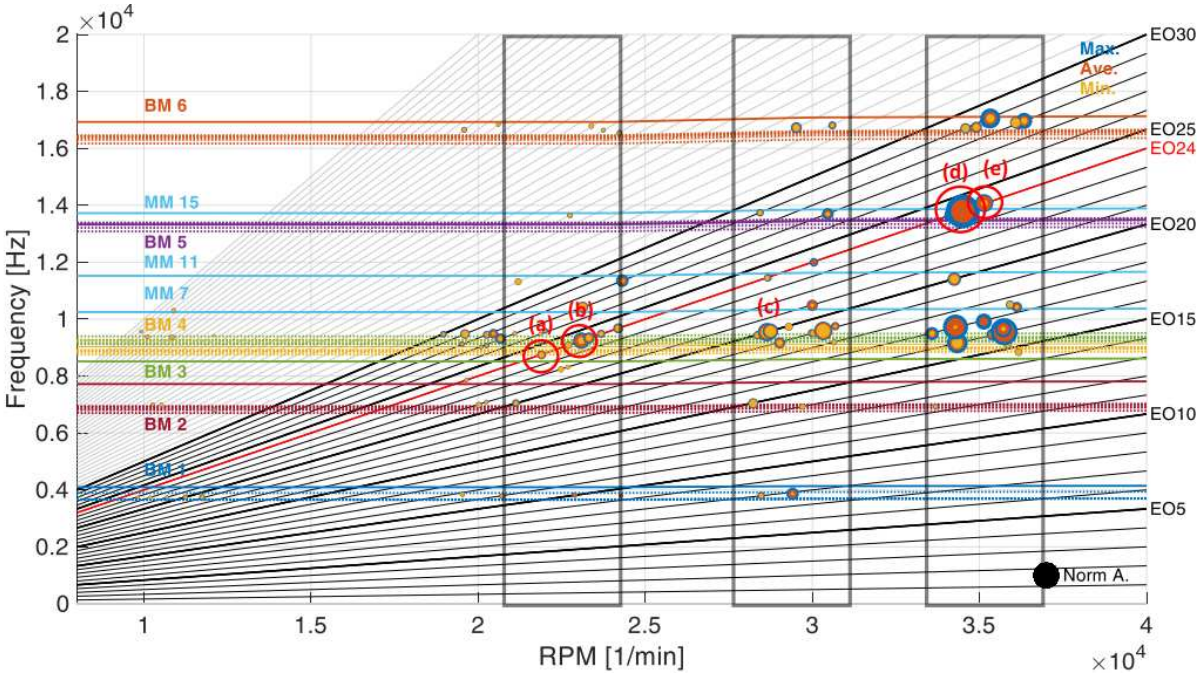

Figure 3.5: Plot of numerically calculated Campbell diagram (colored curves) for the turbine blade and disk modes' critical speeds, superimposed to experimental resonance points (yellow dots) measured with blade tip timing. [4]

Many of the resonance points lie on the Engine order 24 line, in frequencies roughly corresponding to BM3, BM4, BM5, MM15 modes. This is due to the number of guide vanes on the turbine stator being equal to 24. Therefore, the nodal diameter of these resonances is given by the Wilson

and Utengen formula, $24 - 12 \cdot k = \pm ND$ (k any integer) , and therefore ND=0.

Furthermore, many other modes which do not lie on the EO24 line have been measured. In particular, at the speed of 35000 RPM a set of resonances is clustered around the Engine Order 17 line. 17 is the number of blades of the IGV (Inlet guide vane) of the compressor. This suggests the presence of coupled turbine-compressor vibration modes in this frequency region. Applying again the Wilson and Utengen formula, $17 - 12 \cdot k = \pm ND$ (for any integer k), the only solution is ND = 5.

4 Numerical models

4.1 Materials

The material properties relevant to the dynamic analysis of the model include density (ρ), Young's modulus (E), and Poisson's ratio. These properties are isotropic but vary across the different components of the rotor. Additionally, the turbine disk and blades have distinct properties due to the different temperatures they experience. At the standard gas temperature (200°C), the blades exhibit a lower average Young's modulus. Material properties are listed in table 4.1

Features	**Young Modulus E**	**Poisson's Ratio ν**	**Density ρ**
Turbine disk	219500 MPa	0.3	8076 kg/m^3
Turbine blades at 200°C	200640 MPa	0.3	8076 kg/m^3
Shaft	207090 MPa	0.3	7850 kg/m^3
Compressor	71000 MPa	0.33	2770 kg/m^3

Table 4.1: Mechanical Properties of Impeller parts

4.2 Discretization

The discretization of all components is achieved in Ansys with 3D elements with a mix of structured and unstructured mesh. Shaft and blades are discretized with a structured mesh with SOLID186 hexahedral elements. Turbine and compressor disks, which have a more complex geometry, are discretised with non structured mesh composed of SOLID 187 tetrahedral elements.

SOLID186 [19] is a higher order 3-D 20-node solid element that exhibits quadratic displacement behaviour. The element is defined by 20 nodes and has three degrees of freedom per node corresponding to the translations in the nodal x, y, and z directions, and produces elemental matrices of size 60x60.

SOLID187 element [19] is a higher order 3-D, 10-node element. SOLID187 has a quadratic displacement behaviour and is well suited to modelling irregular meshes (such as those produced from various CAD/CAM systems). The element is has 10 nodes and three degrees of freedom per node, corresponding to the translations in the nodal x, y, and z directions and produces elemental matrices of size 30x30.

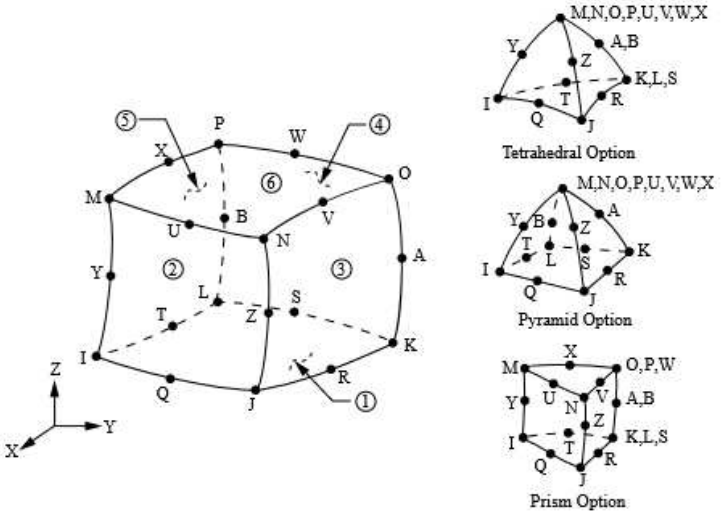

Figure 4.1: Scheme representing element SOLID186 geometry

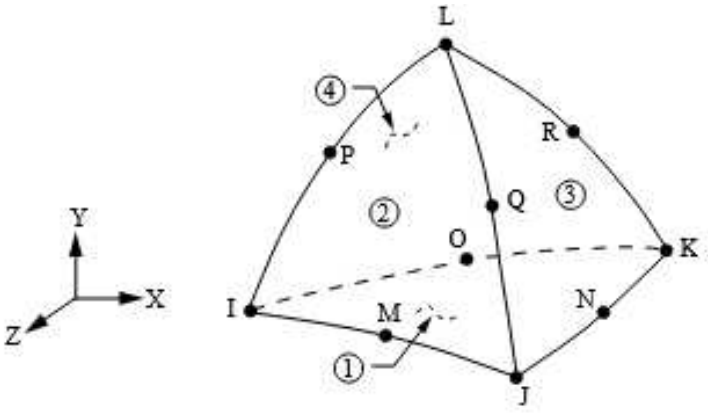

Figure 4.2: Scheme representing element SOLID187 geometry

4.3 Cyclic symmetry turbine sector model

For the calculation steps that require the highest number of iterations of solutions, for assessing the tuned turbine properties, it is convenient to use the turbine sector model, as the number of nodes is slightly higher than 1/12 that of the full turbine.

A boundary condition of symmetry must be imposed on the left and right interfaces of the reference sector with the neighbouring sectors.

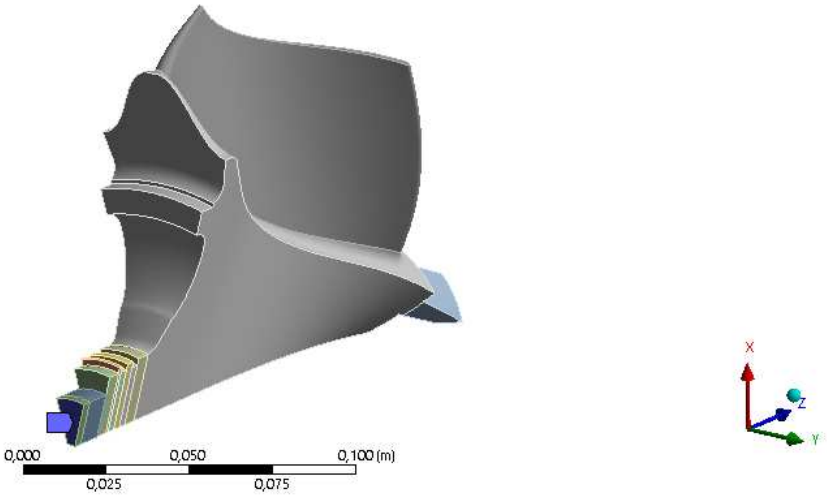

Figure 4.3: Cyclic simmetry model, with clamping BC surface highlighted in blue

In orter to implement the cyclic symmetric condition we need to define the axis of rotation and the two interfaces of the reference sector.

Furthermore a rotating velocity must be applied to the entire model of the reference sector. The axis of rotation coincides with the axis of symmetry.

The sector model counts 392620 nodes in total and 118832 elements.

4.4 Turbine model

In order to understand the dynamics of the tuned and mistuned blade assembly, a model with only the turbine has been created. Cyclic symmetry model is not able to sustain mistuning because mistuning breaks the conditions for cyclic symmetry.

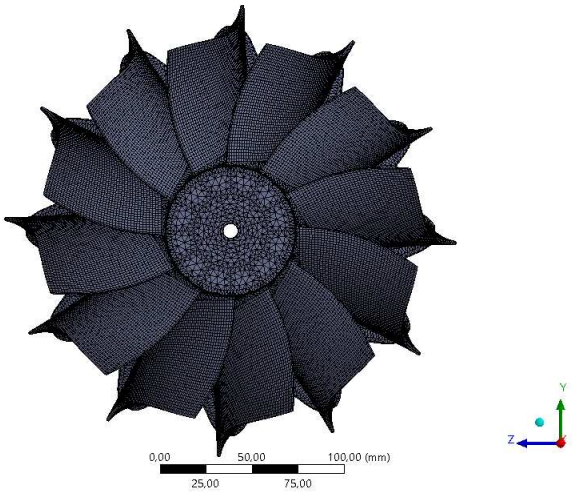

Figure 4.4: Turbine model, axial view

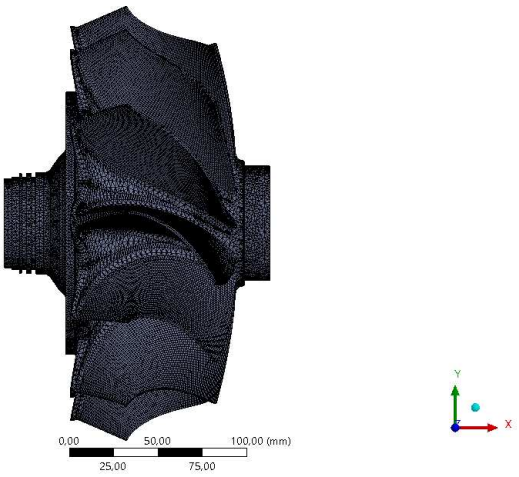

Figure 4.5: Turbine model, side view

The selection of an accurate boundary condition on the interface of the shaft depends on the object of the study. Fixed boundary condition brings to an over-estimation of the natural frequencies. Free boundary condition brings to a gross under-estimation of the natural frequencies but the results can be used for coupling mathematically with the rest of the model using the **Impedance coupling** technique.

4.5 Full rotor model

Finally the full rotor model is employed to represent the structural assembly of the shaft, comprehensive of Turbine side, Shaft, Compressor shaft and bearings.

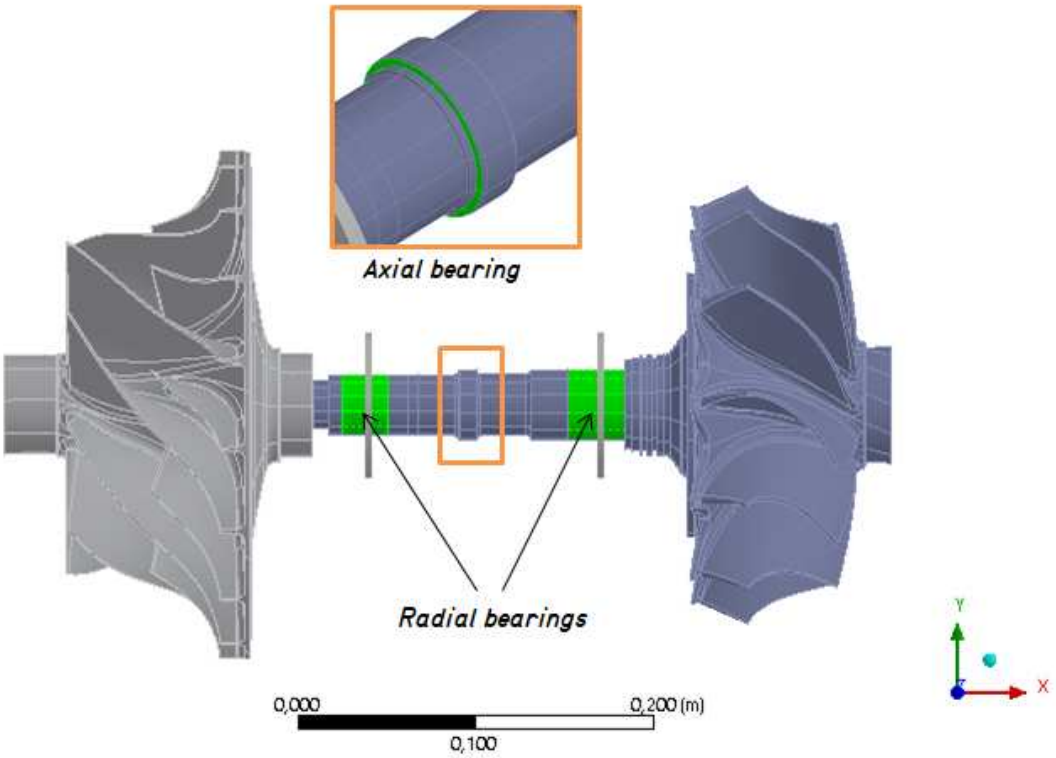

Figure 4.6: Side view of the full rotor model, radial and axial bearing surfaces are highlighted in green

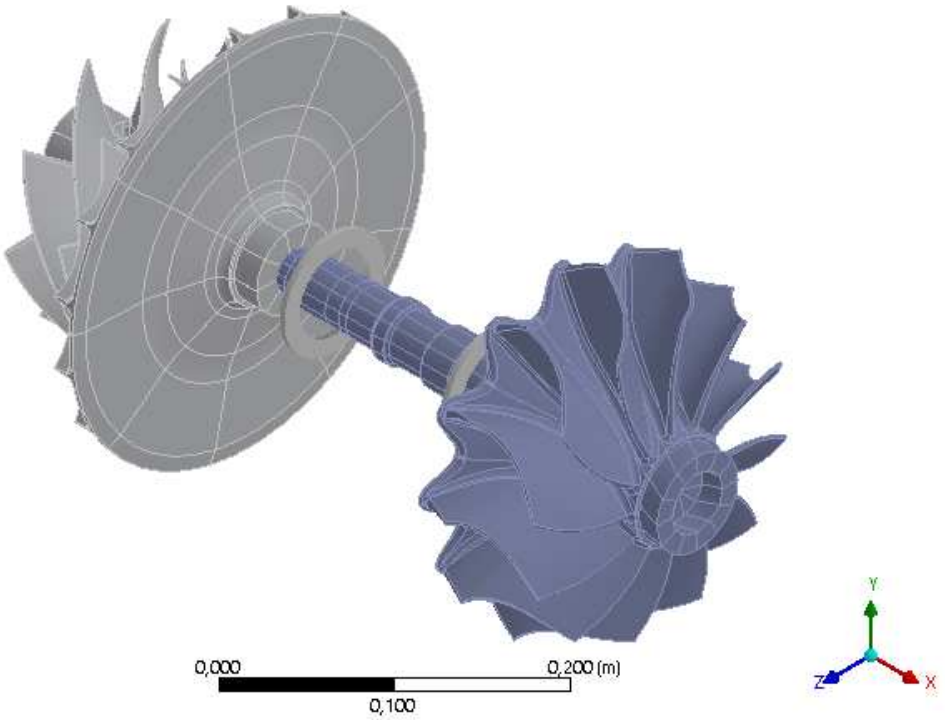

Figure 4.7: View of the full rotor model

Bearing Modeling

Bearings' modelling is complex as it usually involves the study of the non-linear Reynolds equations for the hydro static solution of the oil layer. [18]. Typically solutions are linearized around the working point. This is particularly difficult for a turbo-machines as they experience very different ranges of temperature and speed.
For this thesis we accept the values of stiffness and damping given by the constructor of the turbo-machine Kompressorenbau Bannewitz, These data are found for a reference working condition of 40000 RPM.

We assume that reasonably small deviations around the reference point are not impacting in a significant way the results we want to prove. A sensitivity analysis to the bearings' values is carried in the next chapter.

Axial bearings are modelled on Ansys as 1D connections to remote points with an associated value of stiffness and damping. Radial bearings are modelled on Ansys with 2d connections, with three associated values of stiffness and damping. Regarding the stiffness, the k_{11} and k_{22} terms are different because the bearing is not isotropic. Mixed term k_{21} is responsible for an skew-symmetric term on the stiffness matrix.

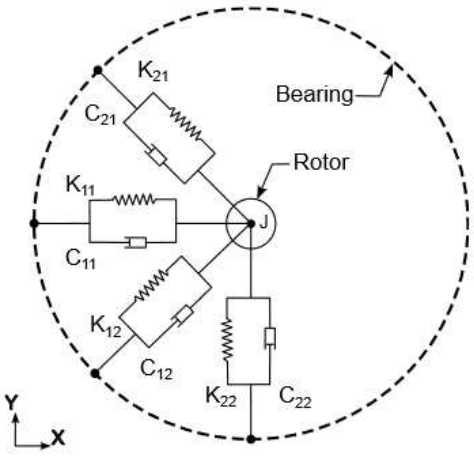

Figure 4.8: Scheme of the 2D linearized radial bearings

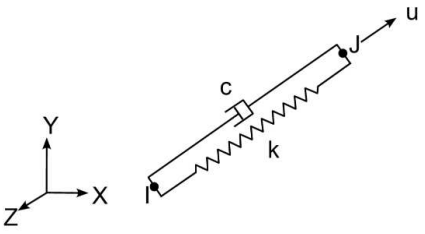

Figure 4.9: Scheme of the axial bearing, I is a remote point on the stator, J is a node of the surface of the axial bearing

4.6 Convergence

For convergence analysis, the conventional method involves the creation of a progressive series of self-contained meshes, in which the finer mesh is obtained by subdividing elements of the previous coarser mesh. This method grants the mesh to be geometrically similar between two steps, and thus makes it possible to observe a monotonic convergence of the frequencies to the exact solution as the number of elements increases.

However, due to the complex geometry of a turbine it is difficult to apply. Subsequently, an alternative technique is proposed for evaluating the convergence by reconstructing a new mesh for each dimension.

Multiple 3d meshes are created with an algorithm specifying a maximum dimension and a quality threshold.

Mash maximum size (s) =	2 mm,	3.1 mm,	4 mm,	4.1 mm,	8 mm

Since for each dimension a completely new mesh is generated, the quality varies randomly from one mesh to another, creating a noise in the convergence. It is possible to write the convergence curve for the j-th natural frequency as the sum of two terms:

$$\omega_{N,j}(s) = m_j(s) + n_j(s) \tag{4.1}$$

where $m_j(s)$ is the monotonously convergent curve as a function of the mesh size, while $n_j(s)$ is the noise term due to the random quality variation. With the assumption that the noise term is random, it modifies convergence curves independently from mode and mesh size. It is possible to calculate the arithmetic mean of the convergence curves of multiple modes:

$$\frac{1}{N}\sum_{j=1}^{N}\omega_{N,j}(s) = \frac{1}{N}\sum_{j=1}^{N}m_j(s) + \frac{1}{N}\sum_{j=1}^{N}n_j(s) \tag{4.2}$$

This way, the noise term $\sum_j n_j(s)$ tends to cancel out statistically due to the central limit theorem. The highest the number of modes N considered in the sum, the less relevant the noise term will be. The sum of the monotonic convergent parts $\sum_j n_j(s)$ converges to a constant value, as slowly as the slowest converging mode.

It is possible to fit the mean value curve by introducing the parameter $\lambda = 1/s$ and perform a best-fit of the type: $a \cdot e^{-b\cdot\lambda} + c$.

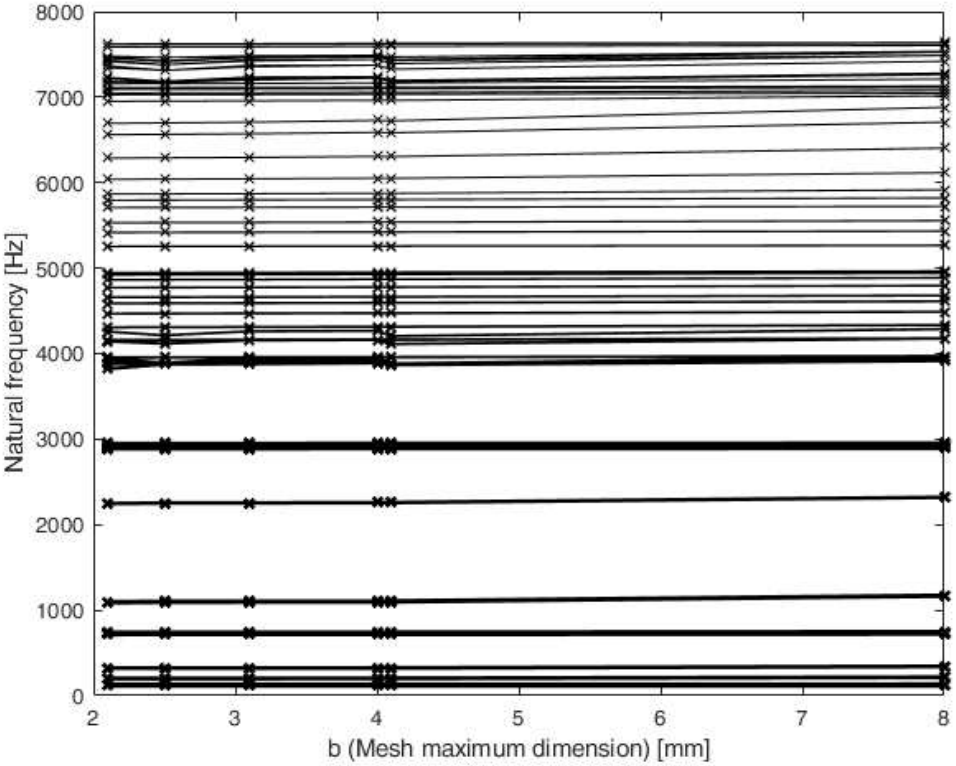

Figure 4.10: Convergence curves for the first 100 modes

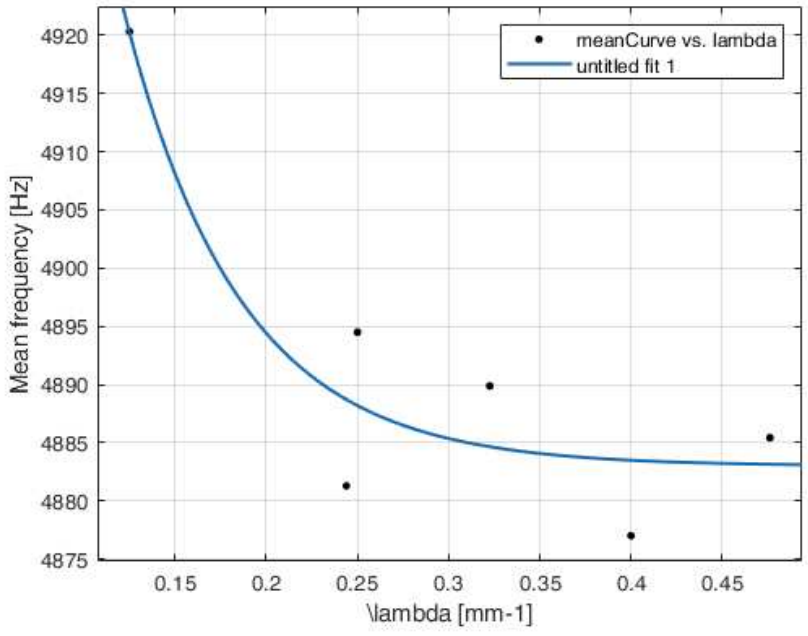

Figure 4.11: Mean frequency vs mesh size

a = 267 Hz
b = -15.76 mm
c = 4883 Hz

Thus it is possible to conservatively assume that a mesh size of 2 mm ($\lambda = 0.5\ mm^{-1}$) is enough to grant convergence of the frequencies of the model.

4.7 Campbell diagram

The Campbell diagram is obtained with the cyclic symmetry model, by applying different rotational speeds and solving the prestressed-modal analysis analysis problem,.

Speeds from 0 to 5000 rad/s (47700 RPM) have been tested, with an incremental step of 250 rad/s (2380 RPM) for each simulation.

Results show that in general the effect of speed on the frequencies is low, causing difference in frequencies of the order of 10 Hz for in the whole span of 0:5000 rad/s.

In general disk dominated modes show a decrease in the resonance frequency with the increase of speed, showing that speed softening is prevailing.

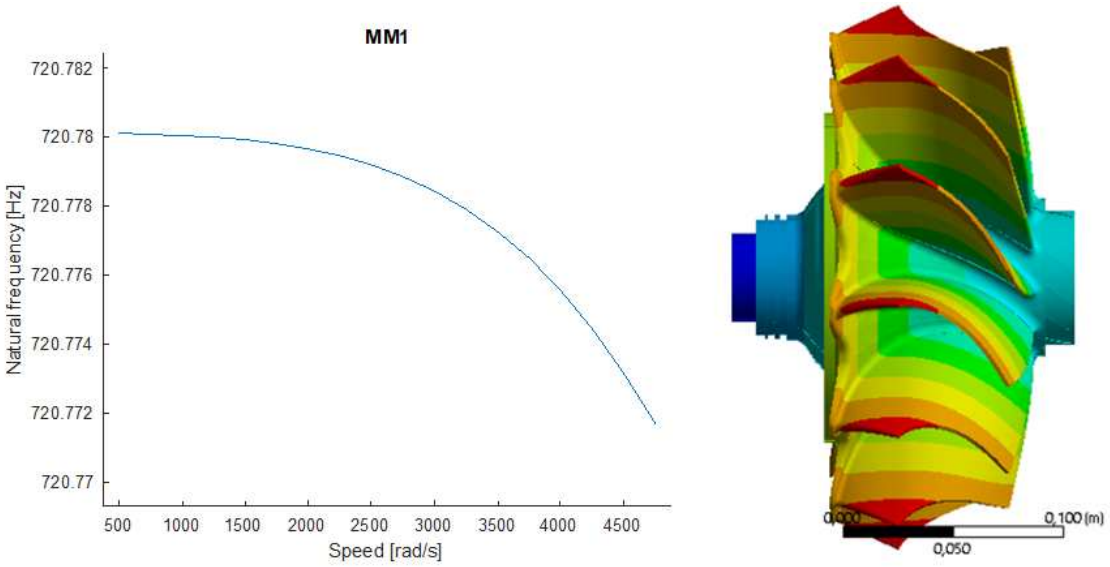

Figure 4.12: Campbell diagram of the first mixed mode (disk dominant)

On the other hand, all the blade modes show an increase in the natural frequency with the speed. This is due to the fact that centrifugal stiffening is considerably more relevant on the blades.

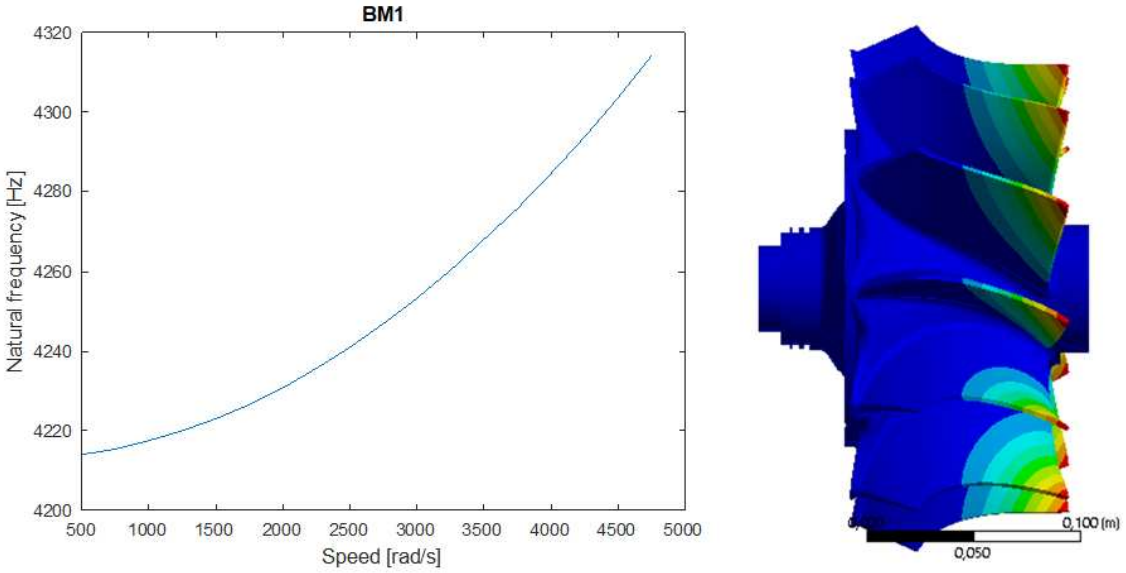

Figure 4.13: Campbell diagram of the first blade mode)

5 Mistuning implementation

Mistuning impacts both density and stiffness of the material. For the implementation of mistuning on a model there are two possible strategies:

- Mass mistuning, which involves altering the density of the blade
- Stiffness mistuning, which involves altering the Young Modulus of the blade

The two strategies are equivalent as they both act on the natural frequency of the blade. Mass mistuning poses more challenges as an artificial mass unbalance is introduced in the rotor model.

In this thesis mistuning is implemented by introducing mistuned values of Young Modulus based on results from the blade-tip timing measurement of the turbine blades.

Due to the manufacturing technique, mistuning on the turbine is significantly more important than on the compressor. In fact the turbine, made from cast steel has a higher degree of material inhomogeneity. Compressor wheel is machined from aluminium, therefore material properties are more homogenous. Mistuning on the turbine is estimated to be larger than mistuning on the compressor for a factor of 2.[1] For this reason, mistuning is initially implemented exclusively on the turbine blades. Later, in the sensitivity analysis chapter, we attempt to introduce mistuning to the compressor blades to observe its effect on the modal properties.

5.1 Experiment

The implementation of mistuning is based on the experimentally determined resonant frequencies of the different blades obtained with the Blade Tip Timing technique. Blade tip timing measurement was conducted on the test bench by increasing or decreasing the angular velocity in order to sweep through the resonances. Critical speeds of each blade are recorded with the procedure described in [1]. Among all the resonance peaks recorded using the Blade Tip Timing technique (for example, in Fig. 2.19), the frequency corresponding to the peak with the greatest amplitude is considered as the critical speed of the blade. This criterion is based on the assumption that the highest peak represents the most significant resonance condition for the blade under examination.

It is important to underline that the amplitude of the resonance peaks is strongly influenced by the operating conditions of the system. Consequently, measurements taken under different

operating conditions may lead to the identification of different critical frequencies. In other words, in different situations, the peak with the largest amplitude may be at a different frequency, thus leading to the large error bars shown in figure Fig. 5.1. This makes it essential to contextualize measurement results in relation to specific operating conditions for correct interpretation and analysis of data.

Under the EO24 condition, the Wilson and Utengen formula predicts that only the nodal diameter of 0 occurs, as can be easily demonstrated:

$$EO - k \cdot b = \pm ND \, , \, \forall k \in \mathbb{N}^+ \; \rightarrow \; 24 - k \cdot 12 = \pm ND \; \rightarrow \; ND = 0, \; k = 2 \tag{5.1}$$

In the frequency region of blade mode 5 (RPM = 35000, Frequency = EO $\cdot RPM \approx 13500Hz$) times of arrival of the blades have been recorded. Subsequently, using the technique described in Section 3.2 , the frequencies of vibration at resonance at each blade have been extracted. Seven takes have been executed, and the result is the average of all the measurements.

Notation remark: $\omega^{exp}_{BMm,NDn,j}$ indicates: Experimental frequency of the **j-th blade** obtained for the mode of **m-th Blade mode family, Nodal diameter n**

Blade index j	1	2	3	4	5	6	7	8
$\omega^{exp}_{BM5,ND0,j}$ [Hz]	13737.5	13774.3	13757.7	13755.1	13803.3	1.3738	13803.8	13783.0

9	10	11	12
13830.6	13832.2	13772.3	13782.6

5.2 Model

Meanwhile, it is possible to employ the cyclic symmetry model to calculate the effect of the Young Modulus on the natural frequencies. An array of different Young Modulus parameters has been implemented as the blade material.

Young Modulus case index, c	1	2	3	4	5	6	7	8	9
Young modulus value, $E_c^{(test)}$ [GPa]	100	190	200	210	300	180	195	216.11	217.22

10	11	12	13	14	15	16
218.33	219.44	220.55	221.66	222.77	223.88	225

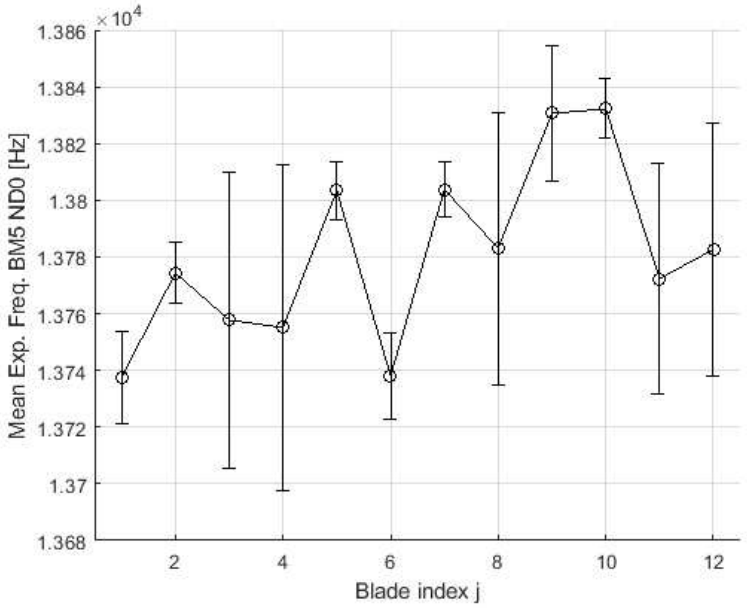

Figure 5.1: Averaged experimental frequencies $\omega^{exp}_{BM5,ND0,j}$ with error bands (2-sigma)

Result of one pre-stressed modal analysis of the cyclic symmetry model consists of a set of modes grouped by Blade Mode Family. Each blade mode family contains 12 modes, with Nodal diameter number ranging from 0 to 6.

Notation remark: $E_c^{(test)}$ represents the test value of Young's modulus, input of the **simulation case of index number c**.
$\omega_{BMm,NDn,c}$ represents the frequency output of the calculation of the **case c, of the mode of Blade Mode family m, with Nodal Diameter n**

For each mode, of Blade mode family j, Nodal diameter k it is thus possible to create a graph with the Young's modules $E_c^{(test)}$ on the abscissa, and the frequencies $\omega_{BMm,NDn,c}$ on the ordinate.

We aim to obtain the most precise estimate possible of the function $\omega_{BMm,NDn}(E)$ which describes the variation of frequencies as a function of Young's Modulus. To obtain this function we interpolate the discrete output represented by the simulation points $\{E_c^{(test)}, \omega_{BMm,NDn,c}\}$.

At first it is possible to assume as a charachteristic, since the analysis is a linear modal analysis, the square root dependency of the frequency on the parameter of stiffness, the Young Modulus:

$$\omega^2_{BMm,NDn} = a_{m,n} \cdot E \tag{5.2}$$

The best fit estimation of $a_{m,n}$ is a single scalar parameter is calculated as the mean for all simulation points:

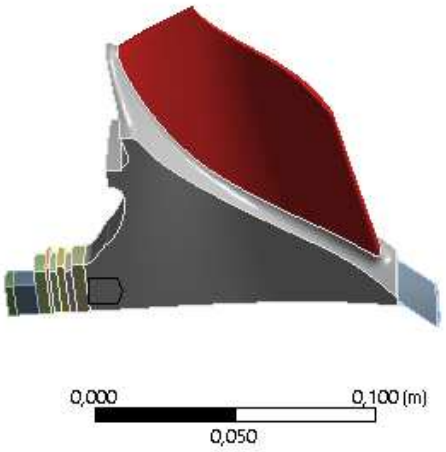

Figure 5.2: Material allocation selection

$$a_{m,n} = \frac{1}{N_c} \sum_{c=1}^{N_c} \frac{\omega^2_{BMm,NDn,c}}{E_c^{(test)}} \tag{5.3}$$

The result for Mode BM5 ND0, shown in figure 5.3, is $a_{5,0} = 946.52 \frac{\text{Hz}^2}{\text{MPa}}$, with a maximum residual of 40 Hz.

Although the linear fit seems to adhere well to simulation points, residuals are not randomly distributed,as shown in Fig. 5.4, indicating additional effects. For cases with a low Young's Modulus residuals are positive, indicating an intensification of the centrifugal stiffening phenomena in these lower stiffness conditions.

For this reason, an alternative interpolation that does not assume linearity should be proposed. One possible approach is to employ a cubic spline to interpolate between the simulation points-

For each interval between two simulation points, $[E_c^{(test)}, E_{c+1}^{(test)}]$, a linear system is solved to determine the four weighting coefficients $p0, m, n, c, q0, m, n, c, p1, m, n, c, q1, m, n, c$ of the Hermite functions $h_{00}, h_{01}, h_{10}, h_{11}$. Weighting coefficients are determined by imposing continuity in the function and its derivative.

The function $\omega_{BMm,NDn,c}(E)$ is therefore piecewise defined.

$$\begin{aligned} \omega_{BMm,NDn}(E) = & h_{00}(E)\boldsymbol{p}_{0,m,n,c} + h_{10}(E)\boldsymbol{q}_{0,m,n,c} + \\ & + h_{01}(E)\boldsymbol{p}_{1,m,n,c} + h_{11}(E)\boldsymbol{q}_{1,m,n,c} \quad , \\ & E \in [E_c^{(test)}, E_{c+1}^{(test)}],\ c = 1, 2, \ldots, N_c \end{aligned} \tag{5.4}$$

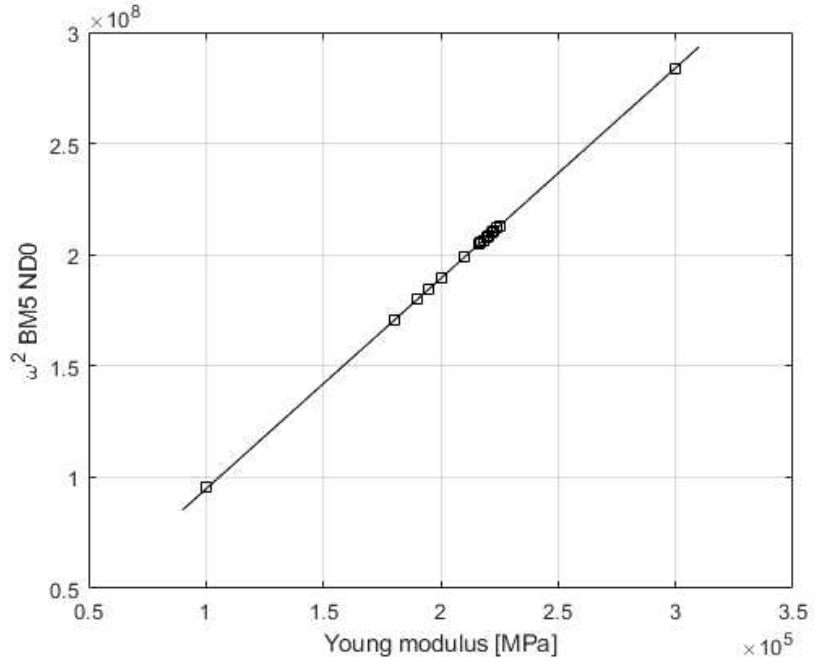

Figure 5.3: Linear fit, BM5 ND0

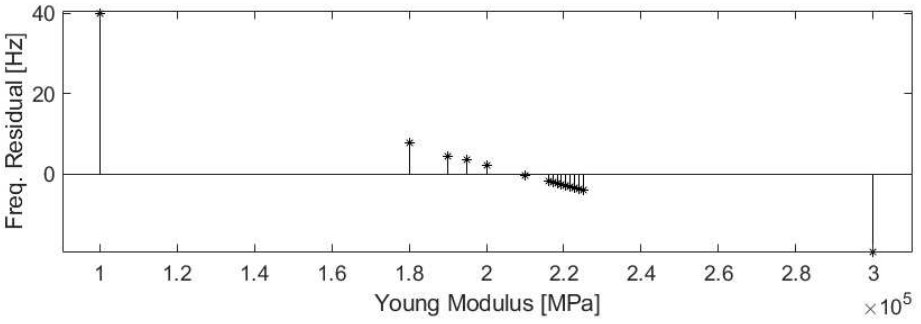

Figure 5.4: Square root fit residuals vs Young modulus

$$
\begin{aligned}
h_{00}(E) &= 2E^3 - 3E^2 + 1 = (1+2E)(1-E)^2 \\
h_{10}(E) &= E^3 - 2E^2 + E = l(1-E)^2 \\
h_{01}(E) &= -2E^3 + 3E^2 = E^2(3-2E) \\
h_{11}(E) &= E^3 - E^2 = E^2(E-1)
\end{aligned}
\tag{5.5}
$$

5.3 Effect of speed

The measured data are obtained by applying a linear RPM sweep to the rotor. The recorded resonant frequencies are therefore referred to blades resonating at different RPMs. To account for this RPM variation, one approach is to study the Campbell curves, which are scaled with the Young Modulus values, in order to find the intersection point with the Engine Order line. The

intersection point changes with the Young's Modulus level, as the Campbell curve of the mode scales up or down, as illustrated by figure 5.5.

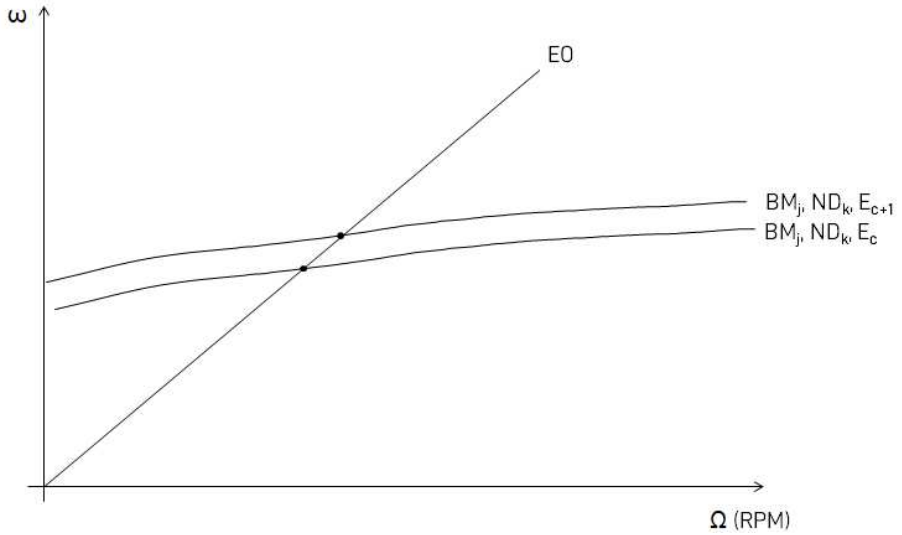

Figure 5.5: Scheme showing the variation of the intersection point with the variation of rotor speed Ω

Suppose we call the Campbell diagram function for a reference Young's modulus E_{ref} $\omega_m, n^{(ref)} = C_{m,n}^{(ref)}(\Omega)$.
This function scales with the Young modulus of the Blade Material E. For an arbitrary Young's modulus, the function can be written as in Eq. 5.6.

$$\omega_{BM_m,ND_n}(\Omega, E) = C_{m,n}(\Omega, E) = C_{m,n}^{(ref)}(\Omega) \cdot \frac{\omega_{BM_m,ND_n}(E)}{\omega_{BM_m,ND_n}(E_{ref})} \tag{5.6}$$

Thus, the intersection point can be found by solving the system with the line $\omega = \Omega \cdot EO$. So it is needed to solve the equation:

$$C_{m,n}^{(ref)}(\Omega) \cdot \frac{\omega_{BM_m,ND_n}(E)}{\omega_{BM_m,ND_n}(E_{ref})} - EO \cdot \Omega = 0 \tag{5.7}$$

It can be solved iteratively and the solution expresses the resonant speed Ω as a function of the young Modulus E. Additionally, the blade frequency ω is equal to $EO \cdot \Omega$. The function the function $\omega_{BM_m,ND_n}(E)$ is eventually found, that keeps into account the speed variation, along the Engine order line.

5.4 Implementation

Once the function describing the effect of the Young's Modulus on the frequency is obtained, it is possible to map the mistuned frequency of each blade to corresponding values of the Young's Modulus. This is achieved by solving the function for the Young's Modulus of the mistuned j-th blade, $E^*_{j,m,n}$.

The process involves substituting the experimentally determined mistuned frequency $\omega^{\text{exp}}_{BMm,NDn,j}$ into the function and solving for $E^*_{j,m,n}$. The resulting values represent the effective Young's Modulus for each blade, accounting for the mistuning effects.

This method provides a straightforward way to evaluate the material property variations responsible for the observed frequencies and allows for assessing the impact of mistuning on the rotor's dynamic behavior.

$$\omega_{BMm,NDn}(E^*_{j,m,n}) = \omega^{exp}_{BMm,NDn,j} \tag{5.8}$$

Using the square root interpolation for determination of the Young's modulus of each blade, the Mistuned Young's modulus of the j-th blade is computed as:

$$E^*_{j,m,m} = \frac{\left(\omega^{\text{exp}}_{BMm,NDn,i}\right)^2}{a_{m,n}} \tag{5.9}$$

j	$E^*_{j,5,0}$ (linear interp.) [GPa]	$E^*_{j,5,0}$ (spline interp.) [GPa]	Deviation (%)
1	215.2951	215.2829	0.0057
2	214.4207	214.4020	0.0087
3	200.4970	200.3767	0.0600
4	201.1247	201.0093	0.0574
5	215.3437	215.3319	0.0055
6	212.4597	212.4267	0.0156
7	200.4842	200.3637	0.0601
8	200.4160	200.2950	0.0604
9	215.3089	215.2969	0.0056
10	214.3297	214.3104	0.0090
11	200.6684	200.5495	0.0593
12	200.4752	200.3547	0.0601

Table 5.1: Mistuned Young modulus values, with linear and spline characteristics, and percentage differences.

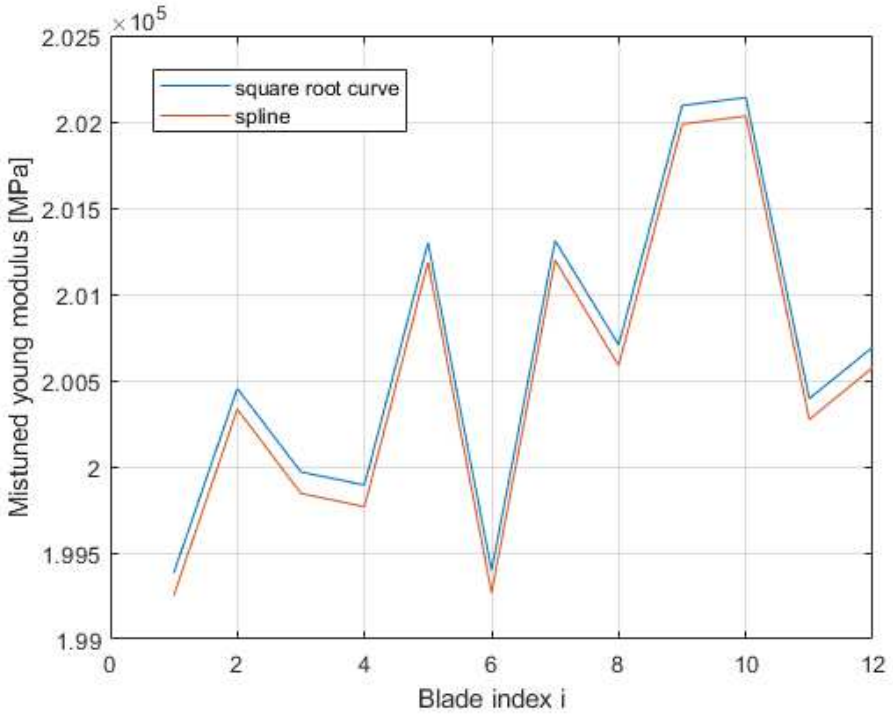

Figure 5.6: Mistuned young modulus of the turbine blades

The mistuned Young Modulus pattern calculated with the linear interpolation is almost identical, with a maximum error of 130 MPa, less than 0.07% of the value, therefore the two methods are considered equivalent. Young's modulus is applied to the turbine blades on the full turbine model and the full rotor model.

6 Reference case, Tuned - Mistuned comparison

This chapter presents the procedure for evaluating the results and comparing the tuned and mistuned models in a reference case, described in Tab. 6.1.

Rotational speed	35000 RPM
Radial bearing stiffness	Value from manufacturer
Axial bearing stiffness	Value from manufacturer
Gas Temperature	200°C
Turbine mistuning	BM5 EO24
Compressor mistuning	Tuned

Table 6.1: Parameters describing reference mistuned case

6.1 Amplitude ratio

Amplitude ratio (AR) is computed as in the paper by Zobel et al [17] as in Eq. (2.16).

Given that modal solutions have been exported with a sensitivity of 0.0001 , for some modes the exported solution data for either the turbine or the compressor is exactly 0. In order to obtain a finite output, the denominator is added to 1e-6. Therefore amplitude ratio is evaluated in the range $10^{\pm 6}$.

By plotting frequency of a mode on the abscissa the amplitude ratio of each mode on the ordinate, the distribution of turbine-dominant, coupled, and compressor-dominant modes in the frequency domain can be observed. This reproduces the plots presented in the paper [17].

6.1.1 Tuned case

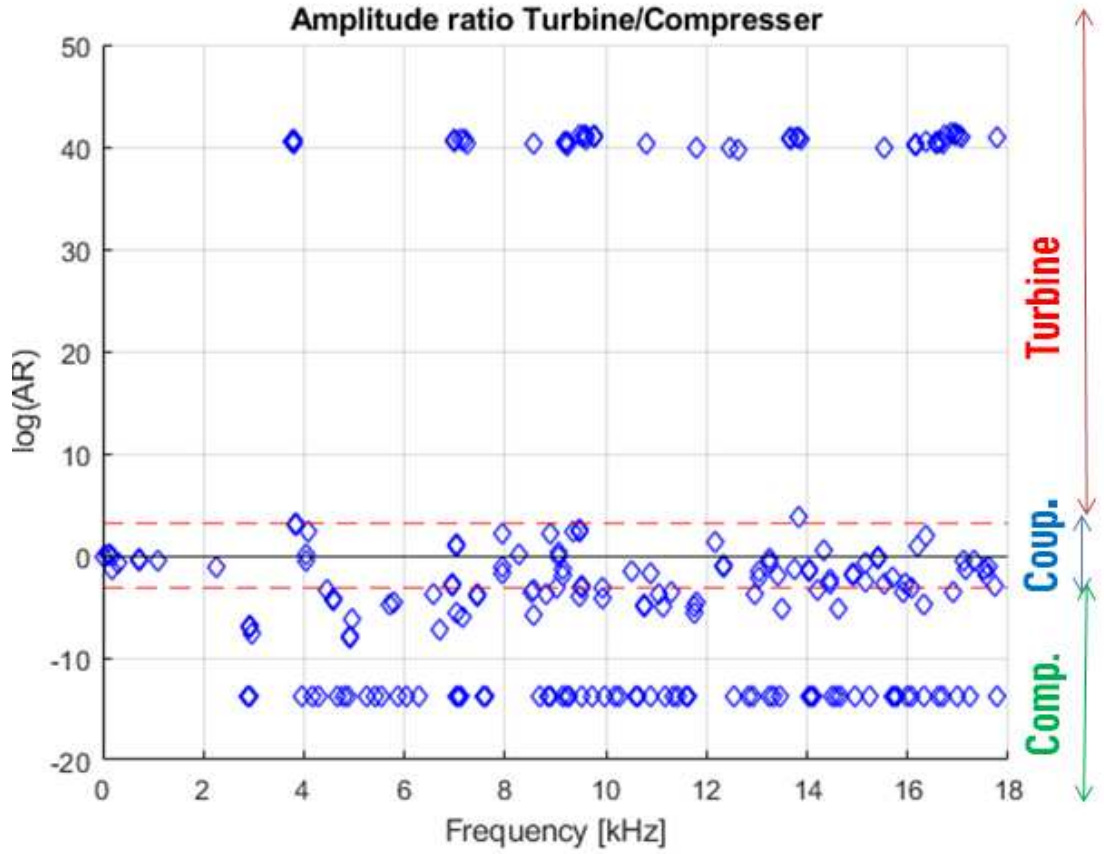

Figure 6.1: Freq-AR plot of reference tuned case

In Fig.6.4 and Fig. 6.1 in the vertical axis is conveniently represented the natural logarithm of the amplitude ratio. The amplitude ratio is defined as the turbine's maximum deformation divided by the compressor's maximum deformation. Therefore in the the positive abscissa area are represented the modes predominantly expressed on the turbine. Negative abscissa is associated to the modes predominantly expressed on the compressor. Modes with zero participation of the turbin tips have been assigned an AR equal to $10^{-}6$, therefore they evaluate to log(AR)=-13.6 in the bottom part of the diagram.
Conventionally, in similar way to the paper [17], a mode is considered turbine-compressor coupled when AR falls the interval [1/25, 25] .This interval, represented by the red dashed lines, is conventionally used to identify coupled modes.

On the left side of Fig.6.4 and Fig.6.1, it can be observed that the low-frequency modes are substantially coupled. The first four modes can be considered rigid motions of the shaft on the bearings, and they are confined within the [0, 240] Hz region. They are represented in Fig. 6.2. Mode 1 corresponds to an axial rotation at a frequency very close to 0. Mode 1 and 2 correspond to roto-translations on the radial bearings in the two orthogonal planes. Mode 4 represents the axial bearing mode, characterized by the uniform axial motion of the impeller at 166 Hz.

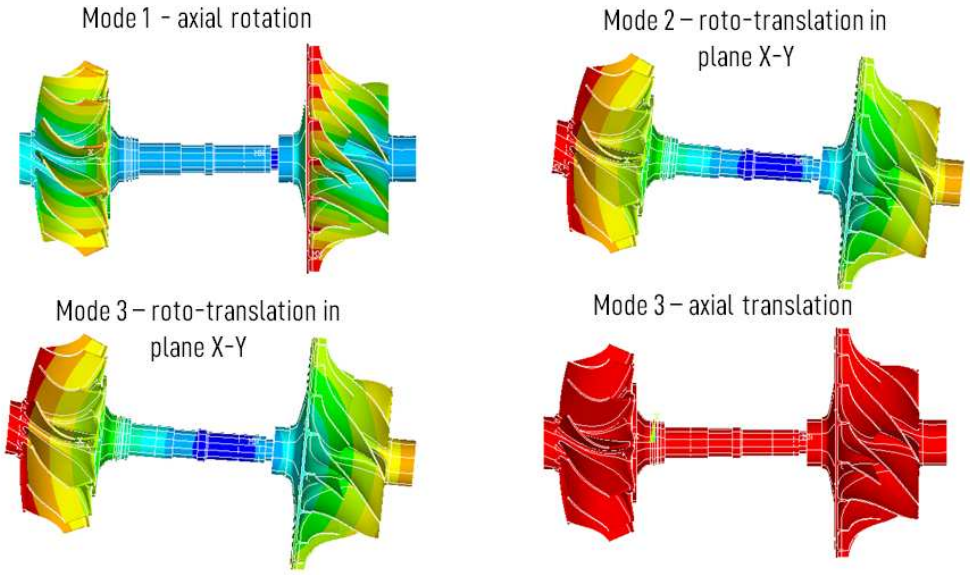

Figure 6.2: Rigid motion solutions

Two additional whole turbine modes occur at low frequency Fig. 6.3. These are Gyroscopic modes, and consist in the precession of the turbine around the rotor axis.

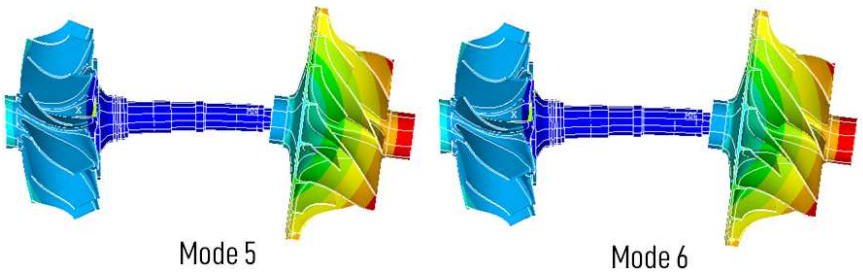

Figure 6.3: Modes 5 and 6 of the tuned rotor

6.1.2 Mistuned case

Figure 6.4 shows the frequency and the logarithm of the amplitude ratio (AR) for modes within the frequency range [0, 18] kHz, considering mistuning applied to the turbine. It is immediately noticeable that, in the tuned case, certain modes are concentrated on the turbine blades. However, in the mistuned case, these modes exhibit a non-zero participation on the compressor. As a result, these modes shift closer to the coupled region. To better understand this phenomenon it may be useful to look at the detailed comparison.

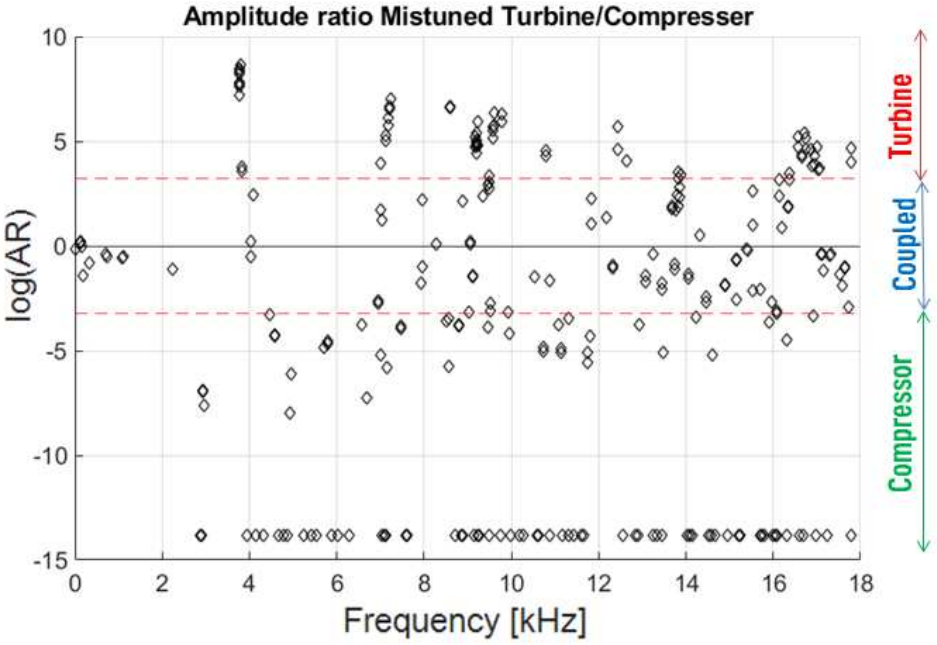

Figure 6.4: Freq-AR plot of reference mistuned case

6.1.3 Comparison

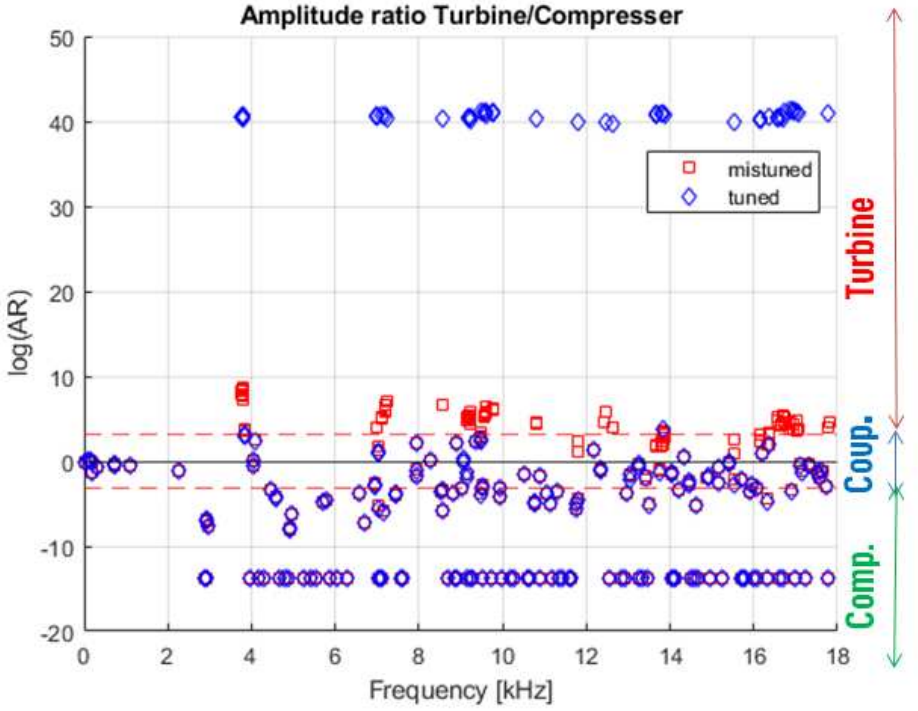

Figure 6.5: Freq-AR plot of tuned and mistuned case

In Fig. 6.5, modes that were turbine-dominated in the tuned case move closer to the coupled region when mistuning is introduced on the turbine. The other modes remain relatively unaffected by mistuning.

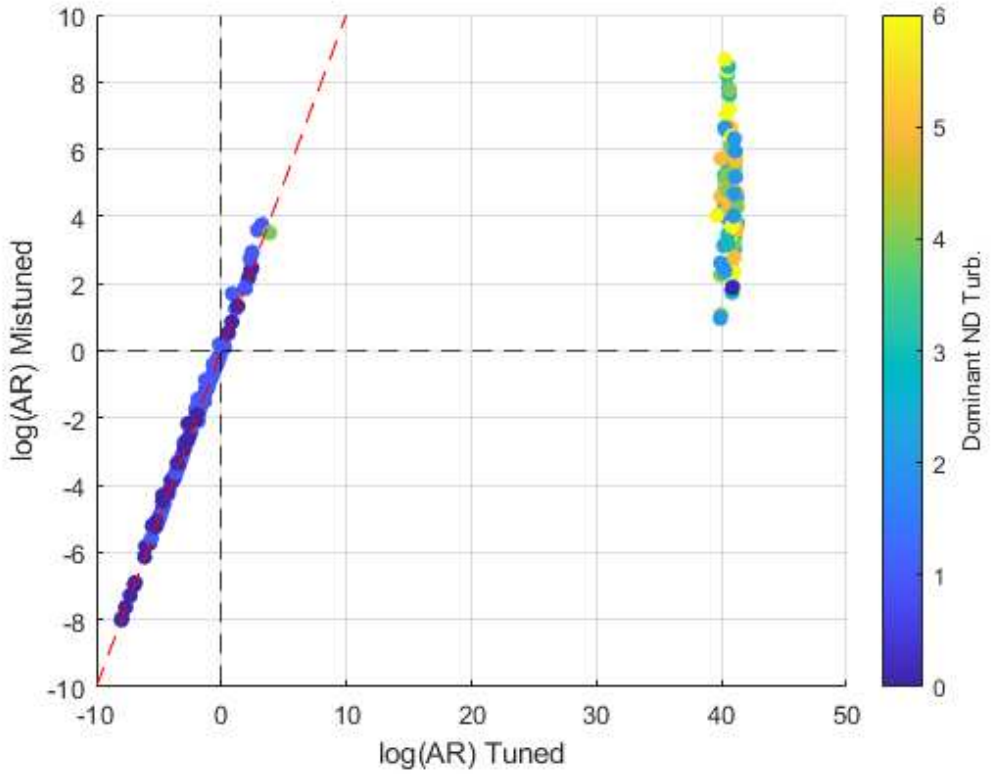

Figure 6.6: Comparison of amplitude ratios for tuned and mistuned modes

Since in this case mistuning does not alter the frequencies too significantly, it is possible to associate mistuned modes to tuned modes based on the frequency proximity. In the diagram in Fig. 6.6, the AR of the tuned modes (x axis) is compared with the respective mistuned modes on the y axis. It is possible to distinguish two sets of modes:

- A set of modes in which the amplitude ratio does not change by introducing mistuning, grouped around the red line x=y
- A set of modes for which mistuning shifts the AR remarkably towards 1. All of these modes are poorly coupled in the tuned case.

It can therefore be said that if a tuned mode is highly coupled, the introduction of mistuning does not change the situation. For very poorly coupled tuned modes, mistuning shifts the amplitude ratio very close to 1. Colour in Fig. 6.6 represents the number of nodal diameters on the tuned turbine. Blue = ND0, Yellow = ND6. It is explained in next section how the calculation of the dominant nodal diameter of the mode is performed.
As shown in Fig. 6.12, these modes are associated with a low number of nodal diameters.

Conversely, the second set is composed of modes that are associated to high number of nodal diameters.

6.2 Calculation of nodal diameter spectrum

Fourier decomposition is needed in order to relate each mistuned mode shape to the tuned mode shapes. Equation (2.22) is implemented in Matlab with the function `fft` (fast Fourier transform).

Since, due to mistuning, more than one blade mode family can compose one mistuned mode, it is necessary to evaluate the Fourier coefficients on multiple points. As blade sectors are identical and coordinates are cyclically periodic, selection of corresponding nodes is straightforward. For computational simplicity, and given the relevance in Blade Tip Timing [1], unless specified otherwise, the Fourier evaluation is limited to the nodes on the turbine tips.

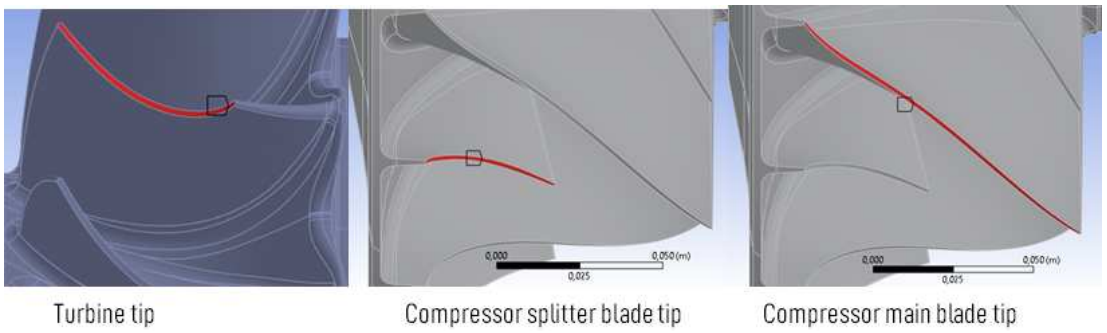

Figure 6.7: Selections on the rotor tips for the calculation of the Discrete Fourier transform on the rotor

In order to evaluate the Discrete Fourier transform, it is needed to transform the modal solution, which is given as an output in Cartesian coordinates u_x, u_y, u_z, into cylindrical coordinates u_x, u_r, u_t, referenced to the axis of rotation.

The x axis coincides with the axis of the rotor, while y and z axes describe the plane normal to the rotor axis. The tangential coordinate can be conveniently computed as the ratio of the deformed position and un-deformed position expressed as complex number. The imaginary part of this ratio corresponds to the angle of deformation Eq. (6.1)

$$u_t = \mathfrak{Im}\{\frac{(y+u_y)+i(z+u_z)}{y+iz}\} \cdot \sqrt{y^2+z^2} \tag{6.1}$$

The radial component is computed similarly, using instead the real part of the complex ratio, which represents the deformation in the radial direction, as in Eq. (6.2)

$$u_r = \mathfrak{Re}\{\frac{(y+u_y)+i(z+u_z)}{y+iz}\}\cdot\sqrt{y^2+z^2} \tag{6.2}$$

Since the axial coordinate of the rotor remains invariant and coincides with the x-axis, axial components u_x are simply:

$$u_x = u_x \tag{6.3}$$

To calculate the DFT, the nodes must be grouped into sets of Z equispaced nodes that belong to the same circular series on a chosen axial plane.

$$\text{for } N_q \in \text{j-th tip} \quad \{x_q^{(j)}, y_q^{(j)}, z_q^{(j)}\} \leftrightarrow \{u_{x,q}^{(j)}, u_{t,q}^{(j)}, u_{r,q}^{(j)}\} \tag{6.4}$$

q is node index, j is the blade index.
Tangential components can be arranged in the table 6.5, and axial components can be rearranged in the table 6.6. In both tables, the values in the same column correspond to nodes belonging to the same circular series. The discrete Fourier transform can then be computed for each column:

$$[\psi_t] = \begin{bmatrix} u_{t,1}^{(1)} & u_{t,2}^{(1)} & \cdots & u_{t,Q}^{(1)} \\ \vdots & \vdots & \cdots & \vdots \\ u_{t,1}^{(j)} & u_{t,2}^{(j)} & \cdots & u_{t,Q}^{(j)} \\ \vdots & \vdots & \cdots & \vdots \\ u_{t,1}^{(Z)} & u_{t,2}^{(Z)} & \cdots & u_{t,Q}^{(Z)} \end{bmatrix} \tag{6.5}$$

$$[\psi_x] = \begin{bmatrix} u_{x,1}^{(1)} & u_{x,2}^{(1)} & \cdots & u_{x,Q}^{(1)} \\ \vdots & \vdots & \cdots & \vdots \\ u_{x,1}^{(j)} & u_{x,2}^{(j)} & \cdots & u_{x,Q}^{(j)} \\ \vdots & \vdots & \cdots & \vdots \\ u_{x,1}^{(Z)} & u_{x,2}^{(Z)} & \cdots & u_{x,Q}^{(Z)} \end{bmatrix} \tag{6.6}$$

- $[\psi_t]$ table with the tangential components
- $[\psi_x]$ table with the axial components

We take each column of ψ_t and ψ_x that constitutes array of size (Zx1) and calculate the discrete Fourier transform according to Eq.(2.22) with `fft` function on Matlab, which returns as output an array $\mathfrak{F}_t$ or $\mathfrak{F}_x$ of size (Zx1).

The complex output of Eq. (2.22) can be interpreted as Amplitude and Phase of the corresponding tuned mode. In this case the phase corresponds to the angular position of the nodal diameter line of the tuned component.

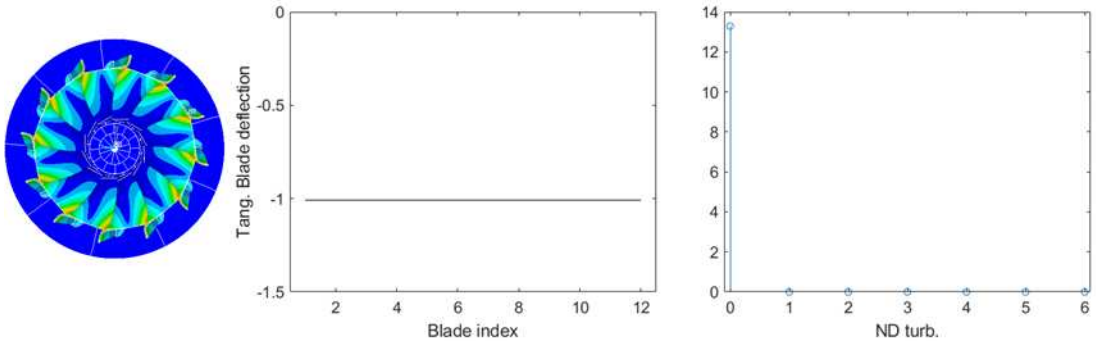

Figure 6.8: Demonstration of blade deflection and nodal diameter spectrum for tuned mode 103

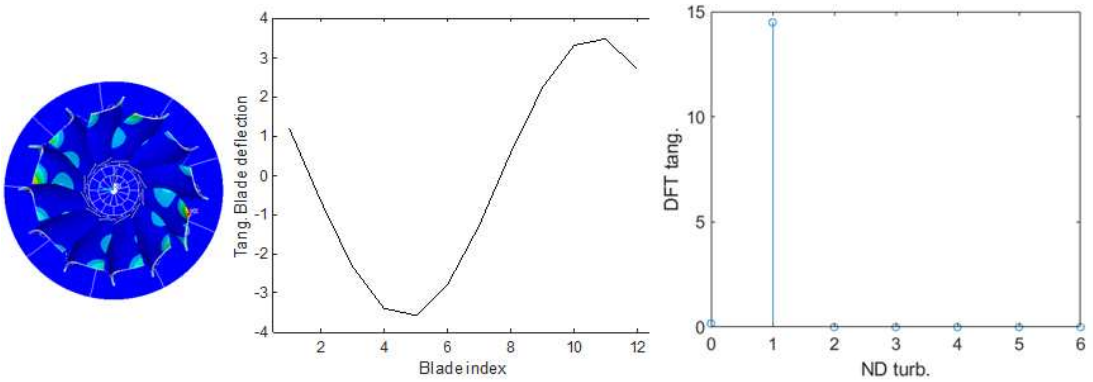

Figure 6.9: Demonstration of blade deflection and nodal diameter spectrum for tuned mode 142

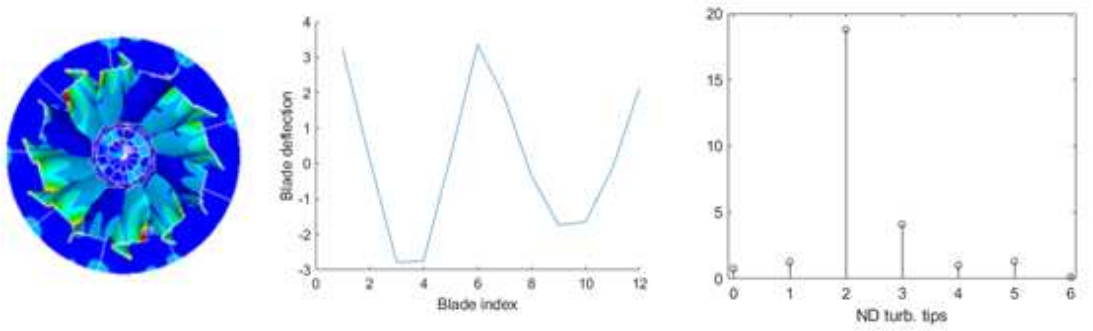

Figure 6.11: Demonstration of blade deflection and nodal diameter spectrum for mistuned mode 230

Dominant nodal diameter is the nodal diameter that has the highest amplitude in the nodal diameter spectrum.

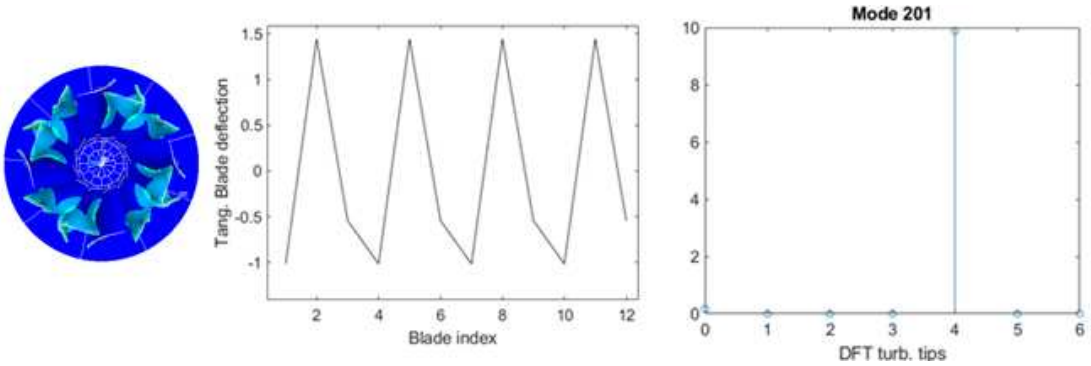

Figure 6.10: Demonstration of blade deflection and nodal diameter spectrum for tuned mode 201

6.2.1 Turbine tips

The dominant nodal diameter of a mode can be plotted against the amplitude ratio to show the effect of the nodal diameter on turbine-compressor coupling. In plot 6.12 the nodal diameter of the turbine is represented on the x-axis, log(AR) is represented on the y-axis. Values which evaluate to 0 on all the turbine tips have been excluded because could not be related to one dominant nodal diameter.

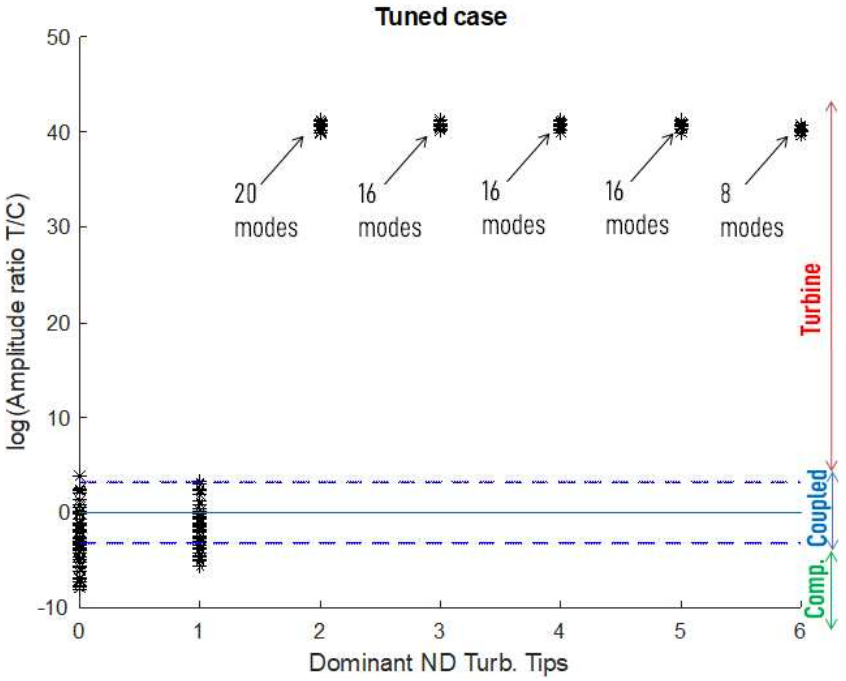

Figure 6.12: Dominant nodal diameter component on the turbine blade tips and Amplitude ratio, for the tuned turbine case

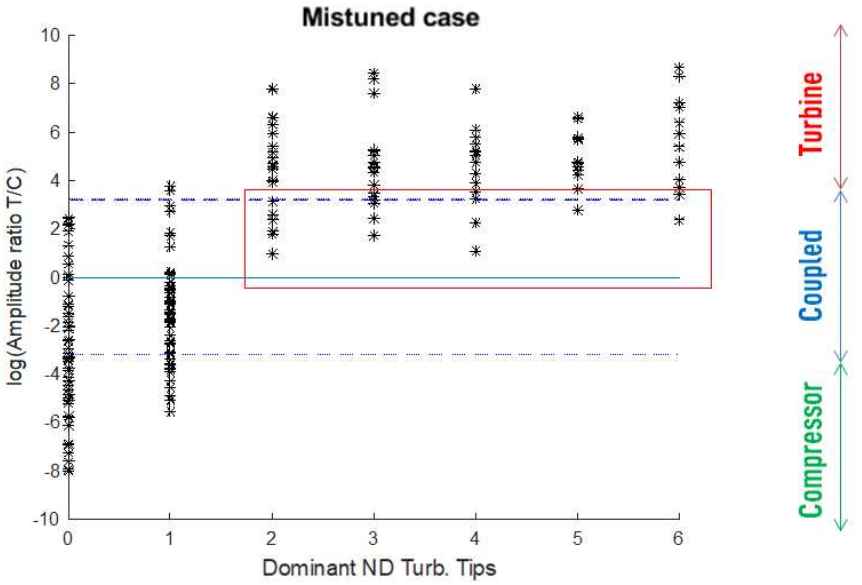

Figure 6.13: Dominant nodal diameter component on the turbine blade tips and amplitude ratio, for the BM5ND0 mistuned turbine

Introducing mistuning, Fig. 6.13, it is possible to note that, although it remains generally true that almost all coupled modes have a nodal diameter of 0 or 1, there are coupled modes even for a nodal diameter greater than one, represented in the red rectangle.

These modes are listed in table 6.2. It is possible to observe that all these modes are expressed primarily on the turbine (AR>1). Furthermore, all modes listed have dominant nodal diameter 0 and 1 on the compressor.

Mode N°	Frequency [Hz]	AR	dominant ND turb.	dominant ND comp.
143	9483.5	20.9	3	0
200	11817.9	2.9	4	0
201	11819.4	9.6	4	0
230	13676.8	6.8	2	1
231	13683.6	6.0	2	1
234	13770.2	5.7	3	1
235	13784.9	11.3	3	0
239	13840.0	10.4	6	0
240	13853.9	16.2	5	0
275	15522.8	2.6	2	0
276	15523.9	13.6	2	0
295	16147.2	10.7	2	0
296	16150.4	22.9	2	0
303	16375.2	23.7	3	0

Table 6.2: List of coupled modes which arise due to mistuning

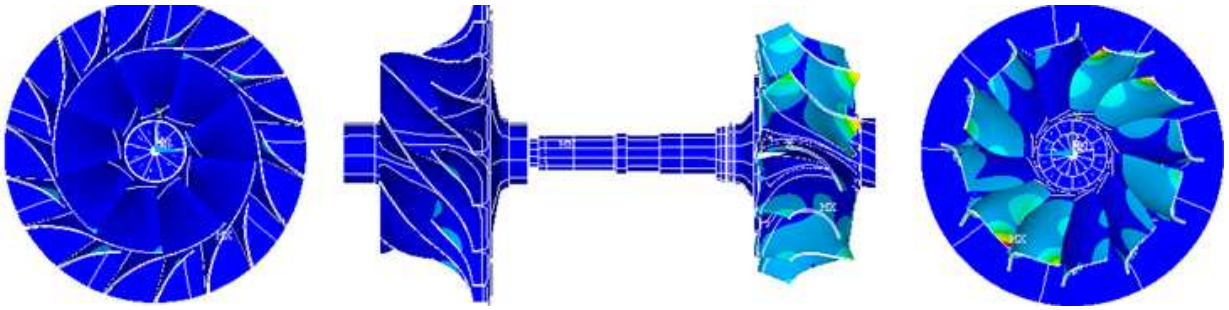

Figure 6.14: Weakly coupled turbine leading mode, Mode 143, AR = 21, Frequency = 9479 Hz

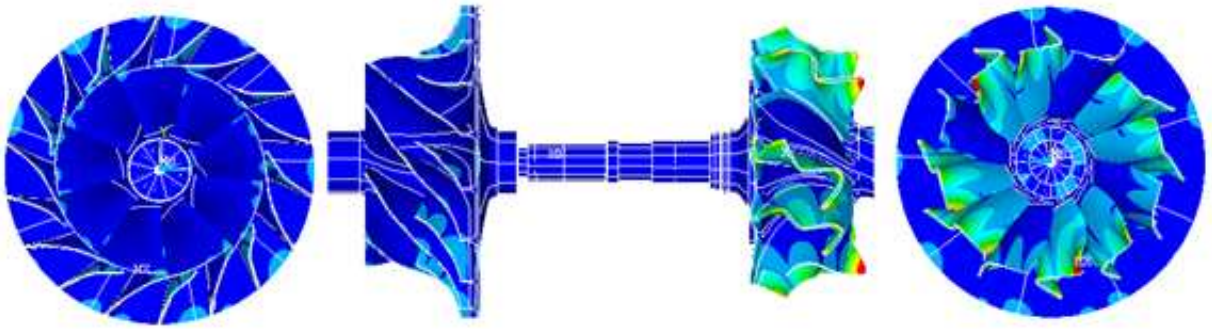

Figure 6.15: Weakly coupled turbine leading mode, Mode 230, AR = 6.9, Frequency = 13667 Hz in the turbine BM5 frequency region

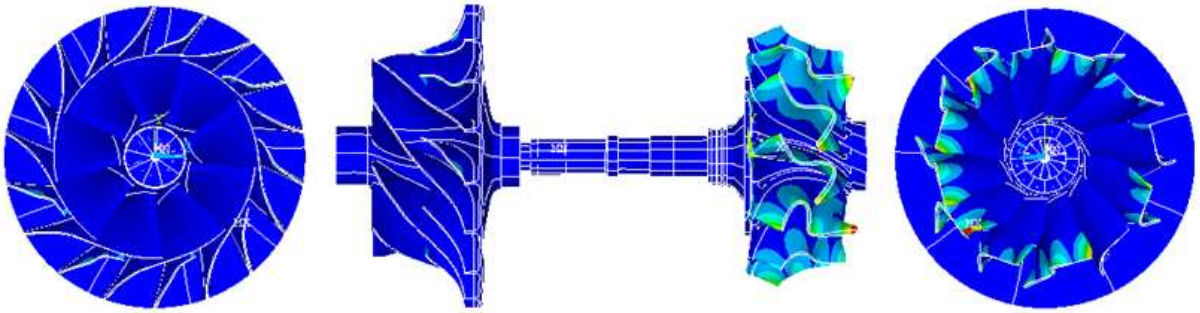

Figure 6.16: Weakly coupled turbine leading mode, Mode 234, AR = 5.7, Frequency = 13770 Hz in the turbine BM5 frequency region

In Figures 6.14, 6.16, and 6.15, several coupled modes with dominant nodal diameters (ND) greater than 1 ($ND > 1$) are shown. These modes are contained within the red rectangle highlighted in Figure 6.13.

Figures 6.14 and 6.16 specifically display two weakly coupled modes. Mode 143 exhibits a dominant ND3 component on the turbine and a dominant ND0 component on the compressor. The coupling between the turbine and compressor occurs primarily through torsional interactions. This coupling mechanism induces a non-zero ND0 component in the turbine's nodal diameter spectrum due to the transmission of the compressor's ND0 component.

Mode 230, on the other hand, corresponds to BM5 with ND2 on the turbine and has a dominant ND1 component on the compressor. This mode represents a bending-coupled mode, where the ND1 component from the compressor is transmitted to the turbine, leading to a non-zero ND1 component in the turbine's discrete Fourier transform (DFT) spectrum. The bending coupling mechanism emphasizes the interaction between the compressor and turbine through shared vibrational energy associated with specific nodal diameters.

These modes demonstrate the coupling phenomena in mistuned systems, where dominant nodal diameter components from one component (e.g., compressor) influence the vibrational characteristics of another (e.g., turbine), resulting in coupled dynamic behavior.

6.2.2 Compressor tips

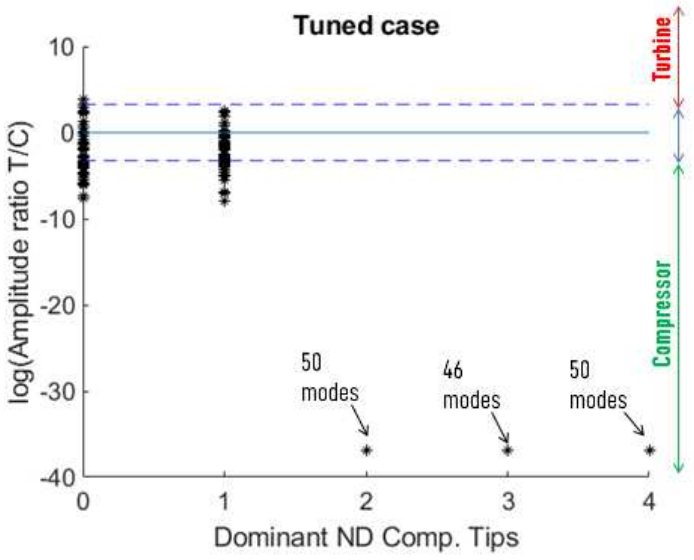

Figure 6.17: Dominant nodal diameter component on compressor main blade tips and amplitude ratio, for the tuned turbine case

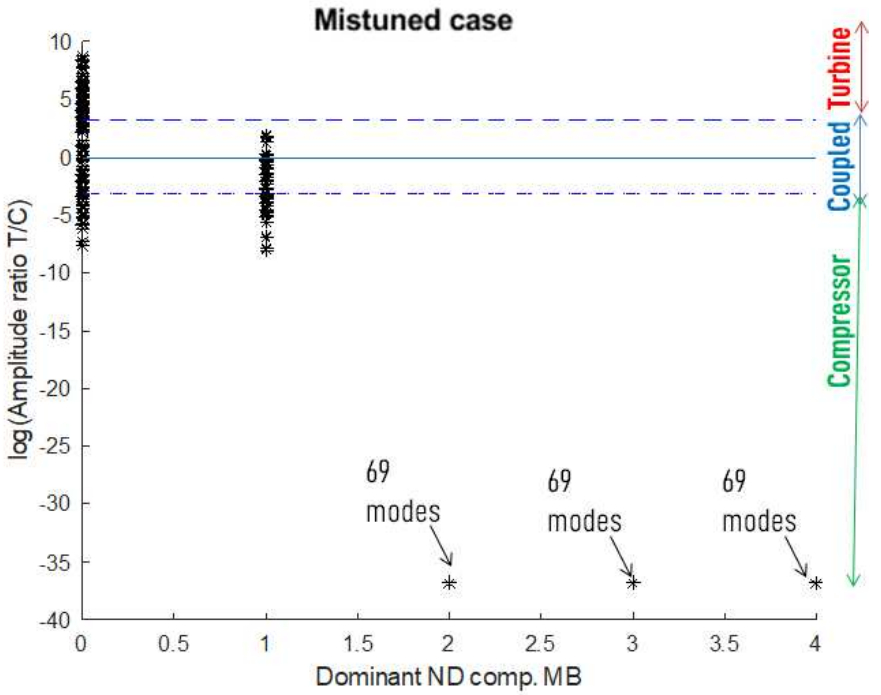

Figure 6.18: Dominant nodal diameter component on compressor main blade tips and amplitude ratio, for the BM5ND0 mistuned turbine

When plotting the dominant nodal diameters on the compressor, we observe a negligible difference between the case of tuned turbine and mistuned turbine, indicating a negligible influence of the turbine mistuning on the nodal diameter components of the compressor. Regarding the tuned compressor, it is possible to confirm that the zero and one nodal diameters are the only ones responsible for the coupled vibration of the turbine and compressor.

6.3 Mode localization(Klauke)

The mode localization parameters proposed by Klauke (2.28) (2.26) (2.24) have been evaluated for all modes on the turbine tips, both in the tuned and mistuned case. In figure 6.19 is shown the effect of mistuning on the mode fill factor. Due to the asymmetry of the rotor model, some degree of localization is inevitable, even in the tuned case. In figure 6.19 it can be observed how the mode fill factor is affected by mistuning. We note that the maximum value of the mode fill factor is 0.4 for the mistuned case and 0.1 for the tuned case.

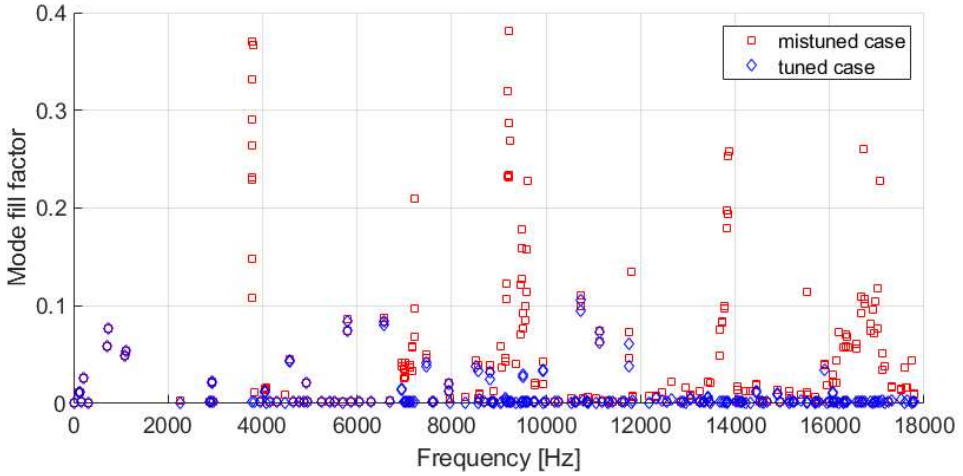

Figure 6.19: For the turbine mode shapes in freq. range [0,18] kHz Natural frequency (x-axis) and mode fill factor (y-axis) for tuned and mistuned case

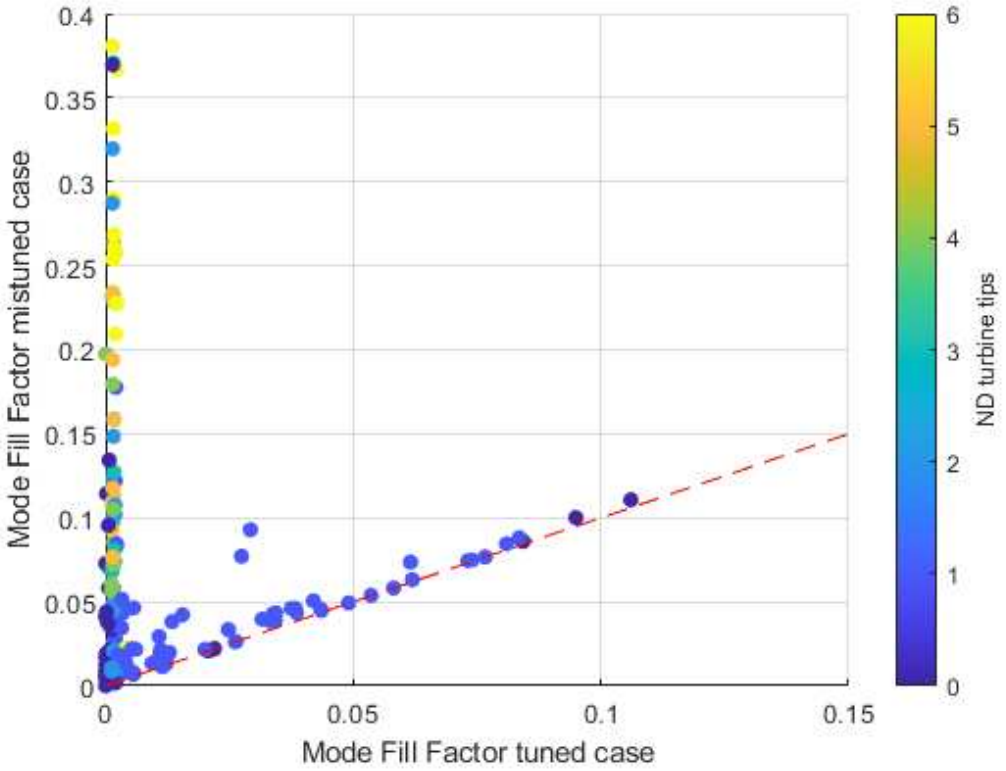

Figure 6.20: For the full rotor modes in freq. range [0,18] kHz, plot of the mode fill factor of the tuned case (x-axis) and mode fill factor of the respective mistuned case (y-axis)

Figure 6.20 shows the general trend with respect to the mode fill factor of a mistuned mode compared to the respective tuned mode (association based on proximity in frequency). Colour

represents the nodal diameter on the turbine, blue = ND0, yellow = ND6. We note that it is possible to recognize two sets of modes:

- Modes whose mode fill factor does not increase substantially with the introduction of mistuning, grouped along the diagonal line which corresponds to the line x=y. All these modes have low nodal diameter, either 0 or 1.
- Modes whose mode fill factor increases considerably introducing mistuning, independently on the tuned mode fill factor. These modes are clustered around the vertical axis.

In Figure 6.21, an example of modal localization is shown, specifically one of the modes with the greatest increase in mode fill factor: the full rotor mode 132, in the tuned case (on the left) and the mistuned case (on the right).

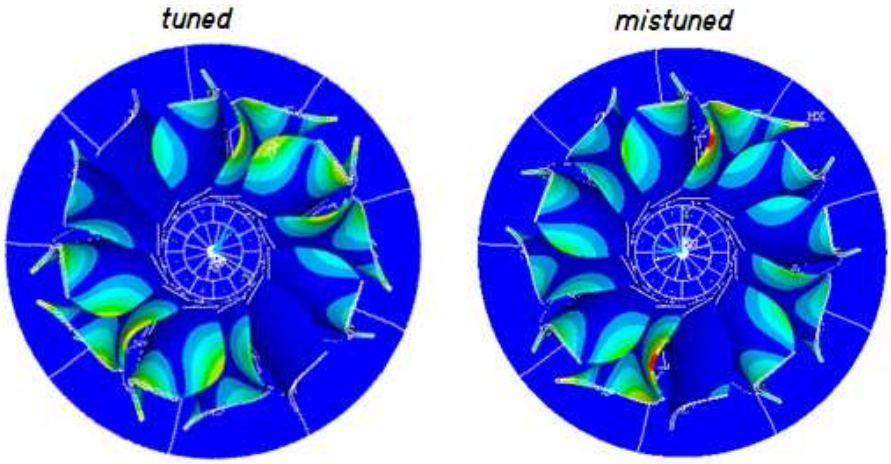

Figure 6.21: Localization of turbine mode shape for full rotor mode 132 in cases tuned (left) and mistuned (right), with dominant nodal diameter 4

Figure 6.22 presents a comparison between the Localization Factor of tuned and mistuned modes. It can be observed that modes characterized by low nodal diameters experience only a minimal increase in the Localization Factor when subjected to mistuning. This indicates that the structural coupling or energy distribution in these modes is relatively unaffected by the imperfections introduced. In contrast, modes with high nodal diameters exhibit a pronounced increase in the Localization Factor, suggesting that these modes are more sensitive to mistuning. The significant rise in the Localization Factor for high-nodal-diameter modes implies a greater concentration of vibrational energy in specific regions, leading to more localized mode shapes.

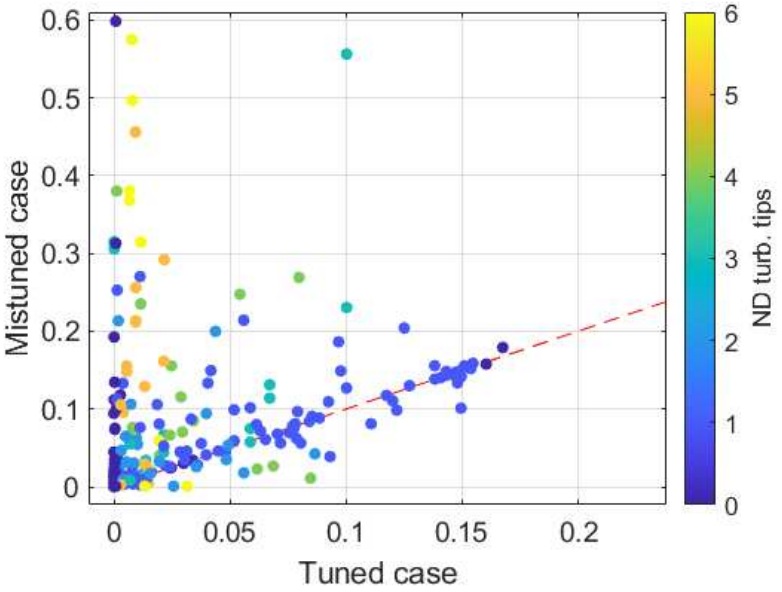

Figure 6.22: Comparison of localization factor between tuned and mistuned modes

6.4 Modal assurance criterion

To evaluate the degree of similarity of two mode shapes, the most popular method is the Modal assurance criterion. Modal assurance criterion is given by a product of normalized mode shapes, that results in a value between zero and 1.

Since the mode solutions are in an arbitrary angular position, it is necessary to compare two different mode shapes by testing the different sector angle configurations by steps of $2\pi/Z$, and choosing the configuration that allows to obtain the highest MAC value.

Given two mode shapes $\boldsymbol{\phi}_A$ and $\boldsymbol{\phi}_X$ the Modal assurance criterion is computed as in Eq. (6.7). [23] [24]

$$MAC(r,q) = \frac{\left|\{\boldsymbol{\phi}_A\}_r^T \{\boldsymbol{\phi}_X\}_q\right|^2}{\left(\{\boldsymbol{\phi}_A\}_r^T \{\boldsymbol{\phi}_A\}_r\right)\left(\{\boldsymbol{\phi}_X\}_q^T \{\boldsymbol{\phi}_X\}_q\right)} \tag{6.7}$$

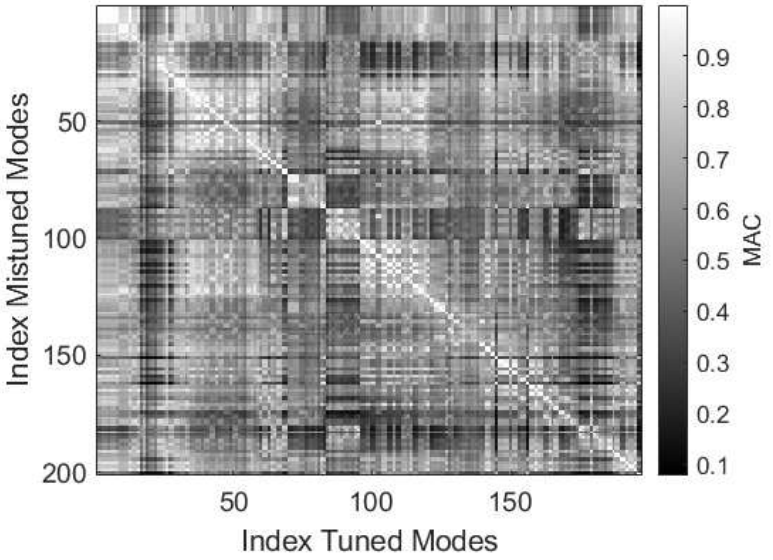

Figure 6.23: MAC values comparing tuned and mistuned modes evaluated on the turbine tips

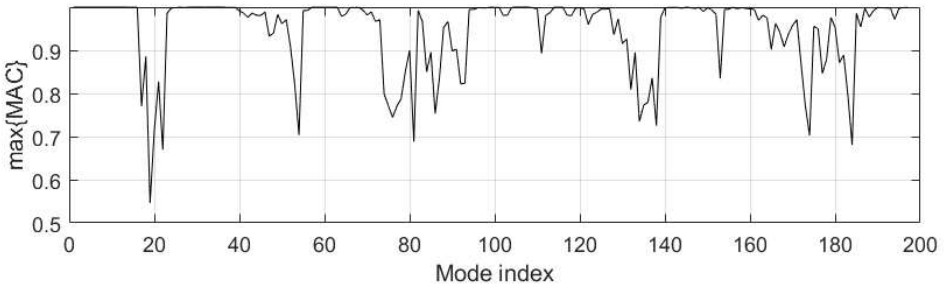

Figure 6.24: MAC value comparing tuned modes to their most similar mistuned mode evaluated on the turbine tips

In the figures, the MAC evaluation is limited to the modes with non-zero components in the turbine. The mode index in Figure 6.24 is ordered by frequency and includes only the modes that are non-zero on the turbine. It can be observed that the introduction of mistuning causes a few selected modes to exhibit MAC values as low as 0.6. This indicates that the mistuning pattern has a high intensity, significantly disrupting the tuned mode shapes and leading to notable deviations in the modal behaviour.

7 Analysis of turbine - compressor coupling

7.0.1 Shaft analysis

Shaft analysis is important for identifying the coupling mechanism for turbine/compressor coupled modes. Since the shaft mesh is structured,nodes are grouped into planes perpendicular to the shaft axis. This structured mesh simplifies the evaluation of shaft modes by allowing the nodal solution to be analyzed section by section.

Bending

To identify bending deformation, the mean deformation of each section in the axial plane is evaluated as in Eq. (7.1).

$$\begin{Bmatrix} U_y \\ U_z \end{Bmatrix} = \frac{1}{N_{\text{nodes}}} \sum_q \begin{Bmatrix} u_{y,q} \\ u_{z,q} \end{Bmatrix} \tag{7.1}$$

Torsion

Torsion angle Θ is computed as the mean rotation angle around the rotor axis for all the nodes of the section. Assuming small displacements, Θ equals the imaginary part of the ratio between two complex numbers: the numerator representing the deformed point and the denominator representing the undeformed point, as shown in (7.2)

$$\Theta_{sec} = \frac{1}{N_{nodes}} \sum_{q=1}^{N_{nodes}} \mathfrak{Im}\{\frac{(y_q + u_{y,q}) + i(z_q + u_{z,q})}{y_q + iz_q}\} \tag{7.2}$$

Axial Behaviour

Axial deformation is simply calculated, for each section as the mean deformation of each node in the axial direction.

$$U_x = \frac{1}{N_{nodes}} \sum_{q=1}^{N_{nodes}} u_{x,q} \tag{7.3}$$

Shaft displacement amplitude ratios

Quantifying the torsion, bending, and thrust components is essential to understanding the coupling mechanism of a mode. These quantities can be used by isolating each of the three mechanisms and comparing their associated displacements and to the maximum displacement value of the shaft.
It is possible to define the Amplitude ratio for the shaft as the ratio between the maximum displacement on the shaft to the maximum displacement on the entire model 7.4.

$$AR_{shaft} = \frac{\max\{u_{shaft}\}}{\max\{u\}} \tag{7.4}$$

$\max\{u_{shaft}\}$ is the maximum total deformation occurring on the shaft. Furthermore, to each of the three mechanisms it is possible to associate an amplitude ratio:

$$AR_{bend} = \frac{\max\{\sqrt{U_y^2 + U_z^2}\}}{\max\{u_{shaft}\}} \tag{7.5}$$

$$AR_{rot} = \frac{\langle r \rangle \max\{\Theta\}}{\max\{u_{shaft}\}} \tag{7.6}$$

$\langle r \rangle$ is the mean radius of the shaft, equal to 2mm.

$$AR_{norm} = \frac{\max\{U_x\}}{\max\{u_{shaft}\}} \tag{7.7}$$

Validation - tuned case

To validate the shaft analysis tool, three modes will be verified, each of which presents a behaviour characterized by either pure bending, torsion and axial movement:

- **Mode 8** Torsion mode, represented in Fig. 2.15
- **Mode 12** Thrust mode, represented in Fig. 2.16
- **Mode 7** Bending mode, represented in Fig. 2.17

Mode8 , pure torsion

In Fig. 7.2 is represented the torsion angle of the shaft for the mode 8. In Fig. 7.4 is represented the mean bending line of the mode, and in Fig. 7.3 is represented the modal deformation of axial direction $U_x(x)$. One can note that both axial displacement and bending evaluate to null or negligible value.

ARflex = 6.5392e-05
ARrot = 0.2880
ARnorm = 0

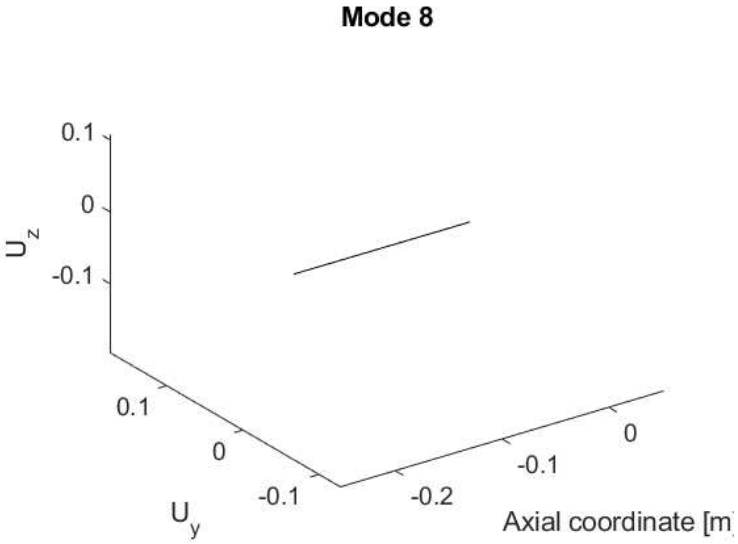

Figure 7.1: Mean bending line of the Mode shape N°8

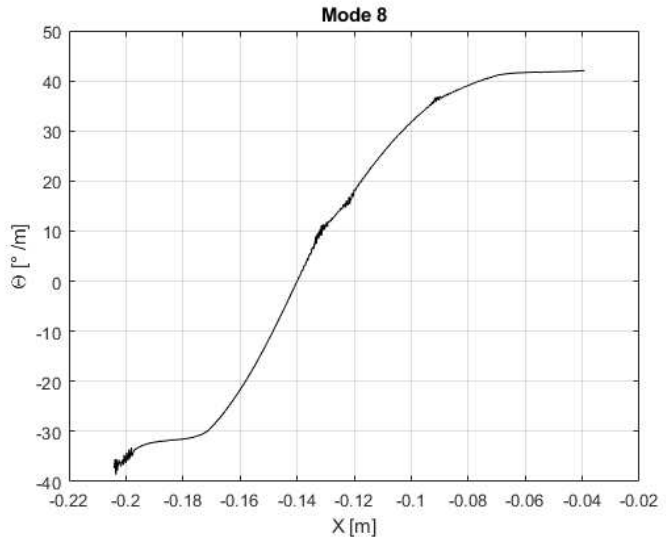

Figure 7.2: Rotation angle due to torsion as a function of the axial coordinate for the Mode shape N°8

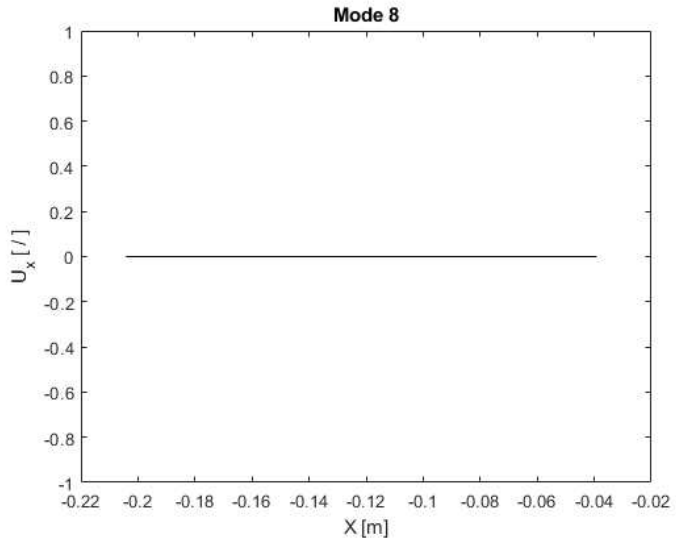

Figure 7.3: Axial displacement as a function of the axial coordinate for the Mode shape N°8

Mode 12, pure axial behaviour

In Fig. 7.2 is represented the modal deformation if axial direction $U_x(x)$. In Fig. 7.4 is represented the mean bending line of the mode, and in Fig. 7.5 the torsion angle of the shaft for the mode 8. One can note that both torsion and bending evaluate to null or negligible value.

AR_{bend} = 7.1738e-05
AR_{rot} = 0.0013
AR_{norm} = 0.8784

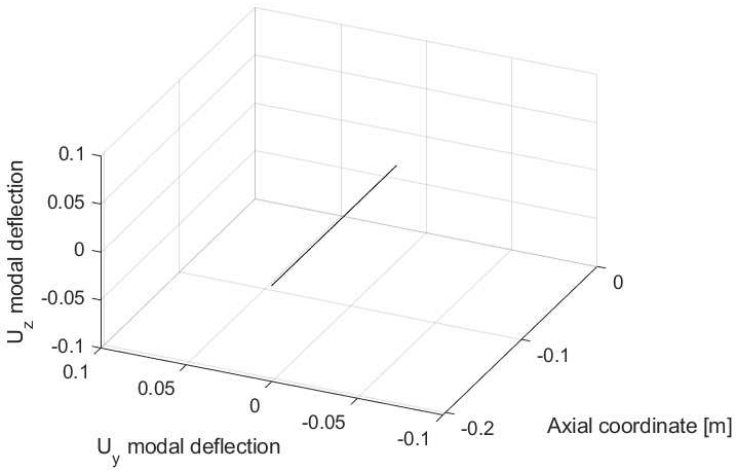

Figure 7.4: Mean bending line of the Mode shape N°12

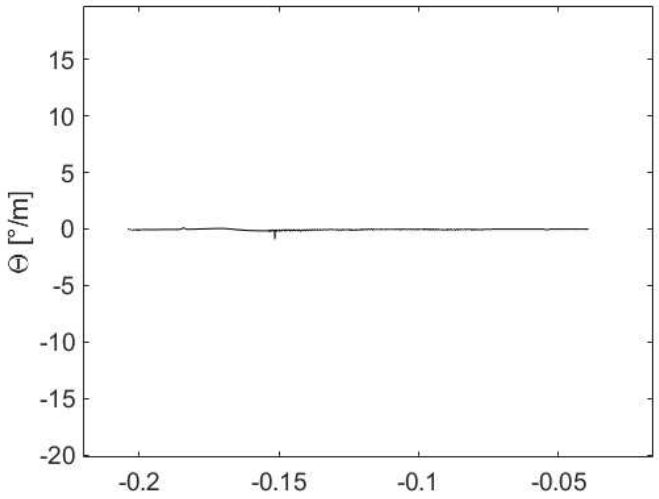

Figure 7.5: Rotation angle due to torsion as a function of the axial coordinate for the Mode shape N°12

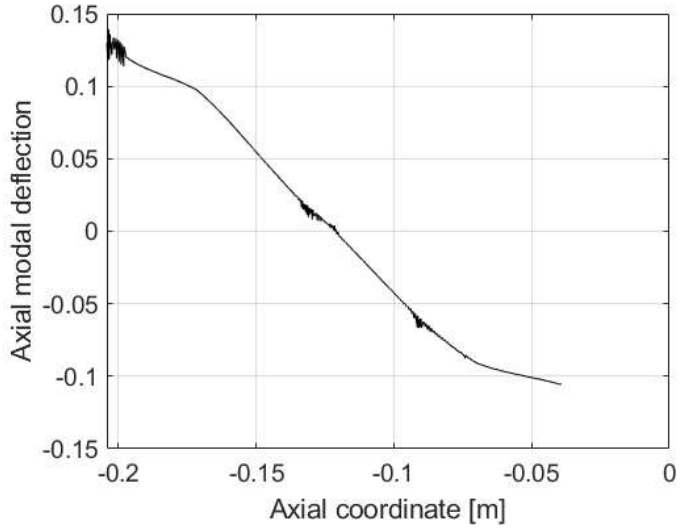

Figure 7.6: Axial displacement as a function of the axial coordinate for the Mode shape N°12

Mode 7, pure bending

In Fig. 7.7 the mean bending line of the mode. In Fig. 7.9 is represented is the modal deformation in axial direction $U_x(x)$, and in Fig. 7.8 the torsion angle of the shaft for the mode 8. One can note that both torsion and axial displacement evaluate to null or negligible value.

ARflex: 0.3449
ARrot: 2.0005e-04

ARnorm: 1.5212e-18

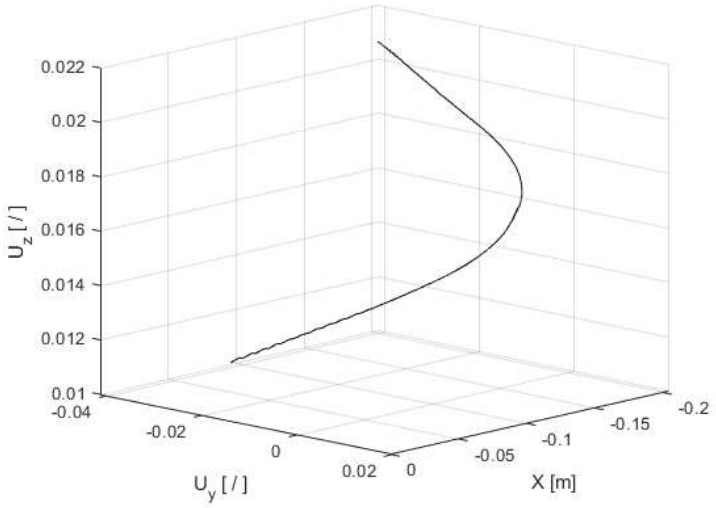

Figure 7.7: Mean of the Mode shape

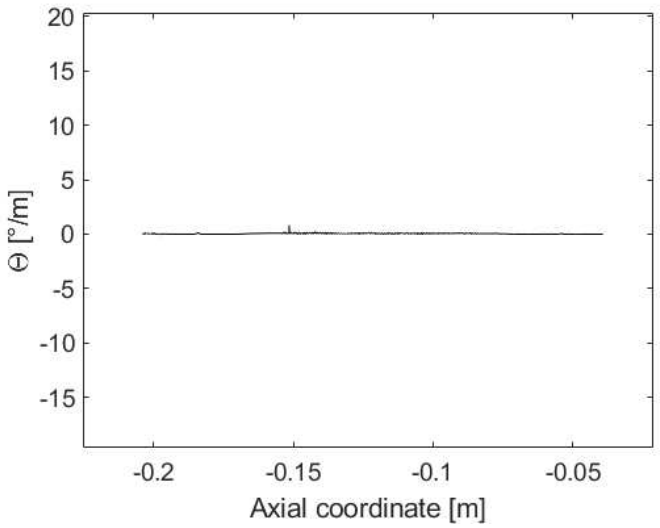

Figure 7.8: Rotation angle due to torsion as a function of the axial coordinate for the Mode shape N°7

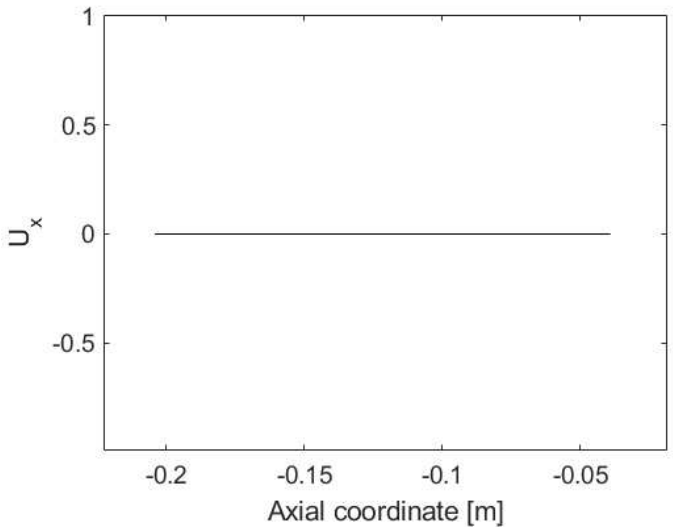

Figure 7.9: Axial displacement as a function of the axial coordinate for the Mode shape N°7

Mistuned results

The main results from the shaft analysis in the reference case are as follows.

Fig. 7.10 represents each mode, with the number of dominant nodal diameters on the turbine plotted on the x-axis and the modal coordinate representing the displacement in the axial direction of the mode on the y-axis. The mode shapes are mass-normalized. For mistuned modes, it is confirmed that the axial coupling mechanism is characterized by a nodal diameter of 0.

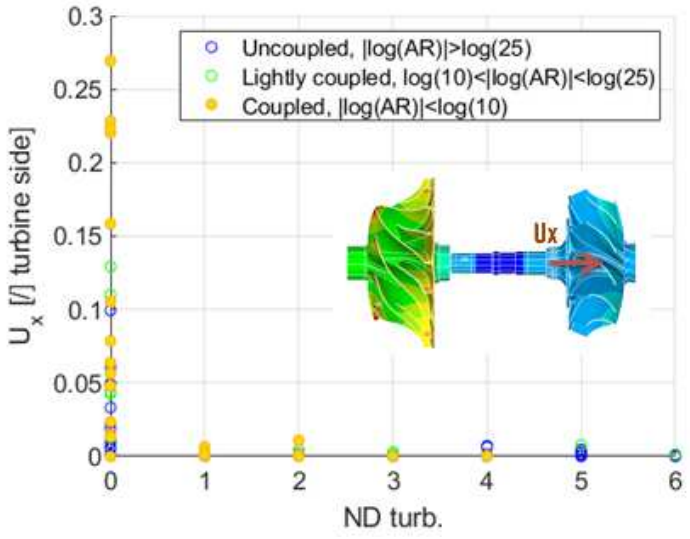

Figure 7.10: Representation of turbine nodal diameter (abscissae) and shaft axial modal displacement on turbine side, for full rotor mass normalized modes

In Fig. 7.11, similar to previous graph, the dominant nodal diameter on the turbine and the torsion angle required on the turbine side of the shaft are represented, for the mass-normalized mode shapes. It is confirmed that the torsion is associated with nodal diameter 0 for mistuned rotors. Despite this, the presence of an important outlier for nodal diameter 2 is recorded.

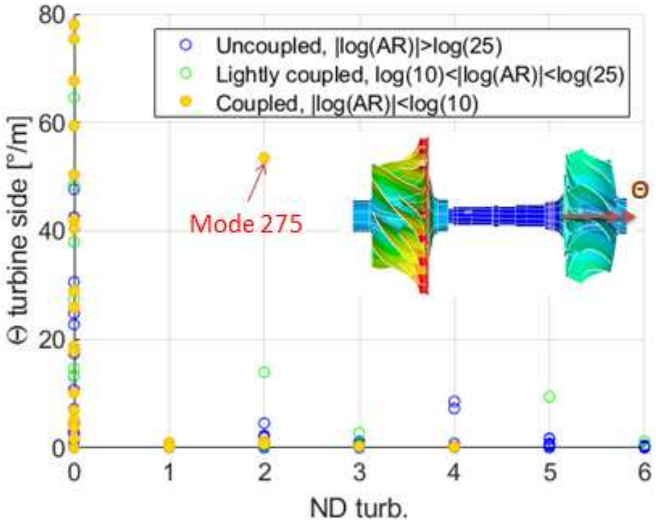

Figure 7.11: Representation of turbine nodal diameter (abscissae) and shaft axial modal rotation due to torsion, on turbine side, for full rotor mass normalized modes

Additionally, in figure 7.11, for each mode, is represented on the x axis the dominant nodal diameter on the turbine and the on the y axis the transverse displacement of the shaft on the turbine side, it is demonstrated that even for mistuned rotors the bending is associated with nodal diameters 1.

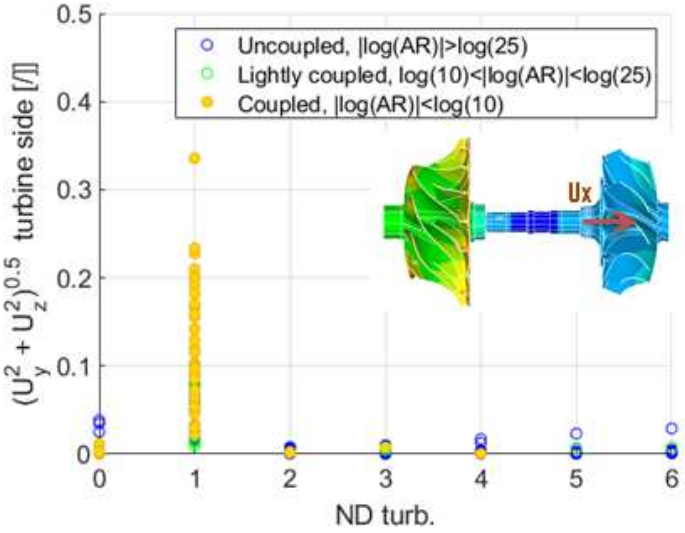

Figure 7.12: Representation of turbine nodal diameter (abscissae) and shaft axial modal displacement on the turbine side, for full rotor mass normalized modes (ordinates)

7.0.2 Physical principle

Figure 6.13 demonstrates that coupled modes exist for nodal diameters other than 0 and 1, which raises questions about the physical meaning of these modes.

Mistuning causes the modes to exhibit multiple nodal diameter components, resulting in an extended nodal diameter spectrum. Consequently, a mistuned mode with a dominant nodal diameter greater than 1 can still exhibit non-zero components for diameters 0 and 1, enabling transmission along the shaft. Note in Fig. 7.13 the nodal diameter spectrum of the tuned mode 130 is concentrated in the ND=2. However, mistuning causes the spectrum to spread across the entire range of nodal diameters, with non-zero contributions at ND=0 and ND=1.

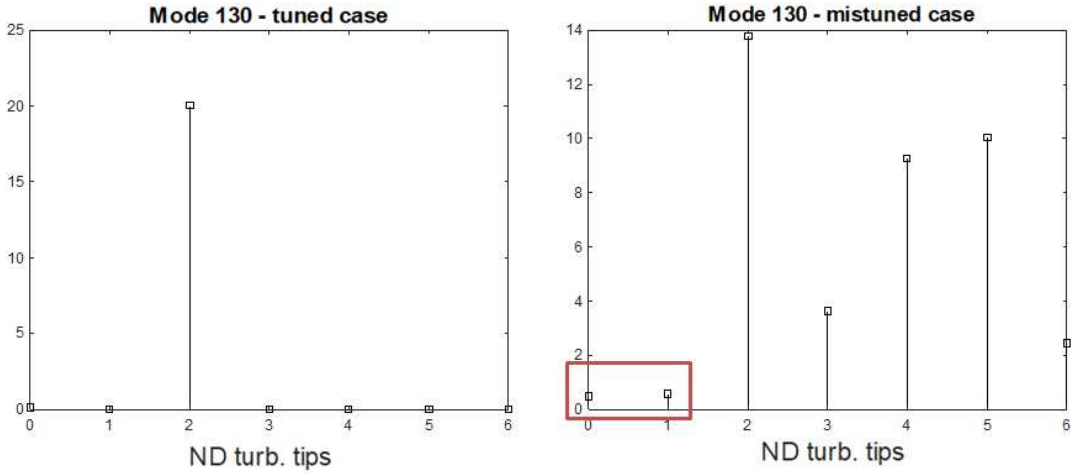

Figure 7.13: Nodal diameter components of the BMND2 tuned mode (left) and the corresponding mistuned mode (right)

A simple mental model to try to understand how mistuning causes vibrations in the turbine is to consider the blades as concentrated masses vibrating in a tangential direction anchored elastically to a stiff frame. Let u represent the eigenvector containing the displacements of each blade for the mode in question. The rotational moment of inertia is proportional to $\sum_{i=1}^{Z} u_i$, which corresponds to the nodal diameter component 0. The translational moment of inertia is given by $\sum_{j=1}^{Z} u_j \cdot \cos(\theta_j)$ in the horizontal direction and by $\sum_{j=1}^{Z} u_j \cdot \sin(\theta_j)$ in the vertical direction, which are exactly proportional to the nodal diameter component 1.

Thus, the degree of torsional coupling of the shaft is influenced by the rotational moment of inertia of the blades. This relationship directly connects the torsional coupling strength to the nodal diameter 0 (ND0) component of the mode, as the ND0 component represents uniform angular deformation across the circumference of the rotor. Higher ND0 contributions indicate stronger interactions through torsional dynamics.

Similarly, the degree of bending coupling is determined by the bending moment of the blades in the transverse direction. This is primarily associated with the nodal diameter 1 (ND1) component of the blades, which reflects the first asymmetric bending mode. A dominant ND1 component signifies enhanced bending interactions between the turbine and the compressor, as vibrational energy is transmitted through non-uniform deformation patterns across the rotor.

	Axial	**Tangential**
ND0	Thrust	Rotation (torsion)
ND1	Bending (rotor tilting)	Bending (rotor translation)

Table 7.1: Summary of the coupling mechanisms and associated nodal diameter

In a real bladed wheel, axial deformation also occurs in addition to the tangential deformations. The nodal diameter 0 (ND0) component in the axial direction is associated with thrust, representing uniform axial motion of the bladed wheel. Similarly, the nodal diameter 1 (ND1) component is associated with *tilting*, analogous to the asymmetric deformation observed in the tangential components.

To better characterize the dynamics of the system, a parameter should be defined for each mode to quantify the relative prevalence of the ND0 and ND1 components on the turbine. This parameter would provide a measure of the contribution of nodal diameter 0&1 components, both axial and tangential, to the overall deformation. First it is possible to define the equivalent 'total' deformation component, taking account of all directions as in Eq. (7.8) Eq. (7.9)

$$DFT_{tot}(ND0) = \sqrt{DFT_{ax}^2(ND0) + DFT_{tg}^2(ND0)} \tag{7.8}$$

$$DFT_{tot}(ND1) = \sqrt{DFT_{ax}^2(ND1) + DFT_{tg}^2(ND1)} \tag{7.9}$$

Furthermore, it would be useful to define a parameter that combines the effect of the ND0 and ND1 components. One possibility is the one described in Eq. (7.10).

$$DFT(ND0\&ND1)^{(equ)} = \sqrt{DFT_{tot}^2(ND0) + DFT_{tot}^2(ND1)} \tag{7.10}$$

Graph in Fig. 7.10 corresponds to the plot for each mode of the Full Rotor, of the parameter $DFT(ND0\&ND1)^{(equ)}$ with respect to the amplitude ratio. The mode shapes are normalized to the maximum deformation value over the entire rotor. The nodal diameter components are evaluated on the turbine tips. Colour represents the prevalence of ND0 over ND1. Yellow points represent the ND1 dominated modes, while blue points represent ND0 dominated modes. It is interesting to note how ND0 and ND1 are complementary in creating the trend of the graph.
It can be observed that the trend of $AR \to 1$ occurs for increasing values of Nodal Diameter Components 0 or 1. The trend is particularly clear and clean for compressor-dominant modes. For the dominant turbine modes, although the general trend is still evident, the existence of some

outlier modes is recorded, which present a high degree of coupling with very low nodal diameter components 0 and 1.

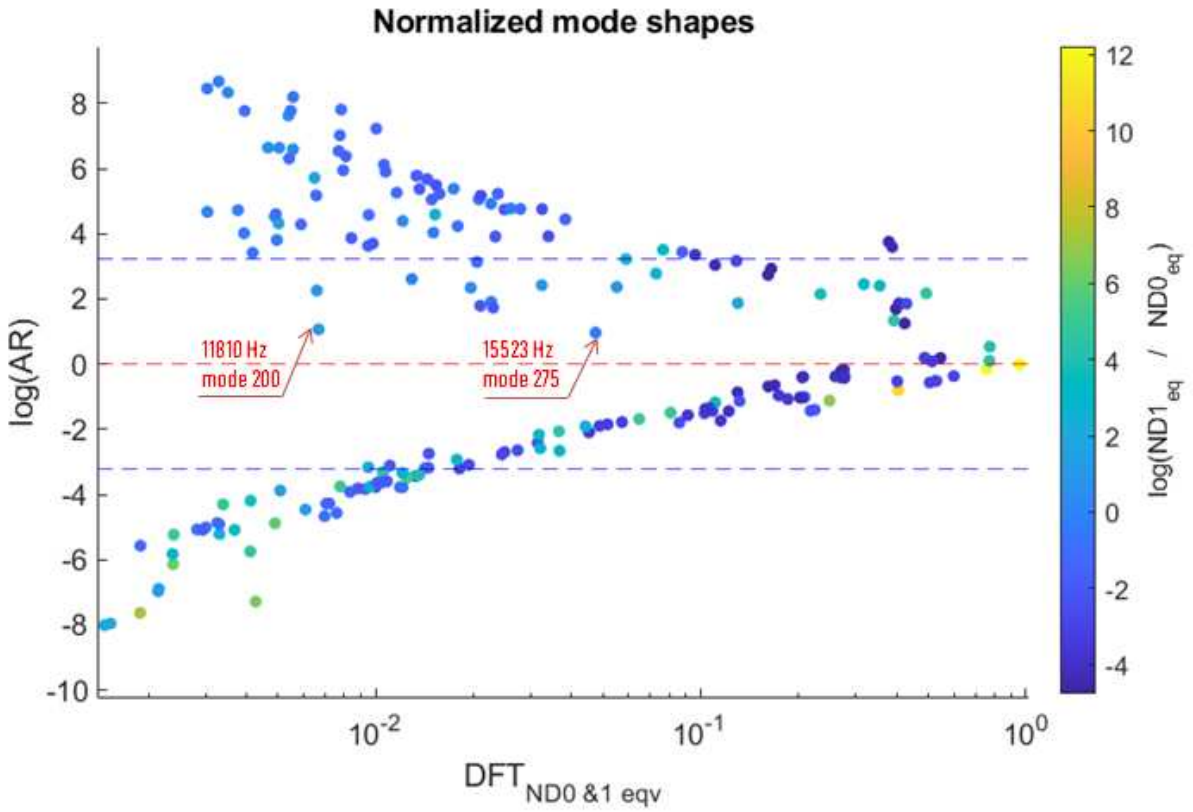

Figure 7.14: Diagram showing the influence of ND0 and ND1 on the Amplitude Ratio

In section 7.1 is attempted an explanation for these outlier modes, involving the comparison of the natural frequencies of turbine and compressor and their distance in the frequency domain in both tuned and mistuned case.

7.0.3 Detailed evaluation of some coupled modes with dominant ND> 1

In Fig. 6.13 the important presence of coupled turbine-compressor modes for nodal diameter >1 is demonstrated. In all the graphs presented so far, the modes have been shown in aggregate form to extrapolate general correlations. However, in order to understand the dynamics of these modes, it is important to go into detail and observe the characteristics of the turbine, compressor and shaft for each of these.

Below are presented a few modes with AR close to 1 and ND>1, which stand out as outliers in some of the correlations presented so far.

Mode 200

Mode N°	200
Frequency	11810 Hz
Amplitude ratio	2.9101
Turbine tip dominant	ND4
Compressor main bl.	ND0
Compressor split. bl.	ND0

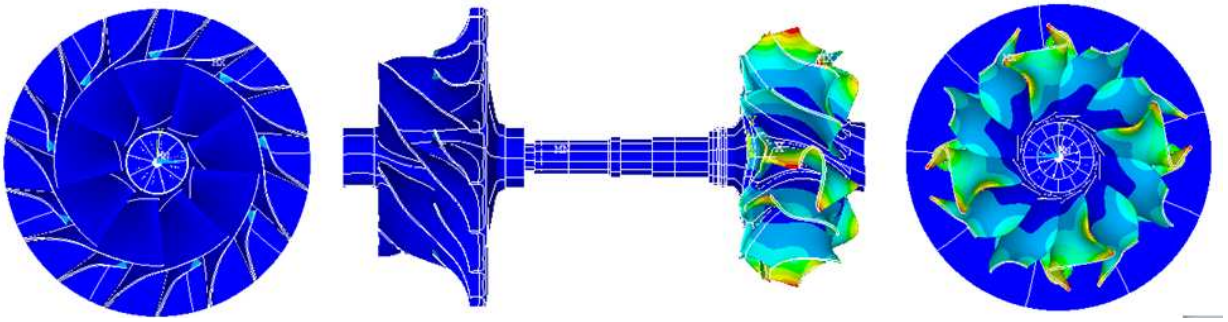

Figure 7.15: Full rotor mistuned mode shape N° 200

This mode is a ND4 turbine leading coupled mode (AR = 2.9) Fig.6.13. On the compressor this mode involves mainly the splitter blades with a clear ND0. Despite this, ND0 and ND1 component are relatively low on the turbine side. On the turbine this mode involves the participation of both disk and blades, and shows a very noticeable displacement in axial direction. 7.15.

The DFT spectrum on compressor and turbine tips evaluates to data in Fig 7.27 and Fig. 7.27.

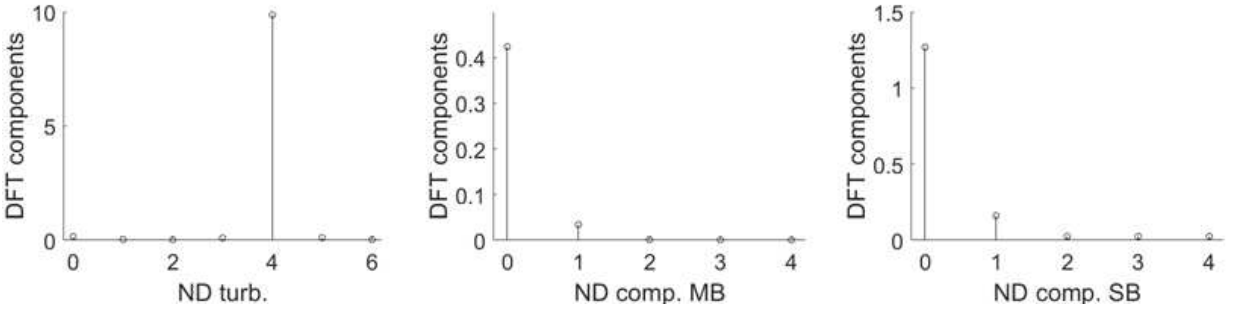

Figure 7.16: Full rotor mistuned mode shape N° 200, DFT components of the tangential modal coordinates evaluated on 1) Turbine Blade tips 2) Compressor Main Blade tips 3) Compressor Splitter Blade tips

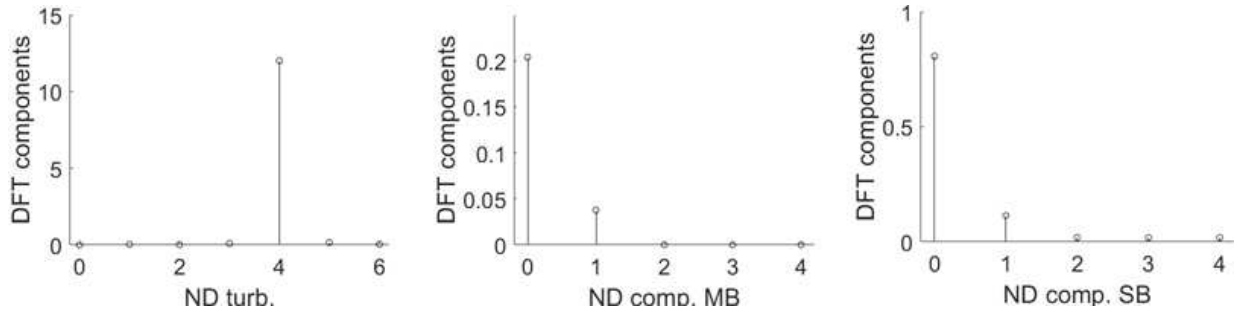

Figure 7.17: Full rotor mistuned mode shape N° 200, DFT components of the axial modal coordinates evaluated on 1) Turbine Blade tips 2) Compressor Main Blade tips 3) Compressor Splitter Blade tips

In the figure 7.27 it is possible to see the tangential DFT components on the three selections, while in Fig. 7.17 the corresponding axial DFT components are shown. It is noted that as far as the turbine is concerned, the axial component prevails over the tangential one, with almost tuned ND4 in both cases. For the compressor, the situation is similar for both the splitters and main blades, with ND0 being dominant and ND1 contributing to a lesser extent. On the compressor the tangential behaviour prevails so we can assume that as far as the compressor is concerned the mode consists of an axial torsion of the compressor.The tangential ND0 component on the turbine is surprisingly low, which is inconsistent with the torsion behaviour of the compressor To try to better understand the physical meaning of this turbine-compressor coupled mode we can focus on the shaft.

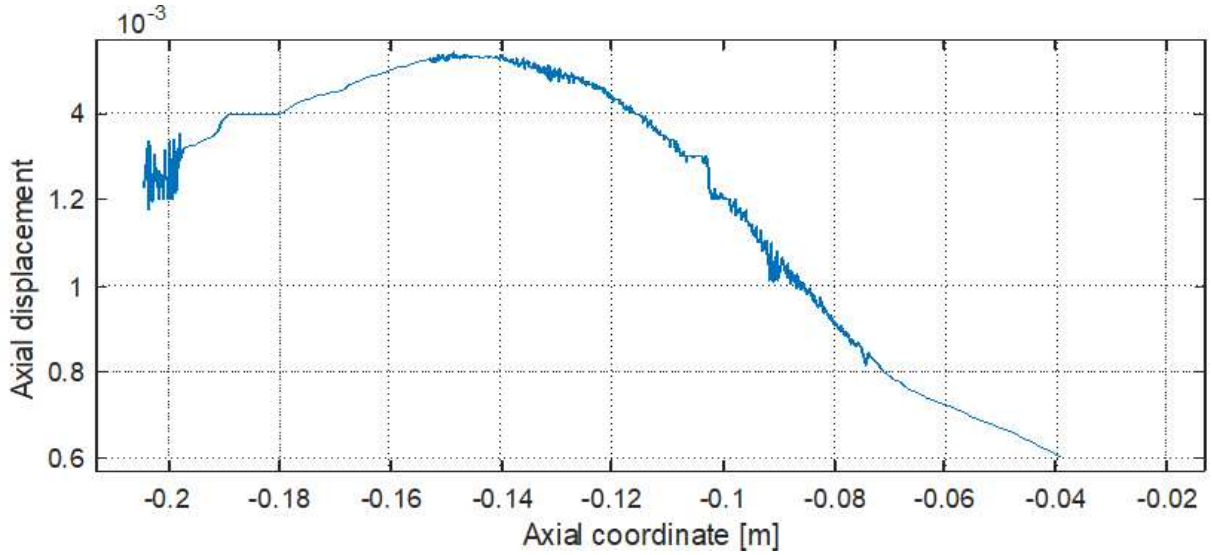

Figure 7.18: Modal coordinate of the shaft axial direction for mode 200

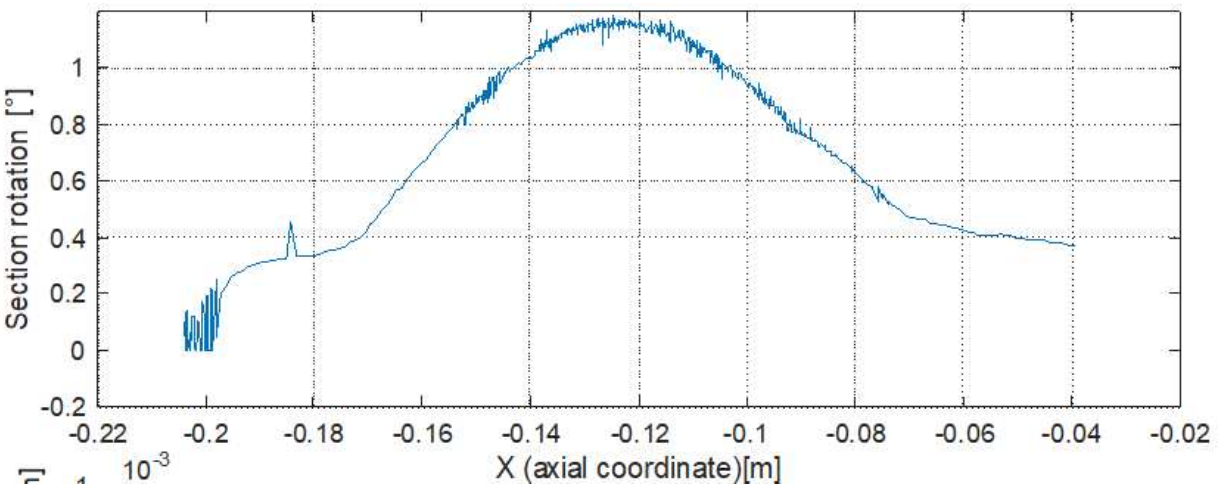

Figure 7.19: Modal coordinate of axial rotation (torsion) of the shaft for mode 200

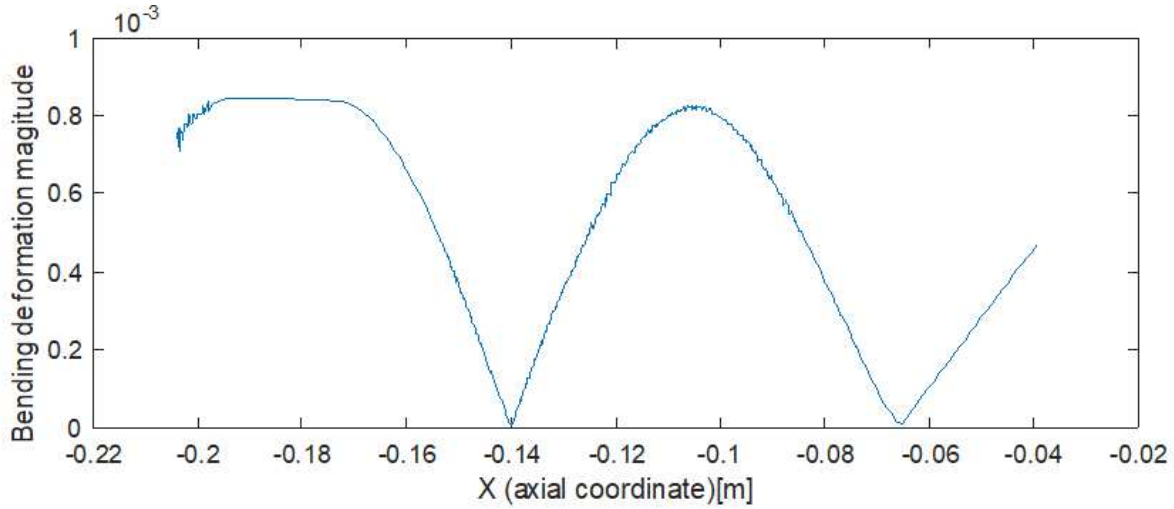

Figure 7.20: Modal coordinate of transversal (bending, absolute value) deflection of the shaft for mode 200

In Fig. 7.18values with the same sign are observed, indicating that the mode expresses a sort of back and forward motion of the rotor on the axial bearing. The highest coordinate is observed at the end of the turbine, in agreement with the observation of strong axial component on the turbine but not on the compressor.

In Fig. 7.20 we observe a two-node bending mode, with participation of both the turbine and the (major) compressor which in fact is observed on the compressor DFT.

In Fig. 7.19 we actually see a torsion mode shape similar to the first torsion mode shape of a torsion bar, with two almost nodes in the extremities. in the right end, corresponding to the turbine, there is a greater torsion component compared to the compressor end which has ND0. This seems in even more evident contradiction to the lack of ND0 components on the turbine.

In order to try to understand better, it is possible to also study the DFT components on the disk and the shaft root of the turbine, in order to see the evolution between turbine ND4 and shaft torsion.

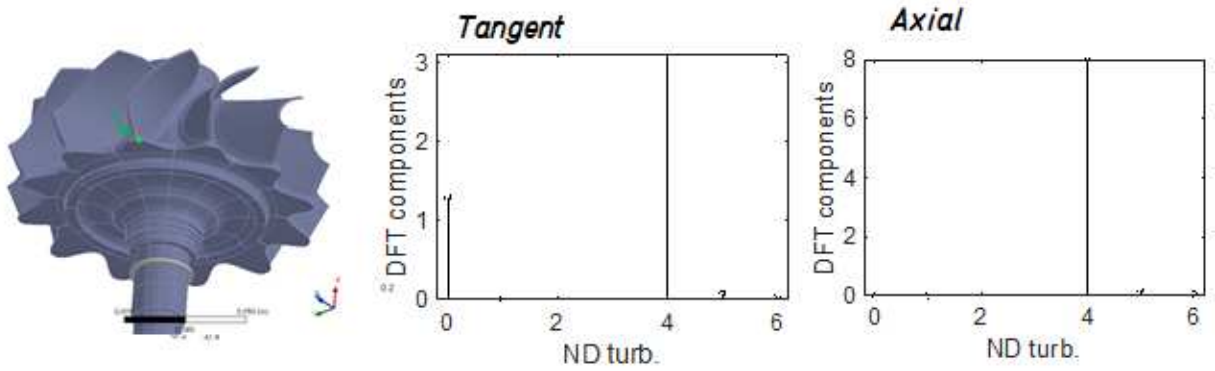

Figure 7.21: DFT results of tangential and axial modal coordinates evaluated on disk point

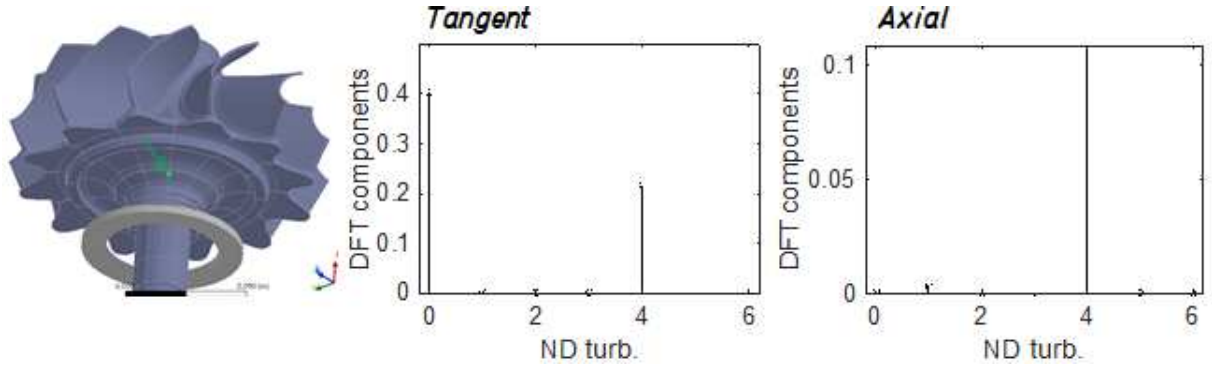

Figure 7.22: DFT results of tangential and axial modal coordinates evaluated on disk shaft root

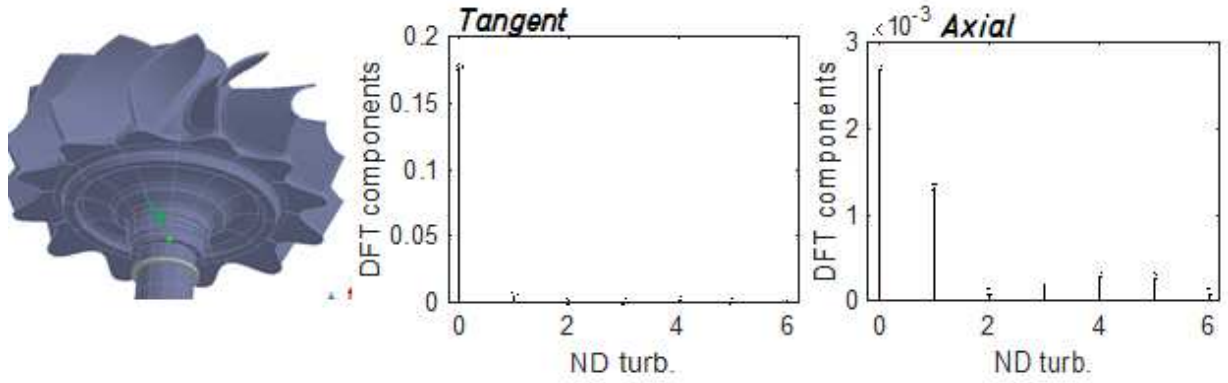

Figure 7.23: DFT results of tangential and axial modal coordinates evaluated turbine-end of the shaft

In figure 7.21 one can see how the situation on the disk, at a point with a rather large radius, is similar to that on the turbine tips. In fact there is a strong ND4 component, mainly in the axial direction. Unlike what is seen on the blades, there is also a significant tangential ND0 component on the disk, indicating a non-zero rotation component that was not observed on the blades. Going

down to a point of the disk with a smaller diameter, Fig. 7.22, the axial ND4 component drops drastically, from 8 to a value just over 0.1. Even the ND0 component which indicates rotation drops from 1.2 to 0.4, however becoming the dominant component at the base of the disk. On the shaft Fig.7.23, we observe that the ND4 component has disappeared almost completely, while the tangential ND0 component due to the torsional motion remains relevant.

Based on the transition shown in Fig. 7.21 to 7.23 it can be observed:

- There is an ND4 component moving in both axial and tangential (mostly axial) directions with very high magnitude, which is however very localized on the turbine disk and constitutes a mode of the turbine at the frequency of this mode.
- From the DFT components of the compressor and turbine to the base of the shaft, the turbine-compressor coupling is due to a combined mechanism of torsion (primary tangential ND0) and axial behaviour (secondary axial ND0). These components are very small with respect to the ND4 component but are dominant on the shaft.

Looking at the tuned modes at the same frequency level, Fig. 7.24, we notice that Splitter blades ND0 on the compressor and the Turbine ND4 appear in two separate modes very close in frequency, with 3 Hz of difference. The mistuning on the turbine therefore creates residual ND0 components which allow it to interact with the ND0 splitter blades mode on the compressor. Although the ND0 components for this mode are very small, the 200 tuned mode is a motion with a high degree of coupling, being an outlier in Diagram 7.14. In next chapter outliers modes like this are examined with the hypothesis that the additional coupling is due to mistuning moving very close to each other the frequencies of turbine and compressor.

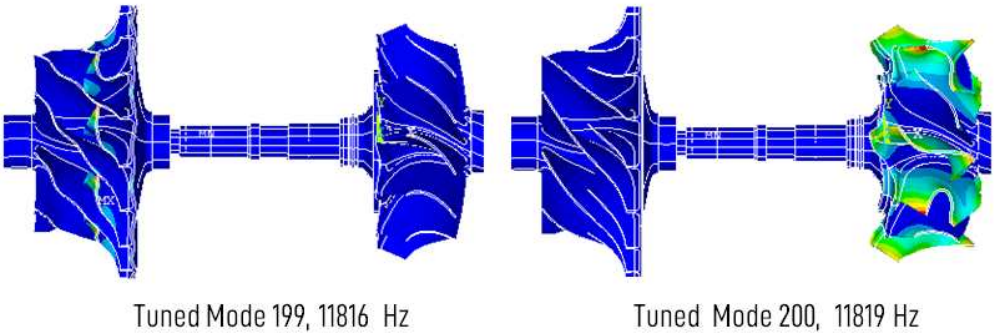

Figure 7.24: Tuned modes 199 and 200, occurring at frequency close to mistuned mode 200

Mode 275

Mode N°	275
Frequency	15523 Hz
Amplitude ratio	2.6324
Turbine tip dominant	ND2
Compressor main bl.	ND0
Compressor split. bl.	ND0

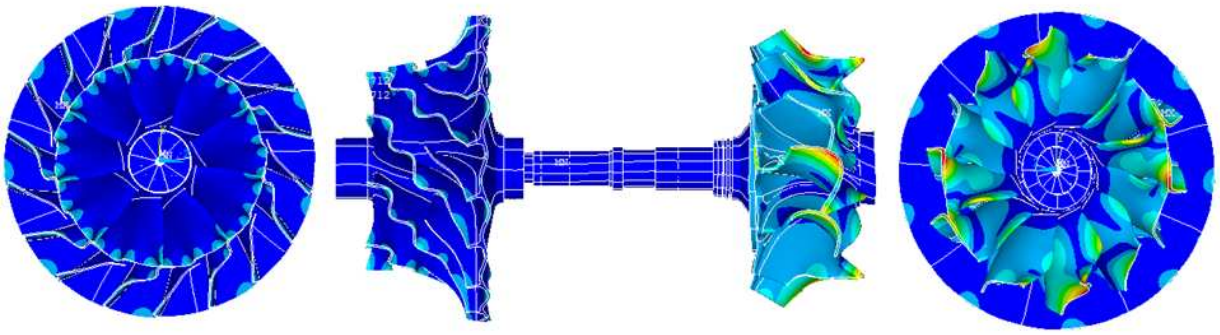

Figure 7.25: Full rotor mistuned mode shape N° 275

Mode 275 is a mixed mode both on the turbine and in the compressor. The AR is very close to 1. It is noted that this mode has a strong ND0 component on the compressor, with a dominant ND2 component on the turbine, predominantly axial. This mode appears similar to case 201, as the ND0 component on the turbine is low (0.025 tangential, 0.02 axial).

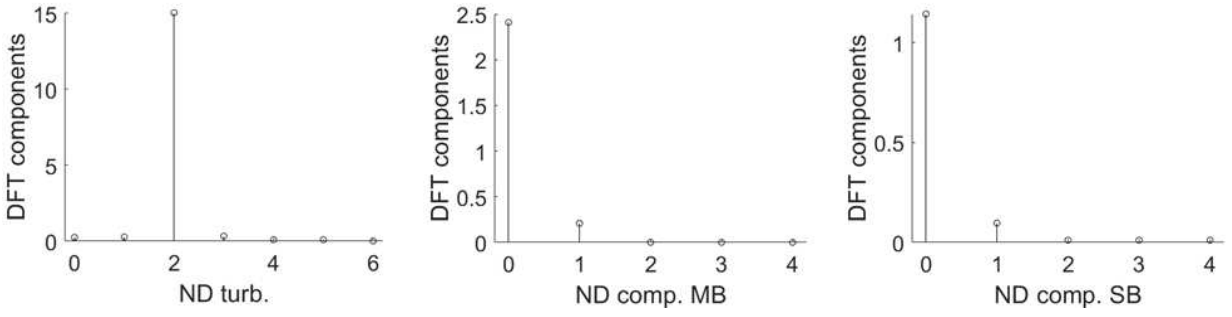

Figure 7.26: Full rotor mistuned mode shape N° 200, DFT components of the **tangential** modal coordinates evaluated on 1) Turbine Blade tips 2) Compressor Main Blade tips 3) Compressor Splitter Blade tips

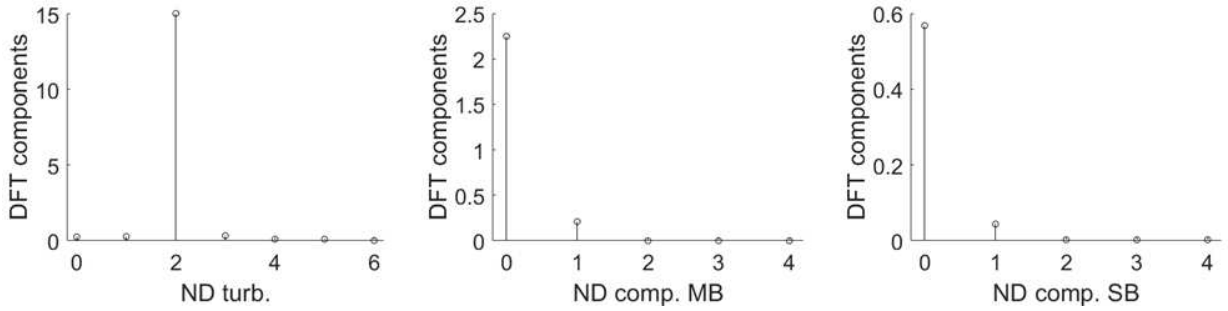

Figure 7.27: Full rotor mistuned mode shape N° 200, DFT components of the **axial** modal coordinates evaluated on 1) Turbine Blade tips 2) Compressor Main Blade tips 3) Compressor Splitter Blade tips

Like for mode 200, to understand more, we can go in detail and perform the fourier decomposition for three cicular point series, going progressively from blade tips to shaft.

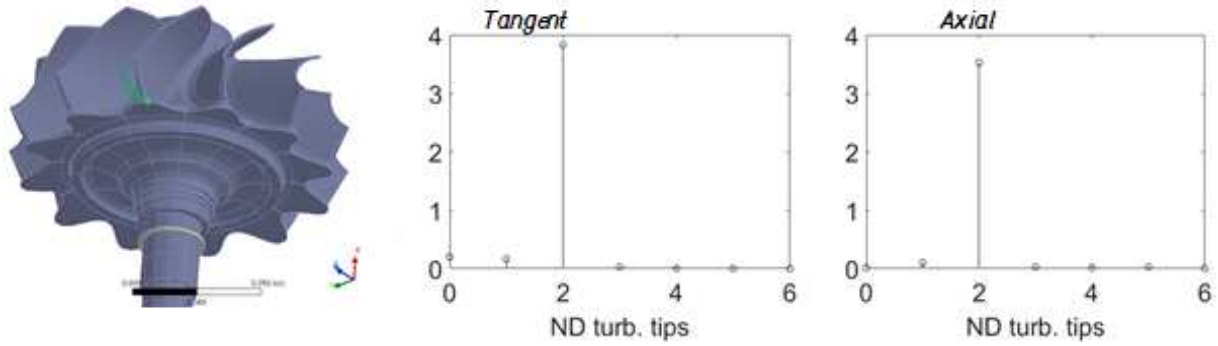

Figure 7.28: DFT results of tangential and axial modal coordinates evaluated on disk point

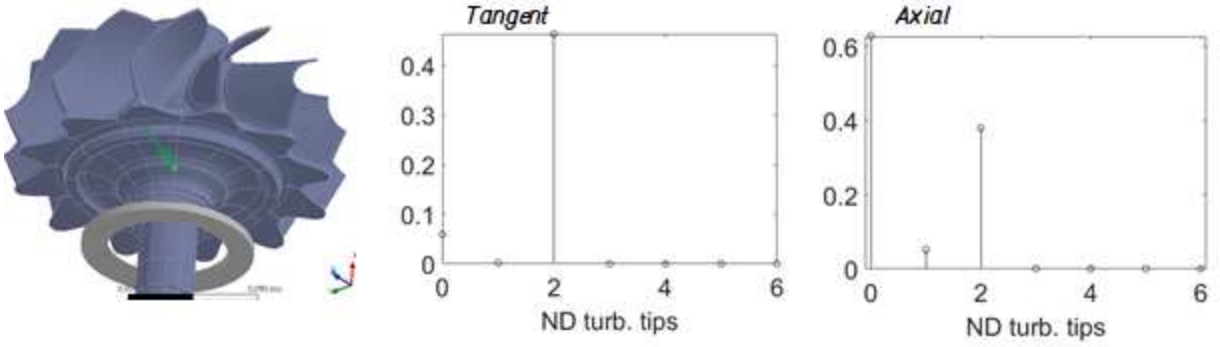

Figure 7.29: DFT results of tangential and axial modal coordinates evaluated on disk shaft root

In Figures 7.28, 7.29, and 7.30, it can be observed that the tangential and axial modal deflections have nearly equal amplitudes. Both components diminish as we move closer to the rotor axis. However, the ND2 components decrease more rapidly, resulting in a dominant ND0 axial component on the shaft. This is associated with normal thrust, which is presumably the primary coupling mechanism for this mode.

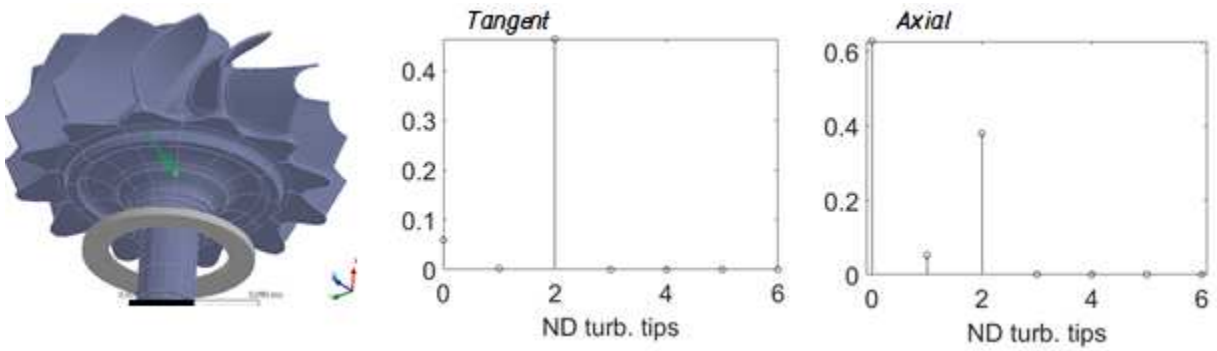

Figure 7.30: DFT results of tangential and axial modal coordinates evaluated on the turbine end of the shaft

Mistuned mode 275 is the superposition of two tuned modes (Fig. 7.31), one specific to the turbine and one to the compressor. Mistuning on the turbine causes non-zero ND0 residual components, which although small interact with the compressor mode.

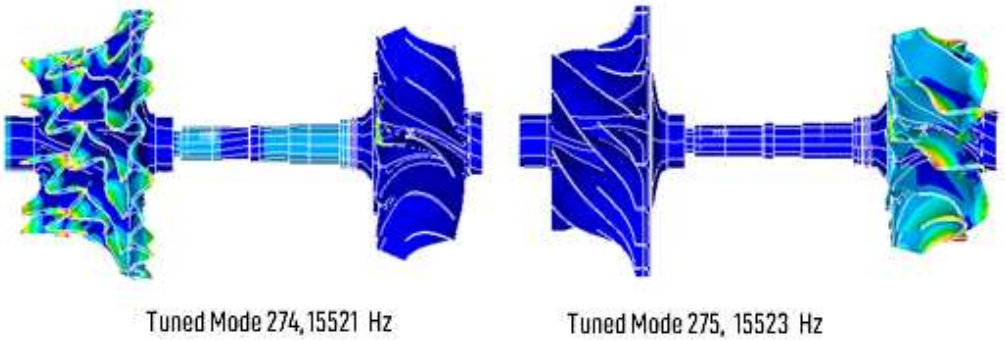

Figure 7.31: Tuned modes in the same frequency range as the 275 mistuned mode

7.1 Subdivision of the model and Impedance coupling

In this section, we aim to understand in greater detail the mechanisms behind the creation of coupled modes. It is interesting to note, as shown in the examples in Figures 7.31 and 7.24, that some mistuned modes can be represented as the superposition of two tuned modes, one predominantly expressed on the turbine and the other predominantly expressed on the compressor.

The common condition is that these two modes are sufficiently close in frequency. However, it is not enough for the two modes to be close or even identical in frequency for a mistuned mode to arise. If we imagine two completely isolated parts that do not mechanically interact, even if they share the same natural frequencies, they do not give rise to common modes. Therefore, the creation of a coupled mode requires some form of mechanical interaction between the two parts.

Ewins, in [25], proposes a method to calculate the interaction of two parts connected through an interface, given the modal properties of the two parts in free configuration. This method utilizes

the transfer functions of the two systems, which can be computed from the modal properties (eigenvalues and eigenvectors) of the two systems.

Mistuning can create small residual ND0 & ND1 components in modes which are dominated by a $ND_{dom} > 1$. Using the equations proposed in [25], we aim to demonstrate how the proximity in frequency and small interaction between the interfaces due to mistuning, lead to coupled modes between the two parts of the model.

7.1.1 Relationship between Amplitude ratio and Frequency response functions

Considering two degrees of freedom of the model, A and B, both amplitude ratio and transfer function between are measures of the coupling of a mode. For a totally uncoupled mode the amplitude ratio between the two points is either zero or infinity. The transfer function (considering just the contribution of one mode), between two points is zero if at least on one of the points A and B the mode shape is null. Considering one mode that is coupled to some degree between point A and B, the transfer function presents a peak in correspondence of the resonant frequency, with a value dependent on the amount of damping.

The *receptance* transfer function, between two points of a mechanical system is defined as:

$$H_{A\to B}(\omega) := H_{B\to A}(\omega) = \frac{\text{Harmonic displacement measured in B}}{\text{Harmonic force applied in A}} \tag{7.11}$$

For a generic MDOF system, the transfer function is given by: [25]

$$H_{A\to B} = H_{B\to A} = \sum_{r}^{N_m} \frac{\phi_{r,A} \cdot \phi_{r,B}}{m_r \cdot (\lambda_r - \omega^2)} \tag{7.12}$$

In case the mass normalized mode shapes ψ are used:

$$H_{A\to B}(\omega) = H_{B\to A}(\omega) = \sum_{r}^{N_m} \frac{\psi_{r,A} \cdot \psi_{r,B}}{(\lambda_r - \omega^2)} \tag{7.13}$$

- $H_{A\to B}(\omega)$ is the *receptance* transfer function between A and B, defined as the ratio between harmonic displacement on
- r : mode number
- λ_r r-th eigenvalue of the system, $\lambda_r = \mathfrak{Re}(\lambda_r) + i\mathfrak{Im}(\lambda_r), \quad \mathfrak{Re}(\lambda_r) = \omega_r^2$
- ω frequency coordinate
- $\phi_{r,A}$ or $\phi_{r,B}$ Mode shape of the r-th at degree of freedom A or B

- m_r Modal mass

The Amplitude ratio between degrees of freedom A and B are defined, for the mode r, as

$$AR_r = \frac{\psi_{r,B}}{\psi_{r,A}} \tag{7.14}$$

for this reason, the displacement transfer function can be written as:

$$H_{A\to B}(\omega) = H_{B\to A}(\omega) = \sum_{r}^{N_m} \frac{\psi_{r,A}^2 \cdot AR_r}{(\lambda_r - \omega^2)} \tag{7.15}$$

The transfer function is the sum of N terms, one for each mode. It is useful to consider only the contribution of the r-th mode, which is the dominant contribution at frequencies close to the r-th natural frequency.

$$H_{r,A\to B}(\omega) = \frac{\psi_{r,A}^2 \cdot AR_r}{(\lambda_r - \omega^2)} \tag{7.16}$$

at the r-th resonance point, with frequency $\omega^2 = \mathfrak{Re}(\lambda_r) = \omega_r^2$:

$$H_{r,A\to B}(\omega_r) = \frac{\psi_{r,A}^2 \cdot AR_r}{i(\mathfrak{Im}\{\lambda_r\})} \tag{7.17}$$

Hence the peak value of the transfer function at the r-th resonance point is linked both to the Amplitude ratio and the importance of the modal coordinate psi evaluated at one of the ends, as well as the stability term ($\mathfrak{Im}\{\lambda_r\}$) contained in the denominator.

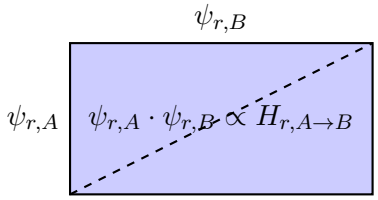

A way to represent the relationship between AR and receptance peak is in Fig. 7.1.1. The transfer function peak is proportional to the area of the rectangle $\psi_r, A \cdot \psi_r, B$, and inversely proportional to the denominator term ($\mathfrak{Im}\{\lambda_r\}$). Amplitude ratio is the ratio between the two sides of the rectangle.

It is always possible to normalize the mode shape for the maximum deflection value, assuming that it is the maximum deflection on the turbine $\psi_{r,A}$ (or on the compressor, it is identical), the expression simplifies to Eq. 7.18. Since the mode shape is no longer mass-normalized, the modal mass appears in the denominator.

$$|H_{r,A\to B}(\omega_r)| = \frac{AR_r}{\mathfrak{Im}\{\lambda_r\} \cdot m_r} \tag{7.18}$$

It is also possible to write Eq. (7.17) under logarithm:

$$|H_{r,A\to B}(\omega_r)| = \log(AR_r) - \log(\mathfrak{Im}\{\lambda_r\}) - \log(m_r) \tag{7.19}$$

Thus, the AR (Amplitude Ratio) of a mode and the peak of the transfer function at the frequency corresponding to the mode are two alternative metrics that indicate how strongly coupled a mode is. These are linked to each other by 7.19

7.1.2 Subdivision of the model

To understand in more detail the reasons and the conditions for turbine - compressor coupling, it is possible to section the model in two subsystems.

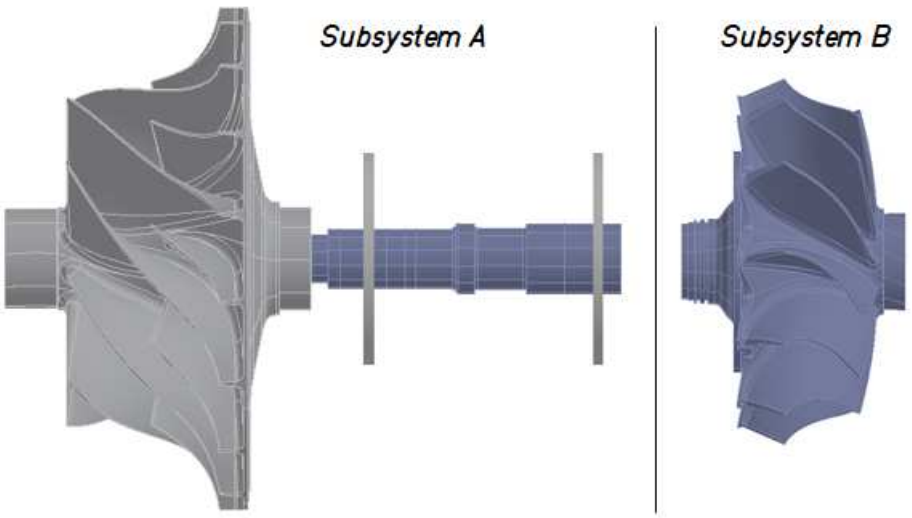

Figure 7.32: Subdivision in the two subsystems

- Subsystem A: composed of compressor assembly and shaft (bearings included)
- Subsystem B: Turbine model

These two subsystems have in common an interface. For the method, the boundary condition in the interface is **free displacement**. Prestressed modal analysis is computed for the two subsystems. As a result we have a set of N_a eigenvalues λ_r, a and eigenvectors $\{\psi_{r,a}\}$ for the subsystem A; we obtain a set of N_b eigenvalues $\lambda_{r,b}$ and eigenvectors $\{\psi_r, b\}$ for the subsystem B.

The eigenvectors of the subsystems A and B can be conveniently evaluated at the blades and at the interface degrees of freedom, neglecting the other DOFs.

$$\psi_{r,A} = \begin{Bmatrix} \left\{\psi_{r,A}^{(tips)}\right\} \\ \left\{\psi_{r,A}^{(interf)}\right\} \end{Bmatrix} \quad , \quad \psi_{r,B} = \begin{Bmatrix} \left\{\psi_{r,B}^{(interf)}\right\} \\ \left\{\psi_{r,B}^{(tips)}\right\} \end{Bmatrix} \tag{7.20}$$

Since the mesh of the two subsystems on the interface is not the same (structured in model A, unstructured in model B), to compare the solutions it is possible them with a polynomial. Since the interface lies on the plane (y,z) the solution components will be written as a polynomial function of y and z. To find the polynomial coefficients one must solve an over-defined linear system.

$$\{\psi^{(interf)}\} = \begin{Bmatrix} \vdots \\ u_{x,i}^{(interf)} \\ u_{y,i}^{(interf)} \\ u_{z,i}^{(interf)} \\ \vdots \end{Bmatrix} \tag{7.21}$$

$$\begin{cases} u_{x,i}^{(interf)} = a_1 + a_2 \cdot y_i + a_3 \cdot z_i + a_4 \cdot y_i.^2 + a_5 \cdot z_i^2 + a_6 \cdot y_i \cdot z_i + \dots \\ u_{y,i}^{(interf)} = b_1 + b_2 \cdot y_i + b_3 \cdot z_i + b_4 \cdot y_i.^2 + b_5 \cdot z_i^2 + b_6 \cdot y_i \cdot z_i + \dots \\ u_{z,i}^{(interf)} = c_1 + c_2 \cdot y_i + c_3 \cdot z_i + c_4 \cdot y_i.^2 + c_5 \cdot z_i^2 + c_6 \cdot y_i \cdot z_i + \dots \end{cases} \tag{7.22}$$

Use of 15 coefficients is enough to obtain a polynomial function that approximates well the solution.
This way, the coefficients of the polynomial become a new synthesised formulation of the eigenvector components. The two alternative formulations for the interface eigenvectors are linked by the matrix [A].

$$\{\psi^{*(interf)}\} = \begin{Bmatrix} \vdots \\ a_j \\ b_j \\ c_j \\ \vdots \end{Bmatrix} \quad j = 1, ..., 15 \tag{7.23}$$

$$\{\psi^{(interf)}\} = [A]\{\psi^{*(interf)}\} \tag{7.24}$$

$$[A] = \begin{bmatrix} 1 & y_i & z_i & y_i^2 & z_i^2 & \cdots \\ 1 & y_i & z_i & y_i^2 & y_i^2 & \cdots \\ \vdots & \vdots & \vdots & \vdots & \vdots & \ldots \\ 1 & y_i & z_i & y_i^2 & y_i^2 & \cdots \\ 1 & y_i & z_i & y_i^2 & y_i^2 & \cdots \end{bmatrix} \tag{7.25}$$

Applying the transformation to the interface eigenvectors on both systems makes it possible to compare them as polynomial coefficients. The first three components a_1 , b_1 c_1 have the meaning of translation in the x,y,z direction respectively. Furthermore, the first order coefficients capture the effects of bending and torsion.

The polynomial transformation is also convenient to reduce the number of interface DOFs limiting computational time. It allows a reduction in size from 3xN_i, $N_i \approx 700$ number of interface nodes to 3x15 = 45 polynomial coefficients. In the example shown in Fig. 7.33 polynomial approximation describes the interface deflection with an error of 0.28%.

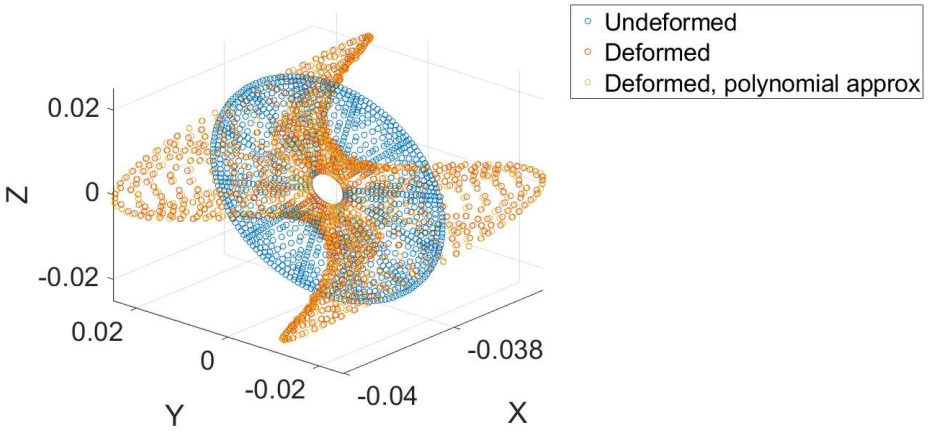

Figure 7.33: Interface of the turbine mode 59

7.1.3 Impedance coupling

Given two substructures that share an interface it is possible to couple with a mathematical procedure. This procedure is based on the frequency response function of the two subsystems, named A and B.

$$[H_A(\omega)] = [\psi_A] \operatorname{diag}\left((\lambda_{r\,(A)} - \omega^2)^{-1}\right) [\psi_A]^T, \tag{7.26}$$

$$[H_B(\omega)] = [\psi_B] \operatorname{diag}\left((\lambda_{r\,(B)} - \omega^2)^{-1}\right) [\psi_B]^T \tag{7.27}$$

Imposing the conditions of equilibria and congruence at the interface, it is possible to demonstrate [25] that the transfer function matrix of the interface, $[H_c]$ is equal to to the sum of the inverse of the transfer function matrices of the two subsystems that compose it.

$$[H_c(\omega)]^{-1} = [H_A(\omega)]^{-1} \oplus [H_B(\omega)]^{-1} \tag{7.28}$$

$$[H_C]^{-1} = \begin{bmatrix} [H_A^{(t-t)}]^{-1} & [H_A^{(t-i)}]^{-1} & \\ [H_A^{(i-t)}]^{-1} & ([H_A^{(i-i)}]^{-1} + [H_B^{(i-i)}]^{-1}) & [H_B^{(i-t)}]^{-1} \\ & [H_B^{(t-i)}]^{-1} & [H_B^{(t-t)}]^{-1} \end{bmatrix} \tag{7.29}$$

- $[H_A^{(t-t)}]$ transfer function matrix of subsystem A between tips and tips DOFs
- $[H_A^{(t-i)}]$ transfer function matrix of subsystem A between tips and interface DOFs
- $[H_A^{(i-i)}]$ transfer function matrix of subsystem A between interface and interface DOFs
- $[H_B^{(t-i)}]$ transfer function matrix of subsystem B between tips and interface DOFs
- $[H_B^{(t-t)}]$ transfer function matrix of subsystem B between tips and tips DOFs
- $[H_B^{(i-i)}]$ transfer function matrix of subsystem B between interface and interface DOFs

The equation (7.28) can be rewritten as:

$$\begin{aligned} [H_{tot}(\omega)]^{-1} &= [H_A(\omega)]^{-1} \oplus [H_B(\omega)]^{-1} \\ &= [H_A(\omega)]^{-1} \left(\mathbf{I} \oplus [H_A(\omega)] [H_B(\omega)]^{-1} \right) \\ &= [H_A(\omega)]^{-1} \left([H_B(\omega)] \oplus [H_A(\omega)] \right) [H_B(\omega)]^{-1} \end{aligned} \tag{7.30}$$

Finally

$$\left[\mathrm{H_{tot}}\,(\omega)\right] = \left[\mathrm{H_B}\,(\omega)\right] \left(\left[\mathrm{H_B}\,(\omega)\right] \oplus \left[\mathrm{H_A}\,(\omega)\right] \right)^{-1} \left[\mathrm{H_A}\,(\omega)\right] \tag{7.31}$$

Considering:

- the n-th mode of the turbine with corresponding eigenvalue λ_B
- the m-th mode of the compressor-shaft subsystem with corresponding eigenvalue λ_A
- The turbine mode can be evaluated in a point in the tips with a value $\psi_B^{(t)}$ and on the interface with a polynomial coefficient $\psi_B^{(i)}$
- The compressor mode can be evaluated in a point in the compressor tips with a value $\psi_A^{(t)}$ and on the interface with a polynomial coefficient $\psi_A^{(i)}$

Then equation (7.31) can be evaluated as:

$$H_{A\to B} = \frac{\psi_A^{(i)}\psi_A^{(t)}}{\omega^2 - \lambda_A} \cdot \left(\frac{\psi_A^{(i)\,2}}{\omega^2 - \lambda_A} + \frac{\psi_B^{(i)\,2}}{\omega^2 - \lambda_B} \right)^{-1} \cdot \frac{\psi_B^{(i)}\psi_B^{(t)}}{\omega^2 - \lambda_B} \tag{7.32}$$

Simplifying and introducing variable $\Delta = \lambda_A - \lambda_B$ that represents the difference between the eigenvalues of the subsystems, the expression evaluates to:

$$H_{A\to B} = \frac{\psi_A^{(i)} \cdot \psi_A^{(t)} \cdot \psi_B^{(i)} \cdot \psi_B^{(t)}}{\lambda_A(\psi_A^{(i)\,2} + \psi_B^{(i)\,2}) + \Delta \cdot \psi_A^{(i)\,2} - \omega^2(\psi_A^{(i)\,2} + \psi_B^{(i)\,2})} \tag{7.33}$$

If the difference Δ between the eigenvalues of the system becomes bigger, then the denominator of the transfer function becomes bigger, and the degree of coupling decreases.

7.1.4 Evaluation of frequencies

Computing the parameter Δ as the difference between the eigenvalues of two modes of subsystem A and B, it is possible to create the tables 7.34 7.35

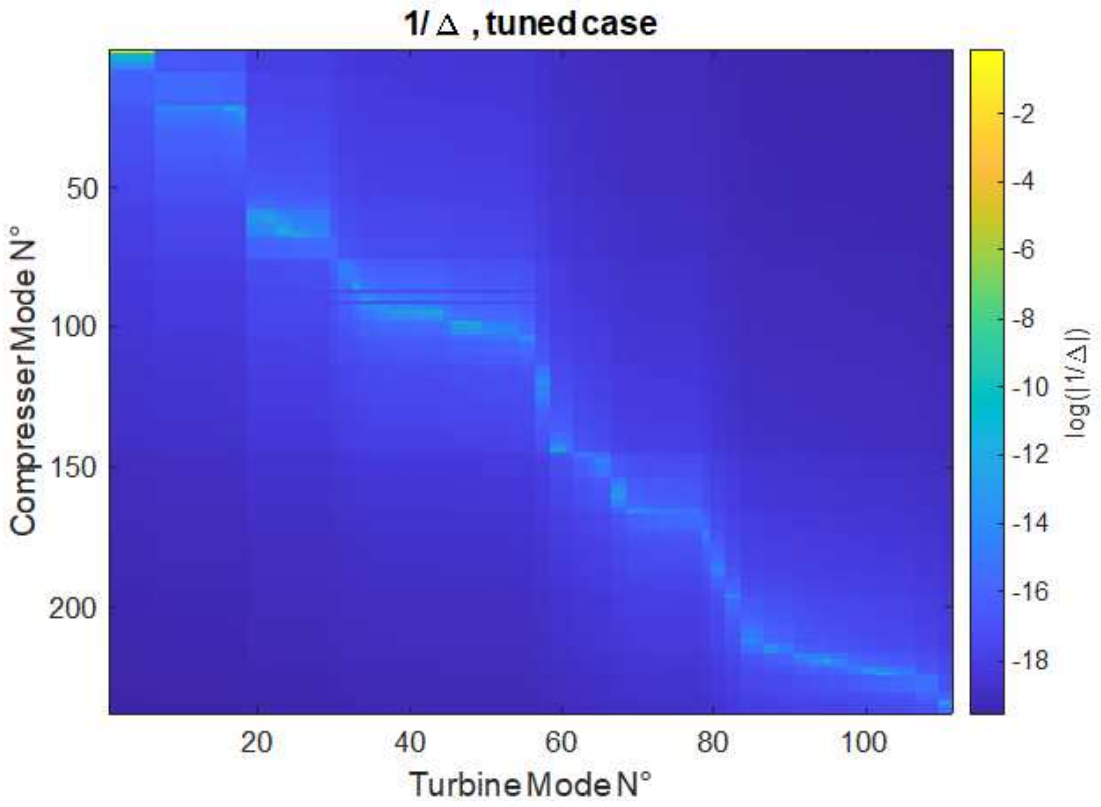

Figure 7.34: Table showing the proximity of eigenvalues of modes of subsystem A (y-axis) and tuned subsystem B (x-axis), in form of the parameter Δ^{-1} ,with $\Delta = \lambda_A - \lambda_B$

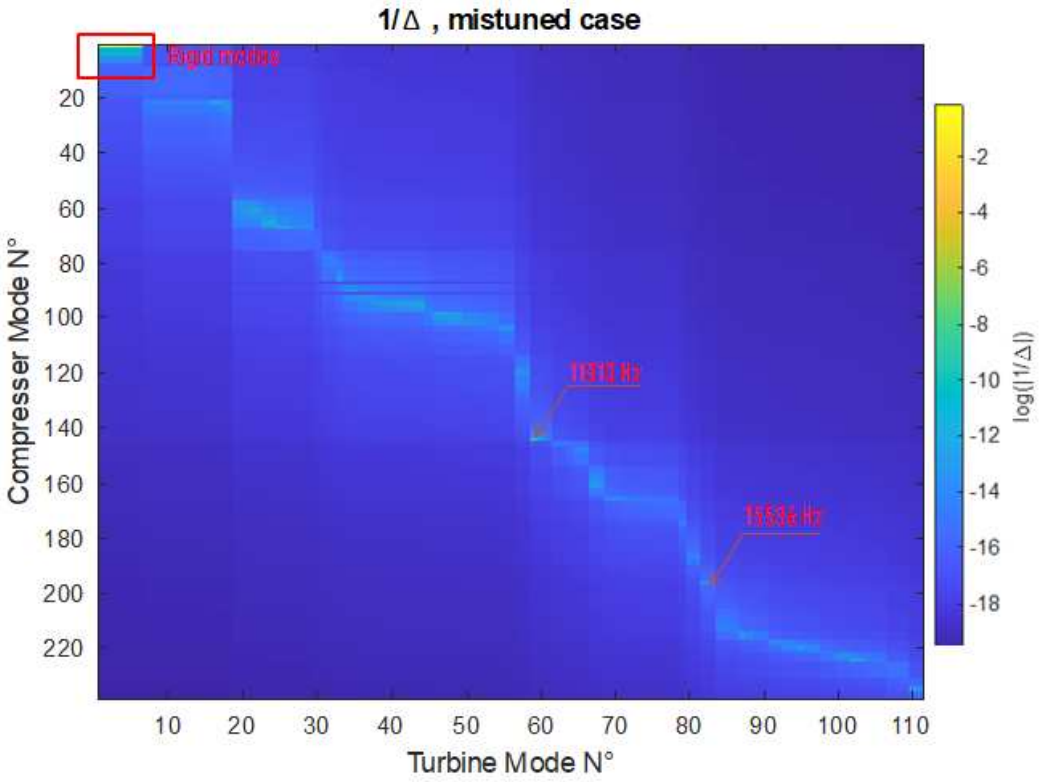

Figure 7.35: Table showing the proximity of eigenvalues of modes of subsystem A (y-axis) and mistuned subsystem B (x-axis), in form of the parameter Δ^{-1} ,with $\Delta = \lambda_A - \lambda_B$

In figures 7.34 and 7.35 there is a light stripe representing the turbine and compressor modes that are closest to each other. It is possible to represent the values in this diagonal stripe with values $1/\Delta$ with respect to the frequency of either the turbine or the compressor, thus creating the graph 7.36. The higher the value, the closer the frequencies are. Blue line represents the values for the tuned case, while red represents the values of the mistuned case. It is noted that the values often coincide, while in some peaks the mistuned value is much higher, given that the scale of the y axis is logarithmic.

7.1.5 Evaluation of the interfaces

In Eq. (7.33), on the numerator is the product of the interfaces of the two subsystems. In fact it appears also on the denominator. Using the polynomial coefficient as a degrees of freedom is convenient because they have a physical meaning. Order 0 polynomial coefficients represent constant motion of the interface. Order 1 represent plane motion of the interface. If product of the interfaces of the two interfaces is zero, then these modes do not interact and they do not create a coupled mode.

Figure 7.37 shows the turbine and shaft interface with tuned turbine (blue) and mistuned turbine (red). It can be seen in (a) how the mistuning causes a rotation component of the shaft-turbine

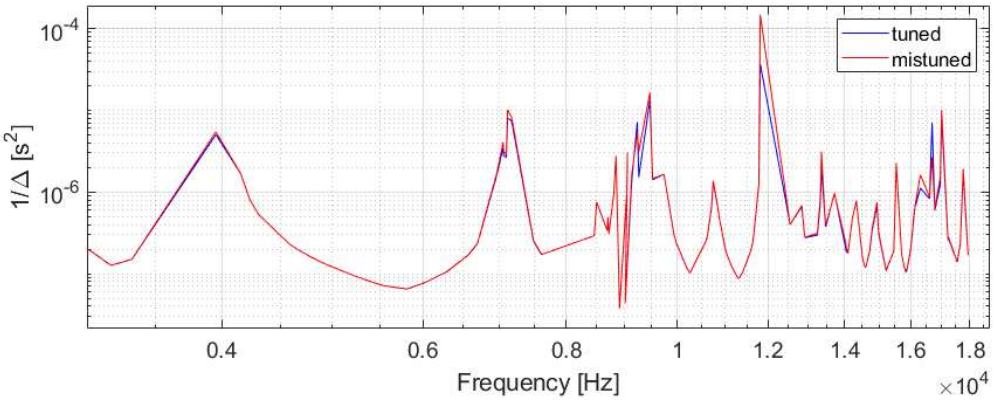

Figure 7.36: Graph of frequency (x-axis) and proximity between two closest pair of poles ($1/\Delta$) on the y-axis

interface. Furthermore in (b) it can be noted that the mode shape at the mistuned interface presents an additional axial translation component (ND0). This proves that the mistuning causes an interface-interface interaction between the turbine subsystem and the compressor subsystem, and for this reason, together with the proximity in frequency, it allows to give rise to the coupled mode shown in the figure 7.15, starting from two modes represented in Fig. 7.24.

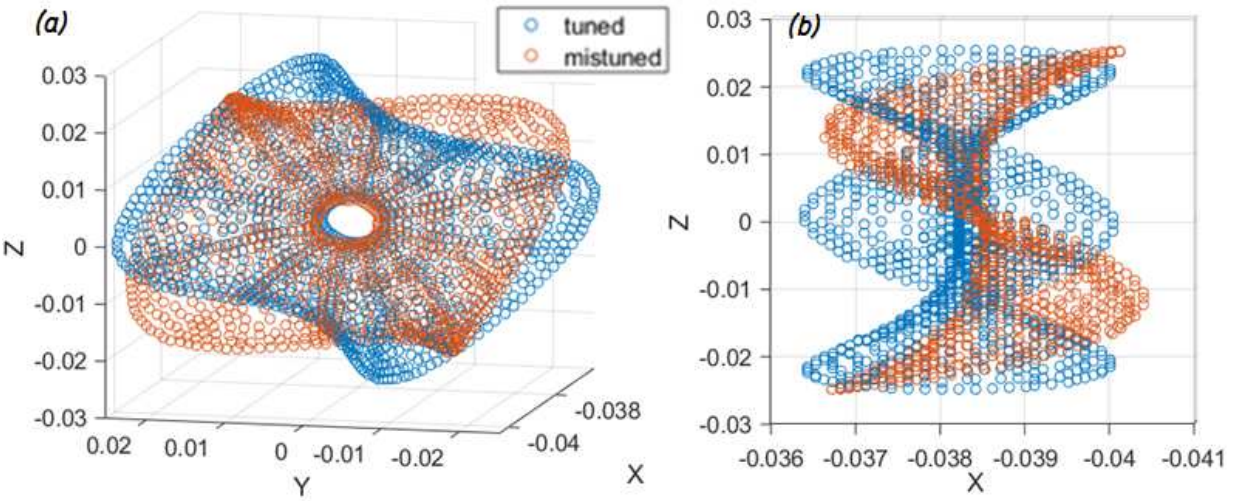

Figure 7.37: Comparison of tuned and mistuned turbine interfaces for mode 59 (11810 Hz) corresponding to full rotor mode 200

8 Sensitivity analyses

8.1 Sensitivity analysis on the bearing conditions

In this section we attempt to repeat the sensitivity study of the modes on the effects of bearing conditions proposed in the [17] study, with the with the inclusion of mistuningin the model.

In this study Zobel, Beirow & al. carried out on the geometry of the same rotor, produced by KBB, they implemented the combinations of boundary conditions reported in the table Tab. 2.4, while varying both the stiffness and the damping coefficient. In this chapter a simplified version is proposed considering the variation in stiffness and leaving the damping unchanged at the values provided by the manufacturer. For the low stiffness case (LS) we use a value equal to 1/100 of the reference value provided by the manufacturer. For the high-stiffness case we use a very high value of stiffness in order to lock the degrees of freedom ($\approx 10^{30}$ times the reference values).

8.1.1 Sensitivity on the radial bearings stiffness

High stiffness

The high radial stiffness condition was implemented with a value equal to 10^{37} times the reference value in order to suppress DOF in the radial direction of the radial bearing surfaces. This causes a significant upward shift in the frequencies.

In fig. 8.1 ,8.2, 8.3 it is noted that the amplitude ratio is not very sensitive to even a large increase in the radial stiffness of the bearings. The reference value is therefore a sufficiently high value such that it can be assimilated to rigid bearings. In the figure 8.3 it is possible to observe some slightly coupled modes that arise in compressor ND2 modes. In the figure 8.4 an example of these modes is shown. It is Mode 77. The additional coupling is attributed to the residual DFT component of amplitude 0.38 for ND0.

In Fig. 8.5 and 8.6 we show the comparison of the mode shapes on the turbine tips with the reference mistuned case. The mode shapes show a high degree of similarity, with MAC values on the diagonal oscillating between 1 and 0.8.

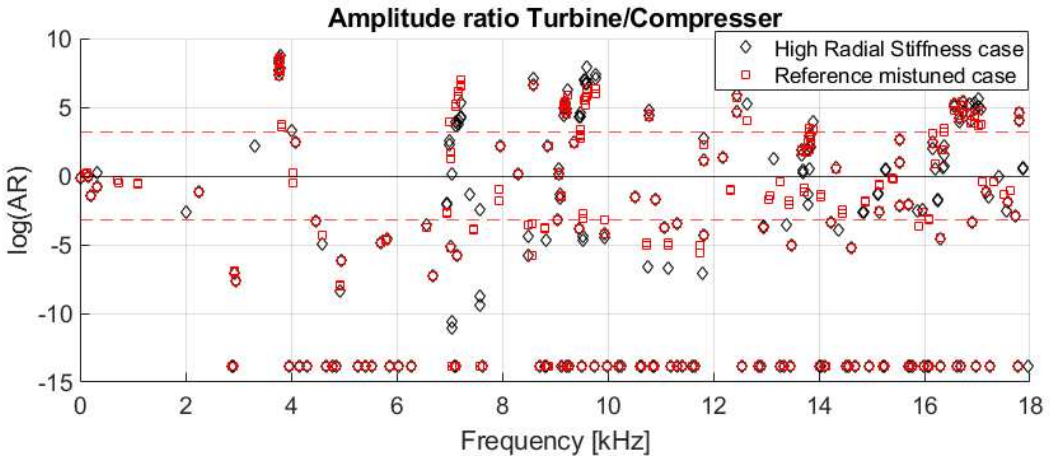

Figure 8.1: Frequency vs Amplitude ratio plot for the modes of high radial stiffness case in the frequency region [0,18] kHz and comparison with reference mistuned case

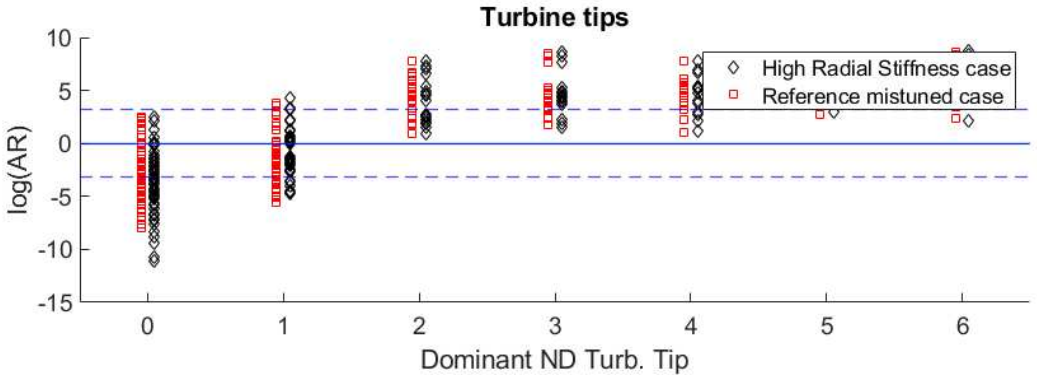

Figure 8.2: Amplitude ratio vs Turbine dominant Nodal Diameter plot for the modes of high radial stiffness case in the frequency region [0,18] kHz

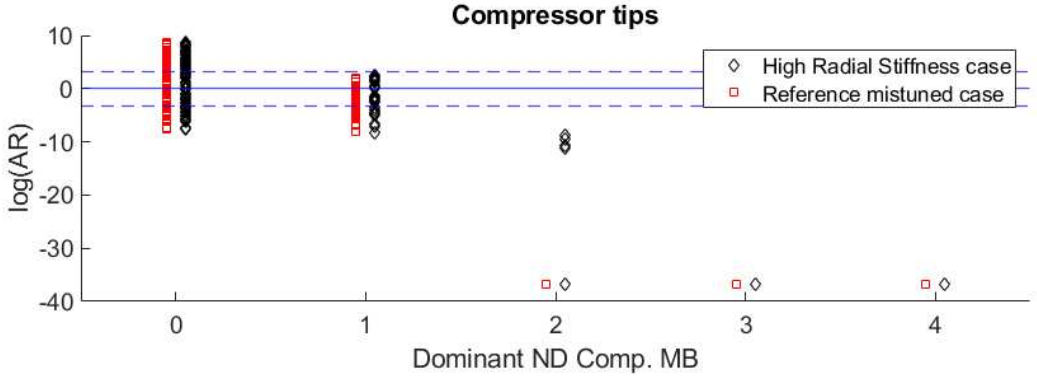

Figure 8.3: Amplitude ratio vs Compressor MB dominant Nodal Diameter plot for the modes of high radial stiffness case in the frequency region [0,18] kHz

Figure 8.4: Mistuned mode 77 for high radial stiffness configuration, illustration and DFT on compressor side

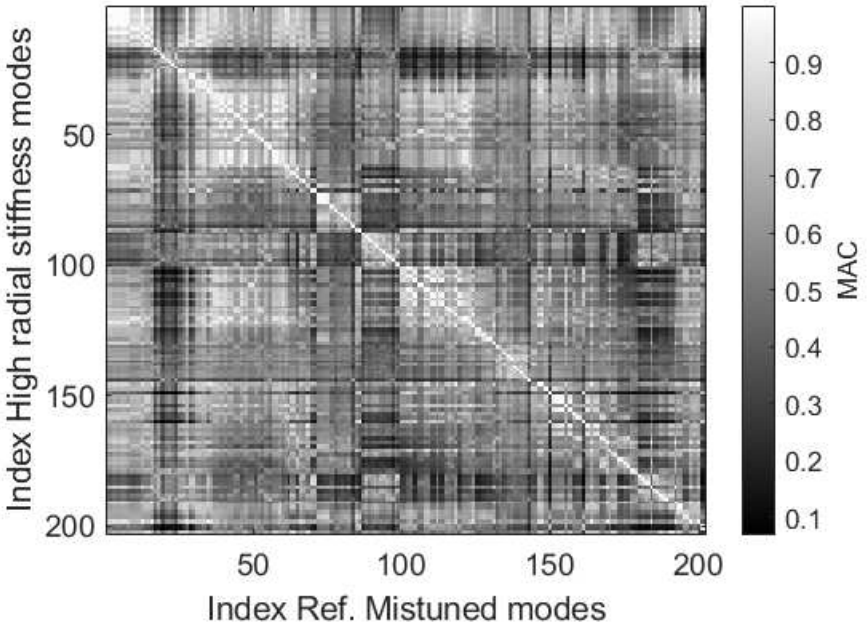

Figure 8.5: Modal assurance criterion table between mode shapes evaluated in turbine tip nodes in Low radial stiffness and reference mistuned case

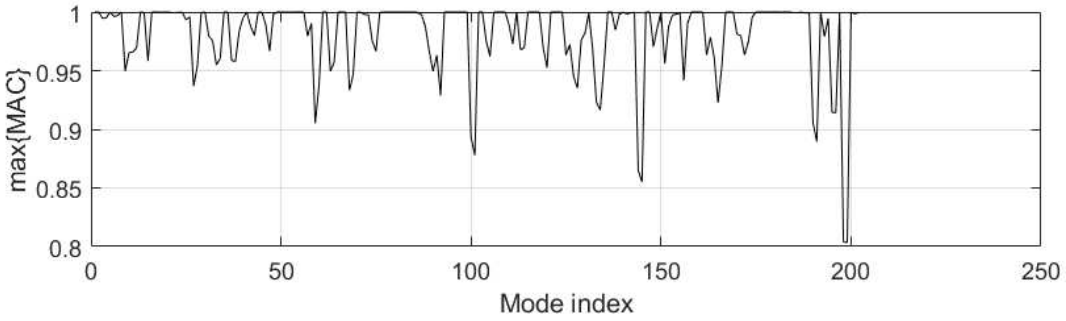

Figure 8.6: Modal assurance criterion table between mode shapes evaluated in turbine tip nodes in high radial stiffness and reference mistuned case

Low stiffness

For the Low Stiffness condition, a value equal to 0.01 times the reference value is used on rare bearings. In figure 8.7 the effect of the decrease in stiffness is shown, with a clear increase in coupled modes. However, a significant number of null modes remain on the turbine (bottom of figure). In figures 8.8 and 8.9 we can see how even modes with ND>1 have a degree of coupling similar to ND0 and ND1.

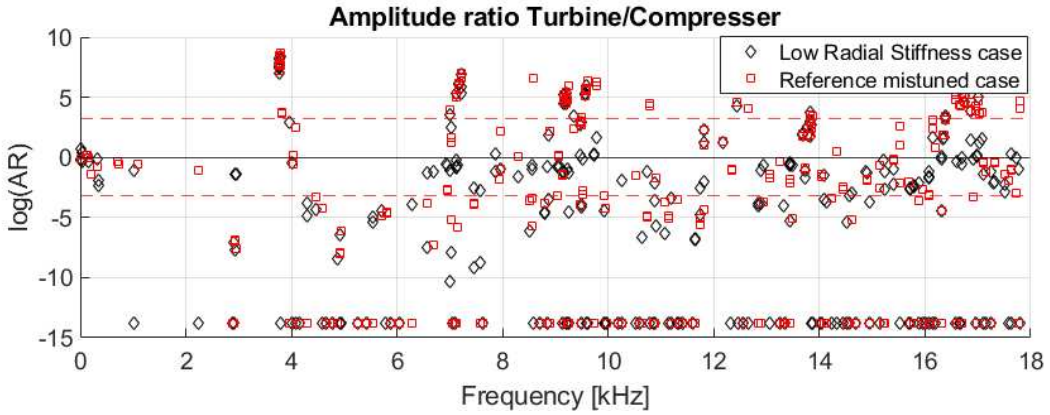

Figure 8.7: Frequency vs Amplitude ratio plot for the modes of low radial stiffness case in the frequency region [0,18] kHz and comparison with reference mistuned case

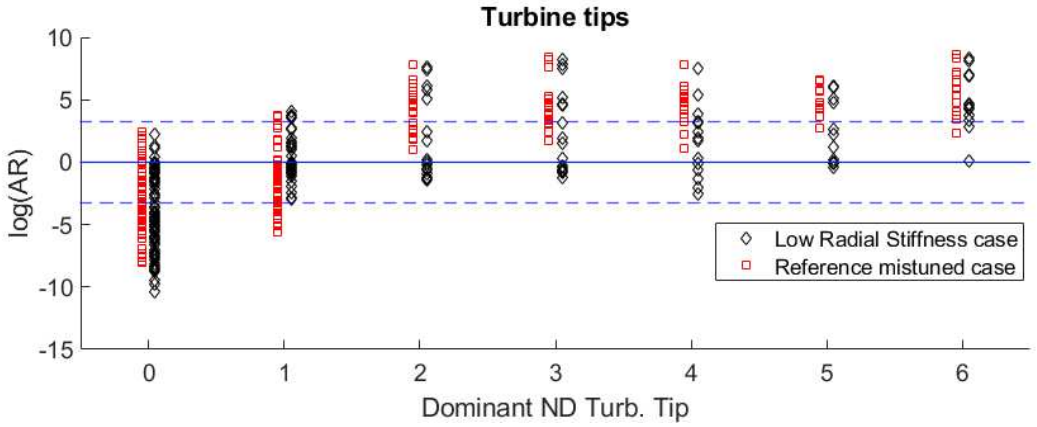

Figure 8.8: Amplitude ratio vs Turbine dominant Nodal Diameter plot for the modes of low radial stiffness case in the frequency region [0,18] kHz

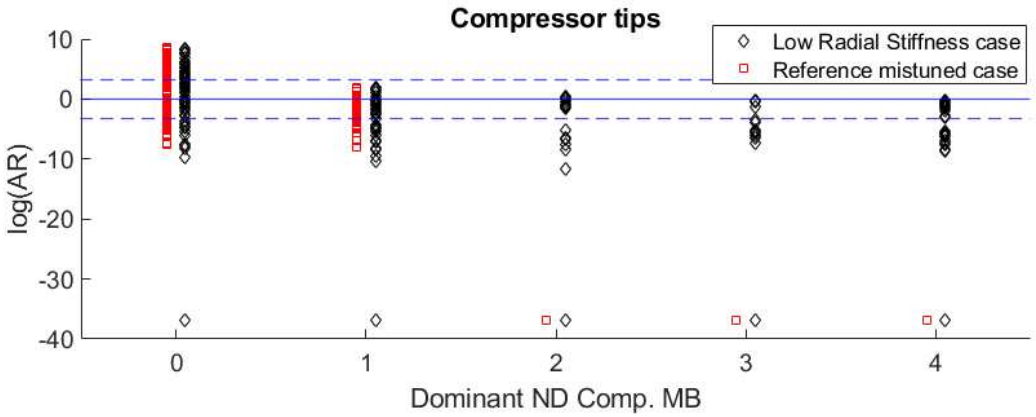

Figure 8.9: Amplitude ratio vs Compressor MB dominant Nodal Diameter plot for the modes of low radial stiffness case in the frequency region [0,18] kHz

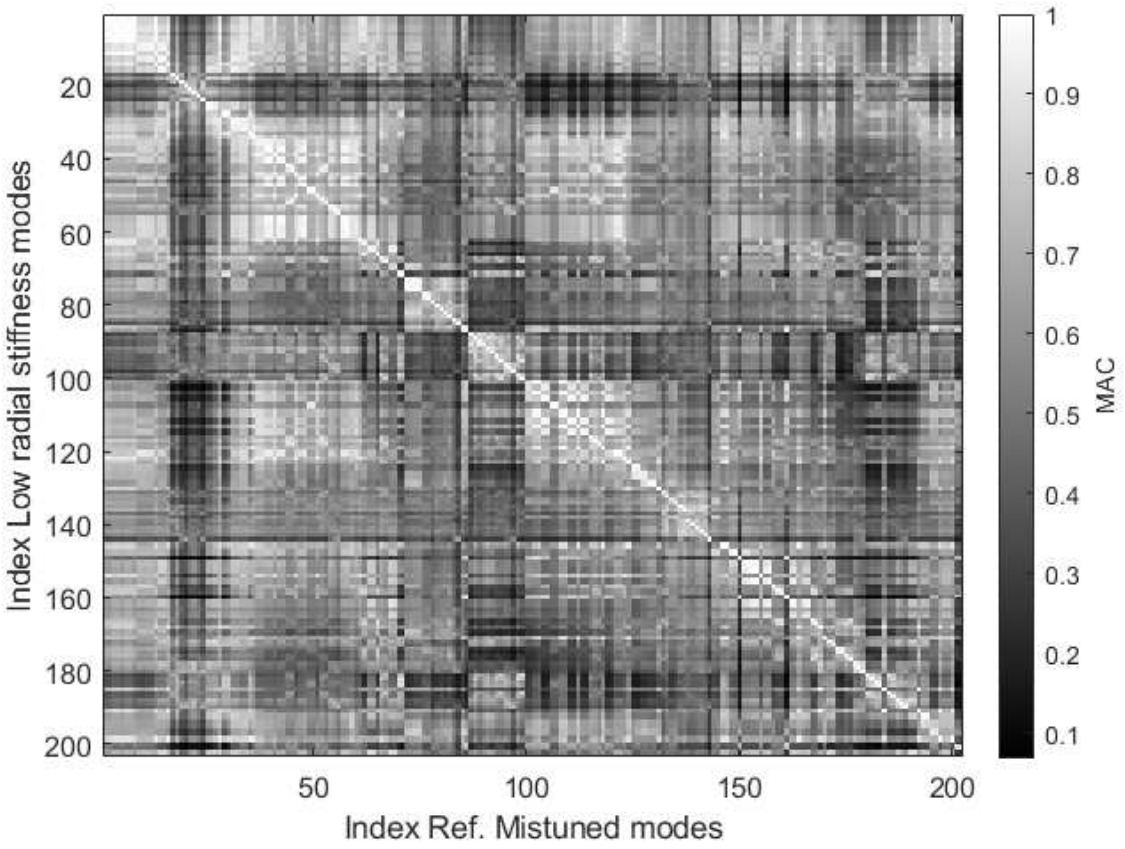

Figure 8.10: Modal assurance criterion table between mode shapes evaluated in turbine tip nodes in Low radial stiffness and reference mistuned case

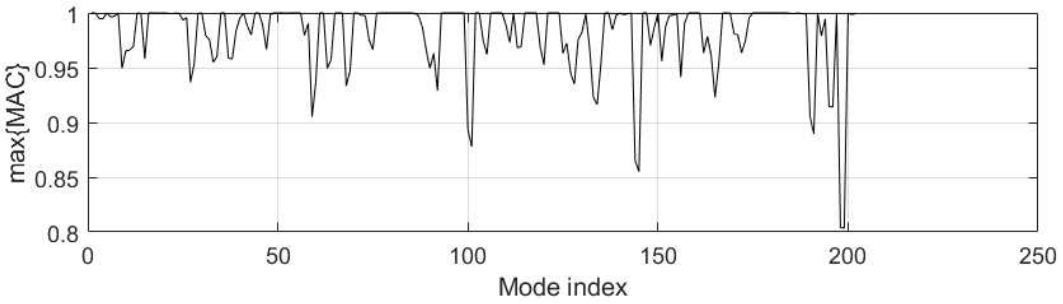

Figure 8.11: Modal assurance criterion between tuned mode and most similar mode

Belowe are shown examples of the additional coupled modes with ND¿1due to the release in the radial stiffness:

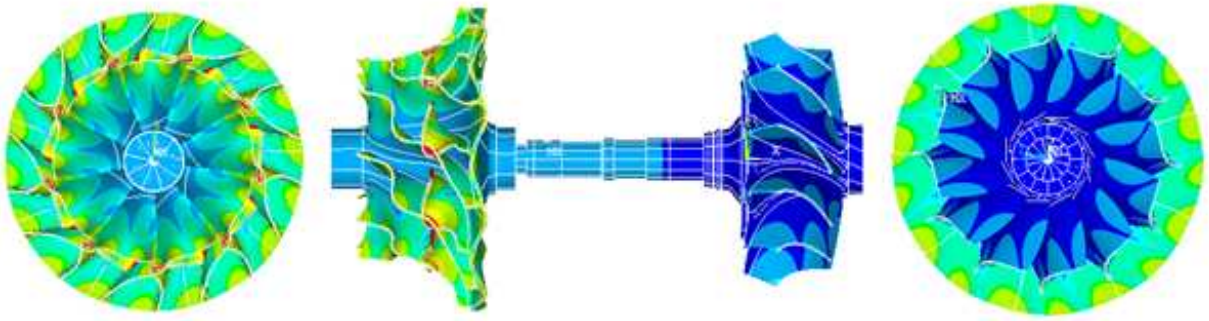

Figure 8.12: Example of coupled mode, Mode 140 mistuned, ND3 dominant on turbine, 9.4658 kHz, AR = 1.22

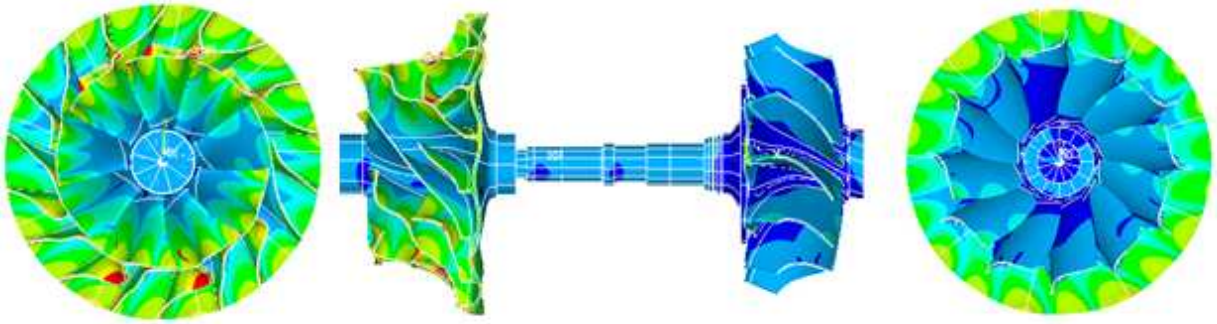

Figure 8.13: Example of coupled mode, Mode 148 mistuned, ND4 dominant on turbine, 9.5208 kHz, AR = 0.84

8.1.2 Sensitivity on the axial bearing stiffness

High Stiffness

The high stiffness axial condition was implemented with a value equal to 10^{30} times the reference value provided by the manufacturer for the axial bearing. The result is the suppression of the axial degrees of freedom on the bearing surface located approximately halfway up the shaft (x = -0.243 m). In Fig. 8.14, we compare the degree of coupling of the modes for the High axial stiffness case and the Reference case. The color represents the dominance of the normal behavior component on the shaft. The dashed red line indicates equal AR values between the two cases. Most modes with a stronger axial component (yellow) are found above the red line, where the modes in the high axial stiffness case exhibit AR values deviating more from 1 than in the tuned case.

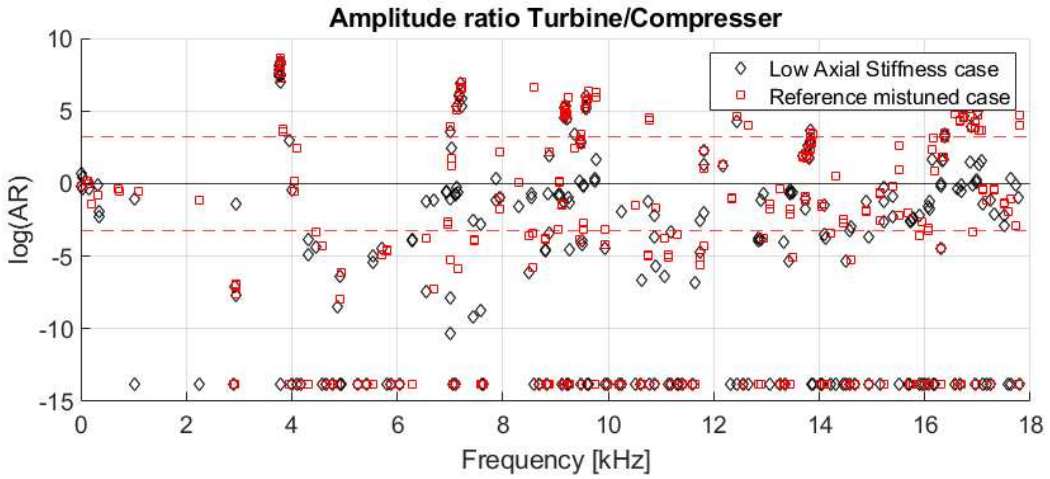

Figure 8.14: Frequency vs Amplitude ratio plot for the modes of the high axial stiffness case in the frequency region [0,18] kHz and comparison with the reference mistuned case.

Figure 8.15 compares the degree of coupling (log(AR)) between the reference mistuned case and the Low Axial Stiffness case, with the different nodal diameters. It is possible to observe small differences in the absolute degrees of coupling, despite some individual modes shifting toward higher or lower values of log(AR). The same is observed by plotting the modes' log(AR) with dominant nodal diameters on the compressor (Fig. 8.16).

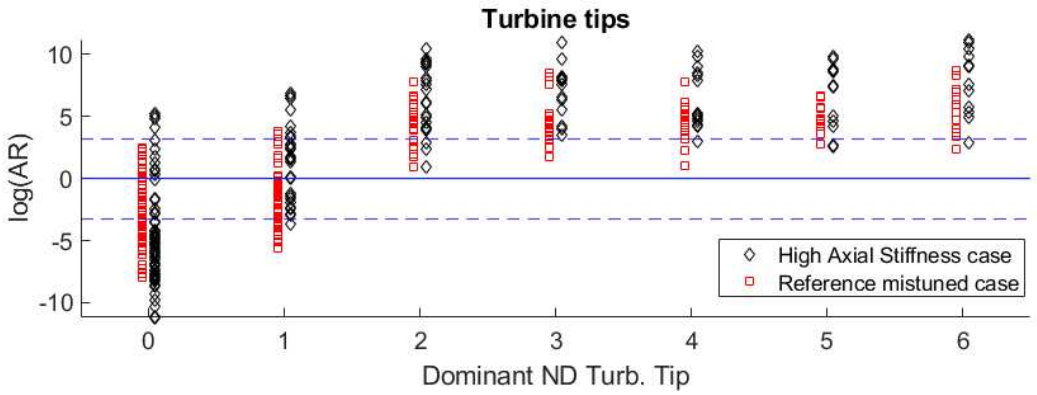

Figure 8.15: Amplitude ratio vs Turbine dominant Nodal Diameter plot for the modes of the high axial stiffness case in the frequency region [0,18] kHz.

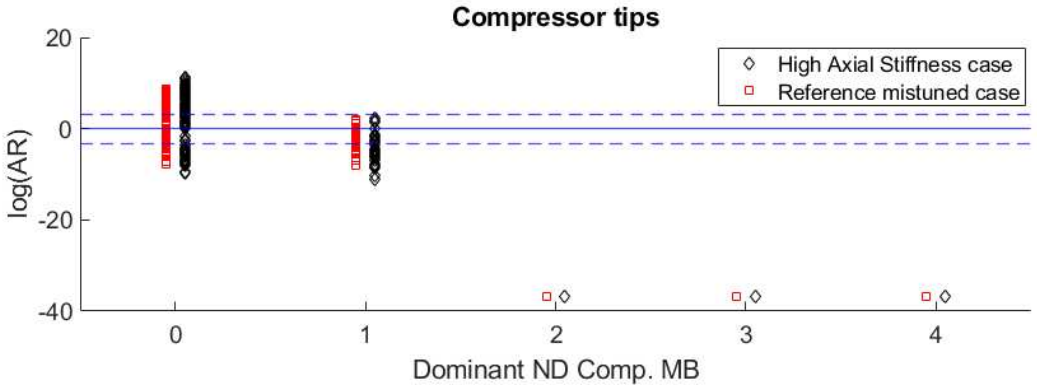

Figure 8.16: Amplitude ratio vs Compressor MB dominant Nodal Diameter plot for the modes of the high axial stiffness case in the frequency region [0,18] kHz.

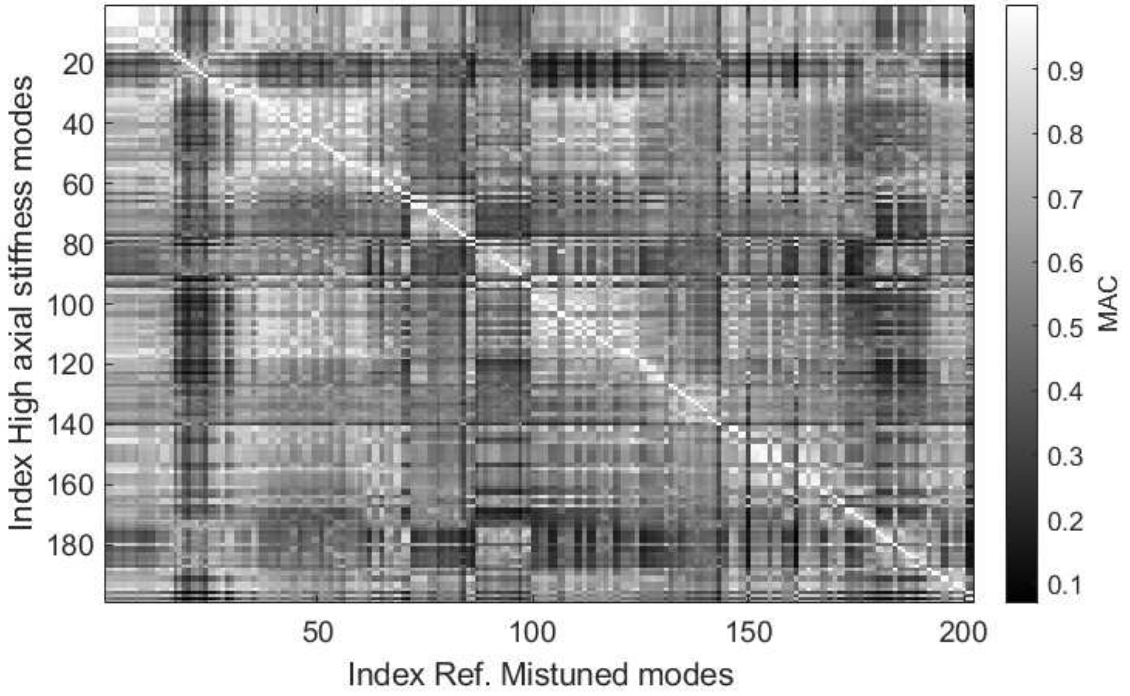

Figure 8.17: Modal assurance criterion table between mode shapes evaluated in turbine tip nodes in high stiffness axial and reference mistuned cases.

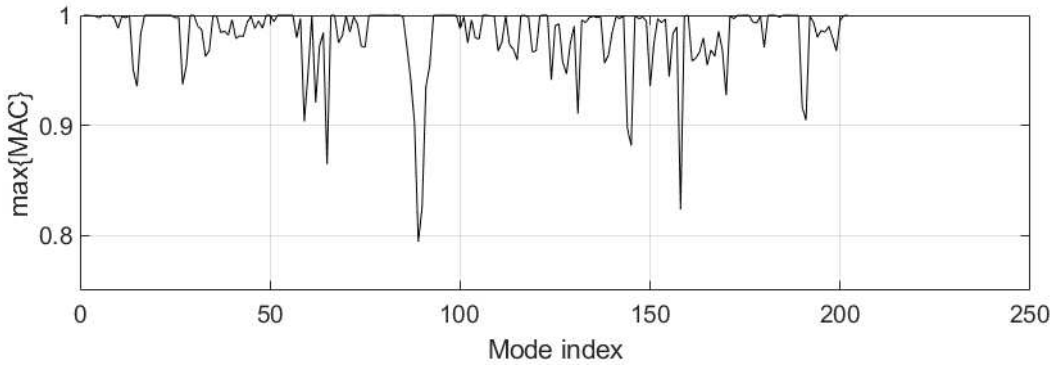

Figure 8.18: Modal assurance criterion table between mode shapes evaluated in turbine tip nodes in high stiffness axial and reference mistuned case

Low stiffness

Evaluation of a low-axial stiffness configuration gives results similar to the reference mistuning case.

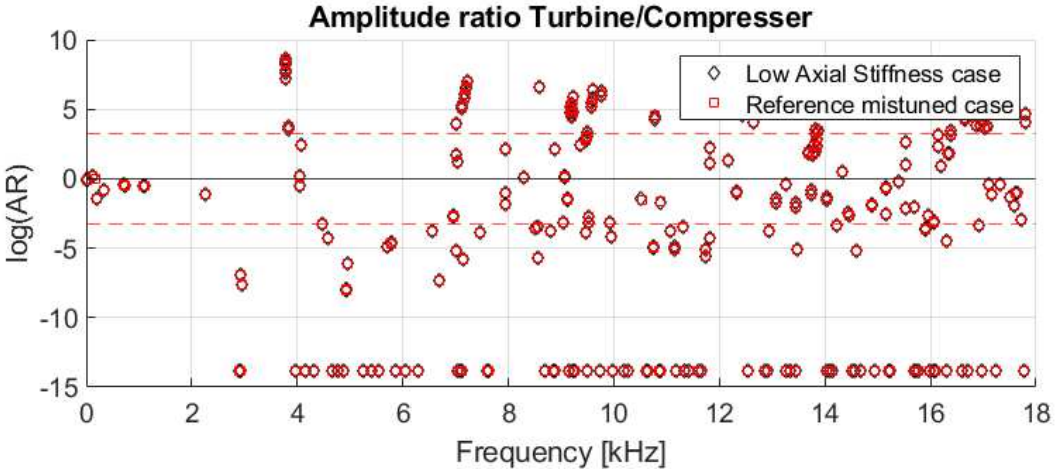

Figure 8.19: Frequency vs Amplitude ratio plot for the modes of low axial stiffness case in the frequency region [0,18] kHz and comparison with reference mistuned case

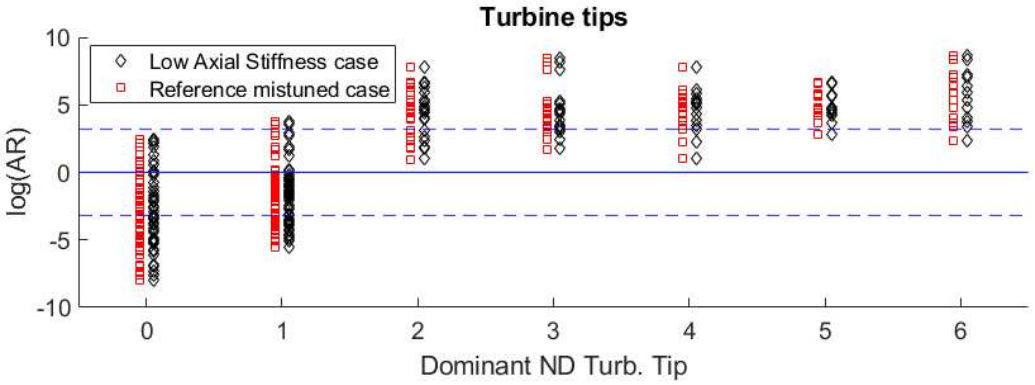

Figure 8.20: Amplitude ratio vs Turbine dominant Nodal Diameter plot for the modes of low axial stiffness case in the frequency region [0,18] kHz

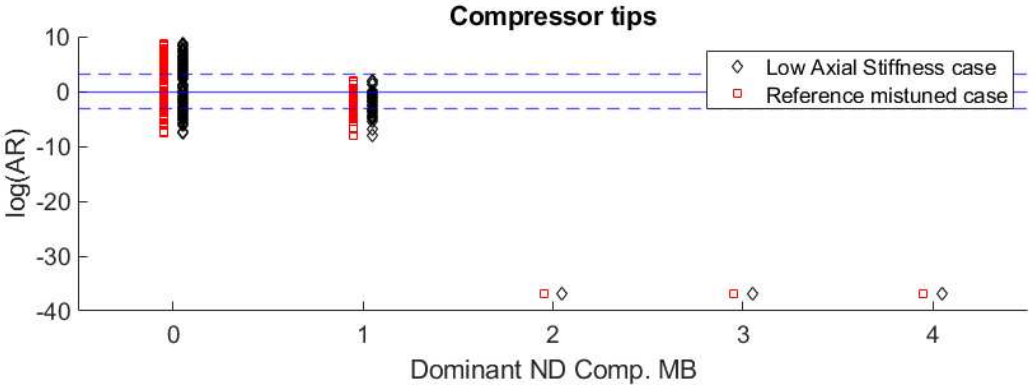

Figure 8.21: Amplitude ratio vs Compressor MB dominant Nodal Diameter plot for the modes of low axial stiffness case in the frequency region [0,18] kHz

Comparison of mode shapes with the MAC criterion shows a very high degree of similarity between the mode shapes in Fig. 8.22. On the diagonal, most modes evaluate to AR close to 1. Fig. 8.23.

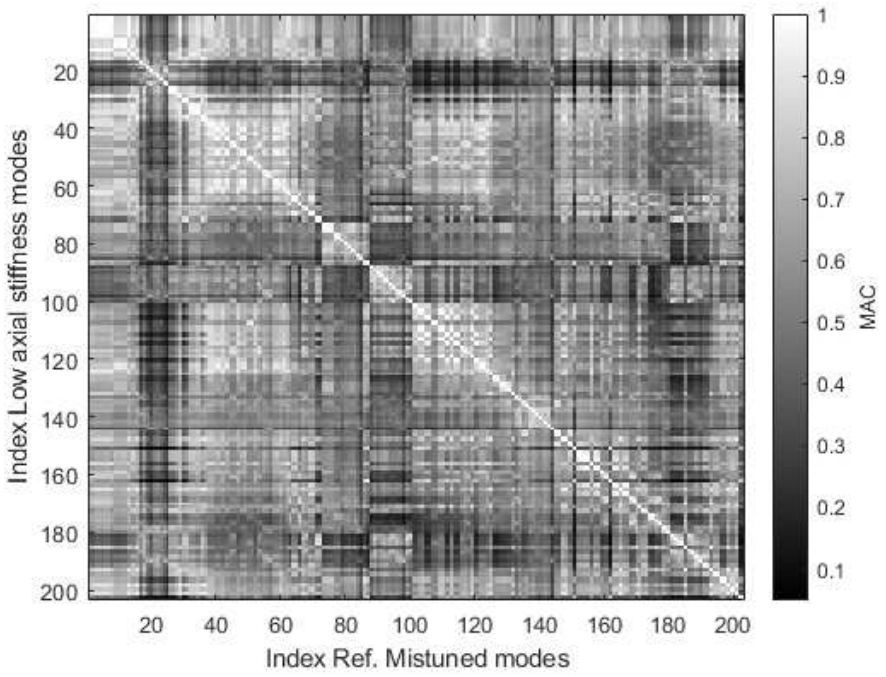

Figure 8.22: Modal assurance criterion table between mode shapes evaluated in turbine tip nodes in low axial stiffness and reference mistuned case

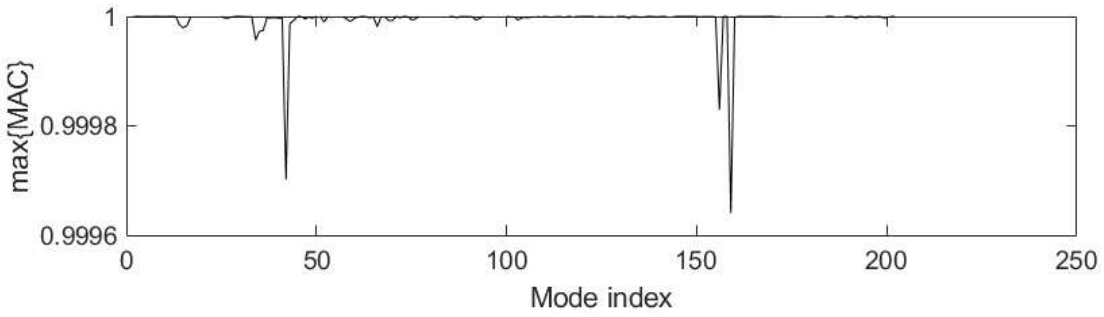

Figure 8.23: Modal assurance criterion table between mode shapes evaluated in turbine tip nodes in Low stiffness axial and reference mistuned case

8.1.3 Simplified shaft model

A model of the shaft representing the bladed wheels as concentrated masses and inertias has been created in Matlab. The shaft consists of 50 nodes and 49 equal-length 3D beam elements. Mass, stiffness and gyroscopic matrices are calculated for each shaft section with the properties

(diameter, moment of inertias) that vary along the axial coordinate. At each node, 3d beam element has six degrees of freedom, represented in Eq. (8.1)

$$\{q^{(el)}\} = \begin{Bmatrix} u_x \\ u_y \\ u_z \\ \Theta \\ \phi_y \\ \phi_z \end{Bmatrix} \tag{8.1}$$

- u_x displacement in axial direction
- u_y, u_z displacement in the x and y directions
- Θ angular deflection in axial direction (torsion)
- ϕ_y, ϕ_z angular deflection in y and z direction associated to bending

The stiffness matrix is computed with Euler-Bernoulli formulation found in [9]. The mass matrix and the gyroscopic matrices are lumped at the nodes [18]. The structure is in series; therefore, elemental matrices are assembled with the technique described in [9] in Fig.8.24 Axial and radial bearings are modelled in the node closest to the actual position of the bearing. Modelling of the boundary conditions imposed by the bearing is achieved by adding stiffness terms on the corresponding entries of the stiffness matrix. As an example, axial bearing is a simple spring connection to a remote point, and is modelled adding the stiffness value to the diagonal of the stiffness matrix, in the index corresponding to the u_x degree of freedom of the node where the bearing is located. Similarly, the radial stiffness is modeled as a 2D connection, and therefore a 2x2 stiffness term, which is added to the stiffness matrix, across the diagonal at indices corresponding to u_y, u_z degrees of freedom of the node whose position corresponds to the radial bearing.

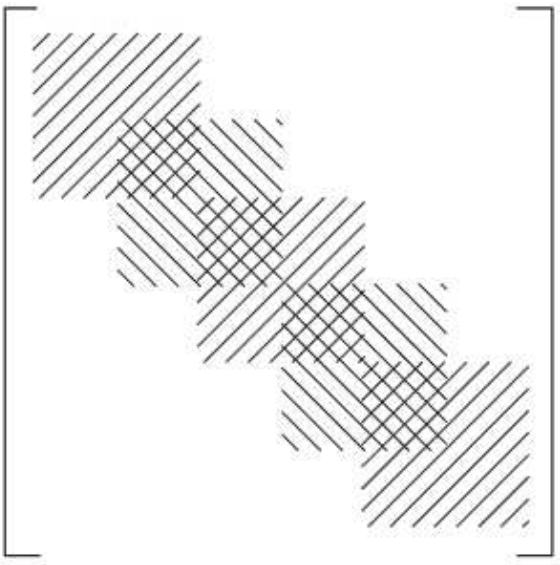

Figure 8.24: Assembling scheme of elemental matrices for structures in series

Eigenvalues and eigenvectors can be calculated numerically given the stiffness, mass and gyroscopic matrices. The modal analysis of this simplified model can be iteratively repeated by testing different boundary conditions of the bearings. In particular, the amplitude ratio of a mode can be calculated between the first and last nodes of the shaft, as shown in Eq. (8.2).

$$AR_{\mathrm{SE}} = \frac{u_i}{u_j}, \text{i first node, j last node} \tag{8.2}$$

It is possible to test different configurations of radial bearings by applying an axial bearing gain of value between 10^{-2} and 10^{5}. By applying these changes it is possible to track how the amplitude ratio changes. In fig. 8.25 shows the amplitude ratio of the first bending mode shape as a function of the gain on the radial bearings.

In Fig. 8.25 it is possible to note that for low values of stiffness gain (axial condition free), the AR of the axial mode is close to 1, as the shaft moves rigidly on the bearing, while increasing the axial stiffness the AR of the axial mode diverges to a very large or very small value, as the mode shapes become concentrated on one side of the shaft relative to the bearing. The bulk of the transition seems to occur for axial stiffness gain around 10^{4}.This finding also supports the results in 8.1.2, in which little variation is noted in the gain values between 10^{-2} and 10^{0}, while a significant decrease in the degree of coupling for the modes with strong axial behaviour is observed as the gain values increase from 10^{0} to 10^{30}..

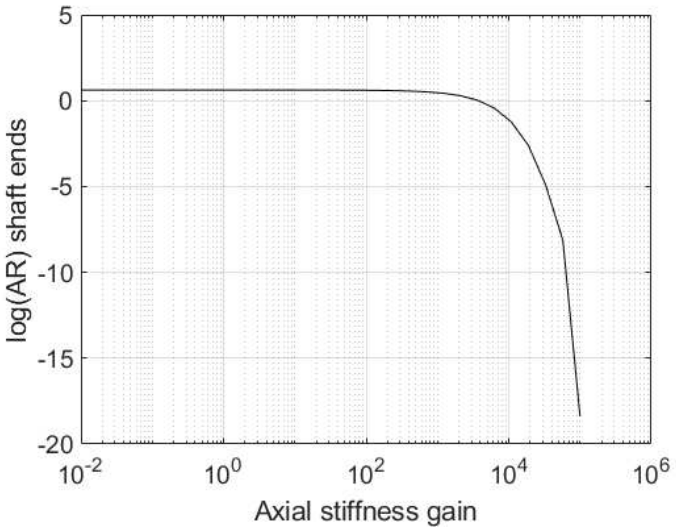

Figure 8.25: Effect of axial bearing stiffness gain on $\log(AR_{SH})$, between the two ends of the shaft, of the first axial mode of the shaft

8.2 Results with different mistuning patterns

In this section we implement mistuning patterns measured for modes different from the one implemented so far, the BM5 ND0. The aim is to confirm the results obtained so far and observe any differences in the occurrence of coupled modes, as well as their impact on frequencies, degrees of localization, and mode fill factor.

8.2.1 BM4 EO17 Mistuning

Thr mistuning pattern measured for mode BM4 EO17 has been implemented on the model with the technique presented in Chapter 5.

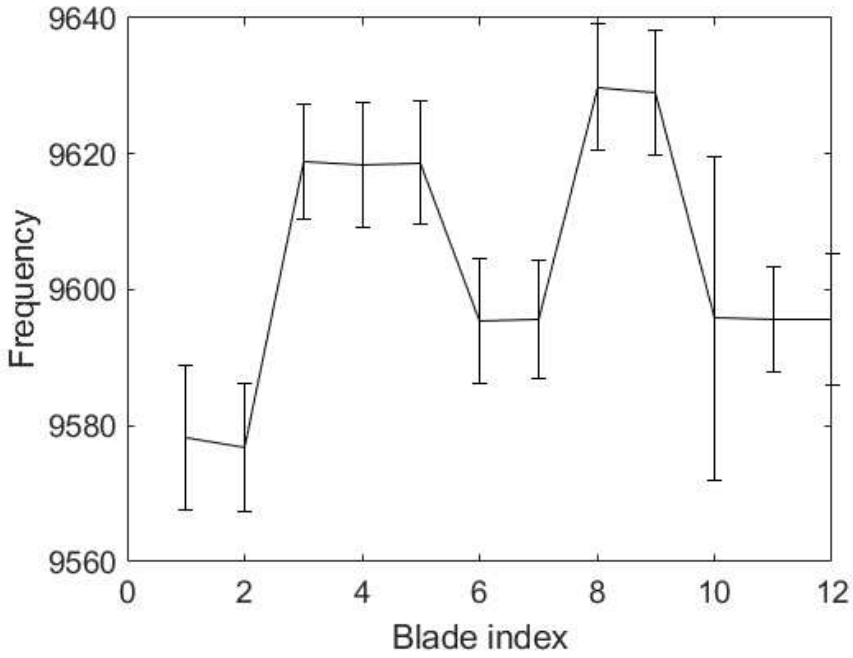

Figure 8.26: Plot of the blades frequencies measured with the Blade Tip timing technique for the BM4 EO17 mode

In Fig. 8.27, the differences in aspect ratios (AR) and frequencies are visible. While the frequencies remain relatively stable, the amplitude ratios (AR) of the modes exhibit significant variation. Turbine-dominated modes are observed in the BM3/BM4 region, which show increased coupling. At high frequencies, above 12 kHz, the number of coupled modes increases significantly. Compressor-dominated modes remain largely unchanged compared to the tuned case, result which is also confirmed in Fig. 8.29. In fig. 8.29 we observe differences only for a few modes.

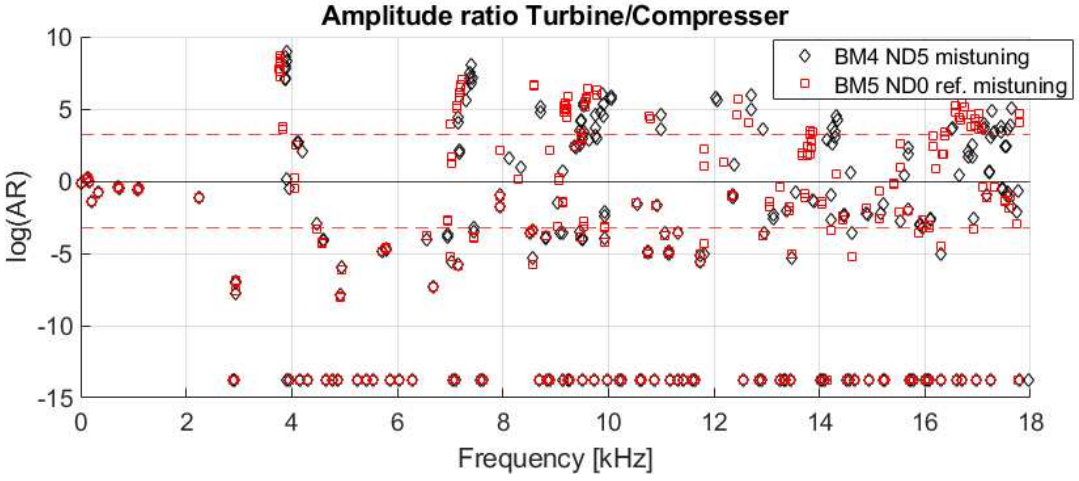

Figure 8.27: Frequency vs Amplitude ratio plot for the modes of BM4 EO17 mistuned case in the frequency region [0,18] kHz and comparison with reference mistuned case

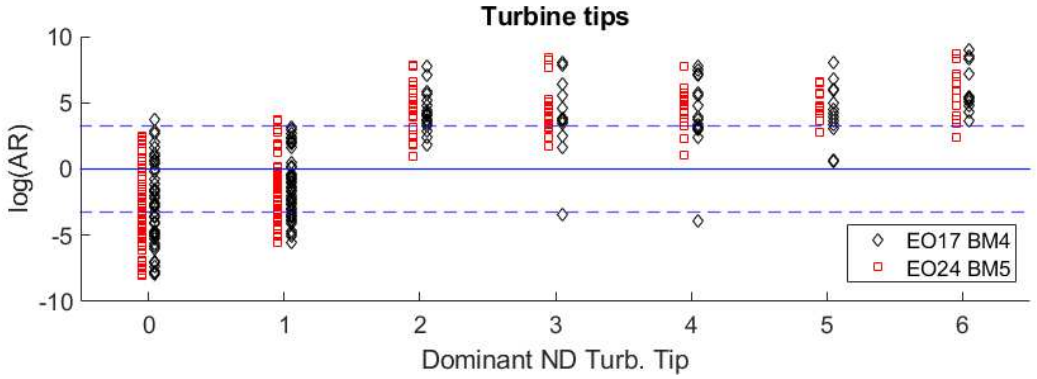

Figure 8.28: Amplitude ratio vs Turbine dominant Nodal Diameter plot for the modes of BM4 EO17 mistuned case in the frequency region [0,18] kHz

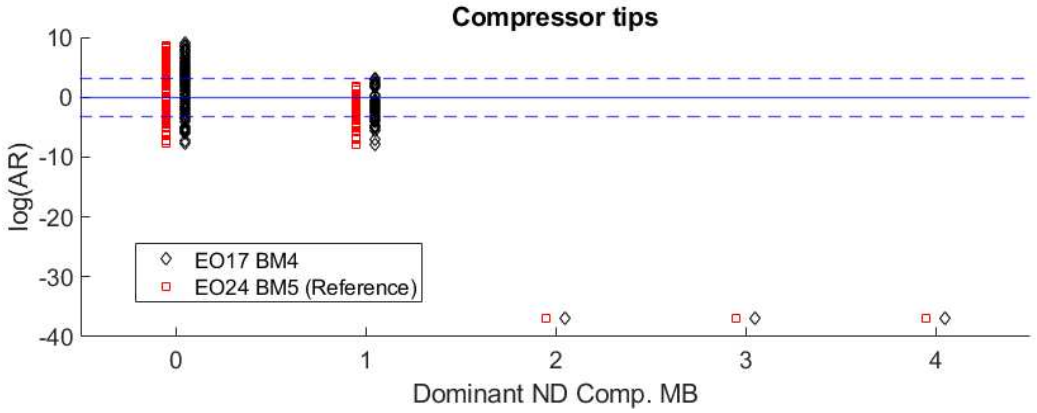

Figure 8.29: Amplitude ratio vs Compressor MB dominant Nodal Diameter plot for the modes of BM4 EO17 mistuned case in the frequency region [0,18] kHz

Comparison of mode shapes with the MAC criterion shows a very high degree of similarity between the mode shapes in Fig. 8.30. On the diagonal, most modes evaluate to AR close to 1, Fig. 8.31.

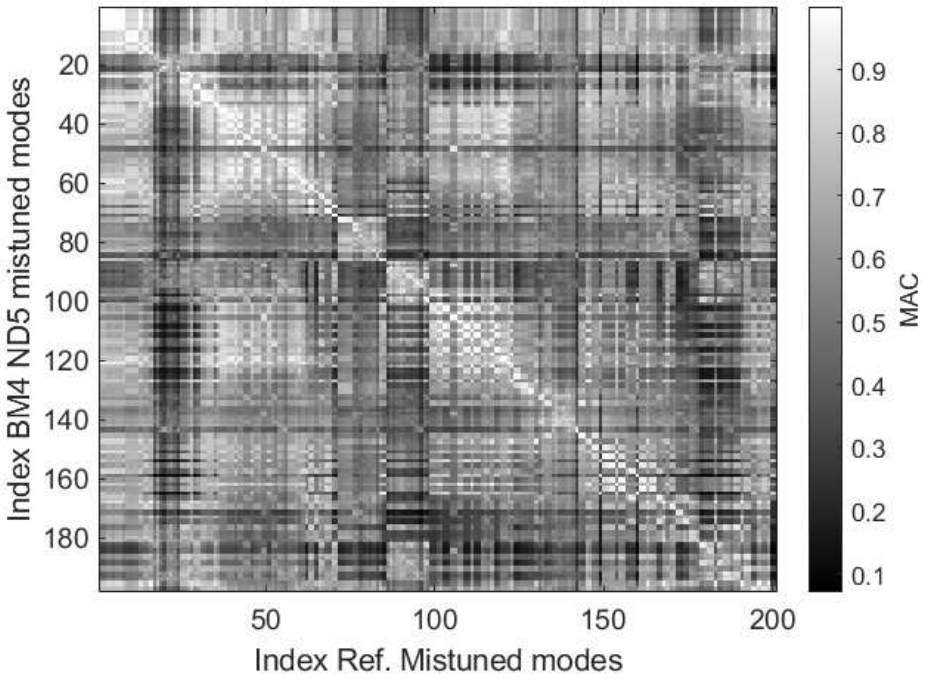

Figure 8.30: Modal assurance criterion table between mode shapes evaluated in turbine tip nodes in BM4 EO17 mistuned and reference mistuned case

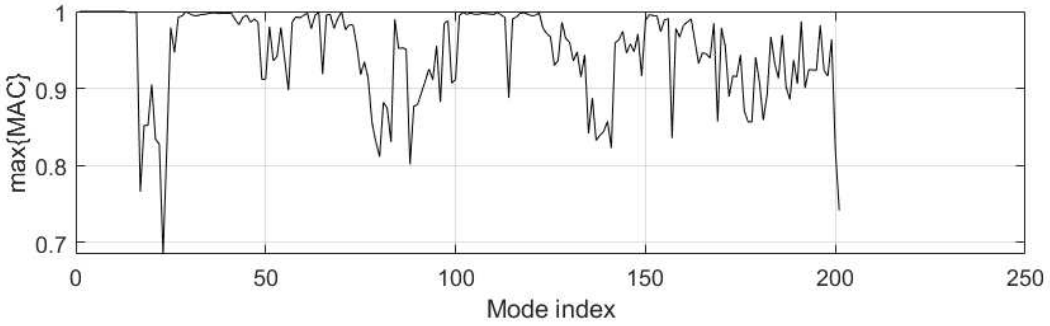

Figure 8.31: Modal assurance criterion table between mode shapes evaluated in turbine tip nodes in BM4 EO17 and reference mistuned case

Following (Fig. 8.32 is the mode which shows the most increase in coupling, mode 316 (and its twin mode 317). Another mode with a high increase in coupling in the BM4/BM3 frequency region is shown in figure 8.32.

It is interesting to analyze the coupling mechanism for the rotor with an additional mistuning pattern compared to the reference case to verify or challenge the invariance of the observations made in the previous chapter. Mistuning patterns can significantly alter the vibrational characteristics of a rotor, influencing both the coupling mechanisms and the distribution of energy across different nodal diameters. To investigate this further, we consider an additional mistuning pattern and compare its effects with the reference case.

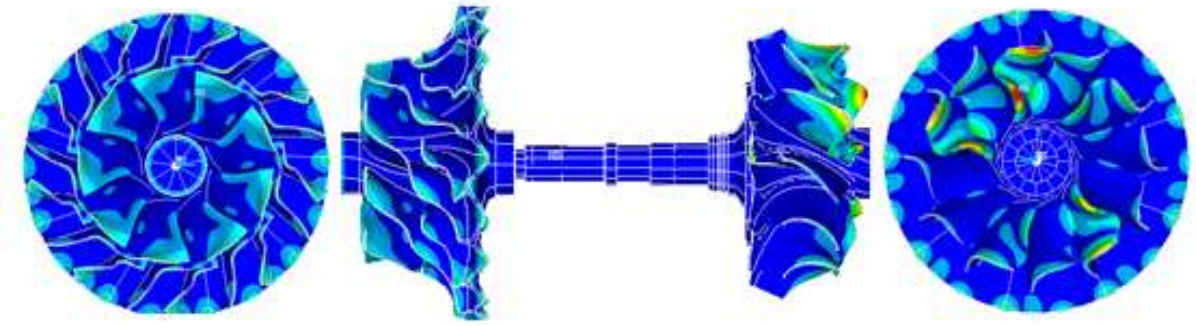

Figure 8.32: Mode 316, with dominant ND 5 on the turbine, 16.860 kHz, AR = 1.89

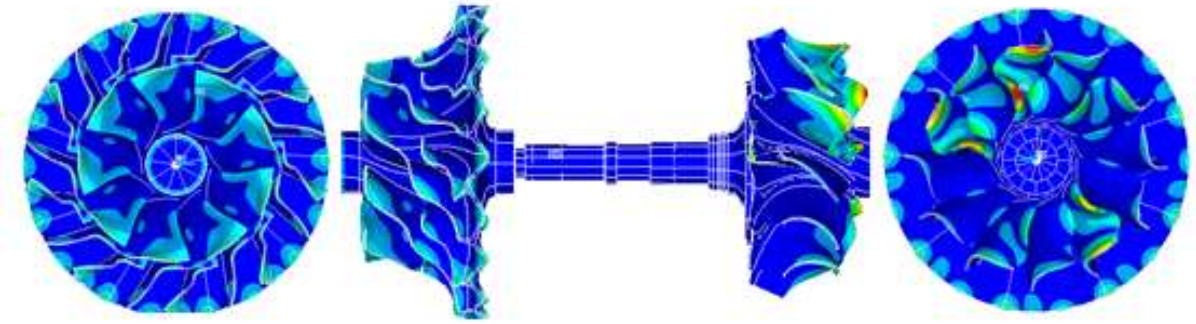

Figure 8.33: Mode 139, with dominant ND 5 on the turbine, 9.197 kHz, AR = 10.3

To this end, we can plot the parameter $DFT(ND0\&1)^{(eqv)}$, defined in Equations (7.8) to (7.10), on the x-axis. This parameter quantifies the equivalent contributions of nodal diameters 0 and 1 in the nodal diameter spectrum, which are key indicators of coupling strength. On the y-axis, we plot the coupling degree, represented as log(AR), where AR stands for the amplitude ratio. This relationship is illustrated in Figure 8.34.

The diagram reveals a clear general trend: as the contributions of nodal diameters 0 and 1 ($ND0$ and $ND1$) increase in the spectrum, log(AR) approaches 1. This trend indicates that higher contributions of these nodal diameters correspond to stronger coupling between the rotor's components. Specifically, the ND0 component reflects torsional coupling effects, while the ND1 component is associated with bending coupling mechanisms. The presence of these components in the spectrum highlights the dominant modes through which energy is transmitted and shared between the two rotors.

This observation aligns well with the results from the reference mistuned case. In both scenarios, it can be inferred that the majority of coupled modes are a consequence of the residual $ND0$ or $ND1$ components in the nodal diameter spectrum. This suggests that the coupling mechanisms are predominantly influenced by these components, and this behavior appears to be consistent.

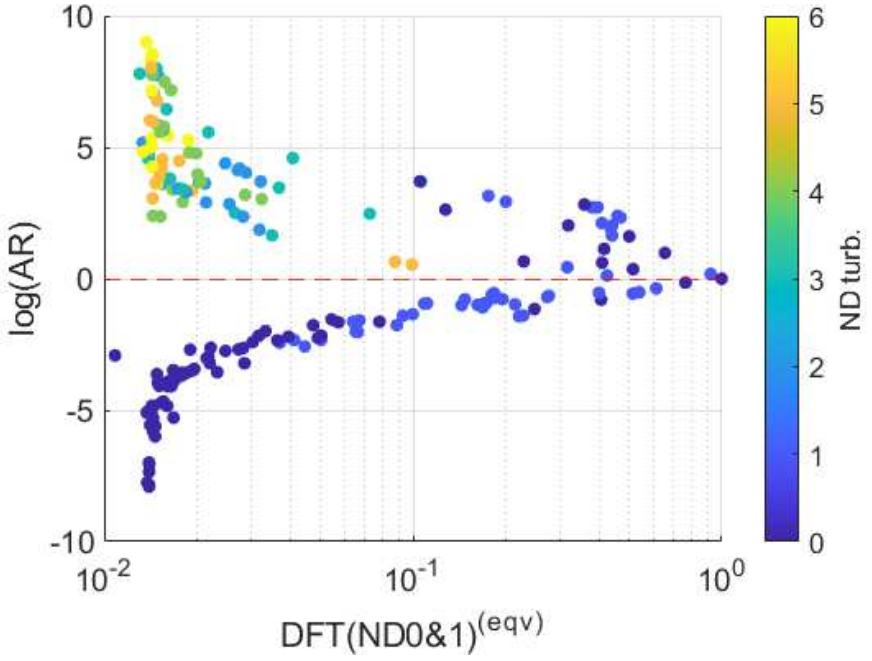

Figure 8.34: Diagram of $DFT(ND0\&1)^{eqv}$ and log(AR) for BM4 EO17 mistuned modes in the frequency range [0,18] kHz

8.2.2 BM5 EO24 Intentional mistuning

In order to mitigate the effects of random mistuning due to material inhomogeneities, uneven wear and other causes, one strategy is to implement an artificial, intentional mistuning with much larger amplitude. This has been proven in [5] to reduce mode localization and intensification. The mistuning pattern is designed to minimize mode localization of the first blade mode family. The intentional mistuning pattern is usually a periodic function. It is implemented on the turbine by removing small quantities of material (tip cropping, trailing edge machining).

It is observed in Fig. 8.35 with the harmonic pattern, and a smaller uncertainty in the frequency measurement, due to the fact that the intentional mistuning has a large amplitude, and the mistuned modes are sufficiently spaced in frequency. Due to this in the BTT results peaks are quite stable.

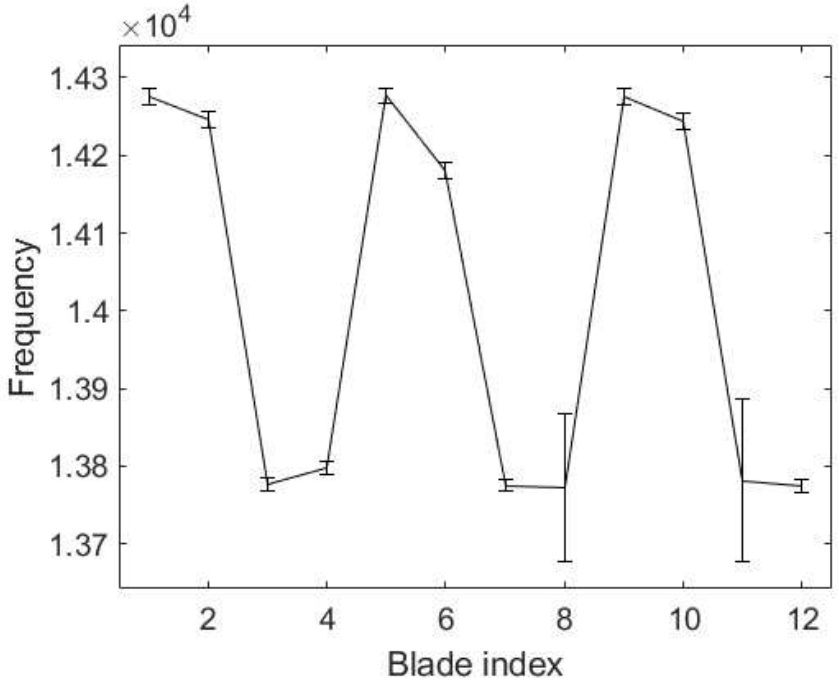

Figure 8.35: Plot of the blades frequencies measured with the Blade Tip timing technique for the intentionally mistuned BM5 EO24 Mode

In the figure 8.38 we observe the variation in terms of AR and frequency compared to the reference mistuned case. As expected, the low frequency modes (rigid and gyroscopic) are not very sensitive to the level of mistuning. For other modes, the mode coupling level changed in both directions. Unlike the previous case, the compressor-leading modes are also slightly shifted due to the level of mistuning. This is likely due to the fact that the level of intentional mistuning brings large variations in stiffness of the blades.

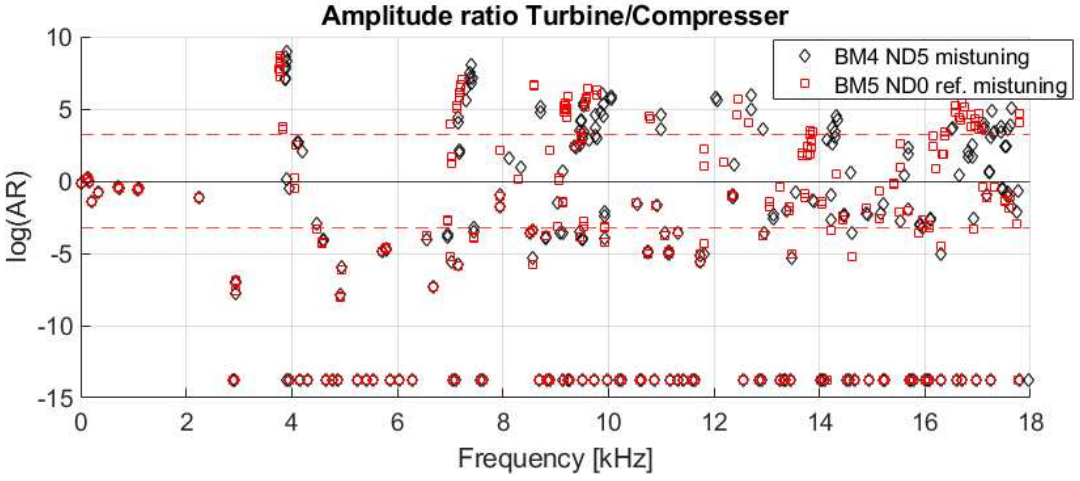

Figure 8.36: Frequency vs Amplitude ratio plot for the IM mistuned case in the frequency region [0,18] kHz and comparison with reference mistuned case

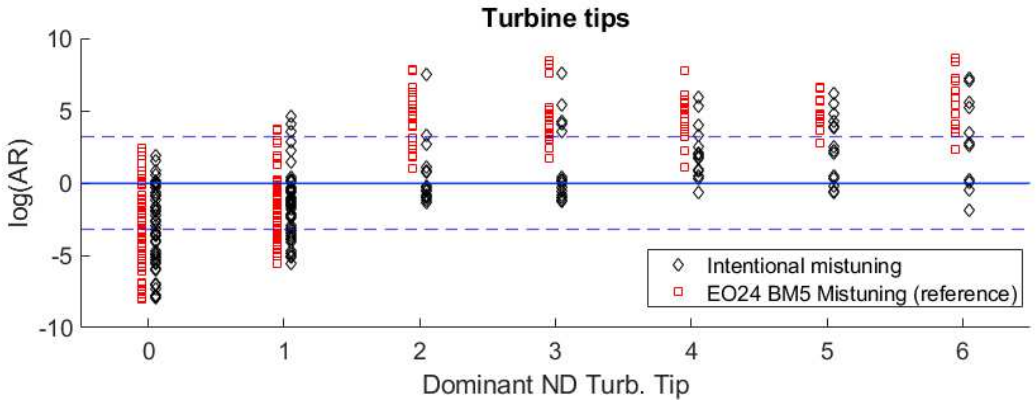

Figure 8.37: Amplitude ratio vs Turbine dominant Nodal Diameter plot for the IM mistuned modes in the frequency region [0,18] kHz

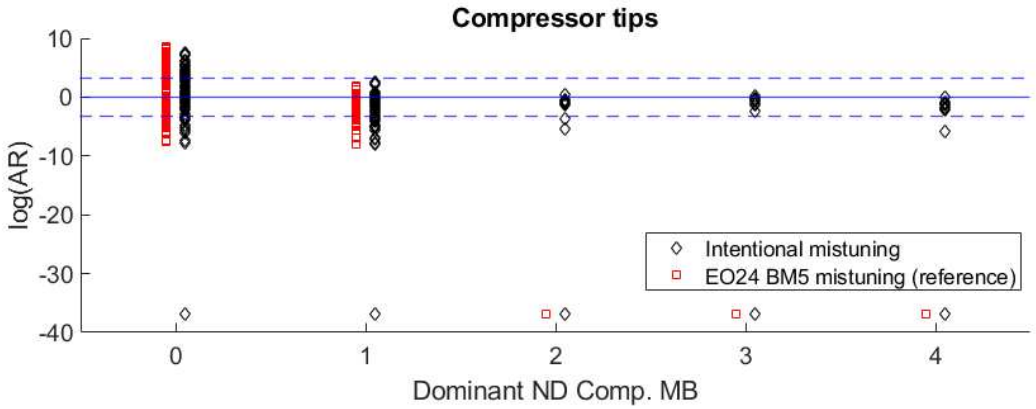

Figure 8.38: Amplitude ratio vs Compressor MB dominant Nodal Diameter plot for the IM mistuned modes in the frequency region [0,18] kHz

Figure 8.39 shows the comparison between the Amplitude Ratio of Reference mistuning case and Intentional mistuning case. It is possible to see that the increase in the degree of coupling is limited to modes expressed primarily on the turbine with nodal diameter higher than 1.

Comparison of mode shapes with the MAC criterion shows a very high degree of similarity between the mode shapes in Fig. 8.40. On the diagonal, modes evaluate to AR close to 1, Fig. 8.41.

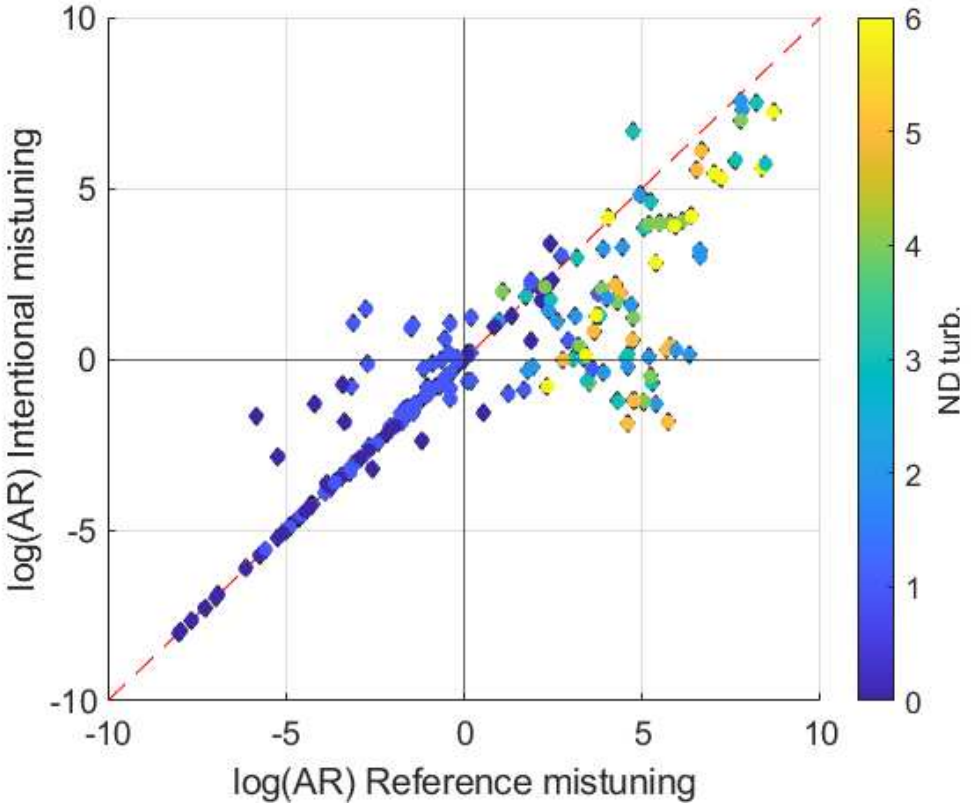

Figure 8.39: Comparison of Amplitude ratio in reference mistuned case and intentional mistuning

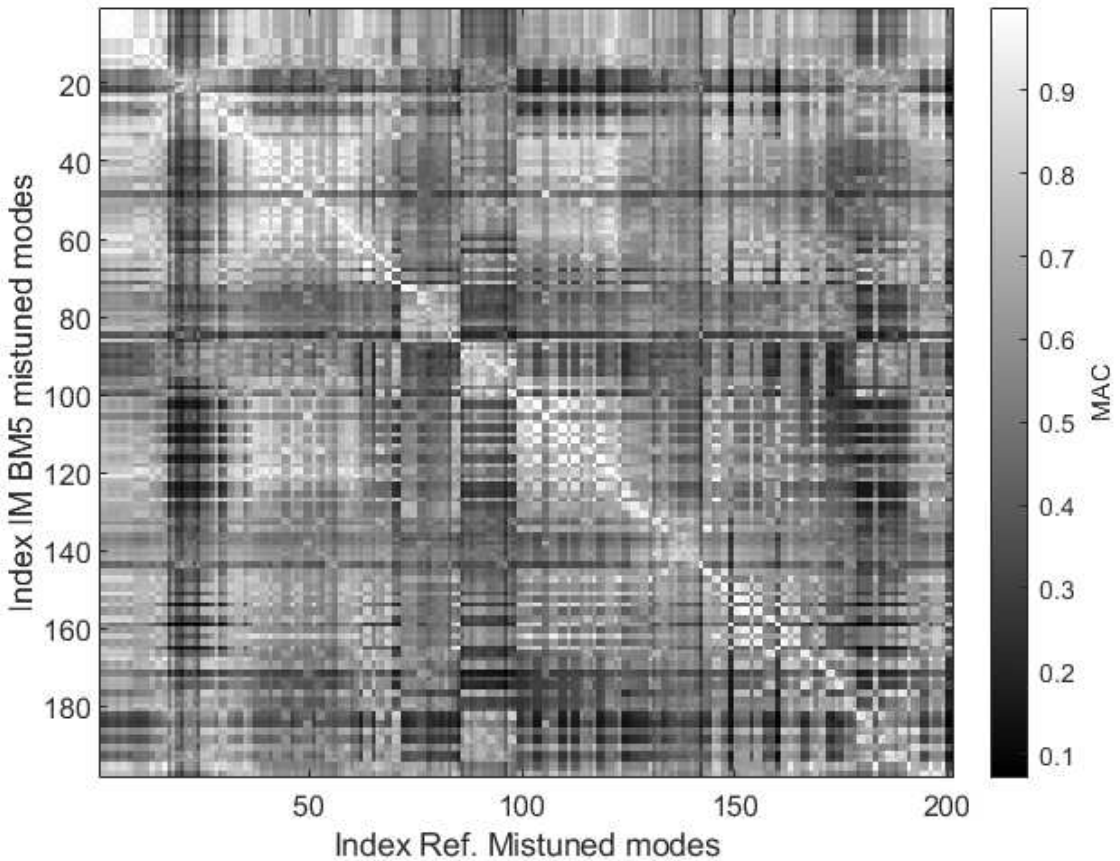

Figure 8.40: Modal assurance criterion table between mode shapes evaluated in turbine tip

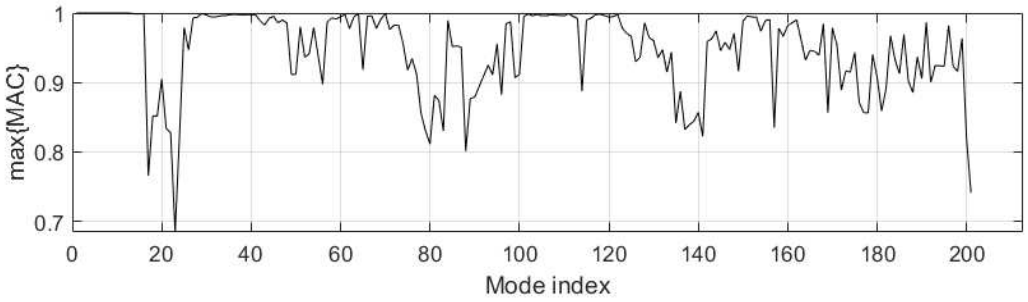

Figure 8.41: Modal assurance criterion table between mode shapes evaluated in turbine tip nodes for the IM mistuned modes and reference mistuned case

In the case with intentional mistuning, an abnormally high number of coupled modes with nodal diameters greater than 1 is observed. We repeat the analysis presented in Chapter 7 using the standard methods to understand the reason behind this large number of coupled modes. Figure 8.42 shows the log(AR) - $DFT(ND0\&1)^{(eqv)}$ plot. Once again, we observe the usual trend of log(AR) approaching 0 as the contributions of ND0 and ND1 components in the nodal diameter spectrum increase. However, a larger number of outlier modes is present.

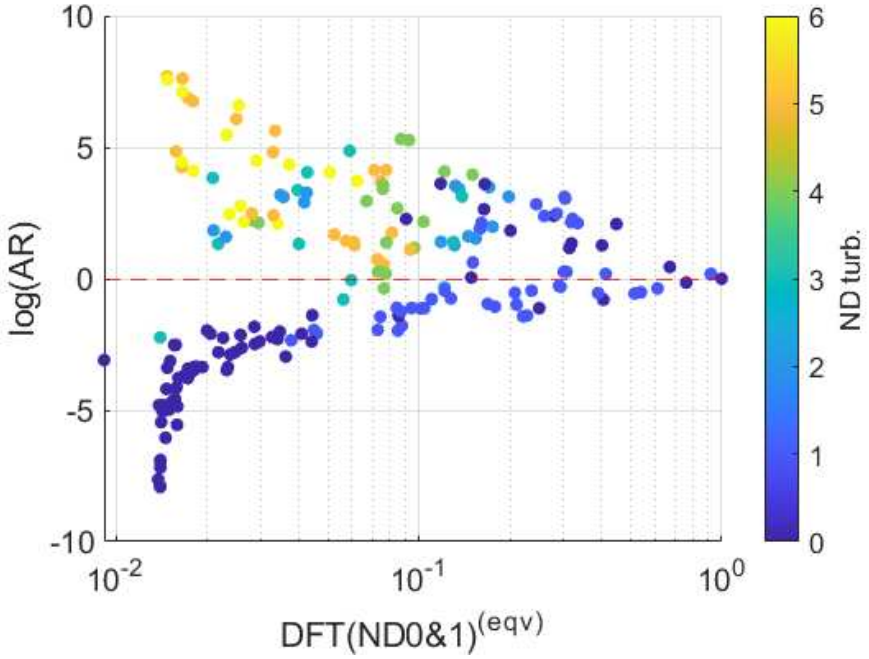

Figure 8.42: Diagram of $DFT(ND0\&1)^{eqv}$ and log(AR) for BM4 EO17 mistuned modes in the frequency range [0,18] kHz

The increase in coupled modes can be partially explained by higher values of DFT components 0 & 1, as shown Figure 8.43. It is possible to see that the majority of modes intentionally mistuned in the $DFT(ND0\&1)^{eqv}$, which takes

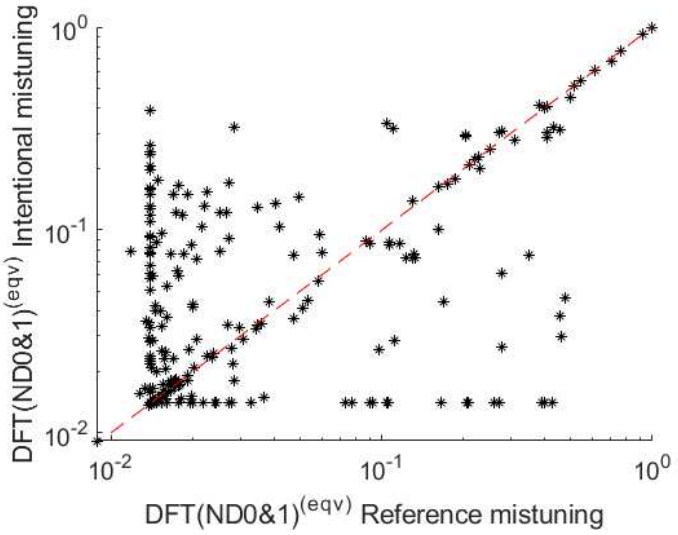

Figure 8.43: Comparison of the amplitude of ND0&1 components in the NDS of Reference mistuning (x-axis) and Intentional mistuning (y-axis)

At the same time, intentional mistuning with high intensity further separates the various resonance frequencies of the turbine, increasing the likelihood of turbine eigenvalues being very close in frequency to compressor eigenvalues. Figure 8.44 shows a comparison of the proximity of turbine and compressor eigenvalues for each given frequency among the tuned, reference mistuned, and intentional mistuned cases. It is evident that intentional mistuning significantly increases the proximity of turbine and compressor eigenvalues for certain frequencies.

The proximity in frequency allows for the merging of compressor and turbine modes, provided there is even a small residual ND0 or ND1 component in the Nodal Diameter Spectrum (NDS), creating a new coupled mode.

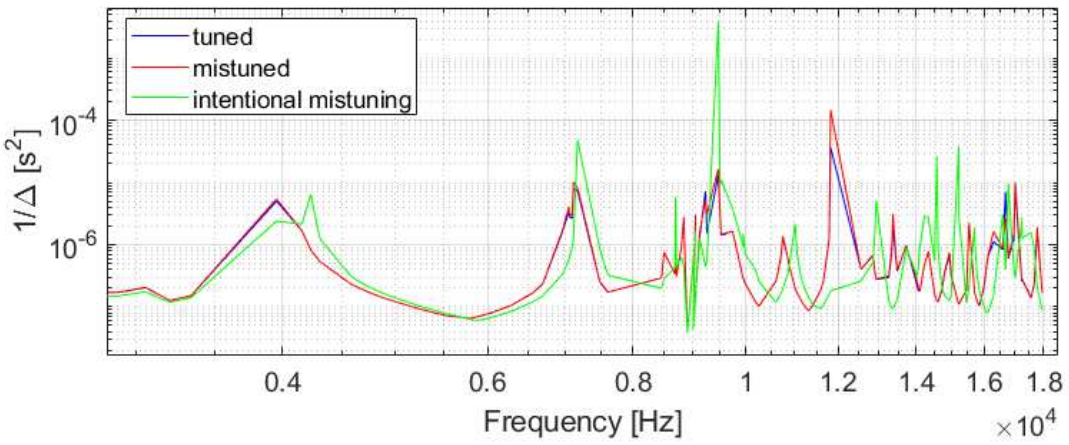

Figure 8.44: Comparison of the eigenvalue proximity, of turbine and compressor eigenvalues, for tuned case, reference mistuned case, intentional mistuning case

This phenomenon, together with the increase in residual ND0 and ND1 components in the Nodal Diameter Spectrum (NDS), helps explain the large number of coupled modes for ND> 1 on the turbine, caused by intentional mistuning.

8.3 Both sides mistuned

In this section a mistuning is introduced also in the compressor. Given the lack of experimental data, it is not possible to implement the procedure explained in 5. Instead, on the compressor we apply a randomly generated mistuning. For the generation of this mistuning we base on the estimation that states mistuning on the compressor has half the amplitude of the amplitude on the turbine. In the first place, the percentage of mistuning on the turbine is computed as the ratio between the frequency of a blade and the mean. The percentage of mistuning in the compressor is generated as a Gaussian random number with half the standard deviation of mistuning on the turbine. This mistuning is applied equally in the Main blades as in the Splitter blades.

Table 8.1: Mistuned Young Modulus values implemented on compressor blades

Sect N°	Main Bl., Young Modulus [MPa]	Sp. Bl., Young Modulus [MPa]
1	71301.30	70628.86
2	71141.65	71052.37
3	70785.14	71056.29
4	71587.93	71455.02
5	70778.21	71498.64
6	71119.18	70989.64
7	71117.43	70966.32
8	70979.60	71244.75
9	71231.5	71232.84

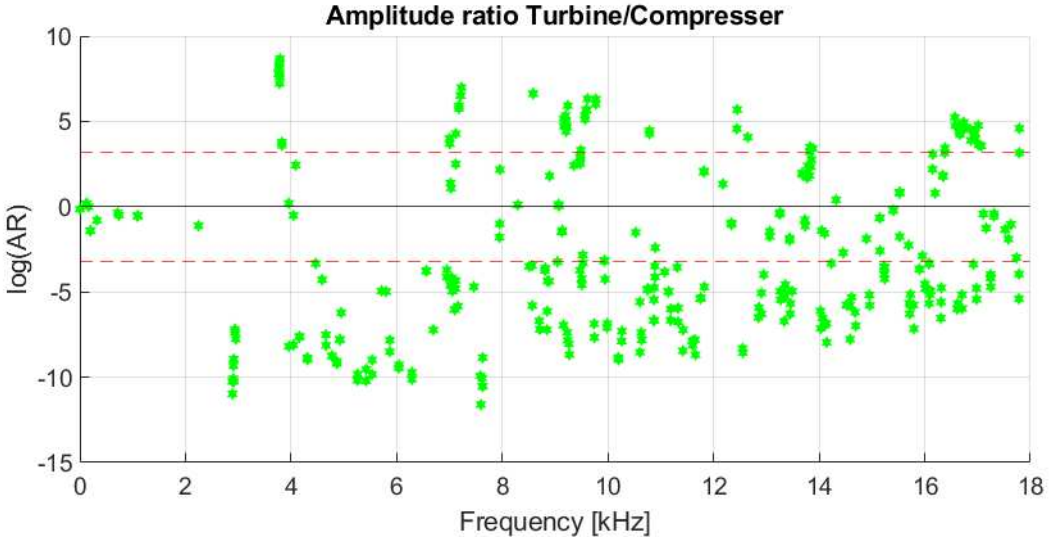

Figure 8.45: Frequency vs Amplitude ratio plot for the modes of mistuned compressor and turbine case in the frequency region [0,18] kHz

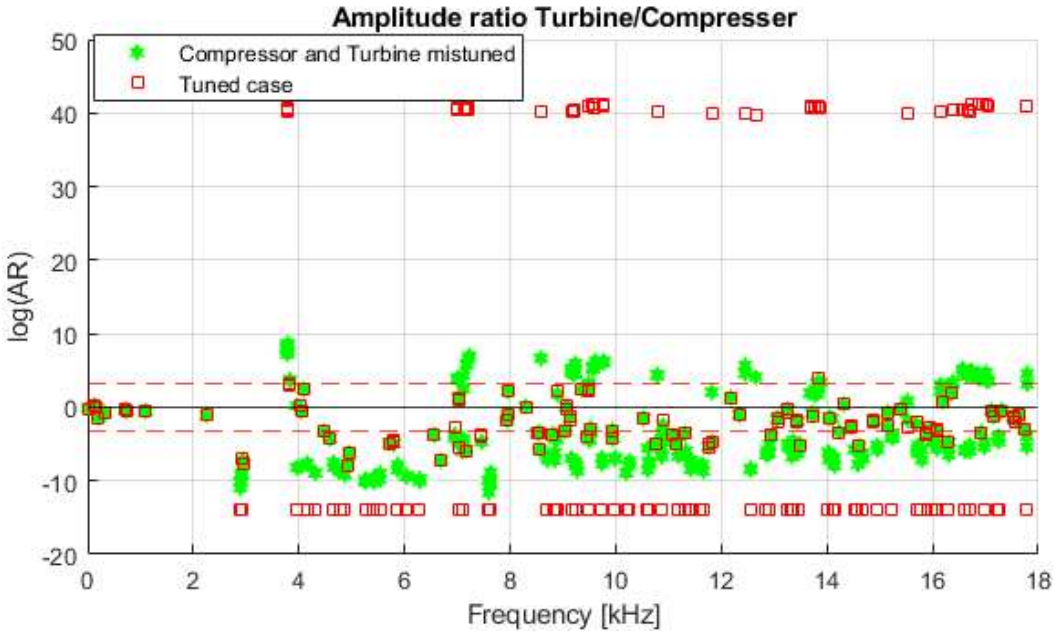

Figure 8.46: Frequency vs Amplitude ratio plot for the mistuned compressor and turbine case as well as the tuned case in the frequency region [0,18] kHz

Figure 8.45 shows the frequency vs. amplitude ratio diagram for the modes in the case with both rotors mistuned. We note how, compared to the figures 6.1 and 6.5, compressor-dominated modes increase the degree of coupling. Furthermore, there are no longer any modes that have zero participation on one of the two bladed sets. In the most localized modes on one of the two rotors there is at most an Amplitude Ratio of 125000. There is a moderate increase in the number of coupled modes, which in the frequency region [0.18] kHz amounts to 93 modes.

In the figure 8.47 the modes of the case with both rotors mistuned are compared with the case with both rotors tuned. In particular, we note the interesting result that there is a correspondence between modes of the two cases in the region of the most coupled modes. In this region, the introduction of mistuning on the compressor does not change the degree of rotor coupling. What changes instead, observing the lower part of the diagram, are the modes which in the case of tuned rotors were extremely compressor-dominated in the mistuned case they move towards the coupled region.

The same binary behaviour is observed in Fig. 8.47 and 8.48 , which show the comparison of the Amplitude Ratios of the Both sides mistuned modes and the Both sides tuned modes. Comparison of modes is possible by associating tuned and mistuned modes by frequency proximity, since mistuning does not significantly alter the eigenvalues. It is observed that the modes are fundamentally divided into two sets: one in which the tuned AR is already close to 1, the mistuning does not increase the degree of coupling, the other set for which the mistuning causes a

substantial approach of the AR to 1 For this last group, high nodal diameters are mainly observed on the turbine.

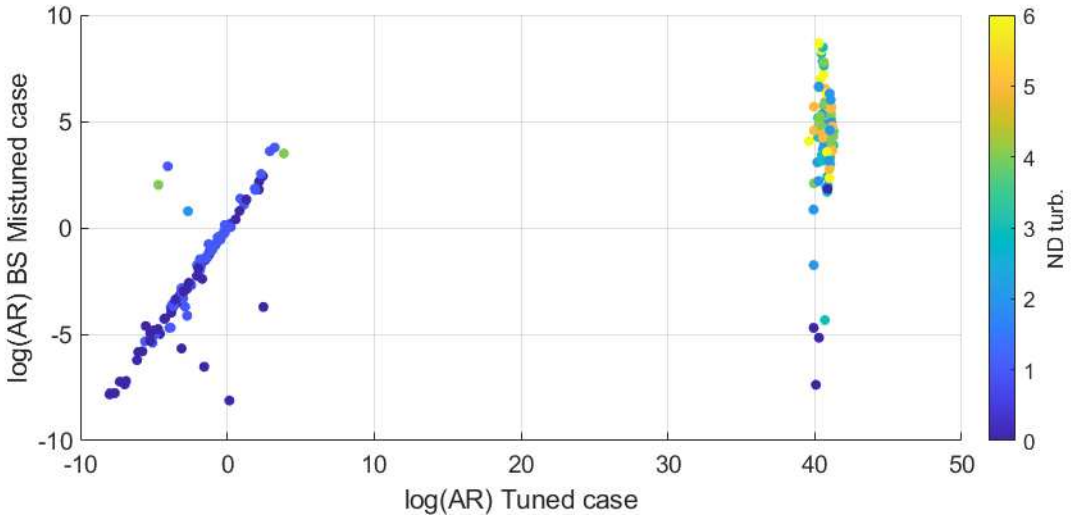

Figure 8.47: Comparison between Amplitude ratio of the Tuned modes and the Amplitude ratio of the both sides mistuned modes. Color represents the dominant nodal diameter in the turbine

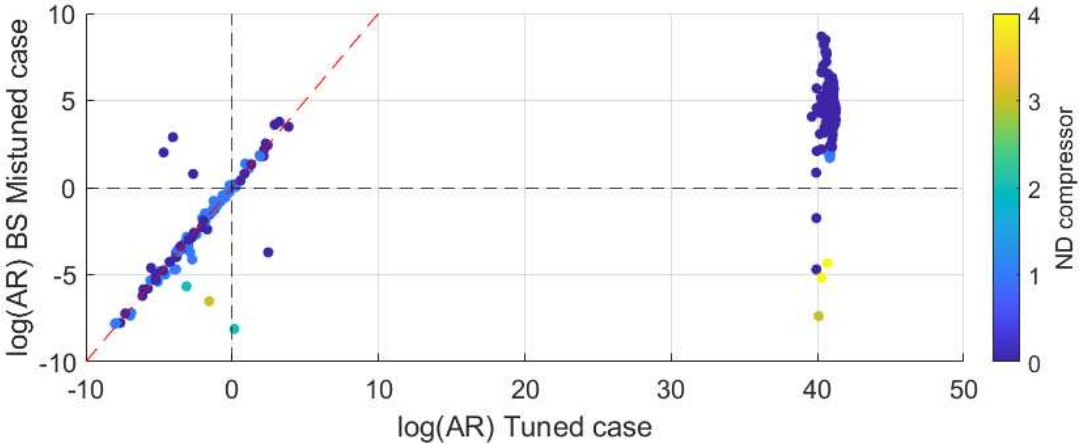

Figure 8.48: Comparison between Amplitude ratio of the Tuned modes and the Amplitude ratio of the both sides mistuned modes. Color represents the dominant nodal diameter in the compressor

It can be seen in Fig. 8.47 that the new modes that become coupled due to mistuning have, if turbine-leading, a high number of nodal diameters on the turbine. Similarly, the new compressor-leading coupled modes that arise due to mistuning exhibit a high number of nodal diameters on the compressor.

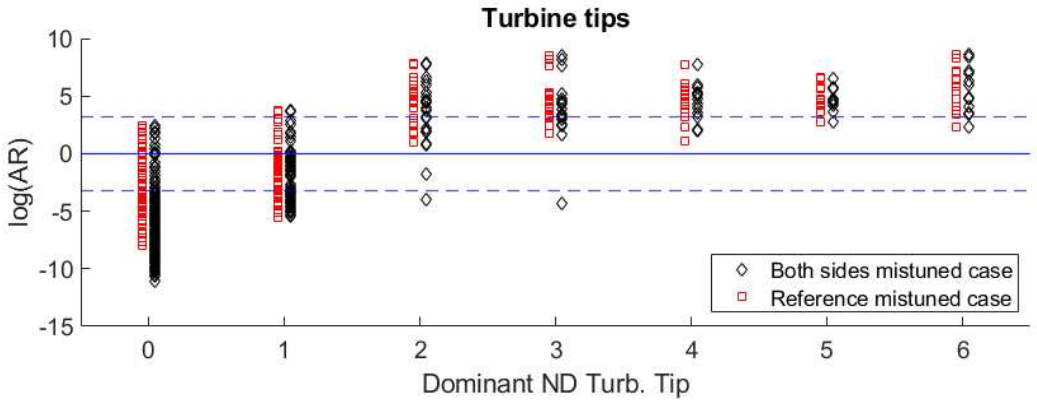

Figure 8.49: Comparison between Amplitude ratio of the Tuned modes and the Amplitude ratio of the both sides mistuned modes. Color represents the dominant nodal diameter in the compressor

Figures 8.49 and 8.50 show the Amplitude Ratio of the modes with dominant nodal diameter on the turbine and dominant nodal diameter on the compressor. Figure 8.49 shows that mistuning on the compressor has an influence, albeit localized to a few modes, on the nodal diameter. Specifically, three modes, with dominant nodal diameters of 2 and 3, shift from being turbine-dominated to compressor-dominated. Additionally, there is a general shift of modes with dominant nodal diameter 0 toward greater participation from the compressor.

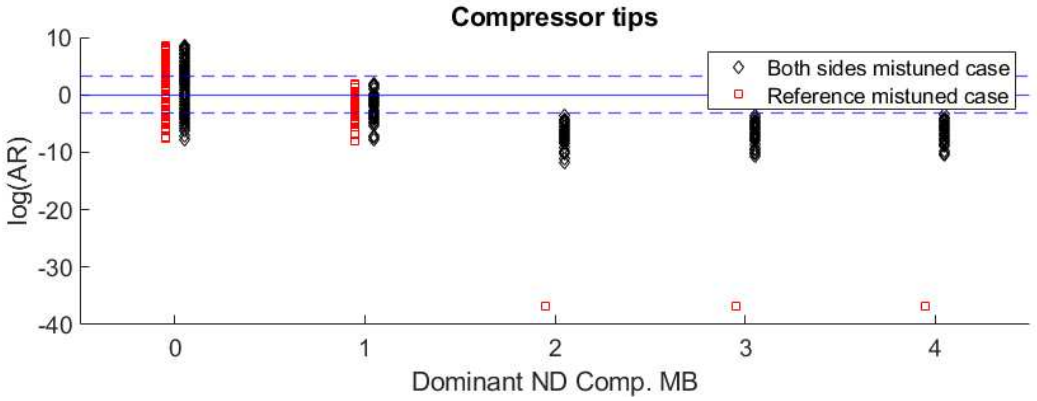

Figure 8.50: Amplitude ratio vs Turbine dominant Nodal Diameter plot for the modes of both sides mistuned case in the frequency region [0,18] kHz

In Figure 8.50, the shift of all modes with ND > 1 on the compressor toward a higher degree of coupling is confirmed.

Comparing the mode shapes of the turbine with those of the tuned compressor, using the MAC criterion (Fig. 8.51 8.52), we observe slight variations in some mode shapes, resulting in MAC values as low as 0.9. This indicates that mistuning in the compressor affects certain modes on the turbine side.

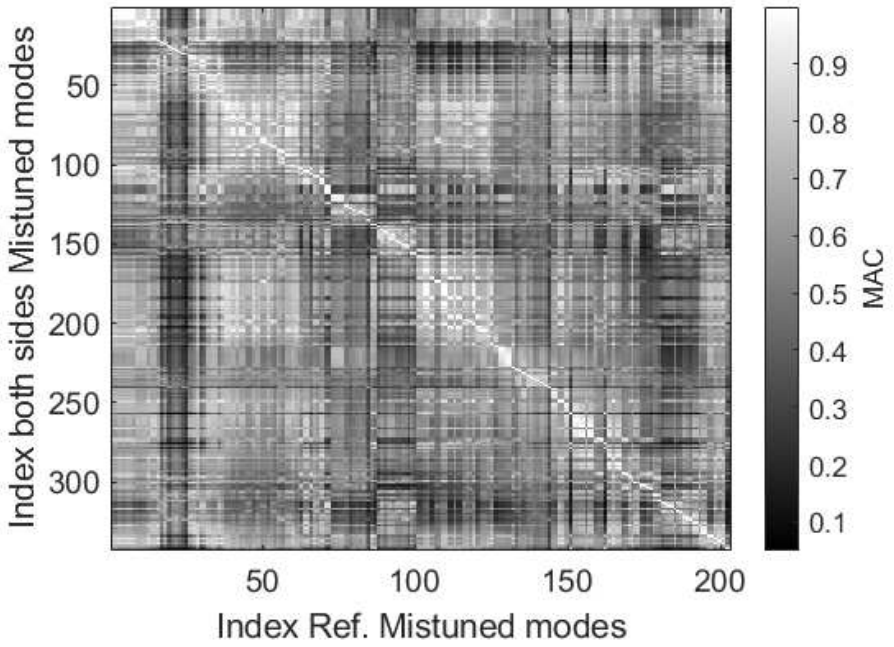

Figure 8.51: Modal assurance criterion table between mode shapes evaluated in turbine tip nodes for the both sides mistuned modes and reference mistuned case

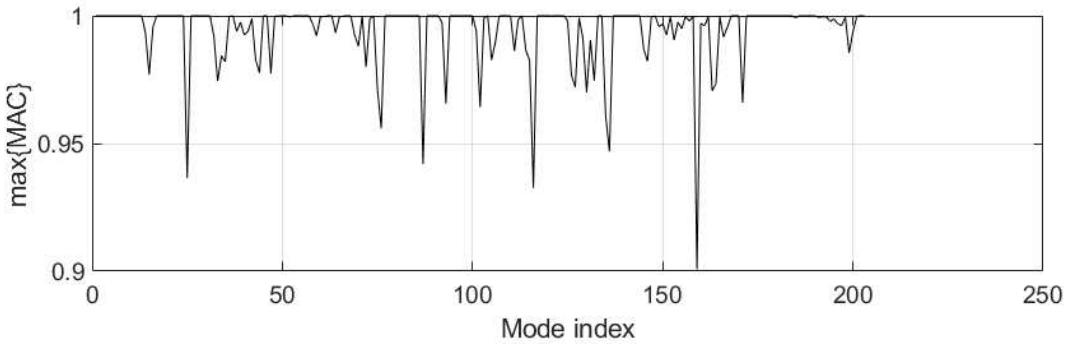

Figure 8.52: Modal assurance criterion table between mode shapes evaluated in turbine tip nodes for the both sides mistuned modes and reference mistuned case

8.4 Effect of rotating damping

Rotating damping is introduced in the reference configuration. The damping value is calculated based on all measurements at resonance points for the BM5 ND0 mode. Rotational pressure is introduced through the rotor strut structure by implementing a proportional pressure matrix based on the stiffness, as shown in Eq. (8.3).

$$[C_r] = \beta \cdot [K] \tag{8.3}$$

The resonance peaks of the BM5 ND0 mode show a mean damping ratio of $\zeta = 0.07$. Therefore, the scalar gain for proportional damping β can be calculated using Eq. (8.4) [19]. We introduce structural damping, attributing all sources of damping to this term.

$$\beta = \frac{2\zeta}{\bar{\omega}} = \frac{2 \cdot 0.0764}{13781 Hz} = 1.11 \times 10^{-5} \tag{8.4}$$

By introducing damping into the equation and running a prestressed modal analysis with the damped solver, a set of modes and eigenvalues is obtained.

The mode shapes and eigenvalues do not change significantly compared to the reference case. The variation in frequency (imaginary part) between corresponding modes is less than 0.001 Hz. The mode shapes are also very similar. As shown in the MAC table 8.53, the diagonal values are either 1 or very close to 1 for all modes. In 8.54, the MAC values of each damped mode are compared with the most similar corresponding modes from the reference case.

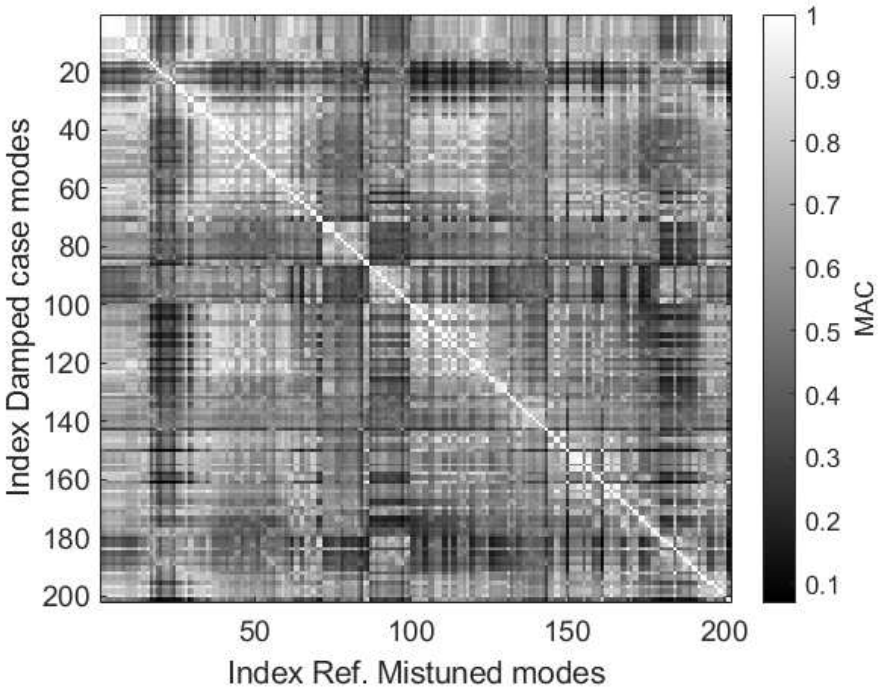

Figure 8.53: Modal Assurance Criterion table for reference and damping case.

Furthermore, it is possible to compare the amplitude ratios of the modes. In Fig. 8.56, each dot represents a mode. The x-axis shows the log(AR) values for the reference case, while the y-axis shows the log(AR) values for the damped case. It can be observed that most of the modes are clustered along the $X = Y$ red dotted line.

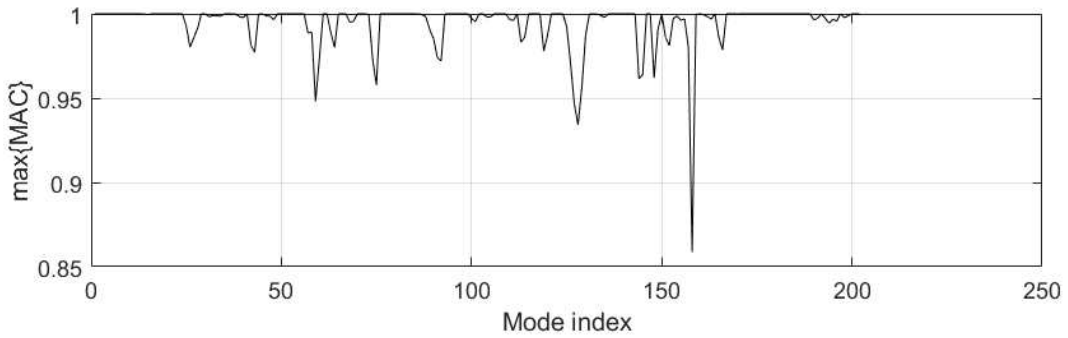

Figure 8.54: Maximum MAC value for each damped mode compared to the reference case.

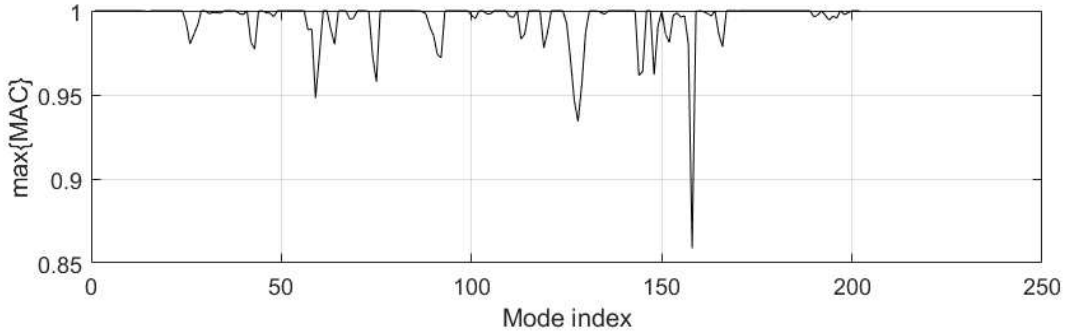

Figure 8.55: Maximum MAC value for each damped mode compared to the reference case.

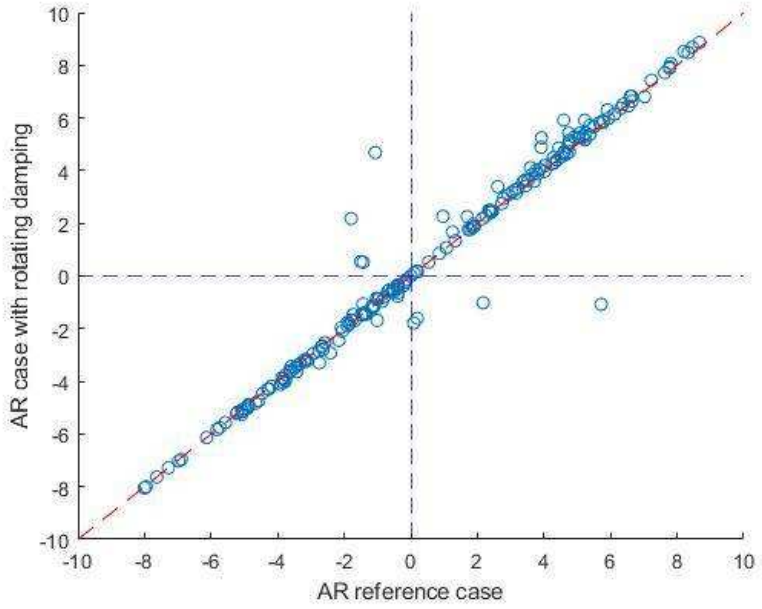

Figure 8.56: Comparison between the amplitude ratio in the reference case (x-axis) and the amplitude ratio in the case with damping.

9 Conclusion

In this thesis the linear modal analysis of a mistuned radial impeller was carried out using finite element models. The bearings were modeled as approximate linear stiffness and damping, using confidential values provided by the manufacturer. Centrifugal pre-stress and spin softening were considered, as well as the gyroscopic effect. Structural damping was instead considered only in a final case study, which demonstrated its negligible effect. However, in this thesis the effect of aerodynamic forces has been neglected, which must be calculated with CFD. The aerodynamic forces cause coupling between the blades, but this is known to be significantly weaker than the structural coupling.

It has been demonstrated through abundance of examples that implementation of mistuning causes the existence of coupled turbine-compressor modes that have dominant nodal diameter > 1. This physical mechanism arises from the asymmetry of mistuned mode shapes. Due to mistuning, blades carry residual torsional or bending momentum (associated to ND0 and ND1 respectively) in modes where ND > 1 is dominant. More in detail, residual axial ND0 components are associated to thrust, tangential ND0 is associated to torsion and ND1, bot axial and tangential is associated to bending of the rotor. This mechanism is demonstrated by the AR diagram with an equivalent parameter that sums the axial and tangential ND0 and 1 components expressed on the turbine. The trend shows the AR converging to 1 as the ND0 and ND1 components increase. There is, however, a considerable number of outliers, especially on the side of the turbine-dominated modes. In these outliers a high degree of coupling occurs despite very low 0 and 1 components.It has been noted that these coupled *outlier* modes are the superposition of two tuned modes, one expressed mainly on the compressor and one expressed mainly on the turbine. These modes, very close in frequency, merge due to mistuning to form a coupled mode. Proximity in frequency alone does not explain the merging of the modes; mechanical interaction is also necessary. In order to better understand the phenomenon of the merging of these modes, the model is dissected into two subsystems, each subjected to modal analysis under free-interface conditions. The theoretical Impedance Coupling technique is then adopted to mathematically couple the two models.

- It has been shown that proximity in frequency favors the coupling between turbine and compressor modes
- It was observed that the mistuning applied on the turbine model modifies the mode at the turbine-shaft interface giving rise to interaction between the two subsystems

The sensitivity analysis with respect to bearing conditions introducing mistuning confirms the results of the paper by Zobel et al. As in the paper, more coupled modes with low stiffness values are observed, and fewer coupled modes with high stiffness values

- for low values of bearing stiffness the shaft behaves as a rigid rigid body, and its modes resemble rigid-body behavior, making them more coupled, with AR values approaching 1.
- for high stiffness values, the modes are primarily localized to one side of the bearing, with AR values diverging to infinity.

There is a transition zone, which is expressed at average stiffness values. For axial bearings, this transition occurs at gain values between 10^3 and 10^5. For radial bearings it is expressed at lower values, as radial bearings are already much stiffer.

Furthermore, mistuning was introduced in the compressor, revealing that more modes predominantly expressed on the compressor tend to approach the coupled region. Finally, the structural damping effect was introduced in terms of damping proportional to the stiffness matrix, assuming all system damping effects are solely attributable to this effect. However, modal analysis results show that the overall effect of structural damping on the dynamic response of the system is negligible.

A future development is to introduce aerodynamic coupling effects, which would increase blade-to-blade coupling and allow observation of how this affects the presence of coupled modes. Furthermore, by computing the aerodynamic forces acting on the blades with stationary CFD analysis, it is possible to compute the forced response of the modes. Forced response analysis allows comparison of the signals measured with BTT with the results of the FEM model. Furthermore, this would allow us to predict the effect of mistuning on the amplitude magnification which in turn allows prediction of the loads on the individual blades for any mistuning pattern.

A further important development, in order to improve understanding of mistuning's impact on impeller dynamics is the creation of a bladed assembly Reduced Order Model of moderate complexity. In fact, the 1-DOF per sector and 2-DOF per sector models are based on too simplified assumptions and do not allow an accurate description of a real bladed assembly. At the same time, the models used in this thesis, consisting in the order of $\approx 10^6$ nodes, demand significant computational resources and time, and do not allow the immediate extraction of conclusions in exact mathematical terms. In section 8.1.3 a shaft model with 3D beam elements was presented, in which the turbine and compressor are modeled as rigid masses. A moderately complex bladed assembly ROM can be created using substructuring techniques ([26]) to integrate with the simplified shaft model.

10 Evaluation Toolbox Documentation

10.1 Preliminaries

Two matlab files need to be created for a new model in order to use the toolbox, for each new model:

- **Node coordinate table**, a table of size [NN x 4] (NN number of nodes) that contains on the columns the sequential indexes and X,Y,Z coordinates of the model.
  It contains, on the first column the ANSYS indexes of the nodes of the model.
  On column 2 are the X coordinates of the nodes of the model
  On column 3 are the Y coordinates of the nodes of the model
  On column 4 are the Z coordinates of the nodes of the model

- Eventually, for each named selection a **named selection table** must be created, a table containing on each row the indeces of the nodes on the named selection. In case of multiple instances (e.g. blade tips) many rows can be pasted next to each other in the table. Node indexes are exported from Ansys named selection.

10.2 APDL snippet for eigenvector extraction

These few lines are needed in order to extract the results of pre-stressed modal analysis on the working folder. Eigenvectors are imported on the folder as text files. One file is created for each mode.

The snippet must be pasted in the input file, right after the introduction to the /POST1 environment of the modal analysis.

```
/POST1

*GET,knotenanzahl,NODE,0,COUNT
*GET,modenanzahl,ACTIVE,0,SOLU,NCMSS

k=1
*DIM,Matrix,ARRAY,knotenanzahl,7
SET,,k
```

```
    *VFill,Matrix(1,1),RAMP,1,1
    *VGET,Matrix(1,2),NODE,1,U,X
    *VGET,Matrix(1,3),NODE,1,U,Y
    *VGET,Matrix(1,4),NODE,1,U,Z
    *VGET,Matrix(1,5),NODE,1,LOC,X
    *VGET,Matrix(1,6),NODE,1,LOC,Y
    *VGET,Matrix(1,7),NODE,1,LOC,Z

    a = k
    *CFOPEN,Eigenvektor_Mode%a%,txt,'/rwthfs/rz/cluster/hpcwork/rwth1562/pietro/
TC-Coupling/COUP11',APPEND

*VWRITE,Matrix(1,1),Matrix(1,2),Matrix(1,3),Matrix(1,4),Matrix(1,5),Matrix(1,6),Matrix(1,7)
    (F10.4,F10.4,F10.4,F10.4,F10.4,F10.4,F10.4)
    *CFCLOS

    *DO,k,1,modenanzahl,1
    *DIM,Matrix,ARRAY,knotenanzahl,7
    SET,,k
    *VFill,Matrix(1,1),RAMP,1,1
    *VGET,Matrix(1,2),NODE,1,U,X
    *VGET,Matrix(1,3),NODE,1,U,Y
    *VGET,Matrix(1,4),NODE,1,U,Z
    *VGET,Matrix(1,5),NODE,1,LOC,X
    *VGET,Matrix(1,6),NODE,1,LOC,Y
    *VGET,Matrix(1,7),NODE,1,LOC,Z

    a = k+1

*CFOPEN,Eigenvektor_Mode%a%,txt,'/rwthfs/rz/cluster/hpcwork/rwth1562/pietro/TC-Coupling
/COUP11',APPEND

*VWRITE,Matrix(1,1),Matrix(1,2),Matrix(1,3),Matrix(1,4),Matrix(1,5),Matrix(1,6),Matrix(1,7)
    (F10.4,F10.4,F10.4,F10.4,F10.4,F10.4,F10.4)
    *CFCLOS
    *ENDDO
```

10.3 Matlab function `extractSolu`

The function extractSolu extracts data from the eigenvector text files generated with the Ansys APDL snippet and uploads them on Matlab creating a **solution table**, a structure containing all the eigenvectors of the full model. It is the most time- and computationally expensive phase

of the evaluation toolbox. Uploading time, for full rotor model is around 10 seconds per mode.
`function extractSolu(rd, node_coords,stMode, endMode)`

- rd: [text string] path of the folder where eigenvector text files are located
- node_coords: [4xN] **Node coordinate table** of the model
- stMode: [1x1] index of the first mode user wants to import
- endMode:[1x1] index of the last mode user wants to import

```
    function solTable = extractSolu(rd, node_coords,stMode, endMode)
    for modeN = stMode:endMode
    filename =['Eigenvektor_Mode', num2str(modeN), '.txt']; %file name of the .txt
file
    fullpath = [rd, filename];
    while exist(fullpath, 'file') ~= 2 %checks if text file has already been
downloaded, otherwise loops pause and message
    pause(1);
    disp('waiting for file');
    end
    rawTable = readtable(fullpath);
    modenAnzahl = endMode-stMode;
    disp(['Mode ',num2str(modeN),' of ',num2str(modenAnzahl),' imported']);

    i = modeN;
    start_index=1;
    end_index = height(rawTable);

    solTable.(['Mode',num2str(i)]).NN =
table2array(rawTable(start_index:end_index,1));
    solTable.(['Mode',num2str(i)]).X =
table2array(rawTable(start_index:end_index,5));
    solTable.(['Mode',num2str(i)]).Y =
table2array(rawTable(start_index:end_index,6));
    solTable.(['Mode',num2str(i)]).Z =
table2array(rawTable(start_index:end_index,7));
    solTable.(['Mode',num2str(i)]).ux =
table2array(rawTable(start_index:end_index,2));
    solTable.(['Mode',num2str(i)]).uy =
table2array(rawTable(start_index:end_index,3));
    solTable.(['Mode',num2str(i)]).uz =
table2array(rawTable(start_index:end_index,4));
    solTable.(['Mode',num2str(i)]).GesamVerf =
sqrt((solTable.(['Mode',num2str(i)]).uz).^2 +
(solTable.(['Mode',num2str(i)]).uy).^2 +(solTable.(['Mode',num2str(i)]).ux).^2);
```

```
    disp(['Solution table for Mode ',num2str(modeN),' of ',num2str(modenAnzahl),'
created']); %display message for progress
    end
    end
```

The **Solution table** created with this function has the hierarchic form:

- Solution table
  - Mode N°
    - NN [NNx1] List of Ansys node numbers
    - X [NNx1] List of X node coordinates
    - Y [NNx1] List of Y node coordinates
    - Z [NNx1] List of Z node coordinates
    - ux [NNx1] List of x displacement component of nodes
    - uy [NNx1] List of y displacement component of nodes
    - uz [NNx1] List of z displacement component of nodes

10.4 Matlab function `reduceSol2NS`

This function reduces the full solution table to certain nodes expressed in a **vector of the named selection**.

`function redsolTable = reduceSol2NS(`*`solTable, NamedSelNN, nodeCoords,stMode, endMode)`*

- solTable: [structure] solution table created with `extractSolu`
- NamedSelNN: [NS x Z] **Named selection array** containing the Ansys node indexes of nodes of interest, NS node of interest, Z instances (blades)
- stMode: [1x1] index of the first mode user wants to import
- endMode:[1x1] index of the last mode user wants to import
- nodeCoords: [4xN] **Node coordinate table** of the model

```
    function redsolTable = reduceSol2NS(solTable, NamedSelNN, nodeCoords,stMode,
endMode)
    allNNs = nodeCoords(:,1); %node indexes (Ansys indexes)
    Z = width(NamedSelNN); %number of items
```

```
    %loop retrieving solutions from the full solution table
    for i=stMode:endMode
    for bladeN = 1:Z
    [~, indices] = ismember(NamedSelNN(:,bladeN), allNNs);

    redsolTable.(['Mode',num2str(i)]).(['Blade',num2str(bladeN)]).NN =
NamedSelNN(:,bladeN);
    redsolTable.(['Mode',num2str(i)]).(['Blade',num2str(bladeN)]).ux =
solTable.(['Mode',num2str(i)]).ux(indices);
    redsolTable.(['Mode',num2str(i)]).(['Blade',num2str(bladeN)]).uy =
solTable.(['Mode',num2str(i)]).uy(indices);
    redsolTable.(['Mode',num2str(i)]).(['Blade',num2str(bladeN)]).uz =
solTable.(['Mode',num2str(i)]).uz(indices);
    redsolTable.(['Mode',num2str(i)]).(['Blade',num2str(bladeN)]).X =
solTable.(['Mode',num2str(i)]).X(indices);
    redsolTable.(['Mode',num2str(i)]).(['Blade',num2str(bladeN)]).Y =
solTable.(['Mode',num2str(i)]).Y(indices);
    redsolTable.(['Mode',num2str(i)]).(['Blade',num2str(bladeN)]).Z =
solTable.(['Mode',num2str(i)]).Z(indices);
    redsolTable.(['Mode',num2str(i)]).(['Blade',num2str(bladeN)]).GesamVerf =
solTable.(['Mode',num2str(i)]).GesamVerf(indices);
    end
    disp(['Mode ', num2str(i), ' done']);
    end


    %for j=1:Z
    %    hold on;
    %    X =redsolTable.(['Mode',num2str(stMode)]).(['Blade',num2str(j)]).X;
    %    Y = redsolTable.(['Mode',num2str(stMode)]).(['Blade',num2str(j)]).Y;
    %    Z = redsolTable.(['Mode',num2str(stMode)]).(['Blade',num2str(j)]).Z;
    %scatter3(X,Y,Z); % activate plot for manual check on the named selection
points
    %end

    disp('Reduced solution table created');
    end
```

Structure of the **reduced solution table** is:

- Reduced solution table
  - Mode N°
    - Blade j
      - NN [NNx1] List of Ansys node numbers

- X [NNx1] List of X node coordinates
- Y [NNx1] List of Y node coordinates
- Z [NNx1] List of Z node coordinates
- ux [NNx1] List of x displacement component of nodes
- uy [NNx1] List of y displacement component of nodes
- uz [NNx1] List of z displacement component of nodes

10.5 Matlab function `AmpRat`

This function calculates the **Amplitude ratio** between the maximum value of total deformation of the mode shapes found on two reduced tables. It gives an error if the two reduced solution tables contain a different number of modes.
If for a mode the denominator (maximum total displacement on reduced sol. table B) is zero, to be able to compute a finite value the denominator is added to a value of 10^{-17}

```
function [AR, MaxA, MaxB] = AmpRat(redSolA, redSolB, stMode, endMode)
```

- AR: [NM x 1] Vector containing Amplitude ratio result
- MaxA, MaxB: [NM x 1] **Named selection array** Maximum values of the reduced solution tables A and B respectively, used to compute the amplitude ratio
- redSolA, redSolB: [structure] **reduced solution table** from function reduceSol2NS
- stMode: [1x1] index of the first mode user wants to process
- endMode:[1x1] index of the last mode user wants to process

```
    function [AR, MaxA, MaxB]  = AmpRat(redSolA, redSolB, stMode, endMode)

    %check if the two solTables have the same number of elements
    if (length(fieldnames(redSolA)) - length(fieldnames(redSolA)))^2>0
    disp('Error: The two structure do not contain the same number of fields');
    end

    Za = length(fieldnames(redSolA.(['Mode',num2str(stMode)]))); %return number of
blades A
    Zb = length(fieldnames(redSolB.(['Mode',num2str(stMode)]))); % return number
of blades B

    for mode = stMode:endMode
    ListA = []; %predefine lists
```

```
        ListB = [];
        for blade = 1:Za %scan all blades of redSolA and list deformations
        ListA = [ListA;
    redSolA.(['Mode',num2str(mode)]).(['Blade',num2str(blade)]).GesamVerf]; %list the
    total deformations of the mode
        end

        for blade = 1:Zb %scan all blades of redSolB and list deformations
        ListB = [ListB;
    redSolB.(['Mode',num2str(mode)]).(['Blade',num2str(blade)]).GesamVerf]; %list the
    total deformations of the mode
        end

        MaxA(mode-stMode+1) = max(ListA);
        MaxB(mode-stMode+1) = max(ListB);

        AR = MaxA./(MaxB+1e-17); % +1e-17 in order to give finite result
        end

        end
```

Two arrays: ListA and ListB are created to list the total deformation components on all the blades. Then out of these lists the maximum value is computed for each mode. Endly, the Amplitude ratio is computed.

10.6 Matlab function `four_decomp`

Executes the discrete Fourier transform over the blades for a reduced solution table. Output is a structure with the Fourier output in different forms. There are two options for executing the Fourier transform: over tangential or axial components. DFT is executed in parallel for all points on the blades' tips, for this reason it is important that the node on the blade tips have corresponding coordinates.

`function four_out = four_decomp(`*redsolTable, stMode, endMode, specifier*`)`

- redsolTable: [structure] **Reduced solution table** from the
- stMode: [1x1] index of the first mode user wants to process
- endMode:[1x1] index of the last mode user wants to process
- specifier: [text string] 't' for tangential component (default) , 'a' for axial component

```
        function four_out = four_decomp(redsolTable, stMode, endMode, specifier)
```

```
    %specifier = 'a', execute with the axial component of deformation
    %specifier = 't', execute with tangential component of deformation
    redSol = redsolTable;
    if strcmp(specifier,'a') ==1
    c =1;
    else
    c =0;
    end

    % 1. Sort the coordinates and displacement components in ascending X(axial
coordinate) order

    Z =length(fieldnames(redSol.(['Mode',num2str(stMode)]))); % retrieve number of
blades

    for mode = stMode: endMode
    for blade = 1:Z
    [Xcoord_sorted,sortIdx] =
sort(redSol.(['Mode',num2str(mode)]).(['Blade',num2str(blade)]).X);
    redSolsort.(['Mode',num2str(mode)]).(['Blade',num2str(blade)]).X =
Xcoord_sorted;
    redSolsort.(['Mode',num2str(mode)]).(['Blade',num2str(blade)]).Z =
redSol.(['Mode',num2str(mode)]).(['Blade',num2str(blade)]).Z(sortIdx);
    redSolsort.(['Mode',num2str(mode)]).(['Blade',num2str(blade)]).Y =
redSol.(['Mode',num2str(mode)]).(['Blade',num2str(blade)]).Y(sortIdx);
    redSolsort.(['Mode',num2str(mode)]).(['Blade',num2str(blade)]).ux
=redSol.(['Mode',num2str(mode)]).(['Blade',num2str(blade)]).ux(sortIdx);
    redSolsort.(['Mode',num2str(mode)]).(['Blade',num2str(blade)]).uy
=redSol.(['Mode',num2str(mode)]).(['Blade',num2str(blade)]).uy(sortIdx);
    redSolsort.(['Mode',num2str(mode)]).(['Blade',num2str(blade)]).uz
=redSol.(['Mode',num2str(mode)]).(['Blade',num2str(blade)]).uz(sortIdx);
    end
    end

    %Check: x coordinates must coincide between blades:
    for blade = 1:Z
    axcoords(:,blade) =
redSol.(['Mode',num2str(mode)]).(['Blade',num2str(blade)]).X;
    end
    if norm(diff(axcoords'))> 5e-4
    disp('Error: axial coordinates of the different features do not correspond.
Fourier decomposition can not be performed correctly with this geometry.');
    end
```

First, in order to compare different blades, it is needed to sort nodes by ascending axial coordinate. After sorting, it is checked whether X components of the nodes on different blades correspond. Successively, it is necessary to create an array suitable or the 'fft' function.

```
    for mode = stMode:endMode
    for blade = 1:Z
    x = redSolsort.(['Mode',num2str(mode)]).(['Blade',num2str(blade)]).X;
    y = redSolsort.(['Mode',num2str(mode)]).(['Blade',num2str(blade)]).Y;
    z = redSolsort.(['Mode',num2str(mode)]).(['Blade',num2str(blade)]).Z;
    ux = redSolsort.(['Mode',num2str(mode)]).(['Blade',num2str(blade)]).ux;
    uy = redSolsort.(['Mode',num2str(mode)]).(['Blade',num2str(blade)]).uy;
    uz = redSolsort.(['Mode',num2str(mode)]).(['Blade',num2str(blade)]).uz;
    hold on;
    %scatter3(x,y,z,'MarkerEdgeColor','k');
    hold on;
    %d = 0.002;
    %scatter3(x+ d*ux,y + d.*uy,z + d.*uz,'MarkerEdgeColor','b');
    %orient(:,blade)= imag(((y+uy)+1i.*(z+uz))./(y+1i.*z));
    %table.(['Mode',num2str(mode)])(blade,:) = sqrt(c.*ux.^2 + uy.^2
+uz.^2).*sign(orient(:,blade));
    table.(['Mode',num2str(mode)])(blade,:) = imag((y + uy + 1i.*(z + uz))/(y +
1i*z))*sqrt(y.^2 + z.^2).*(c-1) + c*ux;
    end
    end
```

Lastly, the FFT is executed and outputs are extracted:

```
    for mode = stMode:endMode

    four_out.(['Mode',num2str(mode)]).cmplxVals =
fft(table.(['Mode',num2str(mode)]));

    %sort in the correct order negative and positive ND
    if mod(Z, 2) ==0 %if number of blades is even
    cut = Z/2+1;
    else
    cut = Z/2+0.5; %if number of blades is odd
    end
    four_out.(['Mode',num2str(mode)]).cmplxVals =
[four_out.(['Mode',num2str(mode)]).cmplxVals(cut+1:end,:);four_out.(['Mode',num2str(mode)]).cmp

    four_out.(['Mode',num2str(mode)]).Mag =
abs(four_out.(['Mode',num2str(mode)]).cmplxVals);

    four_out.(['Mode',num2str(mode)]).Angle =
angle(four_out.(['Mode',num2str(mode)]).cmplxVals);
```

```
    [~,four_out.(['Mode',num2str(mode)]).DominantND] =
max(sum(four_out.(['Mode',num2str(mode)]).Mag')); %find for each mode the dominant
nodal diameter as where the absolute value of the fft is located

    if mod(Z, 2) ==0 %if number of blades is even
    four_out.(['Mode',num2str(mode)]).DominantND =
four_out.(['Mode',num2str(mode)]).DominantND- cut+1;
    else
    four_out.(['Mode',num2str(mode)]).DominantND =
four_out.(['Mode',num2str(mode)]).DominantND- cut;
    end



    %normalize the absolute value table
    for j = 1:length(ux)
    four_out.(['Mode',num2str(mode)]).MagNorm(:,j) =
four_out.(['Mode',num2str(mode)]).Mag(:,j)./(max(four_out.(['Mode',num2str(mode)]).Mag(:,j)));
    end

    %average result on the nodes of the same blade:
    four_out.(['Mode',num2str(mode)]).DFT =
mean(four_out.(['Mode',num2str(mode)]).Mag');
    four_out.(['Mode',num2str(mode)]).DFTnorm =
mean(four_out.(['Mode',num2str(mode)]).MagNorm');

    four_out.(['Mode',num2str(mode)]).Variation =
norm(diff(four_out.(['Mode',num2str(mode)]).MagNorm'));
    four_out.(['Mode',num2str(mode)]).bladePotrait =
table.(['Mode',num2str(mode)])';

    end

    end
```

Output of the structure is:

- Fourier output
  - Mode N°
    - `cmplxVals`: [ZxNS], Z is the number of blades, NS the number of points on the blade, it represents the complex output of the fft function
    - `Mag`: [ZxNS], contains the absolute values of the Fourier transform along the blades

* `Angle`: [ZxNS], contains the phase of the Fourier transform along the blades
* `MagNorm`: [ZxNS], contains the absolute values of the Fourier transform along the blades
* `DFT`: [1xZ] is the mean value, over the different nodes, of the variable `Mag`. It represents the spectrum of nodal diameter (considering both positive and negative nodal diameters)
* `DominantND`: [1x1], is the number of nodal diameter that has the highest value on the DFT
* `DFTnorm`: [1xZ] Variable `DFT` but normalized for the maximum component to be equal to 1

10.7 Matlab function `shaftAnalysis`

Given one full solution table calculates the main shaft properties such as the bending, rotation angle due to torsion, normal deformation along the axial coordinate.

```
function shaftOutput = shaftAnalysis(solTable, modeN, p)
```

- solTable: [structure] **Full solution table** of the full rotor model
- modeN: [1x1] index of the mode user wants to analyse
- p:[1x1] number for specifying whether you want graphs as an output. p = 1 for making graphs, p=0 for only numeric output
- specifier: [text string] 't' for tangential component (default) , 'a' for axial component

10.8 Matlab script `fourierPoint`

This function, given the coordinates of a generic point on the model, generates a circular ring of N points around the rotor axis, then performs the Discrete Fourier Transform of the solution for that point (either for axial or tangential component).

```
X = node_coords(:,2);
Y = node_coords(:,3);
Z = node_coords(:,4);
scatter3(X,Y,Z);




point1 = [-0.0038,0.0144 ,0.0038]; %choose a point
```

```
N =12;
theta = 0:(2*pi/N):(2*pi*(N-1)/N); % angles between the points
RotMat = @(th) [1 0 0; 0 cos(th) -sin(th); 0 sin(th) cos(th)]; %define rotation matrix
    to find the position of the other points
for i = 1:length(theta)
points(:,i) = RotMat(theta(i))*point1'; %calculate tyhe position of all the points
end

indexes = [];
err = [];
for i = 1:N %loop for finding the point with the minimal error
err = ([X,Y,Z] - ones(height(X),1)*points(:,i)');
err = err(:,1).^2 +err(:,2).^2 + err(:,3).^2;
[minerr(i), indexes(i)] = min(err);
hold on;
scatter3(X(indexes(i)),Y(indexes(i)),Z(indexes(i)));
end



ux = solTable_tun.Mode201.ux;
uy = solTable_tun.Mode201.uy;
uz = solTable_tun.Mode201.uz;
y = solTable_tun.Mode201.Y;
z = solTable_tun.Mode201.Z;
%transform deformations to polar (axial, tangential, radial)
u_ax = ux; %axial deformation
u_r = imag((y+ uy + 1i.*(z+uz))./(y + 1i.*z)).*sqrt(z.^2 + y.^2); % radial deformation
u_tang = real((y+ uy + 1i.*(z+uz))./(y + 1i.*z)).*sqrt(z.^2 + y.^2); % tangential
    deformation

figure;
fft1 = [];
fft1 = fft(u_tang(indexes)); %choose to perform the fft on the tangential deflections

DFT=fft1;

if mod(N, 2) ==0 %case even
pivot = ceil(N/2);
DFT =fft1(1:7);
DFT(2:6) = DFT(2:6) + flip(fft1(8:end));
else
pivot = ceil((N+1)/2);
DFT =[DFT(pivot), DFT(1:pivot+1)+ flip(DFT(1:pivot-1))];
end
```

10.9 Matlab function `Klauke`

This function computes the Klauke definitions of Ratio of the DFT components as well as Mode fill factor, Localization grade for one mode given a reduces solution table.

`function [zita, ModeFKeit, xi, LokaGra] = Klauke(`*`FourOut, ModeN`*`)`

- `FourOut`: [structure] Fourier output structure for one reduced solution table, it is the output of the function `four_decomp`
- `ModeN`: [1x1] number of the mode user wants to calculate

```
function [ModeFkeit, zita, csi, LokaGra] = Klauke(fourOut, numMode)

DFT = fourOut.(['Mode',num2str(numMode)]).DFT;
N = length(DFT);

if mod(length(DFT), 2) ==0 %case even
pivot = ceil(N/2);
DFT =[DFT(pivot), DFT(pivot+1:end-1)+ flip(DFT(1:pivot-1)), DFT(end)];
else
pivot = ceil(N+1/2);
DFT =[DFT(pivot), DFT(pivot+1:end)+ flip(DFT(1:pivot-1))];
end
zita = sum(DFT)/max(DFT);

if mod(N, 2) ==0 %case even
CSM_max = N/2;
else
CSM_max = N/2+0.5;
end
ModeFkeit = (zita-1)/CSM_max;

mean(fourOut.(['Mode',num2str(numMode)]).bladePotrait');
[M, Mi] = max(abs(ans));

tipU = fourOut.(['Mode',num2str(numMode)]).bladePotrait(Mi,:);
NDdominant = abs(fourOut.(['Mode',num2str(numMode)]).DominantND);

if floor(N/2) == N/2
NDmax = N/2;
else
NDmax = (N-1)/2;
end

RMS = rms(tipU);
M = max(abs(tipU));
```

```
    if abs(NDdominant) == 0 || abs(NDdominant) == NDmax
    beta = 1;
    else
    beta = sqrt(2);
    end

    csi = M/RMS;

    LokaGra = abs((csi - beta)/(sqrt(N) - beta));

    end
```

10.10 Matlab function `mactable`

This function calculates the **Modal assurance criterion** between the modes contained in two reduced solution tables, creating a MAC table.

`function matrix = mactable(`*`redsolA, redsolB, modeIdxs`*`)`

- `redSolA`: [structure] first reduced solution table for the comparison
- `redSolB`: [structure] second reduced solution table for the comparison
- `modeIdxs`: [Xx1] vector of arbitrary length X, containing the indexes of the modes to include in the comparison

```
    function matrix = mactable(redsolA, redsolB, modeIdxs)
    %extract the reference modes from one blade in the tuned model
    %modIdxs is the vector containing the mode numbers of all the modes you
    %want to compare
    psi_A = [];
    psi_B = [];

    Z = length(fieldnames(redsolA.(['Mode',num2str(modeIdxs(1))]))); %number of
blades
    for j = 1:length(modeIdxs) %for each mode specified in the list

    Eigvect_A = [];
    moden = modeIdxs(j);
    for bladen = 1:Z
    gesamVerf =
redsolA.(['Mode',num2str(moden)]).(['Blade',num2str(bladen)]).GesamVerf;
    Eigvect_A = [Eigvect_A; gesamVerf]; %list the total nodal deformationsin an
arra
```

```
    end
    psi_A = [psi_A, Eigvect_A]; %create an array with total deformations on each
colum for each mode

    %extract solution for the solution table B
    Eigvect_B = [];
    for bladen = 1:Z
    gesamVerf =
redsolB.(['Mode',num2str(j)]).(['Blade',num2str(bladen)]).GesamVerf;
    Eigvect_B = [Eigvect_B; gesamVerf];
    end
    psi_B = [psi_B, Eigvect_B]; %create an array with total deformations on each
colum for each mode
    end

    %unpack psi_b in the blades components
    length_ns = height(psi_A)/Z;
    for bladen = 1:Z
    Psi_B.(['Blade',num2str(bladen)]) =
psi_B(((bladen-1)*length_ns+1):((bladen-1)*length_ns+length_ns),:);
    end

    %vector of the possible orders for correct orientation
    orders(:,1) =1:1:Z;
    for i = 2:Z
    orders(:,i) = circshift(orders(:,i-1),1);
    end

    for i = 1:Z %recompose the arrays B in all the possible orders
    Psi_B.(['ord',num2str(i)]) = [];
    for j = 1:Z
    Psi_B.(['ord',num2str(i)]) = [Psi_B.(['ord',num2str(i)]);
Psi_B.(['Blade',num2str(orders(j,i))])];
    end % Close the inner loop
    end % Close the outer loop



    %i : index of the A mode number
    %j : index of the B mode number
    for i = 1:length(modeIdxs)
    Eigenvect_A = psi_A(:,i);
    for j = 1:length(modeIdxs)
    mac = zeros(Z,1);
    MAC = 0;
    for ord = 1:Z %loop on all the orders to find the max MAC value
```

```
Eigenvect_B = Psi_B.(['ord',num2str(ord)])(:,j);
mac(ord) = calc_MAC(Eigenvect_B, Eigenvect_A);
end
MAC = max(mac);
matrix(i,j) = MAC;
end
end
figure;
pcolor(matrix);
title('MAC matrix');
ylabel('Tuned mode index');
xlabel('Mistuned mode index');
end
```

Output `matrix` is a [X x X] symmetric matrix, with MAC values comparing the reduced solution table A and reduced solution table B.

10.11 Matlab function `calc_MAC`

This function calculates the MAC of two vectors of the same size. It normalizes mode shapes and then it computes the scalar product.

`function MAC = calc_MAC(`*`vector1,vector2`*`)`

- `vector1`: [Fx1] first array
- `vector2`: [Fx1] second array
- `MAC`: [1x1] MAC value

```
function mac_value = calc_MAC(vector1, vector2)
% Check if the input vectors have the same length
if length(vector1) ~= length(vector2)
error('Input vectors must have the same length');
end

% Compute the MAC value
numerator = abs(vector1' * vector2)^2;
denominator = (vector1' * vector1) * (vector2' * vector2);

mac_value = numerator / (denominator+1e-18);
end
```

10.12 Matlab function `normalizeModeShapes`

This function normalises the mode shapes evaluated on turbine tips. It takes as input the reduced solution tables evaluated on the turbine, compressor MB, compressor SB tips. The mode shapes are normalized such that the maximum defrection =1.

`function [TurbN, compMBN, compSBN] = normalizeModeShapes(Turb, compMB, compSB, stMode, endMode)`

- `TurbN` normalised turbine shape reduced solution table
- `compMBN` normalised compressor main bladereduced solution table
- `compSBN` normalised compressor splitter blade shape reduced solution table

```
function [TurbN, compMBN, compSBN] = normalizeModeShapes(Turb, compMB, compSB,
   stMode, endMode)

[~,MaxTurb, MaxMB] = AmpRat(Turb, compMB,stMode,endMode);
[~,MaxTurb, MaxSB] = AmpRat(Turb, compSB,stMode,endMode);

for mode = stMode:endMode
MaxModel(mode) = max([MaxTurb(mode), MaxMB(mode), MaxSB(mode)]);

for blade = 1:length(fieldnames(Turb.(['Mode',num2str(mode)])))
TurbN.(['Mode',num2str(mode)]).(['Blade',num2str(blade)]).GesamVerf =
   Turb.(['Mode',num2str(mode)]).(['Blade',num2str(blade)]).GesamVerf./MaxModel(mode);
TurbN.(['Mode',num2str(mode)]).(['Blade',num2str(blade)]).ux =
   Turb.(['Mode',num2str(mode)]).(['Blade',num2str(blade)]).ux./MaxModel(mode);
TurbN.(['Mode',num2str(mode)]).(['Blade',num2str(blade)]).uy =
   Turb.(['Mode',num2str(mode)]).(['Blade',num2str(blade)]).uy./MaxModel(mode);
TurbN.(['Mode',num2str(mode)]).(['Blade',num2str(blade)]).uz =
   Turb.(['Mode',num2str(mode)]).(['Blade',num2str(blade)]).uz./MaxModel(mode);
TurbN.(['Mode',num2str(mode)]).(['Blade',num2str(blade)]).X =
   Turb.(['Mode',num2str(mode)]).(['Blade',num2str(blade)]).X;
TurbN.(['Mode',num2str(mode)]).(['Blade',num2str(blade)]).Y =
   Turb.(['Mode',num2str(mode)]).(['Blade',num2str(blade)]).Y;
TurbN.(['Mode',num2str(mode)]).(['Blade',num2str(blade)]).Z =
   Turb.(['Mode',num2str(mode)]).(['Blade',num2str(blade)]).Z;
end

for blade = 1:length(fieldnames(compMB.(['Mode',num2str(mode)])))
compMBN.(['Mode',num2str(mode)]).(['Blade',num2str(blade)]).GesamVerf =
   compMB.(['Mode',num2str(mode)]).(['Blade',num2str(blade)]).GesamVerf./MaxModel(mode);
compMBN.(['Mode',num2str(mode)]).(['Blade',num2str(blade)]).ux =
   compMB.(['Mode',num2str(mode)]).(['Blade',num2str(blade)]).ux./MaxModel(mode);
```

```
compMBN.(['Mode',num2str(mode)]).(['Blade',num2str(blade)]).uy =
   compMB.(['Mode',num2str(mode)]).(['Blade',num2str(blade)]).uy./MaxModel(mode);
compMBN.(['Mode',num2str(mode)]).(['Blade',num2str(blade)]).uz =
   compMB.(['Mode',num2str(mode)]).(['Blade',num2str(blade)]).uz./MaxModel(mode);
compMBN.(['Mode',num2str(mode)]).(['Blade',num2str(blade)]).X =
   compMB.(['Mode',num2str(mode)]).(['Blade',num2str(blade)]).X;
compMBN.(['Mode',num2str(mode)]).(['Blade',num2str(blade)]).Y =
   compMB.(['Mode',num2str(mode)]).(['Blade',num2str(blade)]).Y;
compMBN.(['Mode',num2str(mode)]).(['Blade',num2str(blade)]).Z =
   compMB.(['Mode',num2str(mode)]).(['Blade',num2str(blade)]).Z;
end

for blade = 1:length(fieldnames(compSB.(['Mode',num2str(mode)])))
compSBN.(['Mode',num2str(mode)]).(['Blade',num2str(blade)]).GesamVerf =
   compSB.(['Mode',num2str(mode)]).(['Blade',num2str(blade)]).GesamVerf./MaxModel(mode);
compSBN.(['Mode',num2str(mode)]).(['Blade',num2str(blade)]).ux =
   compSB.(['Mode',num2str(mode)]).(['Blade',num2str(blade)]).ux./MaxModel(mode);
compSBN.(['Mode',num2str(mode)]).(['Blade',num2str(blade)]).uy =
   compSB.(['Mode',num2str(mode)]).(['Blade',num2str(blade)]).uy./MaxModel(mode);
compSBN.(['Mode',num2str(mode)]).(['Blade',num2str(blade)]).uz =
   compSB.(['Mode',num2str(mode)]).(['Blade',num2str(blade)]).uz./MaxModel(mode);
compSBN.(['Mode',num2str(mode)]).(['Blade',num2str(blade)]).X =
   compSB.(['Mode',num2str(mode)]).(['Blade',num2str(blade)]).X;
compSBN.(['Mode',num2str(mode)]).(['Blade',num2str(blade)]).Y =
   compSB.(['Mode',num2str(mode)]).(['Blade',num2str(blade)]).Y;
compSBN.(['Mode',num2str(mode)]).(['Blade',num2str(blade)]).Z =
   compSB.(['Mode',num2str(mode)]).(['Blade',num2str(blade)]).Z;
end

end
end
```

Bibliography

[1] M. Sasakaros, L. Mann, M. Shafferus, and M. Wirsum. Determination of vibration properties and reliable frequency estimation for synchronous vibrations through improved blade-tip-timing techniques without a once-per-revolution sensor. In *Proceedings of the ASME 2024 Turbomachinery Technical Conference and Exposition*, 2024.

[2] Li Minghai, Yuanzhe Li, Feng Jiang, and Jie Hu. An optimization of a turbocharger blade based on fluid–structure interaction. *Processes*, 10(8):1569, 2022.

[3] Roman Drozdowski. *Berechnung der Schwingbeanspruchungen in Radialturbinenrädern unter Berücksichtigung realer Bauteilgeometrien.* PhD thesis, Fakultät Maschinenwesen der Technischen Universität Dresden, 2011.

[4] M. Shafferus, M. Sasakaros, M. Wirsum, A. Zobel, D. Vogt, A. Nakos, and B. Beirow. Experimental investigation of synchronous flow-induced blade vibrations on a radial turbine. In *Proceedings of the ASME 2023 Turbomachinery Technical Conference and Exposition*, 2023.

[5] A. Nakos, B. Beirow, and A. Zobel. Mistuning and damping of a radial turbine wheel: Fundamental analyses and design of intentional mistuning pattern. In *Proceedings of ASME Turbo Expo 2021 Turbomachinery Technical Conference and Exposition*, 2021.

[6] Gísli Óttarsson. *Dynamic Modeling and Vibration Analysis of Mistuned Bladed Disks.* PhD thesis, University of Michigan, 1994.

[7] Raj Subbiah and Jeremy Eli Littleton. *Rotor and Structural Dynamics of Turbomachinery.* Springer, 2018.

[8] Thomas Klauke. *Schaufelschwingungen realer integraler Verdichterräder im Hinblick auf Verstimmung und Lokalisierung.* PhD thesis, Brandenburgische Technische Universität Cottbus, 2007.

[9] A. Gugliotta. *Elementi Finiti, Parte I.* Politecnico di Torino, 2002.

[10] Alexander Jan Esper. *Experimentelle Untersuchungen von strömungsinduzierten Schaufelschwingungen in Radialturbinen.* PhD thesis, Fakultät für Maschinenwesen der Rheinisch-Westfälischen Technischen Hochschule Aachen, 2019.

[11] Richard J. Roelke. The effect of rotor blade thickness and surface finish on the performance of a small axial flow turbine. *National Aeronautics and Space Administration Lewis Research Center*, 1982.

[12] A. Wilson and T. Utengen. Turbine blade dynamics and blade-vane interaction in a radial inflow turbine. *AGARD CP 537*, 1993.

[13] Jianyao Yao, Jianjun Wang, and Qihan Li. Improved modal localization and excitation factors for understanding mistuned bladed disk response. *Journal of Propulsion and Power*, 27(1), 2011.

[14] M.-T. Yang and J. H. Griffin. A reduced-order model of mistuning using a subset of nominal system modes. *Gas Turbines Power*, 1999.

[15] D. J. Ewins. Vibration modes of mistuned bladed disks. *Journal of Engineering for Power*, 1976.

[16] M. Klaus. *Strömungsinduzierte Schaufelschwingungen in Radialturbinen mit Beschaufeltem Spiralgehäuse*. PhD thesis, Universität Karlsruhe, 2007.

[17] A. Zobel, A. Nakos, C. Fuhrer, M. Vogt, and B. Beirow. On the influence of bearing modeling details on the dynamical system effects of a mid-size turbocharger rotor. In *Proceedings of ASME Turbo Expo 2023 Turbomachinery Technical Conference and Exposition*, 2023.

[18] G. Genta. *Vibration Dynamics and Control*. Springer, 2009.

[19] Ansys Inc. *Ansys Help*. 2023.

[20] M. P. Castanier and C. Pierre. Modeling and analysis of mistuned bladed disk vibration: Status and emerging directions. *Journal of Propulsion and Power*, 2006.

[21] D. S. Whitehead. Effect of mistuning on the vibration of turbomachine blades induced by wakes. *Journal Mechanical Engineering Science*, 1966.

[22] D. L. Thomas. Dynamics of rotationally periodic structures. *International Journal for Numerical Methods in Engineering*, 1979.

[23] Randall J. Allemang. The modal assurance criterion: Twenty years of use and abuse. *Sound and Vibration*, 2003.

[24] Miroslav Pastor, Michal Binda, and Tomáš Harcarik. Modal assurance criterion. *Procedia Engineering*, 48, 2012.

[25] D. J. Ewins. *Modal Testing: Theory and Practice*. Wiley, 1984.

[26] P. Vargiu, C.M. Firrone, S. Zucca, and M.M. Gola. A reduced order model based on sector mistuning for the dynamic analysis of mistuned bladed disks. *Dynamics of Rotating Machinery*, 2010.